

UNIVERSITE D'AUVERGNE  
ECOLE DOCTORALE  
DES SCIENCES POUR L'INGENIERIE

# T H E S I S

to obtain the title of

**PhD in Computer Science**

of Université d'Auvergne

**Speciality: Medical Image Analysis**

Defended by

Amir YAVARIABDI

## Mapping Endometrial Implants by Registering Transvaginal Ultrasound to Pelvic Magnetic Resonance Images

Prepared at the Image Science for Interventional Techniques  
(ISIT) lab, the ALCoV group

defended on July 25, 2014

### Jury :

<i>Reviewers :</i>	Prof. David FOFI,	Université de Bourgogne
	Prof. Denis KOUAMÉ,	Université Paul Sabatier
<i>Examinators :</i>	Prof. Fabien FESCHET,	Université d'Auvergne
	Ph.D. Jean-Denis DUROU,	Université Paul Sabatier
<i>Invited :</i>	Prof. Michel CANIS,	CHU Clermont and Université d'Auvergne
<i>Director :</i>	Prof. Adrien BARTOLI,	Université d'Auvergne
<i>Co-Advisor :</i>	Ph.D. Chafik SAMIR,	Université d'Auvergne.

# Acknowledgements

I would like to express my sincere gratitude to my PhD advisors, Professors Adrien Bartoli and Doctor Chafik Samir, for their invaluable help and support, their continuous guidance and precious advice during these past three years. Adrien is someone you will instantly love and never forget once you meet him. He has been supportive and he is one of the smartest people I know. I would like to thank you for encouraging my research and for allowing me to grow as a research scientist. Your advice on research has been invaluable. Chafik has been supportive and has given me the freedom to pursue my project without objection. He has also provided insightful discussions about the research. I am also very grateful to Chafik for his scientific advice and knowledge and many insightful discussions and suggestions. He is my primary resource for getting my Math questions answered. I also have to thank the members of my PhD committee, Professors David Fofi, Fabien Feschet, Denis Kouamé, Michel Canis, and Doctor Jean-Denis Durou for serving as my committee members. I also want to thank you for letting my defence be an enjoyable moment, and for your brilliant comments and suggestions, thanks to you.

I thank all the former and present members of the Image Science for Interventional Techniques (ISIT) laboratory: Doctor Abed Malti (nice and helpful person who has been pretty supportive during my PhD, best wishes as you start your career at Inria), Doctor Daniel Pizarro (extremely knowledgeable in just about everything, helpful, and friendly. Best of luck Daniel), Viateur Tuyisenge (so friendly and I am glad to have him as a friend), and Julia Alliot (has been so helpful during my thesis submission and defence). I also thank my other great office mates who have been supportive in every way.

I would especially like to thank gynaecologists and radiologists at CHU Clermont-Ferrand. All of you have been there to support me when I collected data for my Ph.D. thesis.

A special thanks to my family. Words can not express how thankful I am to my mother and father. My parents have sacrificed their lives for myself and provided unconditional care and love. I truly love them so much, and I would not have made it this far without them. I would also like to thank to my best friend and soul-mate. Begum Karabatak has been a great supporter during my bad and good moments. These past three years have not been an easy ride, both personally and academically. I truly thank Begum for staying by my side, even when I was irritable.

# Abstract

Endometriosis is a multifocal gynecologic disorder which forms during the reproductive cycle, mainly causing severe pelvic pain and sometimes infertility. Even though findings at physical examination may be suggestive, medical imaging is mandatory for diagnosis and preoperative surgical planning. The imaging modalities that have mostly been employed for preoperative diagnosis of endometriosis are Transvaginal Ultrasonography (TVUS) and Magnetic Resonance (MR) scanning. TVUS is a reliable method for detecting small endometrial tissues and estimating their depth of infiltration. MR scanning is used as a complimentary examination, since it reveals the patient's pelvic anatomy and large endometrial tissues, and gives high resolution and fine detail 3D images of the patient's pelvis. The radiologists are faced with an overwhelming amount of information when comparing these two imaging modalities but the visual interpretation of these images is not an easy task. Therefore, to ease the task of the medical experts in both interpretation and decision making, we need to move towards more comprehensive visualization techniques. To achieve this, the automatic fusion between TVUS and MR images is needed to remove many of the hurdles involved in determining the best plan and transferring it to surgery to reduce the trauma done to healthy tissues and to avoid under-cutting the implants, which may cause recurrence.

This thesis investigates the applicability of various deformable registration methods to align preoperative 2D TVUS and 3D MR images of the female pelvis. These methods facilitate the transfer of two types of information from TVUS to MR data: 1) the location and shape of endometrial implants, and 2) the implants' depth of infiltration in the host tissue. The major advantage of mapping this information

into the MR data is that the implant’s location and the resection lines can then be clearly defined with respect to the patient’s anatomy. We provide comparisons and experimental results for some deformable intensity- and feature-based registration methods including non-parametric and parametric (e.g. spline-based methods) deformation models. The deformable intensity-based multimodal image registration method is computationally costly and is not well-suited to TVUS-MR registration. Our first goal is to propose a 2D/2D feature-based multimodal image registration and fusion method to cope with the limitations of the MR and TVUS imaging in observing the endometrial implants in the pelvic area. In order to make sure that we obtain clinically meaningful deformations, we use a nonparametric model which is not defined on the basis of a finite set of parameters and is more suited in the absence of prior knowledge. The solution of this energy functional minimization is obtained by a joint-minimization of the contour alignment of the segmented pelvic regions and the internal energy. The main drawback of the feature-based methods is that they highly depend on an expert user’s inputs. To reduce user interaction, we use a parametrization-based approach between manually segmented contours to define dense correspondences. Although this framework decreases the dependency of the method on the expert users, it still needs an expert user to establish a few point correspondences manually which is a challenging and time-consuming process. It is challenging because: 1) There is a huge deformation between the two modalities. 2) In many TVUS data, the implants’ neighboring organs are only partially visible due to the small field of view of the TVUS scanner. 3) The tissues which are exhibited in both MR and TVUS images do not belong to the same slice. Therefore, we further investigate upon an automatic method for determining pairs of corresponding points to decrease the amount of user interaction. To achieve this, we take advantage of the Iterative Closest Point algorithm. Even though this method establishes point correspondences automatically, it still relies on the user to segment the corresponding contours. However, this is clinically acceptable, since manual segmentation of the pelvic organs can be achieved in a reasonable amount of time. Moreover, from a technical point of view, automatic segmentation in this context is virtually impossible

due to three main reasons. First, the endometrial implants can be anywhere in the patient’s pelvic area, so that we need a segmentation algorithm to be able to detect all the tissues and lesions in this region. Second, the small endometrial implants, which can be seen in TVUS images, infiltrate through the walls of organs, therefore it is difficult to automatically segment both the implants and the host tissue with a high precision. Third, the MR images cannot clearly show the organs’ boundary when the endometrial implants connect two pelvic organs, so that the segmentation process is prone to errors. Consequently, we use manual segmentation to avoid incorporating the segmentation errors in TVUS-MR registration process. In the proposed 2D/2D TVUS-MR registration methods, the problem mainly lies in finding the 2D MR slice from an MR volume that matches the 2D TVUS image. Therefore, to further improve the user experience, we propose a slice-to-volume registration method that directly registers a set of 2D curves in the 2D TVUS image to a set of corresponding 3D surfaces in the 3D MR volume. Besides its advantages on avoiding to change the dimensionality of the MR data, slice-to-volume registration is further useful in making a more accurate preoperative surgical planning. This is due to the fact that a computer-aided reconstruction system can precisely reconstruct 3D models of the patient’s pelvic organs from the MR volumetric data, which simply enhances the anatomy of this complex part of the body. Therefore, mapping the endometrial implants and highlighting the resection lines on the 3D models of the patient’s pelvic organs may ease the task of surgeons in planning.

# Publications

1. **A.Yavariabdi**, C. Samir, A. Bartoli: *3D Medical Image Enhancement based on Wavelet Transforms*, Proceedings of the Medical Image Understanding and Analysis Conference (MIUA), London, UK, July 2011.
2. **A. Yavariabdi**, C. Samir, A. Bartoli, D. Da Ines and N. Bourdel: *Mapping Endometrial Implants by 2D/2D Registration of TVUS to MR Images from Point Correspondences*, Proceedings of the IEEE International Symposium on Biomedical Imaging (ISBI), San Francisco, CA, USA, April 2013.
3. **A. Yavariabdi**, C. Samir, A. Bartoli, D. Da Ines and N. Bourdel: *Contour-Based TVUS-MR Image Registration for Mapping Small Endometrial Implants*, Proceedings of the Computational and Clinical Applications in Abdominal Imaging at MICCAI (ABD-MICCAI), Nagoya, Japan, September 2013.

# Contents

<b>1</b>	<b>Introduction</b>	<b>1</b>
1.1	Computer-Aided Diagnosis . . . . .	1
1.2	Endometriosis . . . . .	6
1.3	Diagnosis . . . . .	8
1.3.1	Laparoscopy . . . . .	9
1.3.2	Transvaginal Ultrasound . . . . .	10
1.3.3	Magnetic Resonance Imaging . . . . .	11
1.4	Surgical Treatment . . . . .	12
1.5	Objectives . . . . .	13
1.6	Overview of the Thesis . . . . .	16
<b>2</b>	<b>Background</b>	<b>19</b>
2.1	Introduction . . . . .	19
2.2	Notation . . . . .	21
2.3	Calculus of Variations . . . . .	22
2.3.1	Basic Principles . . . . .	23
2.3.1.1	Definition of a Functional . . . . .	23
2.3.1.2	The Variational Problem . . . . .	24
2.3.2	Generalizing the Variational Problem . . . . .	25
2.4	Function Models Based on Splines . . . . .	26
2.4.1	B-Spline Basis for Polynomial Splines . . . . .	28
2.4.1.1	B-Spline Curve . . . . .	30
2.4.1.2	Uniform Cubic B-Spline . . . . .	32

2.4.1.3	Uniform Cubic B-Spline in Higher Dimensions . . . . .	33
2.4.1.4	Natural Spline . . . . .	34
2.4.2	Radial Basis Functions . . . . .	35
2.4.2.1	The Interpolation Problem . . . . .	36
2.4.2.2	The Thin-Plate Spline . . . . .	37
<b>3</b>	<b>Image Registration</b>	<b>39</b>
3.1	Problem Definition . . . . .	39
3.2	Alignment Measure . . . . .	42
3.2.1	Feature-Based Image Registration . . . . .	42
3.2.1.1	Extrinsic Features (Fiducial Markers) . . . . .	42
3.2.1.2	Intrinsic Features . . . . .	43
3.2.2	Intensity-Based Image Registration . . . . .	43
3.2.2.1	Intensity Alignment Measures . . . . .	44
3.3	Transformation Models . . . . .	46
3.3.1	Nonparametric Deformation Models . . . . .	47
3.3.1.1	Elastic Body Models . . . . .	48
3.3.1.2	Viscous Fluid Flow Models . . . . .	48
3.3.1.3	Diffusion Models . . . . .	49
3.3.1.4	Curvature Models . . . . .	49
3.3.2	Parametric Deformation Models . . . . .	50
3.4	Optimization . . . . .	50
3.5	Interpolation . . . . .	51
3.6	Evaluation of Registration Methods . . . . .	51
3.6.1	2D/2D Evaluation Metrics . . . . .	51
3.6.2	3D/2D Evaluation Metrics . . . . .	53
<b>4</b>	<b>Literature Review</b>	<b>55</b>
4.1	Introduction . . . . .	55
4.2	US-MR Image Registration . . . . .	56
4.2.1	Intensity-Based Methods . . . . .	56

4.2.2	Feature-Based Methods . . . . .	58
4.2.3	Hybrid Methods . . . . .	61
4.3	The Iterative Closest Point Algorithm (ICP) . . . . .	62
4.4	Slice-to-Volume Registration . . . . .	65
4.5	Conclusion . . . . .	68
<b>5</b>	<b>Registration Strategy</b>	<b>70</b>
5.1	Introduction . . . . .	70
5.2	Image Registration . . . . .	71
5.2.1	Point-Based Image Registration Based on Thin-Plate Splines . . . . .	71
5.2.2	Intensity-Based Image Registration with NMI . . . . .	77
5.2.2.1	Deformation Modeling with B-Splines . . . . .	77
5.2.2.2	Similarity . . . . .	79
5.2.2.3	Optimization . . . . .	79
5.3	Experimental Results . . . . .	81
5.3.1	Material . . . . .	81
5.3.2	Results and Discussion . . . . .	82
5.4	Conclusion . . . . .	86
<b>6</b>	<b>Parametrization-Based 2D/2D Registration</b>	<b>88</b>
6.1	Introduction . . . . .	88
6.2	Registration Procedure . . . . .	90
6.2.1	Correspondence by Arc-Length Parametrization . . . . .	90
6.2.2	Densification . . . . .	92
6.2.2.1	Diffusion Regularizer . . . . .	93
6.2.2.2	Divergence and Curl Regularizer . . . . .	95
6.2.2.3	Curvature Regularizer . . . . .	100
6.3	Experimental Results . . . . .	102
6.3.1	Material . . . . .	102
6.3.2	Results and Discussion . . . . .	102
6.4	Conclusion . . . . .	108

<b>7</b>	<b>One-Step ICP-Based 2D/2D Registration</b>	<b>110</b>
7.1	Introduction . . . . .	110
7.2	2D Euclidean Distance Transform . . . . .	112
7.3	Iterative Closest Point Algorithms (ICP) . . . . .	115
7.3.1	Variational Two-Step ICP . . . . .	116
7.3.2	Variational One-Step ICP . . . . .	118
7.3.2.1	Euler-Lagrange Equation . . . . .	118
7.3.2.2	Numerical Approximation . . . . .	119
7.4	Experimental Results . . . . .	122
7.4.1	Material . . . . .	122
7.4.2	Results and Discussion . . . . .	122
7.4.2.1	Tests on Semi-Synthetic Data . . . . .	123
7.4.2.2	Tests on Real Patient Data . . . . .	126
7.5	Conclusion . . . . .	131
<b>8</b>	<b>One-Step ICP-Based 2D/3D Registration</b>	<b>132</b>
8.1	Introduction . . . . .	132
8.2	Registration Procedure . . . . .	136
8.2.1	A Variational Formulation for Two-Step ICP . . . . .	137
8.2.2	A Variational Formulation in One-Step Using Distance Transform	138
8.2.2.1	Euler-Lagrange Equation and Numerical Approximation	139
8.2.2.2	Handling Multiple Surfaces . . . . .	143
8.3	Experimental Results . . . . .	144
8.3.1	Material and Clinical Motivations . . . . .	144
8.3.2	Results and Discussion . . . . .	145
8.3.2.1	Tests on Semi-Synthetic Data . . . . .	146
8.3.2.2	Tests on Real Patient Data . . . . .	155
8.4	Conclusion . . . . .	161
<b>9</b>	<b>Conclusion and Future Work</b>	<b>163</b>
9.1	Conclusion . . . . .	163

9.2	Future Work . . . . .	169
<b>A</b>	<b>Image Resolution Enhancement</b>	<b>171</b>
A.1	Introduction . . . . .	171
A.2	Image resolution enhancement . . . . .	172
A.3	Proposed algorithm for 3D images . . . . .	173
A.4	Experimental result . . . . .	175

# Chapter 1

## Introduction

### Contents

---

<b>1.1</b>	<b>Computer-Aided Diagnosis . . . . .</b>	<b>1</b>
<b>1.2</b>	<b>Endometriosis . . . . .</b>	<b>6</b>
<b>1.3</b>	<b>Diagnosis . . . . .</b>	<b>8</b>
1.3.1	Laparoscopy . . . . .	9
1.3.2	Transvaginal Ultrasound . . . . .	10
1.3.3	Magnetic Resonance Imaging . . . . .	11
<b>1.4</b>	<b>Surgical Treatment . . . . .</b>	<b>12</b>
<b>1.5</b>	<b>Objectives . . . . .</b>	<b>13</b>
<b>1.6</b>	<b>Overview of the Thesis . . . . .</b>	<b>16</b>

---

### 1.1 Computer-Aided Diagnosis

Computer-aided diagnosis has drawn the attention of researchers for decades. A great number of works related to diagnostic radiology and medical imaging has been proposed [1]. The key idea of computer-aided diagnosis is to assist radiologist and surgeons in the interpretation of medical images by employing computer systems to provide complimentary information [2]. Generally, computer-aided diagnosis is considered as a second reader by analysing data and finding abnormalities using digital signal processing, computer vision, and machine learning techniques [3]. Thus, it may ease the task of the medical experts in decision making. Studies on computer-aided diagnosis systems reveal that these systems can improve diagnosis and the accuracy of the radiologist' decision making. Moreover, these systems reduces the increasing

demand of radiologists' time caused by the increasing data volume, decrease risk of obtaining a false-negative result for detecting malignant and cancerous tissues due to fatigue or distraction, and overcome differences in diagnosis which may occur because of differences in radiologists' experiences. The majority of computer-aided diagnosis systems are designed to help the physicians for the following organs: colon, prostate, liver, heart, lung, chest, breast, vascular, skeletal, retina, and the brain.

The concept of computer-aided diagnosis in radiology was established in the 1960s. At that time, many researchers believed that computers could help or even replace radiologists in estimating abnormalities, since machines are more accurate at performing certain tasks than human. In 1963, Lodwick et al. [4] investigated the usefulness of using a computer in the evaluation of bone cancer. In 1964, Meyers et al. [5] developed an automatic system to investigate chest photofluorograms to separate the normal chest radiographs from the abnormal ones by measuring the cardio-thoracic ratio [2]. In 1967, Winsberg et al. [6] proposed a computer-aided diagnosis system to individually analyze breast X-ray images of each patient for detecting abnormalities based on density patterns in different regions inside each breast and between right and left breasts. Although many interesting attempts had been made to understand the usefulness of using a computer in aiding diagnosis, these early reports were not very effective. This is due to the fact that at that time, computers were not enough powerful and advanced digital signal processing techniques and medical imaging scanners were not available.

With advances in digital signal processing, computer vision, and machine learning techniques and the availability of powerful computers, many medical imaging techniques, and large databases of cases, the field of computer-aided diagnosis has grown considerably since the 1980s [7]. Since the mid-1980s, many researchers have tried to employ computers to help physicians in several manners. Generally, computer-aided analysis of medical images obtained from different imaging systems involves two stages: (i) Preprocessing and enhancement, (ii) Image registration, image segmentation, and classification.

**Preprocessing.** Preprocessing is a vital task in medical image analysis, since medical imaging acquisition technologies introduce artifacts and noise in the images. Generally, noise often exist in medical imaging, such as ultrasound, Magnetic Resonance (MR) imaging, Computed Tomography (CT), Single Photon Emission Computed Tomography (SPECT), and Positron Emission Tomography (PET). However, removing noise from medical images is not an easy task, since linear filtering algorithms usually fail. Therefore, the effect of noise may be attenuated by much more sophisticated denoising algorithms such as Bayesian algorithms. This is due to the fact that the denoising process should not destroy anatomical details. This property of the denoising algorithms becomes very important in the case of ultrasound images where the noise corrupting the images often contains relevant medical information useful for diagnostic purposes. Many attempts have been made to develop precise algorithms to discard noise without destroying the anatomical structures. For instance, Sanches et al. [8] propose a Bayesian algorithm which removes additive white Gaussian as well as multiplicative noise. The algorithm is based on the maximum a posteriori criterion and edge preserving priors which preserve the anatomical details. Their algorithm is used for heart tracking in ultrasound images. They show that the ultrasound images present a poor quality, so that the boundaries of the cardiac left ventricle can hardly be seen when the heart has a sudden motion. Therefore, each ultrasound sequence is first passed through their denoising algorithm to estimate the boundary of the left ventricle during the whole sequence. Using their method, a tracker is then able to show the abnormalities in the patient's heart more accurately.

In recent years, the demand for resolution enhancement of pictorial data in medical images has increased in order to assist clinicians to make accurate diagnosis. The task of resolution enhancement in medical images is generally to enlarge a region of interest. However, the main issue of concern is preserving details in the enlarged image. In general, interpolated images have some problems such as losing the contrast and blurring the details. Thus, a robust medical image resolution enhancement technique must be able to cope with these two issues. In this manner, we propose a method for 3D image resolution enhancement based on discrete stationary wavelet transforms

to generate sharp high resolution images (for more details, see Appendix A). The proposed algorithm is applied to the full 3D pelvic MR data volume and we show that the results preserve edge features which help the radiologist to more precisely investigate small lesions in the pelvic area to find abnormalities.

**Image registration.** Detecting abnormalities in medical data can be performed by comparing different images of the same patient. Comparing different images is not an easy task, since there are misalignments and dissimilarities between the images which are related to many factors such as sensor noise, patient movement, different imaging scanners, and different radiation exposure. Therefore, in order to precisely and efficiently compare the images and avoid misalignments, an image registration technique must be used. In this way, Díez et al. [9] propose a deformable registration method to detect abnormal structures in mammographic images which are acquired at different time intervals. They show that after performing the registration, the malignant lesion is clearly visible in the difference image. Moreover, the information which is obtained from the registration process can be used to deeply compare and analyse the lesions in the current image with the previous images.

**Segmentation.** Segmentation is an important step in computer-aided diagnosis. It can be defined as a process of dividing an image into regions of similar attributes. Typically, the aim of segmentation algorithms is to extract important features from the image data, from which a description and interpretation of the image can be provided by the computer. Currently, there is a vast number of segmentation methods proposed for medical data. Image segmentation algorithms can be classified in many ways [10]. Segmenting anatomical structures such as the heart, different regions of the brain, and liver in a medical image is a vital and important step for many clinical applications (e.g. visualization, surgical planning, radiation therapy). Segmentation can be considered as an important tool which helps to make accurate decisions for diagnostic purposes. The rapid development of medical imaging scanners such as CT and MR enables us to generate high resolution and fine detail 3D images of

the human body. This improves the accuracy of diagnosis and understanding of diseases. However, the interpretation of the 3D volumetric data requires a lot of time and energy. Therefore, there is a great demand of automated methods to segment multiple organs in an image and to reconstruct the 3D shape of the organs and tissues to decrease the interpretation burden. In this manner, Ulén et al. [11] propose a multi-region model segmentation method to segment different lesions in an image at a time. They apply their method to heart and lung CT images. They show that automatic segmentation and 3D reconstruction of the segmented organs can significantly help the understanding of this huge quantity of data.

**Classification.** After extracting the desired objects in an image, one can use them as an input of classifier to detect what the extracted features are, for instance, lesion/non-lesion or benign/malignant tissues. In this manner, Osareh et al. [12] propose a computer-aided diagnosis system to automatically classify the breast tissues into cancerous/non-cancerous data.

The above-mentioned studies demonstrate that computer-aided diagnosis is capable of improving the radiologists' performance. Therefore, our main goal in this thesis is to propose for the first time a computer-aided diagnosis system to improve radiologists' performance and surgical planning for endometriosis diagnostic purposes.

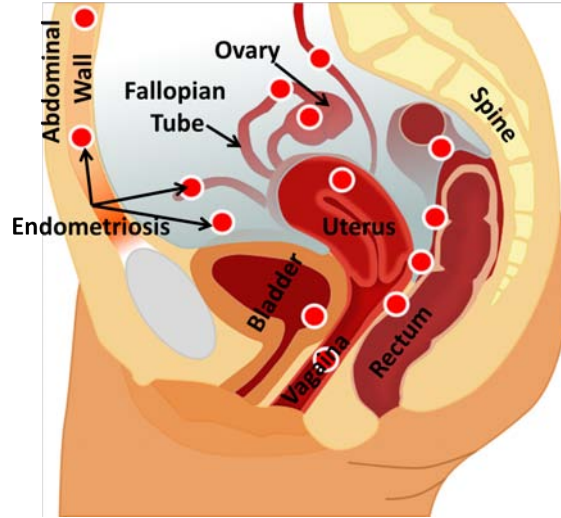


Figure 1-1: The most common localisation of endometriosis. Taken from Wikipedia and modified, <http://en.wikipedia.org/wiki/Endometriosis>.

## 1.2 Endometriosis

Endometriosis is a progressive gynaecological disease in which the cells from the lining of the uterus appear and grow outside of its cavity, typically in the pelvic area [13]. The term endometriosis is derived from the Greek language where “end” means inside, “metra” defines as womb or uterus, and “osis” means disease or abnormality. Endometriosis affects approximately 10% of women of reproductive age [14]. In other words, more than 175 million women across the world must deal with the symptoms of endometriosis during their lives [15].

The most common site of involvement is the ovary, followed in descending order of frequency by deep lesions of the pelvic sub-peritoneal space, the intestinal and the urinary systems [16]. Figure 1-1 shows the most common locations of endometrial lesions in the pelvic cavity. In rare cases, it has been also found inside the bladder, inside the vagina, in the lung, in the nerves, on the skin, spine, and brain.

The symptoms of endometriosis vary widely from patient to patient, with some experiencing no symptoms, and others experiencing the whole gamut. The symptoms

are usually chronic pelvic pain, abnormal bleeding, dysmenorrhea<sup>1</sup>, dyspareunia<sup>2</sup>, and infertility [17]. Among patients that have been diagnosed with endometriosis, up to 30% – 40% may not be able to have children. Note that dysmenorrhea is one of the most common symptoms, and half of the patients with this symptom have been diagnosed with endometriosis [18]. As the disease grows, the pain may progress over time and eventually, the patient may have constant pain, with increased strength during their menstrual cycle. Therefore, this disease may have a substantial negative influence on the patient’s daily life. Consequently, pain is the most prevalent side effect of the disease. In addition to struggling with this tough pain, endometriosis can also have significant influence on patients’ mental well being. In other words, it may cause anxiety, depression, irritability and hopelessness [19]. This is more due to the fact that living with the unknown reason of pain can be far more stressful than living with a chronic medical condition.

Endometriosis has been seen as a progressive disease. Each month during a woman’s menstrual cycle, the endometrial implant responds to the growth and shedding signals as the cells inside the uterine cavity, resulting in internal bleeding. Unlike the cells inside the uterine cavity, there is no outlet for endometrial implant bleeding, which leads to an inflammation due to an immune response. This response results in the formation of scar tissue as part of the healing process and causes severe pain. Sometimes, the scar tissue comes into contact with another inflamed area and forms a band of scar tissue. This process, also known as an adhesion, connects two internal body surfaces that are not naturally connected. This phenomena may lead to urination or bowel movements which also cause chronic pain. Figure 1-2 shows an endometrial implant that connects the uterus to the rectum; those are not connected in healthy patients.

Endometriosis is a common gynaecological disorder associated with infertility and chronic pain. Although this disease has drawn the attention of many for more than a hundred years, the pathology of endometriosis remains unclear, which makes the

---

<sup>1</sup>Dysmenorrhea is painful menstruation.

<sup>2</sup>Dyspareunia is painful sexual intercourse.

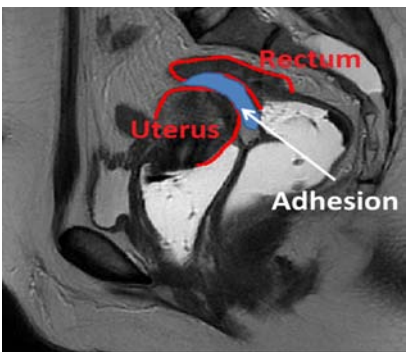


Figure 1-2: An example of endometrial implant which causes forming adhesions. In this example, the endometrial implant connects the uterus to the rectum.

facilitating factors for diagnosis and treatment of symptoms unknown. Regarding the exact cause and pathogenesis of endometriosis, various theories have been proposed. Even though just one theory cannot be able to explain what the cause of endometriosis is, the retrograde menstruation theory, proposed by Sampson in 1924, is the most widely accepted debate on the pathogenesis of endometriosis. Sampson states that the endometriosis is related to retrograde menstruation of endometrial tissue, slough at the duration of menstruation, which retrogrades through the fallopian tubes and into the peritoneal cavity [20]. Retrograde menstruation happens in more than 70% of all women, but more commonly in those with endometriosis [21]. Besides of this theory, another indication to whether a patient has endometriosis is to check the patient's genetic background such as family medical history. The reason is that the patient who has a first-degree relative with endometriosis has a seven times greater chance of developing endometrial lesions [22, 23].

### 1.3 Diagnosis

Many patients with endometriosis experience an average delay of eight years from presenting with symptoms to diagnosis and treatment [21]. This significant delay has a harmful effect on the patients' daily lives and activities, and in some cases fertility [24]. Since patients present with a wide spectrum of symptoms, the diagnosis of endometriosis is difficult. The diagnosis process starts with the observation of

certain symptoms, perusing a comprehensive documentation of the patient's medical history, and physical examination. Physical examination can be useful just if the endometrial implants were located at vulva, vagina, and cervix. However, the existence of endometriosis in these locations is not often. Therefore, physical examination mainly fails to reveal whether the patient has endometriosis or not. Visual inspection by laparoscopy is used as a gold standard for the diagnosis of pelvic endometriosis. However, this method is shown to be inaccurate. Over the time other imaging techniques such as Transvaginal Ultrasound (TVUS), MR, and CT scanning have evolved to greatly ease preoperative diagnosis [13, 16, 17, 25, 26]. However, many researchers believe that CT scanning should not be used to diagnose endometriosis, due to its radiation exposure and lack of contrast resolution. Nowadays, imaging techniques are an important diagnostic tool in the assessment of endometriosis, mapping of the disease's extent, and for creating a preoperative plan for surgical treatment.

### **1.3.1 Laparoscopy**

Laparoscopic visualization is the gold standard for diagnosis of pelvic endometriosis. In laparoscopy, diagnosis is confirmed intraoperatively. During laparoscopy, the pelvic area must be carefully investigated for the existence of endometriosis. After endometriosis has been found, the size, location, and extent of all lesions and adhesions may be recorded [27, 28]. Diagnostic laparoscopy is the most widely used staging system for endometriosis, but only for subtle lesions. In the case of deep infiltrating endometriosis, the value of laparoscopy is limited, as lesions hidden under dense pelvic adhesions are mostly impossible to detect during laparoscopy. In other words, it does not allow the surgeon to see the endometrial implants that are located inside or under the organs and to quantify the depth of infiltration. Figure 1-3 shows an example of laparoscopic visualization for the diagnosis of endometriosis. In this figure, the endometrial implant has infiltrated through the rectal wall, and the depth of infiltration cannot be seen. To cope with these limitations, it is important to construct an endometrial map preoperatively using both MR and TVUS.

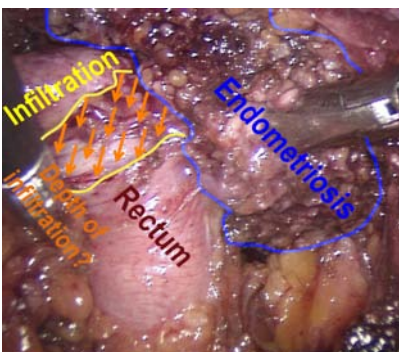


Figure 1-3: A laparoscopic image with the endometrial implant. The yellow line drawn on the laparoscopic image shows that the implant has infiltrated through the rectal wall, though the depth of infiltration cannot be seen.

### 1.3.2 Transvaginal Ultrasound

2D TVUS is normally the first medical imaging modality in patients with pelvic disorders and has shown good accuracy in the diagnosis of endometrial implants. The TVUS procedure involves laying the patient down on a table with bent knees permitting easy insertion of the ultrasound probe. A 6.5 MHz transducer probe combined with saline solution is gently inserted into the vagina, and then an expert moves the probe around the area of interest to see the pelvic organs. In this manner, an acoustic window is generated between the transvaginal probe and the surrounding structure of the vagina tube (e.g. the vagina walls, cervix, uterus, ovaries, rectum, and bladder). Since there is no clue about the location of endometriosis, a radiologist moves the probe in any direction in order to precisely investigate the patient's pelvic area. As the probe moves freely in any direction and the TVUS scanner has a small field of view, a 2D TVUS image cannot include all the pelvic organs. Therefore, multiple 2D TVUS images must be stored in order to allow an expert to carefully investigate the pelvic area. The results of ultrasonography, compared with other diagnostic imaging techniques, allow the radiologist to detect small implants, see the implants that are located inside or under the organs, and determine their depth of infiltration. The main TVUS limitations include their limited field of view and low signal to noise ratio [29]. Figure 1-4 shows TVUS images for two different patients

with different types of endometriosis. Figure 1-4 (a) shows a small implant which is located above the bladder without adhesion, whereas Figure 1-4 (b) shows an implant which cause adhesion. TVUS image in Figure 1-4 (b) clearly indicates the depth of infiltration.

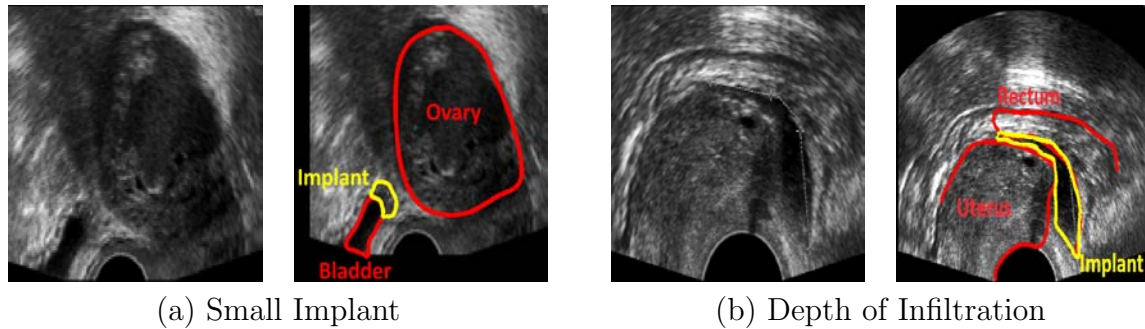


Figure 1-4: 2D TVUS images. (a) shows a small endometrial implant. (b) illustrates the endometrial implant with its depth of infiltration.

### 1.3.3 Magnetic Resonance Imaging

MR imaging is a noninvasive medical test which is based on the absorption and emission of energy in the radio frequency range of the electromagnetic spectrum [30]. This imaging modality is accepted as the most precise technique for assessment of large endometrial implants, since it provides superior soft-tissue contrast resolution. In contrast with TVUS scanning, MR imaging is not operator dependent.

T2 MR imaging scan with or without contrast agent is the standard imaging technique used for detection and anatomical localization of large endometrial implants. Generally, MR images are generated using a 1.5 Tesla whole-body MR system. In this manner, a dedicated phased-array coil is used as a signal receiver. The patient is placed in supine position. The phased-array coil is tuned to be around the patient's pelvic area. In some cases, contrast agents are given to the patients in order to improve the visibility of internal body structures such as the rectum and vagina. Then, a sagittal, axial, and coronal 2D MR sequences are acquired to form a 3D volume of the patient's pelvic region.

The MR images present a global map of the location of the lesions and provide

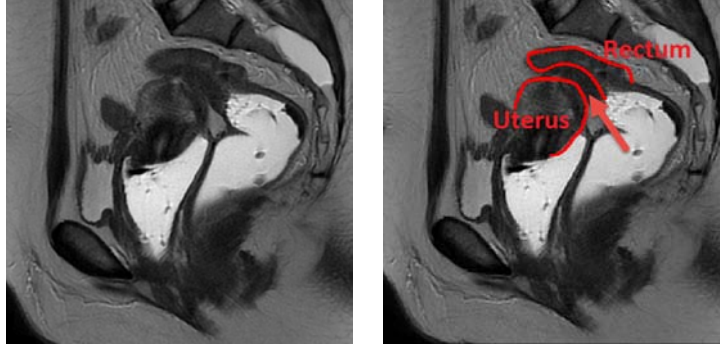


Figure 1-5: An example of a 2D MR slice. This imaging modality is used for visualization of the complex pelvic anatomy. In the case of large endometrial implant which causes adhesion (see Figure 1-2), this imaging technique can show abnormalities, but cannot visualise depth of infiltration.

good contrast between the normal and malignant tissues. However, MR imaging cannot show the small endometrial implants and the depth of infiltration [13, 26]. Figure 1-5 is an example of pelvic MR image. Note that this MR image matches with the TVUS image in Figure 1-4 (b). In this figure the abnormality between the uterus and the rectum is obvious, but the depth of infiltration and the boundary of the uterus and rectum, in which there is an adhesion, are not clearly visible.

## 1.4 Surgical Treatment

There is currently no cure for endometriosis, but there are treatments for pain and infertility related to endometriosis. After preoperative imaging examination, an expert must investigate all the images in order to decide whether a woman has endometriosis. However, an accurate diagnosis should not just indicate the existence of the endometriosis, but should also include such information as depth of infiltration, size of implants, and exact location. This information is necessary to create a preoperative surgical plan in which the desired resection lines are defined and then performed in the operating room. Therefore, completeness of excision highly depends on the precision of diagnosis. Note that the goal is to treat the endometriosis without harming the healthy tissue around it, but to achieve this, one needs very accurate diagnosis which is not easy by current imaging technologies.

Based on the preoperative surgical planning, the surgeon makes at least two small cuts in the abdomen and inserts a laparoscope and other surgical instruments to remove implants or destroy them with intense heat and seal the blood vessels. Some surgeons also remove scar tissues at the surgery time because the scar tissues may be causing pain and reforming adhesions. Although most women have relief from pain with surgery in the short term, pain often returns. This is due to the excision of deep infiltrated implants be left incomplete due to inaccurate planning, so that the implants grow again. Inaccurate pre-operative surgical planning can be because of lack of knowledge of interpreting the preoperative medical images by surgeons. This leads to recurrence or starting surgery off the place where the implant is located.

## 1.5 Objectives

As previously mentioned, preoperative TVUS and MR scanning have formed the most reliable diagnosis procedure for the assessment of endometriosis [13]. These imaging modalities are complementary. Small implants and depth of infiltration are only visible in TVUS while MR visualizes the complex pelvic anatomy [26]. There is currently no system available to construct an endometrial map by combining MR and TVUS.

The registration and fusion between TVUS-MR data can be used to solve the limitations of MR and TVUS at observing endometriosis. This is a difficult technical problem due to the disparity in gray-level intensities (multi-modality), multi-dimensionality, soft tissue deformations, and the limited field of view and low signal to noise ratio of TVUS images.

The TVUS image may exhibit some deformations under certain conditions. The inserting of the transvaginal probe inside the vagina during the TVUS procedure, full bladder, bowel or gas inside the rectum and altered patient positions between the TVUS and MR scanning procedures may deform the pelvic organs. In order to cope with these deformations, deformable registration methods need to be used. The registration process facilitates the transfer of two types of information from a TVUS image to a MR data, which contains superior information on the pelvic

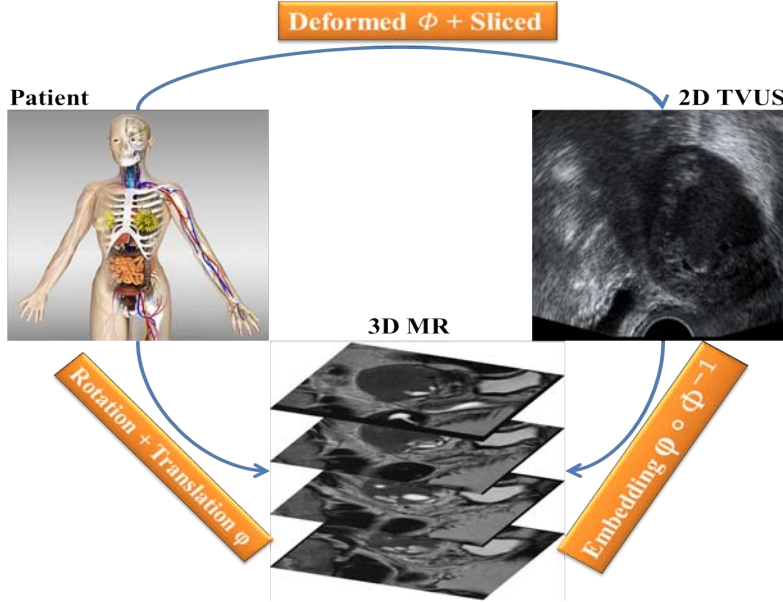


Figure 1-6: The general TVUS-MR registration schema.

anatomy, including the location and shape of endometrial implants and their depth of infiltration in the host tissue. The general TVUS-MR registration schema is shown in Figure 1-6. As it is shown in this figure, the TVUS that we have used in our experiments is a 2D image, or slice, of a three-dimensional object (organs, tissues). This image is deformed by external forces. The MR data volume is a set of 2D slices of a three-dimensional of the pelvic organs and tissues. Then by registering a 2D TVUS image with a MR data, we can retrieve the deformations that was applied to the patient’s organs during TVUS acquisition.

Since there is no algorithm to register a TVUS image with an MR of the woman pelvis, we have explored the possibility of various deformable registration methods. The primary goal of this work is to propose deformable registration methods that may be applied to register a 2D TVUS and a 2D MR data to accurately localise endometrial implants and clearly define resection lines. We have observed from a literature that many existing deformable US-MR image registration methods need to manually establish correspondences between the two modalities. However, the main drawback of these methods is that manually selecting point correspondences are often a challenging and time-consuming process. To reduce the potential expert error and

interaction time, we propose two different methods which take advantage of the organs segmented by the radiologist whilst they inspect the images. We have shown that 2D/2D TVUS-MR registration can improve diagnosis procedures by transferring the extra information from TVUS images into MR images. This information can assist the surgeons to make more accurate preoperative surgical planning, since they do not need to investigate both TVUS and MR individually. Our 2D/2D registration results provide accurate information about location of the implants and their depth of infiltration on the pelvic anatomy. Moreover, we outline the resection lines to ease the surgery planning to prevent over- or under cutting of the endometrial implants during surgery.

To achieve 2D/2D TVUS-MR registration, a reference 2D MR slice from the MR volume that corresponds to a moving 2D TVUS image must manually be chosen by an expert. We have seen from a literature that for registering US to MR images, methods in the state of the art carry out the registration process with the same strategy. This is a limitation since the standard TVUS and MR imaging techniques used for diagnosing endometriosis are 2D and 3D, respectively. Hence, this registration problem is actually a 2D/3D registration, and more specifically a slice-to-volume registration. Then, the secondary goal of this work is to propose a deformable registration method that may be applied to register a 2D TVUS with a 3D MR volume to find a cross-section of volume by a plane or smooth surface, from which the endometrial implants and their depth of infiltration can be mapped into the reconstructed patient-specific organ model from the 3D MR volume. Since the pelvic organs have complex 3D structures, 3D virtual reality models of the patient's organs enhanced the anatomy of this complex part of the body. The advantages of using the 3D MR volume for diagnosis of those large endometrial implants which are visible in MR data are discussed in details by Giusti et al. [31]. They show that the 3D reconstruction of the pelvic organs (namely the uterus, vagina, rectum, and bladder) and large endometrial implants from the 3D MR volume improves the accuracy of diagnosis and can be used for visualization of the complex pelvic anatomy for treatment planning purposes. The surgeon may also use the reconstructed patient-specific model to create a preopera-

tive plan in which the desired resection lines are defined and then performed in the Operating Room. Defining an accurate preoperative plan is only possible when the boundary of organs and implants are precisely defined. However, this is not always possible as the depth of infiltration is generally not visible in the MR data. In order to solve this issue and to improve the accuracy of diagnosis as well as surgery planning for small implants, which are also not visible in an MR volume, we propose to fuse the 2D TVUS image to the 3D MR volume.

## 1.6 Overview of the Thesis

The remaining of the thesis consists of 8 chapters as well as an appendix.

**Chapter 2.** This chapter presents the general tools used in this thesis. In particular, we give the convention and notation, the basic principles of minimization depending on functionals followed by the most relevant spline approximation methods.

**Chapter 3.** This chapter deals with some preliminary concepts related to image registration such as the general registration methodology, the similarity measures, the transformation models, the optimization techniques, and the interpolation methods.

**Chapter 4.** This chapter reviews, without restriction, US-MR image registration methods for other organs and other settings (2D/2D and 3D/3D). The registration methods are categorized into intensity-based, feature-based, and hybrid methods. Moreover, this chapter provides a literature review related to Iterative Closest Point (ICP) based registration algorithms and 2D/3D medical image registration methods.

**Chapter 5.** Since there is no existing system to register TVUS to MR images, this chapter provides a comparison between two different registration approaches—intensity- and feature-based—and investigates their applicability in the case of the TVUS-MR registration problem. The experiments show that the feature-based approach provides more accurate registration results.

**Chapter 6.** This chapter describes a variational approach to map endometrial implants from 2D TVUS to 2D MR images. The proposed method lies in the feature-based approaches. In our registration process, the expert first segments the organs and selects a few corresponding points. More point correspondences are then created using arc-length parametrization between each adjacent points. Then, a deformable registration method is employed to locally register the TVUS image with the corresponding MR slice. We use different non-parametric transformation models and regularization functions such as diffusion, divergence and curl, and curvature. In addition, we also use one of the most popular parametric transformation models which is Thin-Plate Spline (TPS). Our experiments show that the curvature registration method provides more accurate displacement fields than the compared methods.

**Chapter 7.** This chapter presents an automatic 2D/2D deformable registration method to establish point correspondences and estimate deformation between curve correspondences. In this method, we register a 2D TVUS image to a 2D MR image using curve correspondences through a novel variational one-step deformable ICP method. The MR and TVUS data are manually segmented by an expert. Thereafter, a deformable one-step ICP method is used to compute a dense deformation field while establishing point correspondences automatically. This algorithm improves the state of the art algorithms in that it decreases potential expert error and interaction time in selecting point correspondences.

**Chapter 8.** This chapter presents a new deformable slice-to-volume registration method to map endometrial implants from a 2D TVUS image into a 3D MR data. Our technical contribution lies in extension of our 2D/2D one-step ICP method to slice-to-volume registration problem. Moreover, our new formulation can handle multiple curves to surface correspondences, while estimating a deformable transformation. This method markedly extends the current literature on ICP and US-MR image registration.

**Chapter 9.** This chapter provides general conclusions on the various proposals of this manuscript and outlines some of the avenues of future work.

**Appendix A.** This appendix studies 2D and 3D wavelet domain medical image resolution enhancement method. The proposed approach is based on the interpolation of the low resolution input image and the derived high frequency sub-band images obtained using Discrete Wavelet Transform (DWT). Experimental results on both 2D and 3D images show how our method enhances the image's details and preserves edges.

# Chapter 2

## Background

### Contents

---

<b>2.1</b>	<b>Introduction</b>	<b>19</b>
<b>2.2</b>	<b>Notation</b>	<b>21</b>
<b>2.3</b>	<b>Calculus of Variations</b>	<b>22</b>
2.3.1	Basic Principles	23
2.3.2	Generalizing the Variational Problem	25
<b>2.4</b>	<b>Function Models Based on Splines</b>	<b>26</b>
2.4.1	B-Spline Basis for Polynomial Splines	28
2.4.2	Radial Basis Functions	35

---

## 2.1 Introduction

This chapter presents the mathematical background used in the rest of the manuscript. We first summarize the most common notations that have been used in this thesis. We then present the basic principles of minimization depending on functionals followed by describing the most important spline approximation methods.

Here, our aim is to provide the basic tools required to formulate the variational problems in image registration. In this work, we are interested in seeking optimal solutions for minimization problems based on functionals. Since the solution of this energy functional minimization problem is an optimum function, rather than an optimum point, which has to fulfill certain needs based on the application at hand, it is sensible to discuss about the calculus of variations. Thus, in section 2.3, the basic principles of the calculus of variations are discussed. The variational problems wind up with Partial Differential Equations (PDEs) that make such a problem rather hard

to solve. To solve the variational problems, several numerical methods for approximating the solution are known. Spline functions are one of the most widely used approximation approach for solving variational problems. The spline-based functions are special functions in the space of which approximate solutions of the PDEs can be computed. Therefore, in Section 2.4, various spline functions are presented to find approximate solutions to variational problems.

Since the mathematical concepts in this chapter are well-known, we only provide the necessary information and avoid to describe these concepts in more details.

## 2.2 Notation

In this thesis, we use the following notation:

$X$	Pixel coordinate	
$M$	2D TVUS image	
$F$	Set of 2D MR slices	
$C_M$	Set of 2D curves in TVUS image	
$C_R$	Set of 2D curves in MR image	
$\gamma$	Set of space curves in 2D TVUS surface	
$S$	Set of 3D surfaces in MR volume	
$q$	Set of 2D points (e.g. $q \in C_M$ )	
$p$	Set of 2D points (e.g. $p \in C_R$ )	$A \subset B$   $A$ is a subset of $B$
$Q$	Set of 3D points (e.g. $Q \in S$ )	$B \supset A$   $B$ is a superset of $A$
$E$	Energy functional	$a \in B$   $a$ is a member of $B$
$\phi$	Deformation vector field	$\forall$   Universal quantification
$U$	Displacement vector field	$\exists$   Existential quantification
$\lambda$	Smoothing parameter	$\lfloor \cdot \rfloor$   Floor function
$\nabla$	Gradient operator	
$\nabla \cdot$	Divergence operator	
$\nabla \times$	Curl operator	
$\Delta$	Laplace operator	
$U^{(i)}$	$i^{th}$ derivatives of $U$	
$\Pi$	Plane projection	
$\ \cdot\ _p$	The $p$ norm $\left(\sum_{i=1}^n  \cdot ^p\right)^{\frac{1}{p}}$	

## 2.3 Calculus of Variations

Calculus of variations is a branch of mathematical analysis which is related to the problem of seeking a function for which the solution of a definite integral is either the smallest or the largest possible value. This integral which consists of functions and their derivatives is known as a functional. The interest of using calculus of variations is in extremal properties of functions which force the functional reaches a minimum or maximum value when the functions' derivatives (rate of change of the functional) is zero. Many important problems which involve functions of single or several variables are relatively easy to state and perform, however their concept is difficult to prove mathematically, as their solution contains differential calculus. Therefore, calculus of variations includes Ordinary Differential Equations (ODEs) when there is a function with single variable or PDEs when there is a multivariate function.

The modern history of the calculus of variations began in June of 1696 when Johann Bernoulli issued an open challenge to the mathematical world known as the brachistochrone<sup>1</sup> curve problem. Bernoulli gave the world until the end of 1696 the chance of solving the problem, and promised to announce the solution. The problem immediately drew the attention of Jacob Bernoulli, Leibniz, Newton, and Marquis l'Hôpital, and they correctly solved the problem. The idea behind the problem was to create an integral for the traversal time in terms of the unknown curve, and thus change the curve thereby minimum time is achieved. This approach, which is variational calculus, results in an ODE whose solution is a curve. As early as 1728, Leonhard Euler became interested in the calculus of variations. In 1777, Euler published his book "A method for discovering curved lines that enjoy a maximum or minimum property, or the solution of the isoperimetric problem taken in the widest sense". Many mathematicians believe that this book is the birth of the theory of the calculus of variations [32]. The history of the calculus of variations and its application is wide, and we refer the reader to [33] for more details.

To ease the understanding of the reader, some standard terminologies relating to

---

<sup>1</sup>A brachistochrone curve is the path that will carry a point from one location to another in the shortest period of time.

the calculus of variations are shown in Table 2.1. These information will help the readers to better understand the following sections and chapters.

Term	Definition
Calculus of Variations	A field in mathematics concerned with the minimization of a functional over the defining function.
Functional	A scalar function of a function. It can be a definite integral including a function and its derivatives.
Function	A functional depends on one or more functions as input.
Definite Integral	The integral over a domain that defines the functional.
Variational Problem	The estimation of the function which minimizes or maximizes the functional. This kind of problem is known as a variational problem. Note that the estimated function is called an extremal.

Table 2.1: Calculus of variations terminology.

## 2.3.1 Basic Principles

### 2.3.1.1 Definition of a Functional

Let  $\Omega$  be an open bounded set in  $\mathbb{R}^{n+1}$  ( $n$  dimensional Euclidean space) and it is simply connected. A point in  $\Omega$  has known coordinates  $(x, f_1, \dots, f_n) = (x, f)$ . Let  $L = L(x, f, f^{(1)}) \in C^r(\Omega \times \mathbb{R}^n)$  with  $r > 1$ . We also assume  $(x_1, a)$  and  $(x_2, b)$  be two arbitrary points in  $\Omega$ . The space

$$\Gamma := \{f : x \mapsto f(x) \in \Omega \mid f \in C^1[x_1, x_2], f(x_1) = a, f(x_2) = b\}$$

includes all continuously differentiable functions that start at  $(x_1, a)$  and finish at  $(x_2, b)$ . The integral functional  $E \in \Gamma$  can be defined as follows:

$$E[f] = \int_{x_1}^{x_2} L(x, f, f^{(1)}) dx \tag{2.1}$$

A functional  $E$  can be described as a scalar function of a function. This takes one or more functions as input. The output of  $E$  is a real number. Since real numbers are ordered, one can compare functionals  $E[f_1], E[f_2], \dots$  of different admissible functions  $f_1, f_2, \dots$ , and build minimizing sequences of functions  $f_1, \dots, f_n$  with this property:  $E[f_1] \geq E[f_2] \geq \dots \geq E[f_n]$ . Thus, we can say that  $f^* \in \Gamma$  delivers the

minimum of  $E$  if

$$E[f] \geq E[f^*], \forall f \in \Gamma.$$

There are different groups of methods aimed to find the optimum  $f$  including methods of sufficient conditions, methods of necessary conditions (variational methods), and direct optimization methods [34]. Since the aim in this section is to define variational problems, we only provide the fundamental information about the variational methods and avoid to describe the other methods (for more details, see [34]). In variational methods, we only search for necessary conditions of optimality as it is assumed that the compared trajectories are very close to each other. These methods are robust and useful for various extremal problems called variational problems.

### 2.3.1.2 The Variational Problem

The purpose of the variational problem is to find the function  $f$  that minimizes (maximizes) the functional  $E$ . A minimum and maximum (extremum) of a given function can be found where its derivative vanishes ( $\nabla E = 0$ ). If the functional attains a local minimum at  $f$ , and  $\eta = \{f \in C^1[x_1, x_2] | f(x_1) = f(x_2) = 0\}$  is an arbitrary function, then for any number  $\varepsilon$  close to 0

$$E[f] \geq E[f + \varepsilon\eta]$$

The term  $\varepsilon\eta$  is called the variation of the function  $f$ . Since  $\Omega$  is open and  $f \in \Omega$ , then  $f + \varepsilon\eta \in \Omega$  for small enough  $\eta$ . Substituting  $f + \varepsilon\eta$  into the functional  $E$ , leads to:

$$E[f + \varepsilon\eta] = \int_{x_1}^{x_2} L(x, f + \varepsilon\eta, f^{(1)} + \varepsilon\eta^{(1)}) dx \quad (2.2)$$

Equation (2.2) has only a single variable which is  $\varepsilon$ . Therefore, to obtain the minimum or maximum (extremum), we take the derivative of Equation (2.2) with respect to  $\varepsilon$ , and set it to be zero. This yields:

$$\frac{dE}{d\varepsilon}[f + \varepsilon\eta] = \int_{x_1}^{x_2} \left( \frac{\partial L}{\partial f} \eta + \frac{\partial L}{\partial f^{(1)}} \eta^{(1)} \right) dx = 0 \quad (2.3)$$

Now, we can use integration by part to rewrite  $\frac{\partial L}{\partial f^{(1)}} \frac{d\eta}{dx}$ . This results in:

$$\frac{dE}{d\varepsilon}[f + \varepsilon\eta] = \int_{x_1}^{x_2} \left( \frac{\partial L}{\partial f} - \frac{d}{dx} \left( \frac{\partial L}{\partial f^{(1)}} \right) \right) \eta dx + \frac{\partial L}{\partial f^{(1)}} \eta \Big|_{x_1}^{x_2} = 0 \quad (2.4)$$

The last term vanishes as  $\eta = 0$  at the endpoints by definition and thus:

$$\int_{x_1}^{x_2} \underbrace{\left( \frac{\partial L}{\partial f} - \frac{d}{dx} \left( \frac{\partial L}{\partial f^{(1)}} \right) \right)}_{\chi} \eta dx = 0 \quad (2.5)$$

To derive the Euler-Lagrange(EL) from Equation 2.5, we need the fundamental lemma of the calculus of variations.

**Lemma.** Let  $g$  be of class  $C^k$  ( $k$  times continuously differentiable) on  $[a, b]$ , and let

$$\int_a^b g(x)f(x)dx = 0$$

hold for any function  $f$  that is differentiable on the interval  $[a, b]$  and vanishes in some neighbourhoods of  $a$  and  $b$ . Then  $g(x) \equiv 0$ .

According to the fundamental lemma of calculus of variations,  $\chi$  is set to zero so that:

$$\frac{\partial L}{\partial f} - \frac{d}{dx} \frac{\partial L}{\partial f^{(1)}} = 0 \quad (2.6)$$

Equation (2.6) is known as the EL equation for the functional  $E$ . This is the equation that must be used in practice to obtain the extremal  $f$ .

### 2.3.2 Generalizing the Variational Problem

In the previous section, we examined a Lagrangian function with a single input function. Now, we assume that the Lagrange function  $L$  contains  $n$  input functions  $L(x, y_1, \dots, y_n, y_1^{(1)}, \dots, y_n^{(1)})$ . Under this condition, the EL equation can be reformulated as:

$$\frac{\partial L}{\partial y_i} - \frac{d}{dx} \frac{\partial L}{\partial y_i^{(1)}} = 0 \quad (2.7)$$

where  $i = \{1, \dots, n\}$ . Since we have  $n$  conditions,  $n$  possible differential equations must be generated.

In some cases, we might have a function  $y$  with variables  $x_1, \dots, x_n$ . In this situation, the Lagrange function is  $L(x_1, \dots, x_n, y, y_{x_1}, \dots, y_{x_n})$  with  $y_{x_i} = \frac{\partial y}{\partial x_i}$ . The EL equation can be written as:

$$\frac{\partial L}{\partial y} - \frac{\partial}{\partial x_1} \frac{\partial L}{\partial y_{x_1}} - \dots - \frac{\partial}{\partial x_n} \frac{\partial L}{\partial y_{x_n}} = 0 \quad (2.8)$$

In this case, we end up with a single PDE.

Sometimes, we also must deal with higher order derivatives of function  $y$ . So, the Lagrangian is written as  $L(x, y, y^{(1)}, y^{(2)}, \dots, y^{(n)})$ .  $y^{(i)}$  defines the  $i^{th}$  derivative of the function  $y$ . The EL becomes:

$$\frac{\partial L}{\partial y} + \sum_{i=1}^n (-1)^i \frac{d^i}{dx^i} \frac{\partial L}{\partial y^{(i)}} = 0 \quad (2.9)$$

This leads to a higher-order PDE.

In this thesis, several of the above cases may simultaneously be used to meet the requirements. Therefore, we would have to combine the above conditions. Note that to solve the EL equations, one can use a spline-based approximation approach.

## 2.4 Function Models Based on Splines

A spline is a sufficiently smooth polynomial function that is constructed piecewise by gluing together polynomials. The idea of using splines as a smooth piecewise polynomial approximation has its roots in the aircraft and shipbuilding industries. In these industries the aim was to construct smooth shapes having desired properties. Researchers have long made use of splines which consist of a bendable strip fixed in position at a number of points that generate a smooth curve passing through those points. The malleability (elasticity) of the spline material combined with the constraint of the control points would cause the strip to take the shape that minimizes the energy required for bending it between the fixed points, this being the smoothest possible shape. Figure 2-1 demonstrates a historical drafting spline.

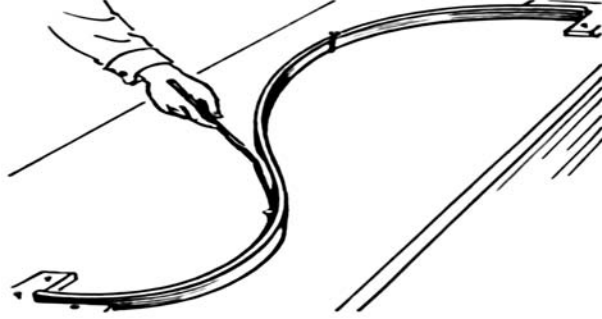


Figure 2-1: A historical spline (Taken from Pearson Scott Foresmann, [www.pearsonschool.com](http://www.pearsonschool.com)).

Mathematically, a spline is a curve, which is mainly needed to be smooth and continuous. It is a piecewise polynomial function of degree  $n$  with function values and  $n - 1$  derivatives that agrees at the points where they meet. The places where these points meet are known as knots or control points. Note that in this section, the knots are denoted as  $k$ . These knots define  $m$  knot intervals  $[k_i, k_{i+1}]$  for  $i \in [0, m - 1]$ . On each knot interval, a spline of degree  $n$  must be defined by a polynomial function of degree at most  $n$ . Note that the knots determine the shape of the curve—they let the curve bends in order to closely follow the data. In other words, splines with few knots are smoother than splines with many knots; though increasing the number of knots increases the fit of the spline function to the data.

Mathematically speaking, a spline  $S : [k_0, k_m] \rightarrow \mathbb{R}$  is a piecewise polynomial function on an interval  $[k_0, k_m]$  divided into  $m$  interval knots  $[k_i, k_{i+1}]$ . The restriction of  $S$  on each knot interval is a polynomial  $p_i : [k_i, k_{i+1}] \rightarrow \mathbb{R}$ , so that:

$$S(x) = \sum_{j=1}^n p_{ij} (x - k_i)^j \begin{cases} \text{if } x \in [k_i, k_{i+1}] \text{ and } i \in [0, m - 2] \\ \text{if } x \in [k_{m-1}, k_m] \end{cases} \quad (2.10)$$

where  $p_{ij}$  is a polynomial function. An example of using a cubic spline is illustrated in Figure 2-2.

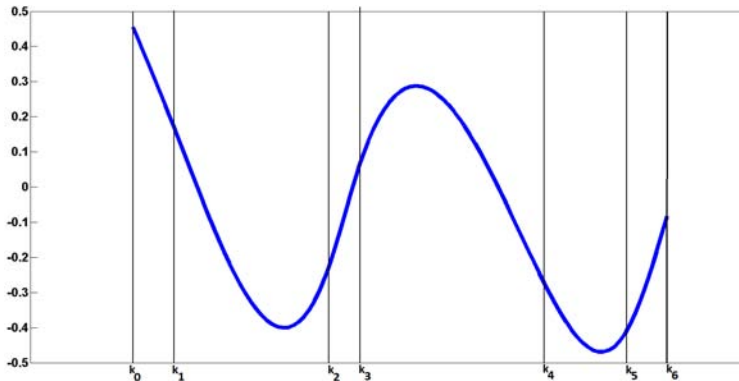


Figure 2-2: An example of using a cubic spline. A cubic spline is a sufficiently smooth polynomial function that is piecewisely defined. It made of 6 polynomial pieces with  $C^2$  continuity over the whole domain  $[k_0, k_6]$ . The width of each knot interval is not necessarily equal.

### 2.4.1 B-Spline Basis for Polynomial Splines

Splines can be expressed as linear combinations of B-splines with a set of knots. These types of splines are commonly referred to as B-splines, where B being short for basis. Therefore, a B-spline is a spline function which has minimal support with respect to a given degree, smoothness, and domain partition. Moreover, a B-spline is a generalisation of a Bézier curve, and it is effective in preventing the Runge's phenomenon<sup>2</sup> without increasing the degree of the B-spline.

B-splines were introduced in the early nineteenth century by Nikolai Lobachevsky. Lobachevsky proposed an infinite univariate spline function with uniform knots, whom classic B-splines are directly connected [35]. In the twentieth century, for the first time, the term B-spline was coined by Isaac Jacob Schoenberg. Schoenberg applied B-splines to statistical data smoothing [36]. Actually, the modern theory of spline approximation has its roots in Schoenberg's work [36]. Gordon et al. [37] formally investigated B-splines in computer aided design.

Basis functions are the fundamental core of the B-spline. The traditional definition of B-spline basis functions employs the idea of divided differences of a truncated power function and is mathematically involved. In the twentieth century, Carl de boor [38]

---

<sup>2</sup>Runge's phenomenon is a problem of oscillation at the ends of an interval that can happen when using higher degree polynomial interpolation.

proposed a recursive relationship for the B-spline basis. By using the Leibniz theorem, Carl de Boor was able to derive the following formula for B-spline basis functions:

$$N_{i,n+1}(x) = \frac{x - k_i}{k_{i+n} - k_i} N_{i,n}(x) + \frac{k_{i+n+1} - x}{k_{i+n+1} - k_{i+1}} N_{i+1,n}(x) \quad (2.11)$$

$$N_{i,1}(x) = \begin{cases} 1 & \text{if } x \in [k_i, k_{i+1}) \\ 0 & \text{otherwise} \end{cases} \quad (2.12)$$

where  $N_{i,n}$  is the  $i^{\text{th}}$  B-spline basis function of degree  $n$  (order  $n + 1$ ) with knots  $k_i < \dots < k_{i+n+1}$  and  $x$  is a parameter variable. Equations (2.11) and (2.12) show that the B-spline basis functions of an arbitrary order can be stably evaluated as linear combinations of basis functions of one degree lower.

The knot  $k_i \in \mathbb{R}$  represents the active area that defines the basis function. It takes  $i + 1$  knots or  $i$  intervals to define a basis function. Since the basis functions are based on knot sequences, the shape of the basis function is just dependent on the knot spacing and not knot values.

Another important feature of the B-spline is its ability to handle situations where the knot vector includes coincident knots. Notably if knots are coincident, the continuity of derivative order is decreased by one for each additional knot. Therefore, the order of continuity of a spline is reduced at the location of coincident knots. Figure 2-3 shows the relationship between a cubic basis function and its knot sequence. Some of the properties of the B-spline basis functions are:

- The sum of the B-spline basis functions for any parameter value  $x$  within a specific interval is always equal to one:

$$\sum_{i=-n}^{m-1} N_{i,n+1}(x) \equiv 1 \quad (2.13)$$

- Each basis function is greater or equal to zero for all parameter values:

$$\begin{cases} N_{i,n+1}(x) = 1 & x \in [k_i, k_{i+n+1}] \\ N_{i,n+1}(x) = 0 & \text{otherwise} \end{cases} \quad (2.14)$$

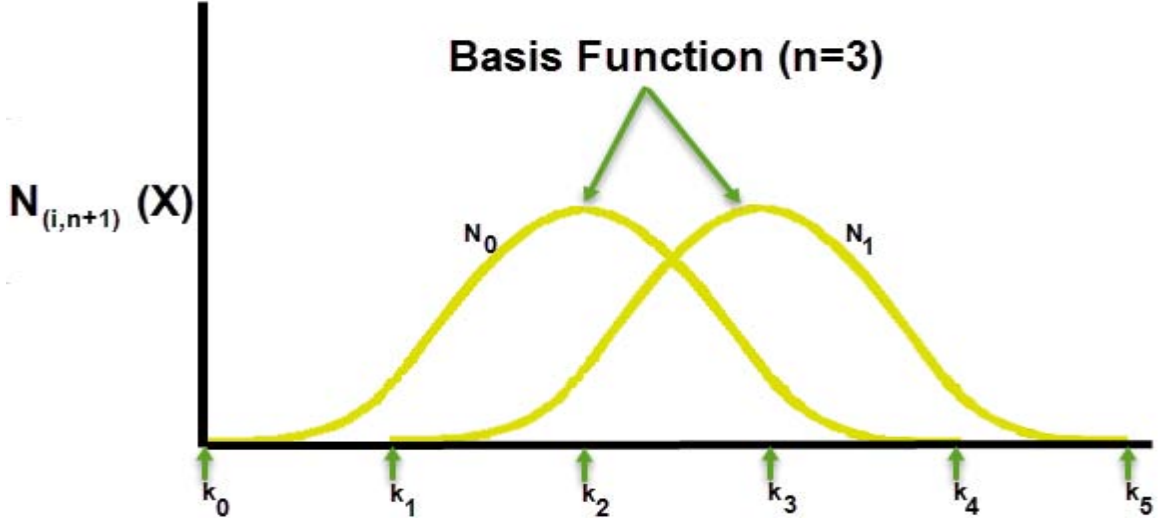


Figure 2-3: An example of B-spline basis function.

- For a given degree  $n$ , the B-splines belong to the highest possible class of continuity for a piecewise polynomial function:

$$N_{i,n+1}(x) \in C^{n-1}([k_i, k_{i+n+1}]) \quad (2.15)$$

- Each basis function has only one maximum value.

#### 2.4.1.1 B-Spline Curve

As mentioned before, splines of a given degree can be expressed as linear combinations of B-spline basis functions of that degree. They are piecewise polynomials of degree  $n$  with  $C^{n-1}$  continuity at the common points between adjacent knot segments. B-splines result of mapping the elements of a knot sequence in parametric space into Cartesian space. A spline curve estimated at a knot leads to a junction point that is the common point shared by two adjacent knot segments. As a reminder, let us take back to knot sequence which we used when we introduced the spline functions:  $k = k_0 < \dots < k_m$ . Since a B-spline of degree  $n$  spans  $n + 1$  knot intervals,  $m - n$  independent B-splines can be defined using knots  $k$ . Then, we need  $2n$  B-spline functions to form a basis of  $S_n(k_0, \dots, k_m)$ . B-splines are totally specified by the curve's data points, knots, curve's order, and B-spline basis functions as seen in

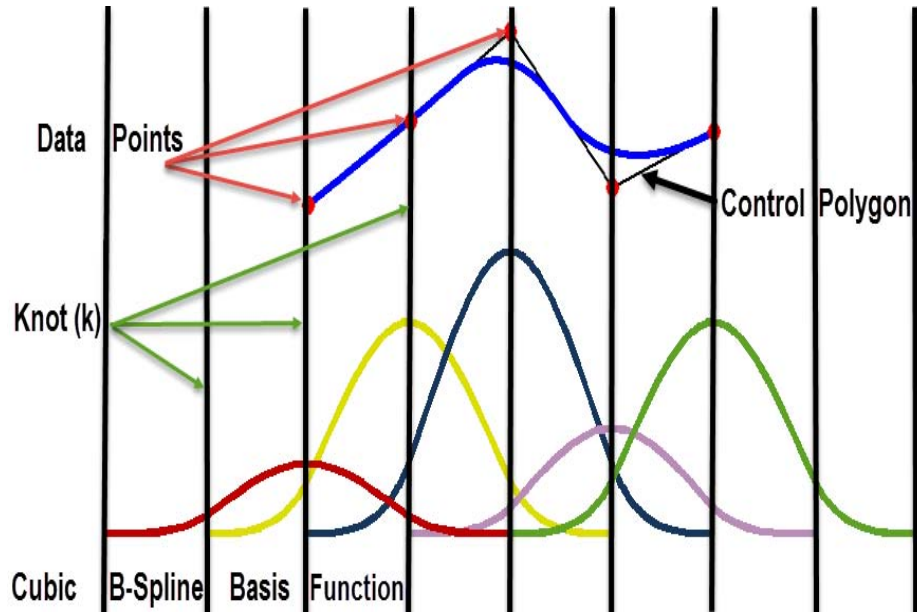


Figure 2-4: : A  $C^2$  cubic B-spline curve with its control polygon.

Equation (2.16).

$$S(k) = \sum_{i=-n}^{m-1} \omega_i N_{i,n+1}(k) \quad (2.16)$$

where  $S$  is written as a linear combination of  $m+n$  basis functions  $N_{i,n+1}$ , and  $\omega$  is the weight of B-splines. Note that in B-splines, the data points are known as the weight or the point coefficients. Each point on a B-spline is a weighted combination of the local data points, which create a control polygon enclosing the curve. An example of using a cubic B-spline is illustrated in Figure 2-4.

Generally, B-splines are divided into two categories: 1) uniform and 2) nonuniform B-splines. When the knots are equidistant the B-spline is uniform and otherwise nonuniform. If the B-spline is uniform, the active segment of all the basis functions forms the same shape over each knot interval. On the other hand, if the B-spline is nonuniform, the active segment of all the basis functions forms a different shape over each knot interval. Therefore, the previously discussed recursive algorithm (Equation (2.11)) is needed to estimate the basis functions. Normally, to determine the spacing between the adjacent knots in a knot vector, different parametrization techniques are employed. Parametrization methods are vital for the modelling of B-

splines, since the spacing of the knot sequence influences the basis functions. In this chapter, we focus on uniform B-splines, therefore a general survey on non-uniform splines is beyond the scope of this chapter. We refer the reader to Brunet [39] for more details.

### 2.4.1.2 Uniform Cubic B-Spline

The uniform cubic B-Spline is a special B-spline which is commonly used for its simplicity and efficiency. It is a B-spline of degree three. This degree is a good trade-off between flexibility and simplicity of the induced computations. As discussed before, the term uniform means that all the knots have equal distances. In this case, the cubic B-spline basis functions are just shifted copies of each others. Using Equation (2.11), we can obtain a closed form expression of the uniform cubic B-spline basis functions. With no loss of generality, we assume that the knot interval is normalized to  $[0 \ 1]$ . Since each interval is transformed to an interval between 0 and 1, a periodic basis can be used to evaluate each curve segment. The  $i^{th}$  basis function of the uniform cubic B-Splines is written as:

$$N_i(x) = \begin{cases} b_3(x) = \frac{1}{6}x^3 & \text{if } x \in [k_i, k_{i+1}) \\ b_2(x) = \frac{1}{6}(-3x^3 + 3x^2 + 3x + 1) & \text{if } x \in [k_{i+1}, k_{i+2}) \\ b_1(x) = \frac{1}{6}(-3x^3 - 6x^2 + 4) & \text{if } x \in [k_{i+2}, k_{i+3}) \\ b_0(x) = \frac{1}{6}(1 - x)^3 & \text{if } x \in [k_{i+3}, k_{i+4}) \\ 0 & \text{otherwise} \end{cases} \quad (2.17)$$

The  $b_i$  ( $i = \{0, 1, 2, 3\}$ ) are weighting functions that indicate how much weight is given to four neighbourhood data points, respectively, based on the value of point  $x$ . The estimation of a cubic B-spline at a point  $x$  is then proportional to a blending of the four weights closest to the point  $x$ . The blending functions are defined as the four polynomials  $b_0, \dots, b_3$  of degree three that forms the cubic B-spline basis functions. Equation (2.18) illustrates a matrix relationship which is used to estimate a periodic

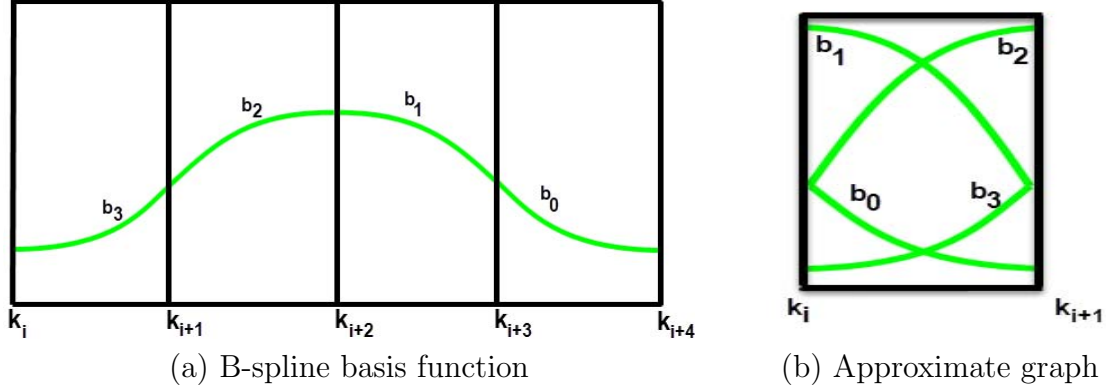


Figure 2-5: Anatomy of a B-spline basis function of uniform cubic B-spline. (a) A B-spline basis function is made of four pieces, each one of which being a polynomial of degree 3. (b) On a given knot interval, the value of a B-spline can be viewed as the blending of the four adjacent coefficients of the B-spline with weights given by the basis functions.

cubic curve at each knot interval.

$$S(x) = [x^3 \ x^2 \ x \ 1] \frac{1}{6} \begin{pmatrix} -1 & 3 & -3 & 1 \\ 3 & -6 & 3 & 0 \\ -3 & 0 & 3 & 0 \\ 1 & 4 & 1 & 0 \end{pmatrix} \begin{pmatrix} \omega_i \\ \omega_{i+1} \\ \omega_{i+2} \\ \omega_{i+3} \end{pmatrix} \quad (2.18)$$

It obviously indicates that, on an active knot interval, a uniform cubic B-spline is a polynomial function of degree three with coefficient obtained by blending the weights of the four non-zero basis functions that belongs to this knot interval. Figure 2-5 gives an illustration of the B-spline basis function for the uniform cubic B-spline.

### 2.4.1.3 Uniform Cubic B-Spline in Higher Dimensions

In this section, the B-splines presented in the previous section are extended to higher dimensions. To achieve this, one can use the tensor product B-spline to extend the univariate B-splines to multivariate. Let  $\{k_{-n_x}, \dots, k_{m_x+n_x}\}$  and  $\{\ell_{-n_y}, \dots, \ell_{m_y+n_y}\}$  be two knot sequences. The tensor product B-spline of degree  $n_x$  along the  $x$ -direction and  $n_y$  along the  $y$ -direction is the function  $S$  from  $[k_0, k_{m_x}] \times [\ell_0, \ell_{m_y}]$  to  $\mathbb{R}$  defined

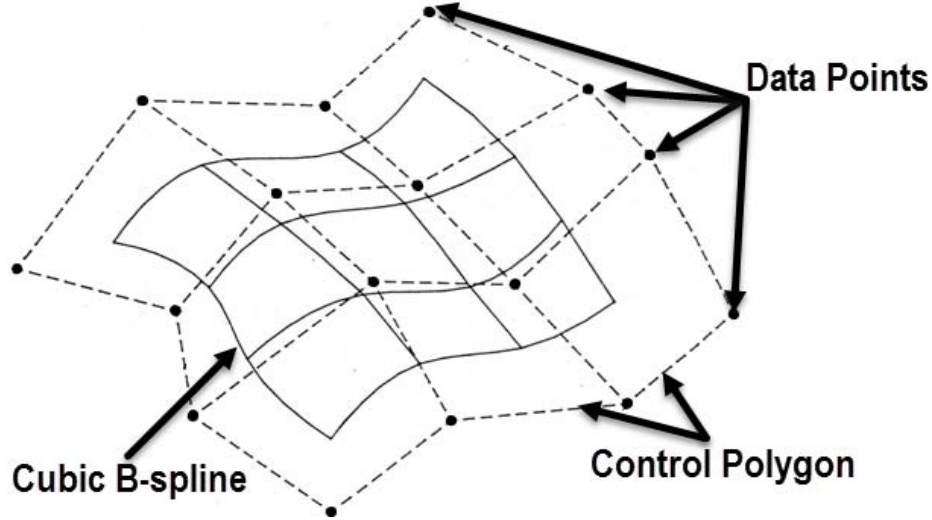


Figure 2-6: A bi-cubic B-spline surface and its control polygon.

as:

$$S(x, y) = \sum_{j=-n_x}^{m_x-1} \sum_{i=-n_y}^{m_y-1} \omega_{ji} N_{j,n_x+1}(x) N_{i,n_y+1}(y) \quad (2.19)$$

This equation reveals that the B-spline surface basis functions are products of two univariate B-spline curve basis functions. In other words, the surface is a weighted sum of surface basis functions. The weights are a rectangular array of knots and it forms the control polygon. Like the B-spline curve, the B-spline surface estimates the shape of the control polygon. Figure 2-6 shows a cubic B-spline surface and the corresponding control polygon. Note that as with the B-spline curve, the B-spline surface is also a set of polynomial pieces. Each piece of the B-spline surface is a two dimensionally represented part of a surface. Thus, each patch of a B-spline surface can be eliminated by a periodic relationship, when the knot spacing is uniform in each direction.

#### 2.4.1.4 Natural Spline

One of the most useful and important application of the splines is to interpolate a set of data points in order to generate either a smooth curve or surface. Natural cubic B-Splines are cubic B-splines whose second derivatives at the two endpoints are

zero. We suppose that  $\{x_j\}_{j=1}^m$  and  $\{y_j\}_{j=1}^m$  are the known data points and a spline interpolates  $n + 1$  knots with a piecewise cubic polynomial. It is well known that the natural spline is the minimum bent function which interpolates the data set. In other words, the shape of natural spline has the minimum strain energy. Generally, it is the solution of the following variational problem:

$$\begin{aligned} & \min_{f \in C^2} B[f] \\ \text{subject to } & f(x_j) = y_j \quad \forall j \in [1, m] \end{aligned} \quad (2.20)$$

where  $B$  is the energy functional that provides the curvature energy over its domain  $\Omega$ . Therefore, it can be written as:

$$B[f] = \int_{\Omega} \left( \frac{\partial^2 f}{\partial x^2}(x) \right)^2 dx \quad (2.21)$$

## 2.4.2 Radial Basis Functions

The approximation of multivariate functions may also be done by radial basis functions (RBFs). The RBF method is a standard tool for interpolating multidimensional data points. The main advantages of this method are threefold: 1) Its ability to handle arbitrarily scattered data. 2) It can easily generalize to several space dimensions. 3) It provides high spectral accuracy<sup>3</sup> which has made it highly useful in several different types of applications such as medical imaging, cartography, neural networks, and the numerical solution of PDEs. Unlike B-splines which are using linear combinations of a set of basis functions that are independent of the data points, in RBFs, one takes a linear combination of translations of a single fundamental radial basis function which is radially symmetric about its centre.

The RBF approach was introduced in 1971 by Rolland Hardy [40]. Hardy presented the method for the multiquadric (MQ) radial function. The method came out from a cartography problem, where a smooth bivariate interpolant to scattered data was required in order to generate curves and to illustrate the topography. Hitherto

---

<sup>3</sup>Spectral Accuracy is a measure of the similarity between the measured curve or surface and the theoretical one.

showed that the interpolation methods such as Fourier, polynomial, and bivariate splines were over smooth or too oscillatory. Hitherto also showed that in one dimensional problems, these interpolation methods can lead to the nonsingular interpolation processes. However, Haar's theorem states that the existence of a set of different nodes for which the interpolation matrix associated with node-independent basis functions is singular in two or higher dimensions [41]. The MQ method was popularized in 1982 by Richard Franke with his famous report on 32 of the most commonly used interpolation methods [42]. Complete tests of these 32 methods were presented and revealed that the MQ method provided the best results among all compared methods. Franl also implied that the interpolation matrix associated with the MQ radial basis function is unconditionally nonsingular, however could not prove it. In 1986, Charles Micchelli [43] was able to prove it, making use of work by Schoenberg from the 30's and 40's. Later, the MQ method was generalized to other radial functions, such as the Thin Plate Spline [44], the Gaussian, the cubic, and so on. In 1990, the RBF methodology once again became popular when Ed Kansa presented a procedure to employ it for solving parabolic, elliptic and (viscously damped) hyperbolic PDEs [44, 45].

#### 2.4.2.1 The Interpolation Problem

Generally, The RBF method works in the  $n$  dimensional Euclidean space  $\mathbb{R}^n$ , which is fitted with the Euclidean norm  $\|\cdot\|$ . Note that the norm need not necessarily be the Euclidean norm; it can be any norm. The function to be approximated has  $m$  known data points denoted as  $x_1, \dots, x_m$ . Moreover, these points are assumed to be all different from each other, otherwise the interpolation matrix associated with the radial basis function would be singular.

Let  $f : \mathbb{R}^n \rightarrow \mathbb{R}$  be an RBF. The RBF interpolant  $f$  takes the following form:

$$f(x) = \sum_{j=1}^m \omega_j \rho(\|x - c_j\|) \quad (2.22)$$

where  $x$  is the free variable,  $\omega_j$  are scalar parameters (weight of the RBF), and  $\rho$  is the RBF kernel. It is univariate and normally continuous function  $f : \mathbb{R}_+ \rightarrow \mathbb{R}$ . The vector  $c_j \in \mathbb{R}^n$  are known as the centres of the RBF.

Name of RBF	$\rho(r) \ r > 0$	Coefficient Matrix Properties	Smoothness
Multiquadratic	$\sqrt{1 + (\varepsilon r)^2}$	Positive Symmetric Definite	Infinitely smooth
Inverse multiquadric	$\frac{1}{\sqrt{1 + (\varepsilon r)^2}}$	Positive Definite	Infinitely smooth
Generalized multiquadric	$(1 + (\varepsilon r)^2)^\beta$	Positive Definite	Infinitely smooth
Gaussian	$\exp(-\varepsilon r)^2$	Positive Definite	Infinitely smooth
TPS	$r^2 \log(r)$	Positive Symmetric Definite	Piecewise smooth
Linear	$r$	Positive Symmetric Definite	Piecewise smooth
Cubic	$r^3$	Positive Symmetric Definite	Piecewise smooth

Table 2.2: Definitions of some RBF kernels [39].

The coefficients  $\omega_j$  can be obtained by solving a linear system  $A\omega = f$ , based on Equation (2.22). The system takes the form

$$\underbrace{\begin{bmatrix} \rho(\|x_1 - c_j\|) & \cdots & \rho(\|x_1 - c_m\|) \\ \vdots & & \vdots \\ \rho(\|x_m - c_j\|) & \cdots & \rho(\|x_m - c_m\|) \end{bmatrix}}_{\text{coefficient matrix}} \underbrace{\begin{bmatrix} \omega_1 \\ \vdots \\ \omega_m \end{bmatrix}}_{\text{variable matrix}} = \underbrace{\begin{bmatrix} f(x_1) \\ \vdots \\ f(x_m) \end{bmatrix}}_{\text{constant matrix}} \quad (2.23)$$

Generally, there are two types of RBFs: 1) the piecewise smooth and 2) the infinitely smooth RBFs. In the latter one, we must have a shape parameter,  $\varepsilon$ . Note that as  $\varepsilon$  approaches zero, the RBF becomes smoother. Table 2.2 gives a list of the most widely used RBFs  $\rho(r)$ . It is worth to note that among the basis functions listed in Table 2.2, the TPS is the most popular RBF method in image registration.

### 2.4.2.2 The Thin-Plate Spline

The TPS is an interpolation and smoothing technique and it is the generalisation of bivariate cubic B-splines. Therefore, it may be used with two or more dimensions. The TPS approach was pioneered by Duchon [46]. The reason that TPS is considered as a natural extension of the cubic B-splines is that both methods must minimize the

following variational problem:

$$\min_{f:\mathbb{R}^n\rightarrow\mathbb{R}} B[f] \quad (2.24)$$

where  $n = 1$  in the natural spline case and  $n \geq 2$  in the TPS case. The functional  $B$  is the curvature energy. If  $n = 2$ , it is defined as:

$$B[f] = \int_{\mathbb{R}^2} \left( \frac{\partial^2 f}{\partial x^2} \right)^2 + 2 \left( \frac{\partial^2 f}{\partial x \partial y} \right)^2 + \left( \frac{\partial^2 f}{\partial y^2} \right)^2 dx dy \quad (2.25)$$

The TPS has been commonly used in medical image registration [47–51].

# Chapter 3

## Image Registration

### Contents

---

<b>3.1</b>	<b>Problem Definition</b>	<b>39</b>
<b>3.2</b>	<b>Alignment Measure</b>	<b>42</b>
3.2.1	Feature-Based Image Registration	42
3.2.2	Intensity-Based Image Registration	43
<b>3.3</b>	<b>Transformation Models</b>	<b>46</b>
3.3.1	Nonparametric Deformation Models	47
3.3.2	Parametric Deformation Models	50
<b>3.4</b>	<b>Optimization</b>	<b>50</b>
<b>3.5</b>	<b>Interpolation</b>	<b>51</b>
<b>3.6</b>	<b>Evaluation of Registration Methods</b>	<b>51</b>
3.6.1	2D/2D Evaluation Metrics	51
3.6.2	3D/2D Evaluation Metrics	53

---

### 3.1 Problem Definition

This chapter provides a basic overview of an image registration framework and its components. Different similarity measures, spatial transformations, optimization techniques, and interpolation methods are defined. The registration methods have been broadly categorized as intensity- and feature-based methods. In the last section, we present various techniques to validate the accuracy of 2D/2D and 3D/2D registration of medical images. Note that the accuracy measurement techniques for 2D/2D registration, can be simply extended to 3D/3D registration problem by considering all coordinates are given in 3D.

Image registration is the process of determining the optimal spatial transformation

that bring one image into spatial alignment with the other. Generally, one of the images is referred to as the reference and the other one as the moving image. Image registration is a classical problem and often serves as a vital task for many applications where it is necessary to match two or more images of the same scene [52]. The images to be registered might be acquired with different sensors (multi-modality) or the same sensor (mono-modality) at different times or different subjects.

Image registration can be handled by feature-based or intensity-based methods [53]. The intensity-based approach compares intensity patterns in images via different correlation costs whereas the feature-based approach uses a set of features from the reference images beforehand and match them with their correspondences in the moving images. Besides what type of image registration approach to use, generally a cost functional  $E$  can be defined to find the optimum transformation:

$$E[\phi] = \lambda E_d[\phi] + (1 - \lambda) E_s[\phi] \quad (3.1)$$

where  $\phi$  is the transformation,  $E_d$  is a similarity (or an alignment) measure,  $E_s$  is the smoothness (or regularizer) functional, and  $\lambda$  is a smoothness parameter. Therefore, registration consists of four components:

- Energy functional: This is a core component of the problem formulation. It consists of a data term (alignment measure) and a regularization term to use in the optimization process. Depending on the input data and the transformation model, the registration problem may be ill-posed based on Hadamard's definition of well-posed problems [54]. If the problem is ill-posed, it generally requires additional assumptions, such as smoothness of the transformation for numerical treatment. This process is known as regularization.
- Transformation: maps each pixel coordinate of the image from moving domain into reference domain. Typically, there are two groups of transformations: global (e.g. rigid and affine) and local transformations. In the first group,  $0 < \lambda < 1$ .
- Optimization technique: searches for optimum transformation that best aligns

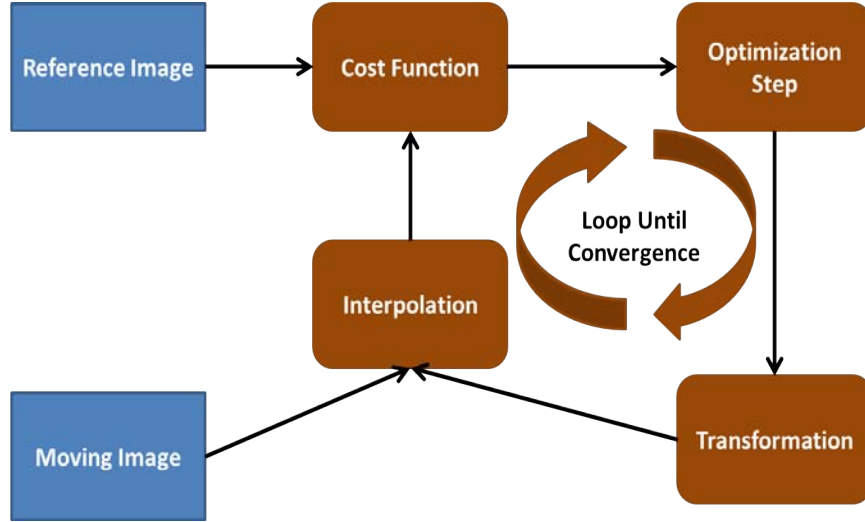


Figure 3-1: A general schematic for the image registration algorithm.

two images according to an energy functional.

- **Interpolation:** determines the intensity value at the point in the reference image after transformation.

An overview of image registration is depicted in Figure 3-1.

Let the moving image  $M$  and the reference image  $F$  be defined in  $\Omega = [0, 1]^d$ , that is a bounded set of  $\mathbb{R}^d$ , where  $d \in \mathbb{Z}^+$  indicates dimensionality. The mapping between the reference and the moving images can be expressed as:

$$F = M(\phi(X)) \quad (3.2)$$

where  $\phi : \mathbb{R}^{d_M} \rightarrow \mathbb{R}^{d_F}$  is the optimum transformation that models the misalignment between two images. In other words,  $\phi$  is a function from  $\mathbb{R}^{d_M}$  ( $d_M$  indicates dimension of the moving image) to  $\mathbb{R}^{d_F}$  ( $d_F$  indicates dimension of the reference image). The aim of the registration is to estimate  $\phi$ , by minimizing (or maximizing) Equation (3.1).

## 3.2 Alignment Measure

Generally, the alignment measures are either based on the distance between corresponding features or intensity variations in two images. Accordingly, image registration can be divided into two classes such as feature-based and intensity-based methods.

### 3.2.1 Feature-Based Image Registration

In feature-based registration methods, firstly, features are identified in the two images and then the corresponding features are used to estimate the transformation by minimizing the distance between them.

$$E_d[\phi] = \sum_{i=1}^N \|p_i - \phi(q_j)\|_p \quad (3.3)$$

where  $q$  and  $p$  are two sets of  $N$  points and  $p \geq 1$ . Note that if  $p = 1$  we get the  $L_1$  norm,  $p = 2$  we get the Euclidean norm, and as  $p$  approaches  $\infty$  the  $p$ -norm approaches the infinity norm. Feature-based registration is an effective registration approach for clinical application, since it can greatly reduce computational costs. The methods based on this approach can be classified into point-based approaches [48,55], curve-based algorithm [56,57], and surface-based methods [58]. The most important task in the feature-based registration approach is to extract corresponding features. Therefore, a preprocessing step is mainly needed to identify features manually or semi-automatically [59]. This makes feature-based registration a user dependent approach. To decrease operator interaction and still take advantage of the computational efficiency of this approach, many researchers try to handle feature extraction and identification automatically. The features can be anatomical features or markers attached to the subject.

#### 3.2.1.1 Extrinsic Features (Fiducial Markers)

Extrinsic features can be defined as the artificial markers attached to the patient. These markers such as dental adapter, skin markers, a mold, or frame, can be non-

invasive [53, 59]. However, some of these noninvasive markers (e.g. skin markers) are not reliable landmarks and provide low registration accuracy because of the elasticity of human skin. On the other hand, the invasive markers such as screw markers [60] and stereotactic frames [61] are reliable features, so that they provide a robust basis for registration. However, they are undesirable and uncomfortable. Extrinsic features can be employed in both mono-modal and multi-modal image registration as they are easily and automatically detectable in both images. Once the correspondences are established, complex optimization to estimate transformation parameters are not required. Therefore, the registration process is swift. Extrinsic features can provide high registration accuracy, but they are more invasive and uncomfortable for the patient and are difficult to attach to the patient.

### **3.2.1.2 Intrinsic Features**

Intrinsic features can be geometrical or anatomical points, lines, curves, or surfaces in the images. These features must be unique and evenly scattered over the images. Moreover, they must carry substantial and characteristic information of the images. Establishing feature correspondences is a challenging task. In this approach, intensive operator interaction is usually involved to identify the correspondences. In addition, the accuracy of the registration is highly dependent on the experience of the user [59]. Identifying features such as corner points, intersection points, local extrema, and boundary of organs [62] can be automatic; however, the accuracy of the registration highly depends on the precision of the detection algorithm. Therefore, a drawback of using intrinsic features is the sparse nature and the difficulty of automatic identification of these features [59].

## **3.2.2 Intensity-Based Image Registration**

Registration using intensity similarity measures involves calculating the registration transformation by optimizing some measure calculated directly from the intensity distribution in the images. The most important intensity similarity measures used for medical image registration are described below. With all these similarity measures

it is necessary to use an optimization algorithm to iteratively find the transformation that maximizes or minimizes certain criterion.

### 3.2.2.1 Intensity Alignment Measures

Intensity-based registration can directly use the image intensity information without segmentation or user interaction, and thus can be achieved fully automatically. It can be done by minimizing an energy functional (Equation (3.1)) which is based on an alignment measure of both images' intensities by estimating the transformation parameters. One of the standard alignment measures is the sum of squared intensity differences (SSD) between the images.

$$SSD = \sum_{X \in \Omega} (F(X) - (M(\phi(X))))^2 \quad (3.4)$$

where  $X$  is the pixel coordinate. This method assumes that the images to be registered differ only by Gaussian noise, which is not always the case. The SSD measure is very sensitive to a small number of pixels that have very large intensity differences between the two images. The effect of these pixels can be decreased by applying the sum of absolute differences [63].

Another method is correlation-like alignment measures which is typically computed for window pairs of the reference and the moving images. This is related with the well-known Pearsons correlation where a linear relationship is assumed to exist between the pixel intensities of the reference and the moving images.

$$CC = \frac{\sum_{X \in \Omega} (F(X) - \bar{F}(X)) (M(\phi(X)) - \bar{M}(\phi(X)))}{\left[ \sum_{X \in \Omega} (F(X) - \bar{F}(X))^2 \sum_{X \in \Omega} (M(\phi(X)) - \bar{M}(\phi(X)))^2 \right]^{1/2}} \quad (3.5)$$

where  $\bar{F}(X)$  and  $\bar{M}(\phi(X))$  are the mean intensities of the reference and the transformed moving images, respectively. This method was presented for multi-modal image registration by Van den Elsen et al. [64]. Recently, there has been an enormous interest in using Cross-Correlation (CC) in multi-modal image registration [65]. In this field, the pixel intensities of the same anatomy are different in the source and

the moving images due to different imaging sensors. With the assumption of existence of a correlation function between the pixel intensities in the two images, CC can still be employed efficiently. One of the well-known variants of CC in this case is called Local Correlation (LC):

$$LC = \sqrt{\frac{1}{N} \left( \sum_{s_j \in M} CC^2(s_j) \right)} \quad (3.6)$$

where  $CC$  is the cross correlation coefficient for the  $j^{th}$  subregion  $s_j$ , and  $N$  is the number of subregions contained in  $M$ . LC has been successfully implemented in rigid and deformable registration tasks [66]. There have been numerous modifications on CC in the literature to address the specified registration conditions [67]. Flatness of the similarity measure maxima due to the self-similarity of the images is the main drawback of the CC. This flatness can be resolved and sharpened by pre-processing and using a vector or edge correlation.

Mutual Information (MI) can also be used as a similarity measure. MI was introduced by two research groups of Viola et al. [68] and Collignon et al. [69] to measure the statistical dependency of two images. MI is widely accepted as a multi-modal registration criterion [70]. The fundamental concept in the definition of MI lies in the statistically significant relationship between intensities distribution of the input images of the registration. Based on Shannon's definition of entropy [71], MI is defined in terms of the marginal and joint probability density functions (pdfs) of the reference and the moving images derived from their normalized joint intensity histograms. Mathematically, this can be written as:

$$MI = \sum_{X_R \in \Omega} \sum_{X_M \in \Omega} p(F(X_R), M(\phi(X_M))) \log_2 \frac{p(F(X_R), M(\phi(X_M)))}{p(F(X_R)) p(M(\phi(X_M)))} \quad (3.7)$$

where  $p(F(X_R), M(\phi(X_M)))$  is the joint probability of the intensities in the reference and moving images,  $p(F(X_R))$  and  $p(M(\phi(X_M)))$  are the marginal distributions of  $F$  and  $M(\phi(X_M))$ . Note that if  $F$  and  $M$  are completely identical,  $p(F(X_R), M(\phi(X_M))) = p(F(X_R)) \cdot p(M(\phi(X_M)))$  and  $MI = 0$  converges to its

minimum; if  $F$  and  $M(\phi(X_M))$  are identical  $MI$  reaches its maximum. Therefore, the transformation parameters can be estimated by maximizing the MI. This method cannot always provide accurate registration results. For example, the changing overlap between two images may result in inaccurate registration with maximum MI [72].

A Normalized Mutual Information (NMI) is used to improve the conventional MI. This method can be seen as the symmetric uncertainty between the reference and the moving images [73]:

$$NMI = 2 \frac{MI}{H(F(X_R)) + H(M(\phi(X_M)))} \quad (3.8)$$

where  $H(M(\phi(X_M)))$  and  $H(F(X_R))$  are the marginal entropies of the moving and the reference images, respectively.  $H(M(\phi(X_M)))$  and  $H(F(X_R))$  can be written as:

$$\begin{cases} H(M(\phi(X_M))) = \sum_{X_M \in \Omega} p(M(\phi(X_M))) \log_2 p(M(\phi(X_M))) \\ H(F(X_R)) = \sum_{X_R \in \Omega} p(F(X_R)) \log_2 p(F(X_R)) \end{cases} \quad (3.9)$$

On the other hand, NMI is also defined by Studholme et al. [72] as follows:

$$NMI = \frac{H(F) + H(M)}{H(F, M \circ \phi)} \quad (3.10)$$

where  $H(F, M \circ \phi)$  is the joint entropy of the reference and the transformed moving images.

$$H(F, M \circ \phi) = - \sum_{X_R \in \Omega} \sum_{X_M \in \Omega} p(F(X_R), M(\phi(X_M))) \log_2 p(F(X_R), M(\phi(X_M))) \quad (3.11)$$

The transformation parameters are estimated by maximization of NMI in which the joint entropy is minimized with respect to the marginal entropies.

### 3.3 Transformation Models

The vital task of registration is to seek a transformation to superimpose and correlate the input images with differences and deformations introduced during imaging acquisitions. The transformation can be divided into the two main categories includ-

ing global transformation and deformable transformation. Global transformations include rigid, affine linear, and perspective transformations. A rigid transformation (isometry) refers to a transformation that preserves distances between every pair of points. Furthermore, it contains rotations, translations, and reflections. In an especial case, reflections are not included in the definition of rigid transformation. This can be achieved by imposing that the transformation also preserve the handedness of data in the Euclidean space. Thus, the rigid registration tries to find the rotations and the translations which map any point in the source image into the corresponding point in the target image. An affine transformation is an important transformation which map any point in the source image into the corresponding point in the target image by applying a linear combination of translation, rotation, scaling and shearing operations [74]. It maps straight lines to straight lines and preserves the parallelism between lines. The perspective transformation differs from the affine transformation in the sense that the parallelism of lines does not need to be preserved.

For most medical images, and for accurate inter-subject registration, more complex geometric transformations which contain many more degrees of freedom are necessary to define the tissue deformation with sufficient accuracy. Therefore, deformable transformations that allow the mapping of straight lines to curves are desired. Commonly, these transformations are divided into two main categories: parametric and nonparametric deformation models. The first approach employs a small number of parameters to define the deformation, whereas the latter method defines a deformation vector at each pixel location.

### **3.3.1 Nonparametric Deformation Models**

Commonly, nonparametric deformable transformations can be separated in four categories: 1) elastic body models, 2) viscous fluid flow models, 3) diffusion models, and 4) curvature models.

### 3.3.1.1 Elastic Body Models

In this deformation model, the object being deformed is modeled as an elastic body. This regularizer has been introduced to image registration by Broit [75] and is probably one of the most used regularizer. The Navier-Cauchy PDEs describing the deformation can be written as:

$$\lambda S[\phi] + (1 - \lambda) (\alpha \nabla^2 \phi + (\alpha + \beta) \nabla (\nabla \cdot \phi)) = 0 \quad (3.12)$$

where  $S[\phi]$  is the force field that derives the registration based on the alignment measure,  $\nabla$  is gradient,  $\alpha$  is the stiffness of the material, and  $\beta$  is Lamé's first coefficient. Elastic-based registration has its advantages and its disadvantages. It is very easy to implement, which is making it quick to use, and its physical motivations make it useful in some cases. However, the deformation must be small and local. In other words, the main limitation of elastic models is their inability to cope with large deformations.

### 3.3.1.2 Viscous Fluid Flow Models

These models do not assume small deformations, and therefore are able to retrieve large deformations. This is relatively easy and straightforward to understand; instead of directly taking the smoothness of a deformation  $\phi$ , this regularizer finds the velocity  $v$  of  $\phi$ , and takes the elastic smoothness of  $v$ . The Navier-Stokes equation defines the deformation as:

$$\lambda S[v] + (1 - \lambda) (\alpha \nabla^2 v + (\alpha + \beta) \nabla (\nabla \cdot v)) = 0 \quad (3.13)$$

where  $\alpha$  and  $\beta$  are the viscosity coefficients. The first term in Equation (3.13), constrains neighbouring points to deform similarly by smoothing the velocity field ( $v$ ). The  $v$  can be written as:

$$v(x, t) = \frac{\partial \phi(x, t)}{\partial t} + \nabla \phi(x, t) v(x, t) \quad (3.14)$$

Equation (3.14) must be integrated to find  $\phi$ . The fluid model was proposed by Christensen [76], and is used in cases where the object being modeled is fluid-like; it

does not accurately represent elastic objects, and can be used to obtain deformations completely altering the nature of an image.

### 3.3.1.3 Diffusion Models

Instead of trying to imitate physical properties as in the elastic or fluid models, this method attempts to estimate the smoothness of the deformation field itself. It has been proposed for optical flow problems by Horn and Schunck [77]. In this method, the deformation is modeled by the diffusion equation:

$$\lambda S[\phi] + (1 - \lambda) \Delta \phi = 0 \quad (3.15)$$

where  $\Delta$  is the Laplacian Operator. This regularizer, ideally, reduces penalties for smooth deformations. Furthermore, its setup allows easily computed EL equations.

The diffusion method is named as such because the PDEs can be viewed as a generalized diffusion equation. Furthermore, these PDEs can be solved through an iterative process. The main advantage of this method is that spatial directions are decoupled, allowing block diagonalization. Additive operator splitting, as proposed by Fischer and Modersitzki [78], permits a linear-complexity solution technique for each block. Hence, diffusion registration is quick, particularly on high-dimensional data. However, the disadvantage of this method is that each component of the resulting deformation is akin to a solution to a heat equation, but a unified model for the resulting deformation field is not clear.

### 3.3.1.4 Curvature Models

This method has been proposed for intensity-based image registration problems by Fischer and Modersitzki [79]. In this case, the deformation is modeled by the equilibrium equation:

$$\lambda S[\phi] + (1 - \lambda) \Delta^2 \phi = 0 \quad (3.16)$$

The curvature regularizer does not penalize affine transform and consequently does not require an additional affine preregistration step.

### 3.3.2 Parametric Deformation Models

Parametric methods provide a group of global transformations that can handle local distortions. Typically, they consist of knots and basis functions. Popular choices for basis functions are the TPS and B-splines (for mathematical details, see Chapter 2). In the parametric approach, the smoothing term may be unnecessary, because the spline basis functions are inherently smooth [80]. However, in order to avoid folding effects (singularities) in the deformation field, an additional smoothing term is needed. The main advantage of parameterized techniques is that the dimensionality of the problem is relatively low and thus fast optimization is possible.

## 3.4 Optimization

The purpose of optimization is to infer the optimal transformation that best aligns two images based on an energy functional (see Equation (3.1)). Therefore, the quality of the registration results highly depends on the choice of the optimization method. Therefore, the choice of an optimization method must depend on the properties of the energy functional. Sotiras et al. [54] classify optimization methods into two categories based on the nature of the variable they attempt to infer: 1) continuous and 2) discrete.

The first category tries to solve an optimization problem where the variables take real values and the cost function is differentiable. There exists a vast amount of continuous optimization algorithms. Continuous optimization methods are mainly iterative algorithms. This simply means that they start from an initial value  $\phi^0$  which is then iteratively updated. Therefore, this class of optimization methods builds a sequence  $\{\phi^i\}_{i=1}^{i^*}$  that may converge towards a local minimum of the cost function along the search direction. The search direction can be specified by utilizing only first-order information or by also considering second-order information. Note that when a cost function contains several minima, the initial value  $\phi^0$  determines which minimum must be considered as a solution. This initial value is thereby significantly important. Commonly used continuous optimization methods include: 1) gradient-descent and

its variants [68, 80–82], 2) Powell’s method [83], 3) downhill simplex method [84], 4) Newton’s method [85, 86], 5) Gauss-Newton algorithm [87], 6) Levenberg-Marquardt optimization [88], 7) Factorization methods (e.g. the Cholesky factorization, QR factorization, and singular value decomposition), 8) Jacobi method, and 9) Gauss-Seidel and its variants [89]. A detailed survey of all these methods is available in [39, 90]. Kelin et al. [80] reported a study comparing some of the continuous optimization strategies in image registration using MI as a similarity metric and cubic B-spline as a deformation model.

Discrete optimization methods aim to solve an optimization problem where the variables takes values from a discrete set. Discrete optimization methods can be classified into three categories: 1) Graph-based methods [91, 92], 2) Message passing methods [93, 94], and 3) Linear programming approaches [95, 96]. A detailed survey of all these methods is available in [54].

## **3.5 Interpolation**

Interpolation is a fundamental component in image registration, and is mainly required to approximate the intensity value at a pixel which does not lie on the transformed image grid. For instance, after transforming the moving image, some points are mapped to non-grid positions. Interpolation is then performed to estimate the values for these transformed points. Note that in the interpolation procedure, the more the number of neighbouring points taken into consideration for the estimation, the higher the precision. The choice of interpolation is dependent on the transformation used for the registration. The most common interpolation methods are bilinear, nearest-neighbor, bicubic [97], spline and inverse-distance weighting [98].

## **3.6 Evaluation of Registration Methods**

### **3.6.1 2D/2D Evaluation Metrics**

The registration accuracies are evaluated using some standardized measures. The registration accuracies that measure global overlap are assessed based on Mean Square

Error (MSE), Dice Similarity Coefficient (DSC) [99], and Hausdorff Distance (HD) [100]. Local registration accuracies are evaluated by Target Registration Error (TRE).

The MSE is mean square distance between the  $N$  transformed moving points ( $\phi(q) \in \mathbb{R}^2$ ) in the moving image and the corresponding ground truth points ( $p^{GT} \in \mathbb{R}^2$ ) in the reference image. Mathematically, this can be written as:

$$MSE = \frac{1}{N} \sum_{j=1}^N \|\phi(q_j) - p_j^{GT}\|_2^2 \quad (3.17)$$

If registration was fully accurate, points  $\phi(q)$  and  $p^{GT}$  would coincide, and then MSE would be zero. Therefore, a low MSE value shows good registration accuracy.

DSC is employed as a statistical validation metric to evaluate the performance of image registration algorithms. It is a measure of the spatial overlap of same foreground labels ( $f$ ) between the reference image ( $F(f)$ ) and the moving image ( $M(\phi(f))$ ) and is defined by:

$$DSC = \frac{2(M(\phi(f)) \cap F(f))}{M(\phi(f)) + F(f)} \quad (3.18)$$

The value of a DSC ranges from 0, indicating no spatial overlap between two regions, to 1, indicating complete overlap. This means that a high DSC value indicates a good overlap between the tissue regions after registration. Note that a high DSC does not mean a good contour overlap. Therefore, the HD measure must be used.

HD measures similarity between the deformed moving image contour  $\phi(C_M)$  and the reference image contour  $C_R$ . Given a finite set of points  $\phi(C_M) = \{\phi(q_1), \dots, \phi(q_N)\}$  and  $C_R = \{p_1, \dots, p_N\}$ , the HD between the point sets is given by:

$$HD(\phi(C_M), C_R) = \max(h(\phi(C_M), C_R), h(C_R, \phi(C_M))) \quad (3.19)$$

where

$$h(\phi(C_M), C_R) = \max_{\phi(q) \in \phi(C_M)} \left( \min_{p \in C_R} \|\phi(q) - p\| \right) \quad (3.20)$$

The HD is used to evaluate the contour accuracy. A low HD value shows good contour overlap.

To quantify the local registration error, we also use the TRE. It is described as

the mean square distance between  $j^*$  corresponding points not used in estimating the deformation. The main challenge in calculating TRE lies in finding corresponding target landmarks. The best target landmarks are those generated by a mechanical device which allows for an accurate positioning of the anatomy. However, this is not achievable for our study. The next best option is to choose anatomical landmarks in the patient’s body and the centroid of an organ. We opt for this type of target points to estimate the local registration accuracy to validate our result. TRE is measured by:

$$TRE = \frac{1}{j^*} \sum_{j=1}^{j^*} \|\phi(q_j^{TAR}) - p_j^{TGT}\|_2^2 \quad (3.21)$$

where  $\phi(q_j^{TAR})$  is the position of target moving points after registration and  $p_j^{TGT}$  are the position of the corresponding target points from ground truth. The target points used in our experiments are centroids and a few boundary points which are not used to estimate the deformation. A low TRE value shows good local registration accuracy.

In some experiments we also use CC (see Equation (3.5)) as a registration accuracy measurement. A CC shows how precise the relationship is between two segmented regions. The value of CC ranges from 0, indicating no correlation between two overlap segmented regions, to 1, indicating very high correlation.

### 3.6.2 3D/2D Evaluation Metrics

The first measure is the mean square distance between the  $N$  transformed moving points embedded in 3D space and the corresponding ground truth points ( $GT$ ). This is defined by:

$$MSE = \frac{1}{N} \sum_{j=1}^N \|\phi(q_j) - Q_j^{GT}\|_2^2 \quad (3.22)$$

where  $\phi(q_j) \in \mathbb{R}^3$  is the position of moving points after registration and  $Q_j^{GT} \in \mathbb{R}^3$  are the position of the corresponding points from ground truth.

Since the MSE does not evaluate the shape of the 2D curves embedded in the 3D space, we used another error measure which does not take the position into account,

but only assesses the organ's shape. Being able to compare the curve after registration with the corresponding ground truth curve is essential to verify registration accuracy. To compare curves, we must first find an appropriate representation. To achieve this, the 2D space curves are simply parameterized by their arc-length and  $N$  points are sampled uniformly. Then, in order to evaluate the similarity between curve pairs, we compare the angle formed by adjacent points. This measure is known as the Shape Error (SE) [101] and is given by:

$$SE = \frac{1}{N-2} \sum_{j=2}^{N-1} \left| \arccos \frac{(\phi(q_{j-1}) - \phi(q_j))^\top (\phi(q_{j+1}) - \phi(q_j))}{\|\phi(q_{j-1}) - \phi(q_j)\| \|\phi(q_{j+1}) - \phi(q_j)\|} \right. \\ \left. - \arccos \frac{(Q_{j-1}^{GT} - Q_j^{GT})^\top (Q_{j+1}^{GT} - Q_j^{GT})}{\|Q_{j-1}^{GT} - Q_j^{GT}\| \|Q_{j+1}^{GT} - Q_j^{GT}\|} \right| \quad (3.23)$$

The SE measure plays a significant role in identifying the similarity between the deformed moving curve and the ground truth curve. A low value of SE means that the curve shapes after registration are very similar even if misplaced.

We use the TRE in a similar way that we have explained in Section 3.6.1. TRE is measured by:

$$TRE = \frac{1}{j^*} \sum_{j=1}^{j^*} \|\phi(q_j^{TAR}) - Q_j^{TGT}\|_2^2 \quad (3.24)$$

where  $\phi(q_j^{TAR}) \in \mathbb{R}^3$  is the position of target moving points after registration and  $Q_j^{TGT} \in \mathbb{R}^3$  are the position of the corresponding target points from ground truth. Similarly, the target points are centroids and a few boundary points which are not used during registration process.

# Chapter 4

## Literature Review

### Contents

---

<b>4.1</b>	<b>Introduction</b>	<b>55</b>
<b>4.2</b>	<b>US-MR Image Registration</b>	<b>56</b>
4.2.1	Intensity-Based Methods	56
4.2.2	Feature-Based Methods	58
4.2.3	Hybrid Methods	61
<b>4.3</b>	<b>The Iterative Closest Point Algorithm (ICP)</b>	<b>62</b>
<b>4.4</b>	<b>Slice-to-Volume Registration</b>	<b>65</b>
<b>4.5</b>	<b>Conclusion</b>	<b>68</b>

---

### 4.1 Introduction

In general, the main goal of image registration is to estimate the spatial transformation by minimizing an objective functional in order to align a moving image with a reference one. Image registration has been an active topic of research for decades. Since numerous techniques were proposed, many researchers have tried to provide general reviews of the field. In these instances, a first general survey of image registration methods was presented in 1992 by Brown [63]. In 1998, Maintz et al. [53] proposed a survey of medical image registration. In 2000, Rohr et al. [102] provided a general survey of elastic registration of multimodal medical images. Chmielewski et al. [103] presented various image registration methods in 2001. In the same year, Pluim et al. [70] presented a survey of entropy-based image registration techniques. In 2003, a comprehensive survey of image registration methods was presented by Zitova et al. [67]. This paper classified image registration techniques as feature-based and

intensity-based methods. Since 2004, many other researchers have tried to summarize the existing image registration methods, e.g., [54, 104–107]. A thorough categorization of deformable medical image registration techniques has been presented in 2013 by Sotiras et al. [54]. However, most of these reviews are to a certain extent outdated due to the rapid progress of the field.

It is obvious that, due to the diversity of images to be registered and due to the various types of deformations it is impossible to design a general method that can be applied to all registration problems. Therefore, a general survey on image registration methods is outside the scope of this chapter, as many of them are not applicable to our TVUS-MR registration problem. Since there is no state of the art algorithm to register TVUS images with MR images of the female pelvis, our primary purpose in this chapter is to review the current literature related to US-MR image registration for other organs. We classify US-MR image registration techniques as intensity-based, feature-based, and hybrid methods. Furthermore, this chapter includes ICP-based registration algorithms and 2D/3D medical image registration methods.

## 4.2 US-MR Image Registration

### 4.2.1 Intensity-Based Methods

Intensity-based US-MR registration is a tremendously challenging task and is rarely used to find transformation parameters. The main reason of this difficulty is that US contains a speckle image of tissue boundaries, whereas MR provides information on tissue density. Various similarity measures have been proposed to solve US-MR registration specifically. Roche et al. [108] rigidly register 3D US with 3D MR images of the brain. Their similarity measure is based on the correlation ratio method [109]. They correlate the US images with both the MR and the MR gradient magnitude; this procedure allows them to account for intensity variations at tissue boundaries. They use Powell’s method as an optimization technique. Their method significantly outperforms the conventional correlation ratio and mutual information measures in terms of robustness. However, their method is designed for the brain which is mostly

rigid and would fail if applied to the deformable soft tissues of pelvic organs.

Craene et al. [110] employ the MI and the finite element deformation model to find the deformation between MR and US images of the liver. Beside this, they introduce a new optimization technique called Perturbation Stochastic Approximation (PSA). It contains an MI term and a weighted term based on the linear elastic energy, to balance the action of the similarity measure. In each step, the gradient of the cost function is determined using the finite difference method, and in the next step different perturbations of the subset of the active vertices, to stochastically estimate the mutual information gradient, are performed. Then, the average of MI is estimated and added to the cost function.

Mitra et al. [51,111] present a method to register Transrectal US with MR prostate 2D images which employs B-spline free-form deformations with a new procedure of computing the NMI. The B-spline registration uses uniform pixel grids over the MR domain whereas NMI is used as an intensity similarity measure. In their work, the NMI is computed from the texture images generated from the amplitude responses of the directional quadrature filter pairs. They show that the entropy between Transrectal US and MR images is typically more than the entropy of texture images due to variations in the gray levels. Therefore, B-spline registration with NMI computed from texture images is more accurate than that with NMI computed from intensity images. The optimization is done with the quasi-Newton optimization method as Limited Memory Broyden-Fletcher-Goldfarb-Shanno (L-BFGS) algorithm [112]. However, in their tests, the feature-based image registration method using TPS deformation model mainly provides the best result. Although their NMI-based method is used in prostate Transrectal US-MR image registration, it does not mean that it is applicable to our registration problem because of mainly two reasons. First, their images just include prostate with its internal structures, so that, applying directional quadrature filter to both images can smooth the intensity variations. However, in our data we mainly deal with multiple organs in the female pelvic area, and each organ has a completely different internal structures, thus applying the directional quadrature filter cannot provide homogeneous signal intensity. Second, the MR and

TVUS acquisition procedures for detecting endometriosis is completely different from the prostate. Therefore, our data has completely different intensity pattern. Our MR images are acquired after injection of the contrast agents which helps an expert to clearly distinguish between organ boundary and its internal structure by obtaining homogeneous white pixels inside the organs (i.e. bladder, uterus, rectum, and bowel). However, the contrast agents are not used during TVUS acquisition which leads to obtain TVUS images with inhomogeneous hyperintense signal intensity, especially inside the organs. However, this is not the case in prostate, since both Transrectal US and MR images have very similar patterns.

#### 4.2.2 Feature-Based Methods

It is clear that the advantage of using an intensity-based method is that it operates directly on the image gray values, without prior data reduction by the user or segmentation. Therefore, it must lead to high registration accuracy. However, relationship between US and MR intensities mainly does not exist so that the minimization can get easily stuck in a local minimum which leads to low registration accuracy. To discard the limitations of the intensity-based US-MR registration methods, researchers have used feature-based registration approach to superimpose US with MR images.

Singh et al. [98] develop a manual deformable registration method to fuse MR data volume to Transrectal US data volume. However, the procedure of placing control points to align both the surface and structure inside the prostate would require significant user interactions. Thus, in order to decrease user interaction various semi-automatic and automatic registration methods have been proposed in the literature.

Reynier et al. [113] propose a surface-based registration method for prostate internal radiotherapy. In their method, the prostate from the MR and Transrectal US volumes is first manually segmented and then, the segmented surfaces are used to manually establish point correspondences. The Transrectal US surface is then rigidly registered with the MR surface. Finally, elastic registration is used to estimate the deformation between the two modalities. The advantage of their method is its ability to model the deformation using octree-spline [114]. Optimization is done with the

Levenberg-Marquardt algorithm. Clinical and phantom images are used to assess their algorithm.

Daanen et al. [115] use octree-spline elastic registration to fuse 3D Transrectal US into 3D MR image prostate volumes for dosimetric planning of brachytherapy. Their registration determines prostate motion between the two acquisitions as well as prostate deformations. To achieve this, the prostate from the MR and Transrectal US volumes is manually segmented and then, the segmented surfaces are used to manually establish point correspondences. A pre-registration, consisting of superimposing the centres of gravity of Transrectal US surface and MR surface, initializes the unknown transform. From this initial estimate, rotation and translation parameters between two surfaces, as well as local deformations are estimated. The method is derived from the octree-spline elastic registration proposed by Reynier et al. [113]. A total of 8 patient data sets are used to assess their algorithm.

Narayanan et al. [116] propose a method to elastically register Transrectal US-MR prostate surfaces. The prostate from MR and US volumes is first segmented via a discrete dynamic contour [117] using manual selection of a few boundary points. In the next step, the MR surface is rigidly registered with the Transrectal US surface via extended weighted procrustes analysis [118]. After the rigid registration, a deformable model [119] is employed to locally register the MR surface with the Transrectal US surface. Finally, the 3D MR image is elastically aligned with the 3D Transrectal US image using these boundary conditions. In this work, the prostate from the MR and Transrectal US volumes is first manually segmented and then, the segmented surfaces are used to manually establish point correspondences.

Natarajan et al. [120] elastically register the MR volume with the Transrectal US volume for prostate biopsy. In their method, the prostate from the MR and Transrectal US volumes are first manually segmented. Thereafter, an expert manually selects corresponding points on each pair of surfaces. Their registration method involves two main steps. First, the US volume is rigidly registered with the MR data and then, the method of Narayanan et al. [116] and Karnik et al. [121] are used to estimate surface deformation.

Lange et al. [122] propose a 3D/3D feature-based deformable registration method in which the center lines of the portal veins in liver are used as features. In their work, the vessels are first segmented and their center lines extracted from MR and US image volume. Corresponding points on the center lines of both modalities are determined by ICP algorithm with B-Spline transformations. To achieve this, the search is restricted to a radius and the direction of the vessels.

Mitra et al. [48,49] register 2D Transrectal US to 2D MR to assist prostate biopsy. This work uses TPS deformation model with automatic chosen correspondences to map the 2D MR prostate images into the Transrectal US images. They assumed that the 2D MR/Transrectal US corresponding slices are found on visual inspection by an expert. Then, the prostate regions are segmented using the method Ghose et al. [123] from corresponding MR and Transrectal US images. The corresponding points are generated by a triangulation approach based on geometry of the segmented prostate contours in the respective modalities. The principle component analysis of the contours are used as the underlying framework for their algorithm. The Transrectal US image principle axes are projected and centered on the MR prostate contour. Then, triangles are generated by joining the adjacent intersection of principal axes forming a quadrant and dropping a perpendicular from the midpoint of the line joining these intersection. The adjacent intersection points and the point of intersection of the perpendicular dropped on the prostate contour comprise a triangular approximation of the prostate region in the quadrant. Likewise, other quadrants of the shape are processed for both images. Moreover, instead of considering only the contour points for deformable registration, certain points inside the prostate contour are also considered for a smooth deformation of the internal glandular structure of the prostate. After establishing point correspondences, deformable registration is then solved with a TPS. The drawback of this method is that it cannot handle concave shapes.

Biomechanical models have also been used to model the organs and their surrounding tissues with applications in US-MR image registration problems. In this manner, Hu et al. [124,125] use a biomechanical model of prostate to simulate deformation and learn a statistical shape motion model. This model is then used to

constrain registration.

### 4.2.3 Hybrid Methods

Cosse et al. [126] propose a method to register 3D US prostate and rectum images onto 3D MR images. The MR image is first segmented using graph-cut while the US image is manually segmented. Segmentation results in a set of 3D surfaces in both modalities. Registration is then carried out in two steps. First, rigid ICP is performed using the surface of the rectum and the prostate. Finally, a deformable demons algorithm presented by Pennec et al. [127] is applied to distance maps resulting from globally registered surfaces.

Lu et al. [128] develop a semi-automatic hybrid registration algorithm to register 3D high intensity focused US kidney and liver images onto 3D MR images with the purpose of mapping therapy planning into coordinate system of US. At first, linear affine transformation parameters are computed by a set of points which are manually selected by an expert. Afterwards local deformation is described by the Free-Form Deformation model based on B-splines and MI [129]. In their work they show that US-MR registration using [129] is not possible, since mutual information function must be quasi-convex with as few local extrema as possible. However, the speckle noise in US images and interpolation artifacts often make it difficult to have such behaviours. In order to remove the undesired local extrema and create smooth mutual information function, the algorithm use the following steps. Firstly, the US images are filtered by total variation minimization and oscillatory functions [130]. Then, the Histogram Partial Volume (HPV) interpolation algorithm [131] is used to estimate the joint histogram, which uses an approximation function of Hanning windowed sinc [132] as kernel function of partial volume interpolation. A simple iterative gradient descent technique is used to optimize the cost function.

Lange et al. [133] Combine anatomical landmark information as a constraint and normalized gradient field as the symmetric measure. Their method improves the mean of point distances comparison with the rigid and the TPS registration which are based only on landmarks. In their method TPS registration is the fundamental method of

deformable registration. To obtain a better match, the intensity information is also integrated into the optimization problem as a constraint. The objective function consists of a normalized gradient field as a similarity measure and a regularization term, which indicates the level of smoothness of the deformation field. A Discretize-Optimize approach is used as an optimization technique.

### 4.3 The Iterative Closest Point Algorithm (ICP)

ICP algorithms establish a set of correspondences by searching for closest point to moving data on the reference data, estimate a transformation which superimpose the moving data to those correspondences established by searching from the transformed moving data. In other words, ICP algorithms establish correspondences based on a closest distance criterion and estimates least-square rigid transformation relating two data sets. The algorithm then reestablishes the correspondences and continues until it converges to the local minimum. As rigid ICP, deformable ICP has also two inner steps. However, instead of finding rigid transformation parameters, a deformation field must be found [134]. This can be done by minimizing a cost function including a data term and a smoothing term. Besl and MacKay [135] and Chen and Melioni [136] estimate a global rigid transformation. In both methods each step of the iteration is optimal with respect to the estimated correspondences. The main difference in the two methods is that in the method propose by Besl et al. [135] correspondences are established by using the closest-point heuristic, while in Chen et al. [136] correspondences are determined only along the surface normal. Besl et al. [135] present a general registration strategy called Iterative Closest Point (ICP). For each iteration of registration process, the closest point in one surface is determined from all the points relative to another surface. These point correspondences are used to align the image by optimizing the transformation. Note that, the iterations in ICP algorithms are due to the fact that they iteratively improves the assigned correspondences. Due to ICP's simplicity and efficiency, many different ICP algorithms have been proposed that affect all phases of the algorithm from the minimization procedure to the selection and matching of points [137–139]. Therefore, ICP methods are distinguished by

type of deformation they recover, and by the way in which these deformations are found.

Although ICP algorithms have been applied to various registration problem, there are multiple critical issues that need to be considered. Generally, ICP methods converge to the correct solution when the initial position of the two data sets is adequately close. If not, ICP may get stuck in a local minimum. To solve this issue, pre-registration which is also known as coarse registration has been used. In ICP methods, the closest point computation step is the bottleneck of the algorithm because of the quadratic complexity ( $O(n^2)$ ) in establishing the correspondence of each point. We can conclude that the most computationally expensive step in the ICP algorithm is finding the closest points. However, as suggested by Besl [135] and demonstrated by Zhang [140], the closest point complexity can be decreased to  $O(n \log n)$  by use of k-d tree structure [141]. Friedmankd et al. [142] use the closest point algorithm based on the k-d tree to significantly improve the execution time of the classical ICP [135]. In this work, the k-d tree structure converts the closest point computation to the search of a binary tree. At each node of the tree, a test is performed to decide which side of a hyperplane the closest point will lie on. Using this method, large regions of the search space can be pruned at each level in the search. ICP based on caching closest points proposed by Simon [143] is another approach to improve the speed of the classical ICP [135]. In this work, the data point correspondence search is only among a subset of model points which are the closest at the previous iteration. Nuchter et al. [144] combine k-d tree with caching in order to further improve the speed of ICP.

In order to improve the accuracy of ICP-based algorithms different strategies have been proposed. The simplest and easiest strategy that can be used is outlier rejection. Closest point computation may easily find wrong correspondences because of errors or the existence of non-overlapping between two data sets. Normally, an outlier rejection technique thresholds the error. The threshold can be tuned manually, or can be 10% of worst pairs [137, 145, 146]. Some other techniques employ a simple and an efficient outlier rejection rule, called *X84* [147, 148]. In addition, Phillips et al. [149] use statistical analysis in order to remove outliers from point correspondence procedure

of ICP method. To achieve this, a new data term called Fractional Root Mean Square Distance is added to the ICP's formulation of finding point correspondences.

Another way to improve the robustness of the classical ICP is to use fuzzy correspondences. Note that all the methods thus far mentioned, treat the correspondences as strictly binary variables. Other methods relax this constraint using fuzzy correspondence [150]. Generally, two different approaches exist in literature. Wells [151], Cross et al. [152], and Hinton et al. [153] propose a probabilistic approach. The point sets registration explicitly formulate as a maximum likelihood (ML) estimation problem, to fit Gaussian Mixture Model (GMM) centroids to the data points. The well-known Expectation Maximization (EM) algorithm is employed to solve the registration problem. This algorithm consists of two steps: 1) the E-step estimates the correspondence under the estimated transformation from previous iteration. 2) the M-step updates the transformation parameters based on the current correspondences. Wells [151] includes an extra uniform distribution term to handle outliers. Hinton et al. [153] propose a very similar algorithm that can deal with the local deformations between two handwriting digits. B-spline as well as linear affine transformation are used to estimate the deformation. Note that Wells [151] and Cross et al. [152] only solve for rigid transformations. The key problem shared by all probabilistic approaches is that they do not enforce one-to-one correspondence. To solve this problem Gold et al. [154], Rangarajan et al. [155], and Chui et al. [150, 156] model point sets registration as a joint linear assignment-least square optimisation problem. To solve this optimisation problem, deterministic annealing and softassign are used. Combination of this two methods guarantee one-to-one correspondence. The resulting methods are very similar to EM-ICP algorithm.

In order to improve both the robustness and the computational efficiency of classical two-step rigid ICP, a distance transform is also introduced by Fitzgibbon et al. [138]. The distance transform allows one to merge the two inner steps into only one. Fitzgibbon et al.'s one-step ICP computes rigid 2D/2D and 3D/3D registration of a single pair of shapes. The registration error is minimized using the Levenberg-Marquardt algorithm. The literature on ICP is wide, and we refer the reader to the

recent survey by Castellani et al. [146] for more details.

## 4.4 Slice-to-Volume Registration

2D/3D medical image registration has received considerable attention and has been applied to various problems. 2D/3D registration may refer either to registration of projective data to 3D data (for example, a 2D projective X-ray image with 3D CT images [101,157,158]) or to registration of a single tomographic slice to 3D volumetric data (for example, a 2D US slice with 3D CT images [159]). The first case, which is known as projective registration, tries to find correspondences between a 2D image and a projection of a volume to planes. The second case, which is also known as slice-to-volume registration, seeks to find correspondences between a 2D image and a cross-section of volume by a plane or warped surface. This can be considered as an extreme case of 3D/3D registration where one of the images reduces to one slice. Note that in projective registration, there does not exist a one-to-one correspondence between the 2D and 3D data. This leads to fundamentally different registration methods in comparison to slice-to-volume registration. In this work, we focus on slice-to-volume registration, therefore a general survey on projective registration methods is beyond the scope of this section. We refer the reader to Markelj et al. [160] for a recent comprehensive review. Note that many researchers adapt the ICP algorithms to the projective 2D/3D registration problem [161].

To date, different slice-to-volume registration methods have been proposed. However, there are no report of slice-to-volume TVUS-MR registration for female pelvis organs. One of the approaches to solve slice-to-volume registration problem is to use a so-called compounding technique [162–164]. Heldmann et al. [165] try to register a CT volume with US slices using this technique. In this manner, the US slice is compounded into volume by interpolating and then a 3D/3D image registration method is employed. However, they practically show that registration using compounding technique cannot provide reasonable results. They also reveal that matching a CT volume to artificially reconstructed volumetric US data does not provide comprehensive information for the surgeon. Therefore, various other approaches have been used

to solve slice-to-volume registration problem. Below we summarize some of them.

Fei et al. [166] investigate intensity-based registration methods to rigidly align real time interventional MR image slices with a high resolution preoperative MR volume. Their algorithm uses for interventional MR-guided radio frequency thermal ablation of prostate cancer. They use a multi-resolution and multi-start strategies with two intensity similarity measures to avoid local maxima. The multi-start strategy is used to restart registration process with randomly perturbed parameters obtained from a uniform distribution about the initial transformation values at the current resolution being used. They employ MI and correlation coefficient as similarity measures. The correlation coefficient is used at two lower resolution whereas MI is used at full resolution. This is due to the fact that correlation coefficient surfaces are much smoother than MI. In other words, at low resolution, MI surfaces are noisy and contain many local maxima. However, at full resolution, MI has sharper peak than correlation coefficient. For optimisation, they use downhill method [84] or Powell's method [83].

Gill et al. [167] propose a similar method to Fei et al.'s method [166] to register the prostate interventional MR image slices with a high resolution preoperative MR volume. In contrast with Fei et al.'s method [166], their algorithm completely discards the multi-start strategy and only use multi-resolution strategy with two levels of resolution. Firstly, their algorithm register a single slice, but it did not provide good registration accuracy. The reason is that a single slice may not contain enough information, thus the registration can easily stuck in local minima. Therefore, they use two slices in unison to boost the precision of their registration results.

Xu et al. [168] propose an intensity-based method to align a small region of CT fluoroscopy image with a corresponding region in a CT volume in order to provide information about the position of the target lesion with respect to the imaging plane. Their registration algorithm assists lung biopsy. It is used a hieratical multiresolution and multi-start strategies to avoid local minima. The local deformation between the two regions is modelled by an affine transformation. The Levenberg-Marquardt algorithm is employed to solve the sum of square difference cost function. Since a multi-start strategy is used, multiple candidate transformations between the two

regions are obtained. The true transformation of the CT fluoroscopy region is chosen from these candidate using similarity voting. The chosen transformation is then combined with a Kalman filter to predict the lesion’s position for the next frame.

Helmann et al. [165] propose a variational deformable slice-to-volume registration to align series of 2D MR slices with 3D MR volumes. They minimize an objective function made up from a distance term (sum of square differences) and a smoothing term (curvature-based) with respect to a 3D nonlinear deformation field by using Gauss-Newton optimisation method. In contrast to compounding techniques, they evaluate the distance of the images only on the two-dimensional manifold where the data is known. The vital task in their algorithm is the choice of regularizer. They show that at least second-order regularization is needed to successfully avoid kinks and to estimate smooth deformation.

Ferrante et al. [169] propose a deformable intensity-based mapping algorithm between a 2D MR slice and a 3D MR volume. They try to find a linear plane transformation and an in-plane deformation field. This is achieved by using Markov Random Fields.

Osechinskiy et al. [170] propose a deformable intensity-based registration to map a 2D histology image to a MR brain volume. Their registration method involves two main steps. First, a rigid transformation is estimated and then a 3D dense deformation is found. Note that the deformation field is parameterized by various classes of spline functions such as TPS, Gaussian elastic body splines, or cubic B-splines. TPSs are used in a novel way to parameterize a smooth 3D deformation of a 2D surface. More specifically, control points are placed in a regular grid on the 2D image domain, and a 3D warp is modeled by three independent TPS functions. Their registration framework provides a flexible selection of cost function similarity measure such as SSD, CC, MI, NMI. Finally, they conclude that the CC cost function works better than other similarity measures, and registration with TPS model is the fastest. Multiresolution Levenberg-Marquardt optimization strategy is used to minimize the cost function.

Dalvi et al. [171] propose a feature-based slice-to-volume approach to rigidly reg-

ister 2D MR images to 3D MR volumes of the human brain. Their algorithm extracts phase congruency image features that are then matched using classical ICP [135].

## 4.5 Conclusion

Since there is no method to register TVUS images with MR images of the female pelvis, we have reviewed the current literature related to US-MR image registration for other organs. All these methods compute transformation 2D/2D or 3D/3D registration of a pair of 2D images or a pair of 3D volumetric data, respectively. The methods have been classified into three different categories such as intensity-based, feature-based, and hybrid-based methods. We see that US-MR intensity-based registration is a relatively unexplored topic. This is due to the fact that US-MR intensity-based registration is difficult task since the US contains a speckle image of tissues boundaries, whereas the MR provides information on tissues intensity. Feature-based registration is mainly used to register US with MR images, since it can be applied to any image. To improve both intensity- and feature-based methods, some researchers combine both approaches. It is observed from all these methods that spline-based deformable models have been mainly used for US-MR fusion. Since there is no system available to register TVUS to MR images, in next chapter, we provide a comparison of the two different registration approaches and investigate the applicability of these methods in TVUS-MR registration problem.

We have also discussed the state-of-the-art of iterative closest point algorithm. Many different ICP algorithms have been proposed that try to improve the computational time or robustness. In order to improve both the robustness and the computational efficiency of classical two-step rigid ICP, a distance transform is introduced. The distance transform allows one to merge the two inner steps into only one. In contrast to Fitzgibbon et al.'s one-step rigid ICP, in this thesis, we use a variational procedure to obtain nonlinear deformations and handle multiple curve to surface correspondences. Moreover, in chapter 8, the proposed method attempts to solve slice-to-volume deformable registration whereas Fitzgibbon's method solves the 3D/3D or 2D/2D rigid registration problems.

We have also shown that the 2D to 3D medical image registration can be classified into two categories: projective methods and slice-to-volume methods. We see 2D/3D image registration has received considerable attention in the topic of projective registration. However, there are few publications in the context of slice-to-volume registration. This approach tries to find correspondences between a 2D image and a cross-section of a volume by a plane or a warped surface. Most methods in the literature rely on an intensity-based similarity measure. However, US-MR registration with an intensity similarity measure may easily fail. In chapter 8, we propose a new deformable feature-based slice-to-volume registration method to establish point correspondences and to estimate deformation between a set of curves (from TVUS) and a set of corresponding 3D reconstructed surfaces (from 3D MR).

# Chapter 5

## Registration Strategy

### Contents

---

<b>5.1</b>	<b>Introduction</b>	<b>70</b>
<b>5.2</b>	<b>Image Registration</b>	<b>71</b>
5.2.1	Point-Based Image Registration Based on Thin-Plate Splines	71
5.2.2	Intensity-Based Image Registration with NMI	77
<b>5.3</b>	<b>Experimental Results</b>	<b>81</b>
5.3.1	Material	81
5.3.2	Results and Discussion	82
<b>5.4</b>	<b>Conclusion</b>	<b>86</b>

---

### 5.1 Introduction

In this chapter, we provide a comparison of the two different registration approaches—intensity- and feature-based—and investigate the applicability of these methods in the TVUS-MR registration problem. After analysing Chapter 4, we may realize that feature-based registration based on a spline representation of the deformation field has been widely used as the deformable model in US-MR alignment. Among all spline-based point driven deformable image registration techniques, the TPS technique introduced by Fred Bookstein [47] is one of the most commonly used methods for deformable medical image registration and anatomical shape analysis. We also find that NMI is among the most applied measures of similarity in the literature of multimodal image registration [53, 54, 63, 67, 70, 102, 104, 105, 172]. Therefore, in this chapter, we consider a point-based registration using TPS deformations [47] and an intensity-based registration using NMI and B-splines deformation [173] to align

pre-operative TVUS to MR images whereby we can experimentally discover which strategy and technique works best in our problem.

## 5.2 Image Registration

Let us point out again that registration methods try to optimize an objective functional or a similarity measure that indicate how accurately two images are registered. The similarity measures can be based on the differences or probability density of the intensity values and/or the distances between certain homogeneous features in the two image sets to be registered. Consequently, medical image registration has been divided roughly into two categories: 1) feature-based or 2) intensity-based methods. Here, we focus on two widely used methods in multimodal medical image registration; we choose one method from each category. In this manner, we choose a feature-based registration using TPS deformations with manual point selection [47] and an intensity-based registration using NMI and B-splines deformations [173] to register and fuse pre-operative TVUS into MR images. Note that, Mitra et al. [51] subjected these methods to thorough test of Transrectal US-MR registration for prostate biopsy, and found that both methods can successfully register 2D Transrectal US to 2D MR images. However, in their tests, the TPS method proposed by [47] was the best one. Although these methods are used and shown to be applicable in Transrectal US-MR image registration, it does not mean that they are applicable to our registration problem since we deal with different soft tissue organs and anatomical structures. In addition, in both MR and Transrectal US images, the prostate region has homogenous intensity which is not mainly the case in our problem. Therefore, it is necessary to apply these two methods to our data to find out whether they are applicable or not, as well as their advantages and disadvantages.

### 5.2.1 Point-Based Image Registration Based on Thin-Plate Splines

In point-based registration, the spatial transformation which is required to minimize the distance between point correspondences can be computationally efficiently

estimated and applied to image data sets. However, it usually require to extract corresponding points manually or semi-automatically, which makes this an operator-intensive and -dependent approach. Here, since the aim is to investigate the applicability of the TPS method proposed by Bookstein [47] in TVUS-MR registration problem, we consider the simplest way of resolving the correspondence problem. Therefore, an expert manually establishes the dense correspondences between soft tissue organs i.e. bladder, rectum, uterus and ovaries in both TVUS and MR. To achieve this, the following strategy has been used to establish point correspondences. First, the available soft tissue organs in the TVUS moving image  $M$  and in the corresponding 2D MR reference slice  $F$  were segmented by an expert. This step helps to construct two sets of curves,  $C_M$  and  $C_R$ , representing the boundary of the corresponding organs in both images. Second, an expert manually selects points on each pair of curves. Therefore, two new sets of  $N$  points,  $q_i = (x_i, y_i)$  and  $p_i = (x'_i, y'_i)$  ( $i = 1, \dots, N$ ), between the two images are established.

To date, numerous different image registration algorithms which are employing point correspondences have been proposed. Indeed the TPS technique pioneered by Fred Bookstein [47, 174–176] is the most commonly used point driven image registration algorithm. A thin-plate is conceived as a 2D thin metal plate which when tacked by a point or a set of points produces bending of the surface in the  $z$ -direction:

$$z(x, y) = -\rho(r) = -r^2 \log(r) \quad (5.1)$$

where  $r$  is the 2-norm distance (Euclidean distance) of the points on the surface from the tacked points. Here,  $\rho$  is a fundamental solution of the biharmonic equation  $\Delta^2 \rho = 0$ , the equation for the shape of a thin steel plate lofted as a function  $z(x, y)$  above the  $xy$ -plane.

As mentioned before, The TPS is a widely used basis function for representing coordinate mapping from  $\mathbb{R}^2$  to  $\mathbb{R}^2$ , when a set of corresponding points are established. In its regularized form, the TPS transformation involves the affine model as a special case. Following is a brief mathematical description of the 2D image registration based on TPS model.

The TPS minimizes the quadratic variation functional of the potential energy that reflects the amount of variation that should be small for a good mapping function. Then, the TPS interpolant  $\phi(x, y)$  minimizes the bending energy or the integral bending norm:

$$R[\phi] = \int_{\Omega} \left( \left( \frac{\partial^2 \phi}{\partial x^2} \right)^2 + 2 \left( \frac{\partial^2 \phi}{\partial x \partial y} \right) + \left( \frac{\partial^2 \phi}{\partial y^2} \right)^2 \right) dx dy \quad (5.2)$$

Notably the transformation function has the form

$$\phi(x, y) = \sum_{i=1}^N \omega_{ij} \rho(\|(x_i, y_i) - (x, y)\|) + a_{j1} + a_{j2}x + a_{j3}y \quad (5.3)$$

where  $j = 1, 2$ ,  $\rho = r^2 \log r$  is the radial-basis function and  $\omega_{ij}$ 's are the weights allocating to each of control point of the moving image.  $\phi(x, y)$  must have square integrable derivative if

$$\sum_{i=1}^N \omega_{ij} = 0 \quad \text{and} \quad \sum_{i=1}^N \omega_{ij} x_i = \sum_{i=1}^N \omega_{ij} y_i = 0 \quad (5.4)$$

The boundary conditions in Equation (5.4) guarantee that the thin-plate does not rotate or bend when influenced by the loads of the points.

Once the interpolation conditions are considered as  $\phi(x_i, y_i) = p_i$ , we rewrite  $r_{ij} = \|q_i - q_j\|$ ,  $i, j = 1, \dots, N$  as the distances between all the data points  $q_i$  and  $q_j$ . Then, the following linear system is obtained:

$$\begin{bmatrix} K & Q \\ Q^T & O \end{bmatrix} \begin{bmatrix} W \\ A \end{bmatrix} = P \quad (5.5)$$

The matrices are defined as

$$K = \begin{bmatrix} 0 & \rho(r_{12}) & \cdots & \rho(r_{1N}) \\ \rho(r_{21}) & 0 & \cdots & \rho(r_{2N}) \\ \cdots & \cdots & \cdots & \cdots \\ \rho(r_{N1}) & \rho(r_{N2}) & \cdots & 0 \end{bmatrix}_{N \times N}$$

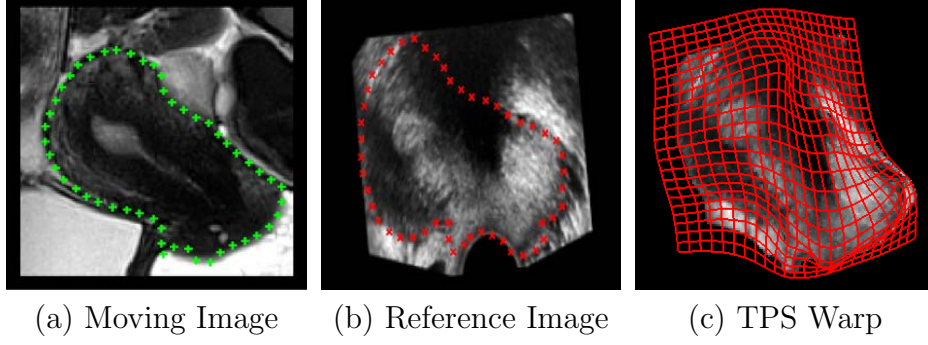


Figure 5-1: Example of exact principal warp. (a) shows a reference image with selected control points (+). (b) shows a moving image with selected control points (×). (c) shows the exact principle warps of the configuration.

$$Q = \begin{bmatrix} 1 & x_1 & y_1 \\ 1 & x_2 & y_2 \\ \dots & \dots & \dots \\ 1 & x_N & y_N \end{bmatrix}_{N \times 3} \quad ; \quad W = \begin{bmatrix} \omega_{11} & \omega_{12} \\ \omega_{21} & \omega_{22} \\ \vdots & \vdots \\ \omega_{N1} & \omega_{N2} \end{bmatrix}_{N \times 2}$$

$$A = \begin{bmatrix} a_{11} & a_{12} \\ a_{21} & a_{22} \\ a_{31} & a_{32} \end{bmatrix}_{3 \times 2} \quad ; \quad P = \begin{bmatrix} x'_1 & x'_2 & \dots & x'_N & 0 & 0 & 0 \\ y'_1 & y'_2 & \dots & y'_N & 0 & 0 & 0 \end{bmatrix}_{2 \times (N+3)}^\top$$

where  $W$  is the unknown matrix for the TPS weight parameters,  $A$  is the unknown matrix for the affine parameters, and  $O$  is a  $3 \times 3$  matrix of zero. Thus, the linear system of equations can be solved by least-squares estimation as the coefficient matrix:

$$\begin{bmatrix} W \\ A \end{bmatrix} = \begin{bmatrix} K & Q \\ Q^\top & O \end{bmatrix}^{-1} P \tag{5.6}$$

The interpolation conditions ( $\phi(q_i) = p_i$ ) exactly map the points on the moving image onto the reference corresponding points. An example TPS transformation is shown in Figure 5-1. However, since there might be errors in the localization of the point correspondences across two images, mapping exactly one point to its correspondence is not always a desirable approach. To solve this problem, the localization errors of the correspondences can be considered by substituting the interpolation to approx-

imation and regularization TPS [177]. This is accomplished by the minimization of the following variational problem:

$$E[\phi] = \sum_{i=1}^n \underbrace{\frac{(p_i - \phi(q_i))^2}{\sigma_i^2}}_{\text{data term}} + \lambda \underbrace{R[\phi]}_{\text{smoothing term}} \quad (5.7)$$

where  $R[\phi]$  is defined in Equation (5.2),  $\sigma_i^2$  is the sum of the covariances of the points  $p_i$  and  $q_i$  across both images, and  $\lambda$  is a smoothing parameter.  $\lambda$  is a positive scalar and balances the amount of smoothing. Thus, as  $\lambda$  approaches zero ( $\lambda \rightarrow 0$ ), Equation (5.7) turns out to behave more similar to the TPS interpolant. In other words, when  $\lambda$  is small, we obtain a solution with good approximation behavior. Notably in the limit of  $\lambda \rightarrow 0$ , we have an interpolating transformation. On the other hand, when  $\lambda$  has high value, we obtain a very smooth transformation. Consider that, when  $\lambda$  approaches infinity, we have an affine transformation that has no smoothness energy  $R[\phi]$  at all. The weighting of the correspondence localization error with the inverse of the variances guarantees that when the variance is high (i.e. the measurements are uncertain), less penalty is given to the approximation error at this point.

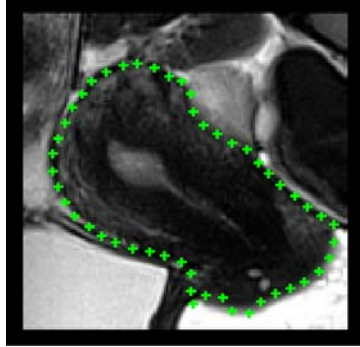
Finally, the quadratic approximation term of Equation (5.7) can be analytically introduced into the linear system of equations of Equation (5.5) as:

$$\begin{bmatrix} K + n\lambda C^{-1} & Q \\ Q^T & O \end{bmatrix} \begin{bmatrix} W \\ A \end{bmatrix} = P \quad (5.8)$$

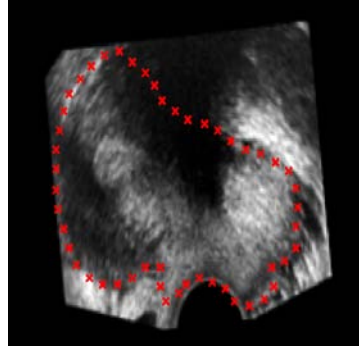
where:

$$C^{-1} = \begin{bmatrix} \sigma_1^2 & & 0 \\ & \ddots & \\ 0 & & \sigma_n^2 \end{bmatrix}$$

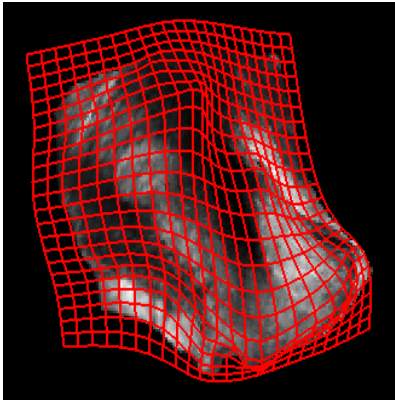
Introducing the term  $n\lambda C^{-1}$  leads to a better linear system and a robust numerical solution. After obtaining the affine and TPS weight parameters, the moving image pixels are transformed using  $\phi$  as in Equation (5.3). An example of approximating TPS is shown in Figure 5-2.



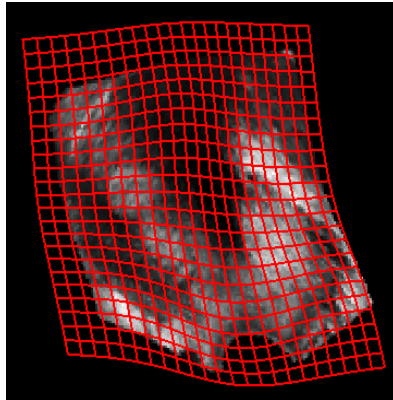
(a) Reference Image



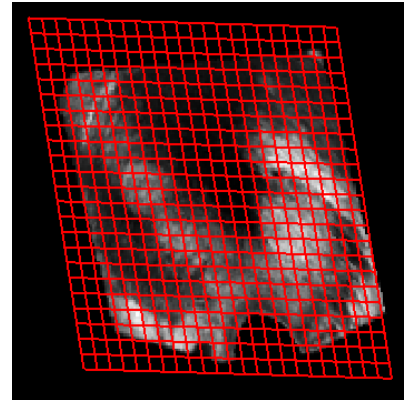
(b) Moving Image



(c)  $\lambda \rightarrow 0$



(d)  $\lambda = 0.01$



(e)  $\lambda \rightarrow \infty$

Figure 5-2: Performance of approximating TPS visualized by deforming a regular grid. (a) shows a moving image with selected TPS control points ( $\times$ ). (b) shows a reference image with selected control points ( $+$ ). (c) shows the exact warps of the configuration ( $\lambda \rightarrow 0$ ). (d) and (e) depict the smooth warps with different choice of the smoothing parameter ( $\lambda = 0.01$  and  $\lambda \rightarrow \infty$ , respectively). In the limit of  $\lambda \rightarrow \infty$  we obtain a very smooth transformation which is nearly an affine transform.

## 5.2.2 Intensity-Based Image Registration with NMI

In this part, we focus on an intensity-based registration using NMI and B-splines deformations [173] to register pre-operative TVUS with MR images. In Rueckert et al.'s method [173], the local deformation of the soft tissue organs is described by cubic B-splines. The basic idea of this method is to deform an object by estimating an underlying control polygon (also known as mesh of control points) [178–180]. The estimated deformation controls the shape of the 2D or 3D objects and provides a smooth and continuous  $C^2$  transformation.

### 5.2.2.1 Deformation Modeling with B-Splines

We consider that  $\Omega \in \mathbb{R}^2$  be an image domain,  $\Psi$  as a mesh of  $n_x \times n_y$  ( $n_x$  and  $n_y$  are width and height of the image, respectively) knots  $k_{i,j}$  with a uniform spacing  $\delta$ . Then a cubic B-spline may be defined as a 2D tensor product of 1D cubic B-spline:

$$\phi_{local}(x, y) = \sum_{l=0}^3 \sum_{m=0}^3 b_l(u) b_m(v) k_{i+l, j+m} \quad (5.9)$$

where  $j = \lfloor y/\delta \rfloor - 1$ ,  $i = \lfloor x/\delta \rfloor - 1$ ,  $u = x/\delta - \lfloor x/\delta \rfloor$ ,  $v = y/\delta - \lfloor y/\delta \rfloor$ , and  $b_l$  represents the  $l$ th basis function of the 1D cubic spline [181] given as:

$$N_i(x) = \begin{cases} b_3(u) = \frac{1}{6}u^3 \\ b_2(u) = \frac{1}{6}(-3u^3 + 3u^2 + 3u + 1) \\ b_1(u) = \frac{1}{6}(-3u^3 - 6u^2 + 4) \\ b_0(u) = \frac{1}{6}(1 - u)^3 \end{cases}$$

In contrast with the TPS [47], cubic B-splines are locally adjusted, which decreases computational cost even for a large number of knots. It is apparent from Equation (5.9) that the deformation at any knot  $(x, y)$  is estimated by its 16 ( $4 \times 4$ ) surrounding neighbourhood. More specifically, each knot  $k_{i,j}$  has an effect on its ( $4 \times 4$ ) area that is a sub-domain of  $\Omega$ . Therefore, the basis functions of cubic B-splines have just a limited supports. For instance, changing a knot influence the transformation just in the local area of that knot. The knots  $k$  behave as parame-

ters of the cubic B-splines, and the resolution of control polygon  $\Psi$  (mesh of knots) changes the degree of non-linear deformation. More specifically, when the distance between knots are large, the estimated deformation would be much more similar to an affine transform. On the other hand, a small spacing of knots permits modeling of nonlinear deformations. Therefore, we can conclude that the computational cost and degrees of freedom highly depend on the resolution of the control polygon. The trade-off between computational complexity and degree of deformation is still an empirical choice that is chosen by the precision needed to model the deformation of the object versus the increase in computing time. In spite of this, the best approach is to use a hierarchical multiresolution approach proposed by Lee et al. [179]. In this method, the resolution of the control polygon is increased together with the image resolution in a coarse to fine fashion.

Now we consider that  $\Psi^1, \dots, \Psi^L$  be a hierarchy of control polygons at different resolutions. The interval between the knots decreases as the resolution increases from  $\Psi^L$  to  $\Psi^{L+1}$ . Note that, the interval between the knots in  $\Psi^L$  is double of the those in  $\Psi^{L+1}$ . The new locations of the knots in  $\Psi^{L+1}$  can be calculated from  $\Psi^L$  employing the B-splines subdivision algorithm [182]. Note that each control polygon  $\Psi^L$  defines a local transformation  $\phi_{local}^L$  at each level.

A penalty term which regularizes the deformation is introduced to force the cubic B-spline generates smooth transformation. The general form of such a penalty term has been deeply discussed by Wahba [183]. Note that, in 2D case, the cubic B-spline is equivalent to the TPS integral bending norm defined in Equation (5.2) and is written as:

$$R[\phi] = \int_{\Omega} \left( \left( \frac{\partial^2 T}{\partial x^2} \right)^2 + 2 \left( \frac{\partial^2 T}{\partial x \partial y} \right) + \left( \frac{\partial^2 T}{\partial y^2} \right)^2 \right) dx dy \quad (5.10)$$

where  $\phi$  is the transformation that consists of  $\phi_{global}$ , i.e. an affine transformation and  $\phi_{local}$  a non-linear transformation. It is to be noted that the regularization term is zero for affine transformation. A step-by-step description of the cubic B-spline based deformation is given in Algorithm 5.1.

---

**Algorithm 5.1** The NMI-based registration method using B-splines [173].

---

- 1: **Input:** A moving image (M) & a reference image ( $F$ )
  - 2: **Initialization:**
  - 3: **Compute** the optimal affine transformation parameters  $\Theta$  by maximizing  $D_{NMI}$
  - 4:  $\Psi \leftarrow \Psi^0$  % Initialize the control points  $\Psi$
  - 5: **Repeat**
  - 6: **Compute**  $\nabla E = \frac{\partial E(\Theta, \Psi^L)}{\partial \Psi^L}$
  - 7: **while**  $\|\nabla E\| > \varepsilon$  **do** % Gradient descent procedure
  - 8:      $\Psi^L \leftarrow \Psi^L + \mu \frac{\nabla E}{\|\nabla E\|}$  % update the control points  $\Psi^L$
  - 9:     **Compute**  $\nabla E$
  - 10: **end while**
  - 11: **Increase** the resolution of the current control points  $\Psi^L$  to  $\Psi^{L+1}$
  - 12: **Increase** the resolution of the both images
  - 13: **Until** finest level of resolution is achieved
- 

### 5.2.2.2 Similarity

As mentioned before, the multimodal image registration proposed by Rueckert et al. [173] uses B-splines and tries to maximize the similarity of pixel intensities using the NMI. Studholme et al. [72] has experimentally proved that NMI is more robust in multimodal registration than MI proposed by Maes et al. [184]. Here, the NMI image similarity is denoted as  $D_{NMI}$  and defined in Equation (3.10).

### 5.2.2.3 Optimization

The energy function consists of two terms. The first term corresponds to the cost associated with the image similarity  $D_{NMI}$ . The second term represents the cost associates with the smoothness of the transformation  $R$  as in Equation (5.10). The cost function is defined as:

$$E(\Theta, \Psi) = -D_{NMI}(F, \phi(M)) + \lambda R[\phi] \quad (5.11)$$

where  $\Theta$  is the affine transformation parameters,  $\phi$  is the deformation field and depends on  $\Theta$  and  $\Psi$ ,  $\lambda$  is a smoothing parameter,  $F$  is a reference image, and  $M$  is a moving image.  $\lambda$  is the trade-off between alignment of the images and the smoothness of the transformation. It is to be noted that the smoothness factor is of more importance at finer resolutions than coarser resolutions.

The optimization procedure involves two main stages. In the first stage, an iterative multiresolution search strategy [185] is used to find the affine parameters  $\Theta$ . To achieve this, we must maximize the image similarity measure defined in  $D_{NMI}$ . In the second stage, the nonlinear transformation parameters are estimated as a function of the cost functional in Equation (5.11). A simple gradient descent optimization is used. The algorithm stops since the magnitude of the gradient of the cost function  $\|\nabla E\|$  be less than a small variation  $\varepsilon$ . An example of NMI-based image registration [173] is shown in Figure 5-3.

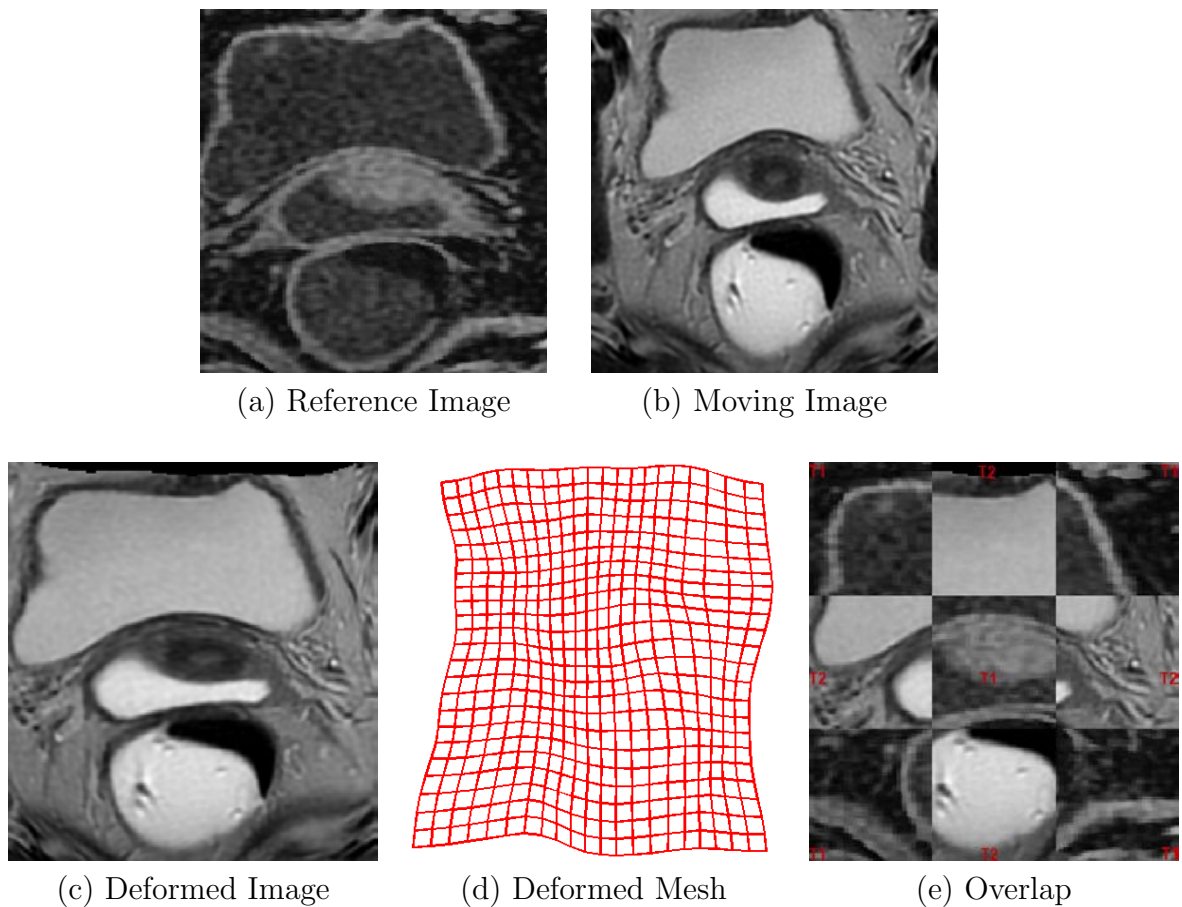


Figure 5-3: Example of multimodal image registration. (a) shows a T1 MR image which is selected as a reference image. (b) shows a T2 MR image selected as a moving image. (c) shows the registration result and (d) indicates its deformed mesh. (e) shows the overlap images.

## 5.3 Experimental Results

### 5.3.1 Material

The study is carried out on ten patients. For each patient, TVUS and MR imaging are used to examine their pelvic organs. TVUS is performed using a high-frequency Siemens Endocavity Curved Array Ultrasound probe (6.5 MHz) and Siemens Sono-line Elegra Ultrasound machine. Axial  $T_2$  MR slices with slice thickness of 5 mm, repetition time of 44083 – 49397 ms and echo time of 82.18 – 85.09 ms are acquired with a 1.5 Tesla GEM Suite. Images used for the experiments have an average image size of  $192 \times 192$ . The reference MR slice from MR volume that corresponds to the moving TVUS image is manually chosen by an expert. Therefore, we assume that the TVUS slice is parallel to the corresponding MR slice. Note that in principle the MR slice which is corresponding and parallel to the TVUS slice must be obtained by rotating the MR volume with respect to the rotational angle of TVUS image and then retrieving the MR slice parallel to the TVUS slice. However, we do not have any information regarding to the TVUS rotational angle in our current experimental process. The soft tissue organs (i.e. bladder, uterus, ovary, rectum) in both TVUS and MR slices are manually segmented by an expert and then manually selects points at each pair of curves. We compare the registration using TPS that uses point correspondences [47] against the registration using NMI computed from raw intensities of the multimodal images [173]. In NMI-based registration, we use a multi-resolution strategy to reduce processing time whereby the TVUS and MR images are subsampled by a factor of three. These dimensions are subsequently doubled until the optimisation of the parameters is completed with both images at their full resolutions. The cubic B-splines deform at each resolution to maximize the NMI computed from intensities of the images. The algorithms are implemented using MATLAB and tested on an *i5* core 3.3 GHz with 16 GB RAM.

### 5.3.2 Results and Discussion

We demonstrate the accuracy of the TPS-based [47] and NMI-based [173] deformable registration methods by quantitative and qualitative tests on real world data sets. Registration accuracy is evaluated in terms of DSC and TRE. The aim of these experiments is to provide a comparison of the two different registration approaches and investigate whether they are applicable to TVUS-MR registration problem or not. Therefore, we apply both methods to four different soft tissue organs including the bladder, uterus, rectum, and ovary.

DSC assesses the global overlap of the segmented organs. A high DSC value indicates a good overlap between the tissue regions after registration. In addition, to quantify the local registration error, we use the TRE. It is described as the mean square distance between corresponding points not used in estimating the deformation. As mentioned before, the main challenge in calculating TRE lies in finding corresponding target landmarks. The best target landmarks are those generated by a mechanical device which allows for an accurate positioning of the anatomy. However, this is not achievable for our study. The next best option is to choose anatomical landmarks in the patient’s body such as boundary of organs and their internal anatomical structures. We opt for this type of target points to estimate the local registration accuracy to validate our result. Notably a low TRE value shows good local registration accuracy. In our experiments, the target points are 15 points which are not used for registration. The DSC, TRE, and computational time for NMI-based registration [173] and TPS registration [47] are tabulated in Table 5.1. We observe that the TPS registration which uses point correspondences located over the segmented contours always has much higher average DSC and lower average TRE values over the NMI-based registration method, except for patient 9 where the dark shadows near the boundary of ovary in TVUS image help NMI to register the internal structures of the ovary more accurately (see Figure 5-4 rows 5 and 6). In addition, the TPS registration [47] is much faster than NMI-based registration method [173].

Figure 5-4 shows the registration results for patients 1, 3, and 9. Images in rows 1–

	Intensity-based: NMI [173]			Point-based: TPS [47]		
Patient	DSC	TRE (Pixel)	Time (sec)	DSC	TRE (Pixel)	Time (sec)
1	0.715	20.287	124.902	0.993	0.848	3.09
2	0.692	26.132	104.190	0.990	1.134	2.78
3	0.944	4.932	119.811	0.984	0.546	2.05
4	0.884	12.119	164.970	0.988	1.774	1.86
5	0.400	44.310	131.041	0.998	0.056	2.07
5	0.595	36.330	201.557	0.991	2.191	2.35
6	0.824	16.880	99.940	0.995	0.112	3.03
7	0.676	27.061	110.733	0.999	0.024	3.28
8	0.375	50.559	50.992	0.997	0.063	2.39
9	0.960	2.074	129.819	0.991	5.586	2.58
10	0.904	7.194	140.056	0.989	0.644	2.91
Mean	0.725	22.532	125.267	0.992	1.180	2.581
$\sigma$	0.206	16.099	38.097	0.004	1.630	0.474

Table 5.1: A comparison of registration accuracies of the NMI-based registration with TPS registration.  $\sigma$  is the standard deviation of the measures. The average DSC and TRE values indicate that TPS has high local and contour registration accuracy whereas NMI-based registration method usually fails.

2 belong to patient 1, rows 3–4 dedicate to patient 3, and rows 5–6 belong to patient 9. In this figure, the checkerboards can visually indicate the accuracy of NMI-based method and TPS method. As seen in Figure 5-4 for patients 1 and 3, the NMI-based registration method provides less accurate results which is also evident from Table 5.1. For instance, for patient 1, the NMI-based registration partially aligns the organ boundary. It is observed that the instant variation in intensities and contrast (i.e. on the lower contour region), would significantly decrease the registration accuracy. For patient 3, the checkerboards clear that the NMI totally fail to register the uterus boundary. This is mainly due to the fact that a probabilistic relationship between TVUS and MR intensities does not exist as TVUS image contains a speckle image of tissues boundaries, whereas MR provides information on tissue density. However, for these two patients, the TPS method provides high registration accuracy; this is obviously visible at the boundary of organs.

Images in rows 5 – 6 show registration results for patient 9, in which the NMI-

based registration method provides lower TRE value than the TPS method. As seen in Figure 5-4 for patient 9, the checkerboards show good region (the ovary) overlaps that are also evident from Table 5.1 for both methods. The reason that TPS method provides higher DSC values is that the TPS registration [47] is based on point correspondences primarily located on the organ boundary which results in higher contour accuracy. Although the region overlaps for the NMI-based method is lower than the TPS method, lower TRE value is obtained for the same patient with the NMI-based registration method as seen in Table 5.1 and Figure 5-4. It is also obvious from checkerboards that a better internal ovary structure alignment is achieved by using NMI-based method for patient 9. There may be a reason that NMI-based provides good registration accuracy for this patient: The dark region at the top of the ovary in both TVUS and MR images helps NMI to establish a good probabilistic relationship between TVUS and MR intensities which leads to a better alignment of the internal structures of the ovary. Moreover, since these probabilistic relationship between TVUS and MR intensities become weaker at the boundary of the ovary, the registration accuracy decreases at those points which leads to the lower DSC value.

Finally, the evaluation and the experimental results show that the TPS registration method gives accurate registration results whereas the NMI-based method mainly fails. The reason that NMI-based method has low registration accuracy is that the intensity variation between the MR and TVUS images is high so that the maximization of NMI mainly fails to reach a global maximum. Despite of this, the NMI-based registration method shows that when a probabilistic relationship between TVUS and MR intensities exists, it can provide better local registration accuracy as it considers all the pixels on the image rather than considering just set of points on the boundary of organs.

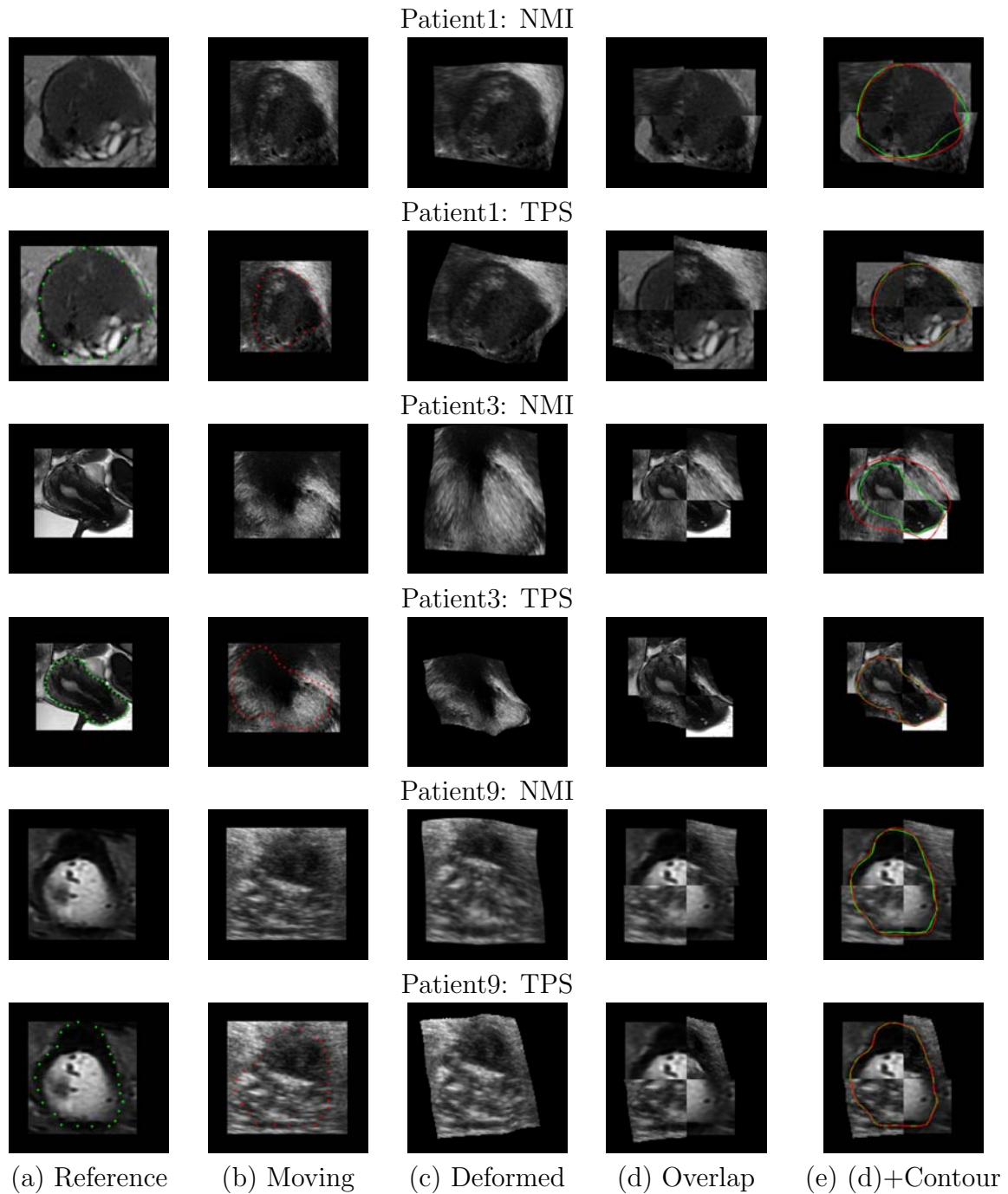


Figure 5-4: Examples for patient 1, 3, 9, respectively. Registration results for NMI-based registration method [173] and TPS [47] in rows. (a) shows a MR image which is selected as a reference image. (b) shows a TVUS image selected as a moving image. (c) shows the registration result. (d) and (e) indicate overlap image with and without contour, respectively. In the overlap images, the top right and the bottom left belong to the deformed TVUS data and also the top left and the bottom right belong to the MR data.

## 5.4 Conclusion

In this chapter two image registration methods such as TPS registration method and NMI-based method are used to register 2D TVUS with 2D MR images. The main purpose of this chapter is to provide a comparison of the two different registration approaches and investigate the applicability of these methods in TVUS-MR registration problem. This is an important task as there is no system available to register TVUS to MR images. NMI approach makes direct use of the original image data and the other is based on matching discrete geometric feature points. Both approaches have their relative advantages and disadvantages.

The advantage of using NMI-based method is that it operates directly on the image gray values, without prior data reduction by the user or segmentation. Theoretically, it is the most flexible of the registration approach, since it does not start by reducing the gray-level image to relatively sparse extracted information, but uses all the available information throughout the registration process which may lead to high local registration accuracy. However, NMI-based method has two main disadvantages. First, probabilistic relationship between TVUS and MR intensities mainly does not exist so that the maximization of NMI mainly cannot reach to an optimum value. This results in low contour accuracy (i.e. related to DSC measures). Second, this method requires estimating the joint histogram between two images which cause to increase computing time significantly. Since, the probabilistic relationship between TVUS and MR intensities does not exist and we need to have high contour accuracy to precisely localize endometrial implants, one must use point-based registration approach (e.g. the classical TPS method) to cope with the limitations of the multimodal intensity-based registration approach. Point-based registration is versatile in the sense that it, at least in theory, can be applied to any image, no matter what the object or subject is. Another advantage of this method is that since the set of identified points is sparse compared with the original image content, a point-based method has very fast optimisation procedures. A drawback of this method is that manually selecting point correspondences are often a challenging and time-consuming

process.

Based on the advantages and drawbacks of the feature- and intensity-based approaches and our experimental results, we find that the feature-based registration approach is an appropriate choice as it can apply to any image and provides high registration accuracy, even though it is a user-dependent method. On the other hand, the intensity-based approach is a limited method, since the probabilistic relationship between TVUS and MR images does not mainly exist. In the next chapter, different feature-based registration methods will be proposed to decrease user interaction by performing certain registration steps automatically while still relying on the user to guide the registration. Moreover, our experiments show that spline transformations do not perform well in the presence of local distortions. In order to cope with this problem, we will consider formulations of registration based on diffusion, first-order div-curl, and curvature regularizer. These lead to a range of non-parametric transformations.

# Chapter 6

## Parametrization-Based 2D/2D Registration

### Contents

---

<b>6.1</b>	<b>Introduction</b>	<b>88</b>
<b>6.2</b>	<b>Registration Procedure</b>	<b>90</b>
6.2.1	Correspondence by Arc-Length Parametrization	90
6.2.2	Densification	92
<b>6.3</b>	<b>Experimental Results</b>	<b>102</b>
6.3.1	Material	102
6.3.2	Results and Discussion	102
<b>6.4</b>	<b>Conclusion</b>	<b>108</b>

---

### 6.1 Introduction

In this chapter, we develop a variational approach to map endometrial implants from 2D TVUS to 2D MR images. In the previous chapter, we showed that one of the main challenges in TVUS-MR image registration is to correlate TVUS images to MR images. Generally, the small endometrial implants and their depth of infiltration are only visible in TVUS (see Fig. 6-1 (a)) while MR gives an accurate anatomical location of large implants (see Fig. 6-1 (b)) [26]. TVUS has relatively poor spatial and tissue contrast resolution compared with MR. Its images have low resolution. It has a small field of view and has a short range of penetration due to the use of a high-frequency transducer. These artifacts as well as multi-modality and soft tissue deformations make TVUS-MR registration challenging, especially in the design of a robust intensity

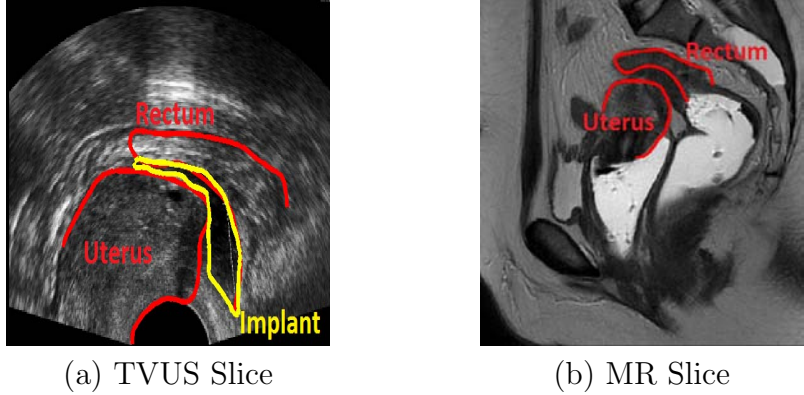


Figure 6-1: The most commonly used preoperative imaging modalities for detecting endometriosis: (a) TVUS and (b) MR images with a small endometrial implant. This example illustrates that TVUS reveals the depth of infiltration when MR does not but provides a global map of the location of the lesions with respect to the anatomy.

similarity measure. Therefore, our solution to this problem must lie completely in features-based approach, as concluded in Chapter 5. However, the main drawback of this method is that manually selecting dense point correspondences is a challenging and time-consuming process. To reduce the potential expert error and interaction time, we use a parametrization-based approach between shape contours to define dense correspondences. To this end, the expert first segments the organs and selects a few point correspondences. More point correspondences are then created using parametrization between each adjacent points. It is worth to note that the implants can be just seen in the TVUS images, so that there is no corresponding points at implants. We use a variational method to obtain a high accuracy solution of the PDEs representing the displacement field. The idea for our variational approach is to model the deformable image registration as a deformation process of certain material driven by internal forces. We use three different types of regularizer (internal forces). The first regularizer is the sum of the norm of the gradients of the deformation field in each dimension. The major disadvantage of first-order regularization is that it penalizes flow variations too much. To alleviate this limitation we use div-curl regularizer. Since the first-order and div-curl regularizations are sensitive to the global affine transformation, another smoothness term which is known as curvature regularizer is

used. This regularizer penalizes the curvature of the displacement field. Note that the usage of the regularization functional is to maintain the quality of the deformation field such that the deformation is an injective mapping. Furthermore, our model is not defined on the basis of a finite set of parameters (i.e. parametric methods) and is more suited in the case of no prior knowledge. Therefore, it has greater flexibility than spline-based methods such as TPS and B-splines [105]. We compare our method with the TPS [186] registration method. Experimental results illustrate the potential and efficacy of our method and visually show that the displacement field based on the TPS method is not as accurate as ours.

## 6.2 Registration Procedure

This section consists of two main parts, the first part discusses the procedure of selecting corresponding points on the moving and reference images. In part two, we provide solutions for three different nonlinear PDEs which are driven from different differential operators (regularizers). In this chapter, a numerical technique based on the finite difference method is used to solve the PDEs. Finite difference formulas for first, second, third, and fourth derivatives are given in Table 6.1.

---


$$f^{(1)}(x) \approx \frac{f(x+h) - f(x-h)}{2h}$$

$$f^{(2)}(x) \approx \frac{f(x+h) - 2f(x) + f(x-h)}{h^2}$$

$$f^{(3)}(x) \approx \frac{f(x+2h) - 2f(x+h) + 2f(x-h) - f(x-2h)}{2h^3}$$

$$f^{(4)}(x) \approx \frac{f(x+2h) - 4f(x+h) + 6f(x) - 4f(x-h) + f(x-2h)}{h^4}$$


---

Table 6.1: Central finite difference formulas for first, second, third, and fourth derivatives.

### 6.2.1 Correspondence by Arc-Length Parametrization

Finding the dense correspondences between soft tissue organs i.e. bladder, rectum, uterus and ovaries in both TVUS and MR data is a challenging task, even for an

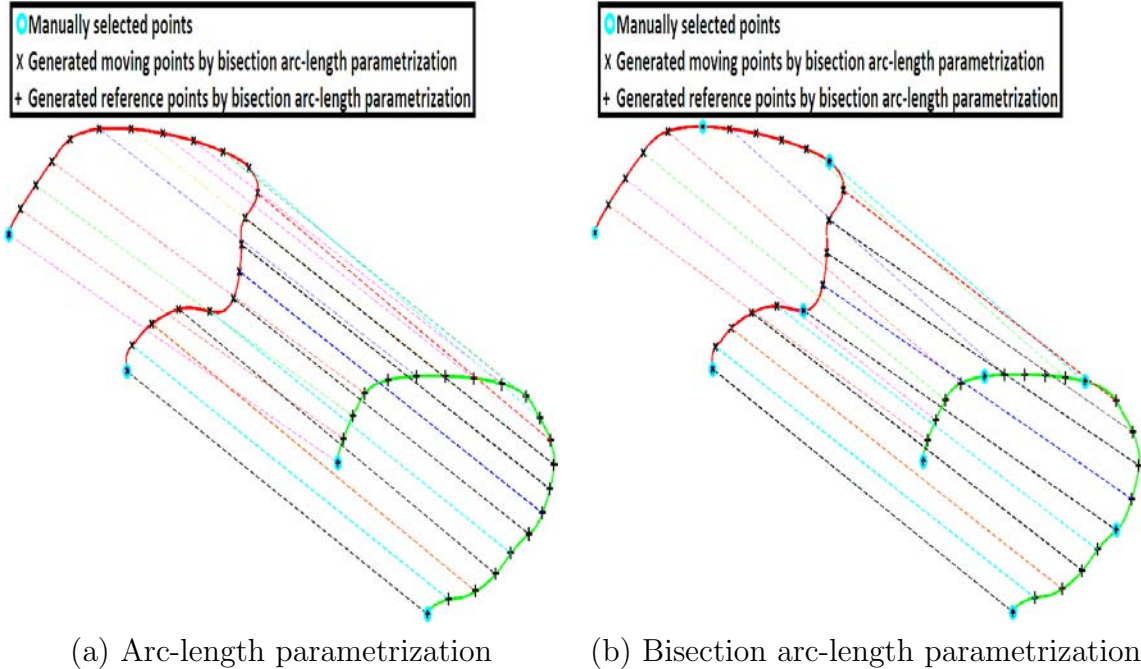


Figure 6-2: Examples of establishing correspondences by arc-length parametrization. (a) shows equally spacing point on each contour with a known starting and ending points. (b) shows equally spaced point on each curve segment (o). Looking blue points on (b), we can see that points on (a) are wrong

expert. Therefore, the following strategy has been developed to resolve this problem. First, the available soft tissue organs in the TVUS moving image  $M$  and in the corresponding 2D MR reference slice  $F$  are segmented by an expert. This step helps to construct two sets of curves,  $C_M$  and  $C_R$ , representing the boundary of the corresponding organs in both images. The simplest approach to establish correspondences between shape contours is to select a starting point on each contour and equally space an equal number of points on each boundary. However, as we see in Figure 6-2 (a), equally spacing point on each contour with a known starting point does not give a reasonable group-wise correspondence, and can lead to very poor models. To solve this problem, an expert manually selects a few points (normally, five to ten points) at each pair of curves. Finally, arc-length parametrization is used between each adjacent points to establish dense correspondences. Therefore, two new sets of  $N$  points,  $q_j$  and  $p_j$  ( $j = 1, \dots, N$ ), between the two images are established. As we see in Fig-

ure 6-2 (b), our strategy gives a reasonable group-wise correspondence, and can lead to accurate correspondences. This figure depicts a moving curve (red curve) and a reference curve (green curve). Points are shown with two different colors, the blue points are the manually selected points and black points generated using bisection arc-length parametrization. One of the main advantages of the bisection arc-length parametrization method is that selected points are included in the point sets which is not normally the case in the classical arc-length parametrization method; this leads to better registration accuracy.

### 6.2.2 Densification

After establishing dense point correspondences, a general class of rigid transformation may be applied to remove rotation and translation between the two images. The operator uses corresponding points to compute the rigid model parameters.

The deformable registration computes the displacement field,  $U : \mathbb{R}^2 \rightarrow \mathbb{R}^2$ , that minimizes an energy functional consisting of sum of square residuals of corresponding points  $(q_j, p_j)$  and a regularization term:

$$E[U] = \frac{\lambda}{2} \sum_{j=1}^N \|q_j + U(q_j) - p_j\|_2^2 + \frac{(1-\lambda)}{2} R[U] \quad (6.1)$$

where  $\Omega = [0, 1]^2$  is the image domain and  $0 \leq \lambda \leq 1$  is a smoothing parameter.  $R$  is a regularizer term. The most bewildering point in image registration is ill-posedness of the problem. Without loss of generality, a problem is well-posed in the sense of Hadamard if it has a solution which is unique and depends continuously on the data; otherwise it is known as ill-posed. From a mathematical point of view, the regularizer should make the registration problem well-posed, i.e., leads to a unique minimizer and preferably to a convex objective function [105]. In this chapter, we examine different approaches to address ill-posedness by adding a regularizer  $R$ . The idea is to measure quality of different regularizers in the TVUS-MR image registration problem and to choose the best candidate with respect to the measure of choice. Since the regularizer  $R$  is a differential operator and the choice of the differential operator is crucial for an

effective registration, we try different choices of the differential operator which leads to different displacement fields and also to different EL systems of coupled nonlinear PDEs. We provide solutions for three different cases:

1. Diffusion regularizer, defined as sum of the norm of the gradients of the deformation field in each dimension:

$$R[U] = \int_{\Omega} \|\nabla U\|_2^2 d\Omega \quad (6.2)$$

2. Divergence and curl regularizer, by which the deformation is considered as the result of two types of differential operators, namely the curl and divergence operators. The curl operator is responsible for the vorticity of the deformation field while the divergence operator is responsible for compressibility of the deformation field:

$$R[U] = \int_{\Omega} \underbrace{\|\nabla \cdot U\|_2^2}_{div.} d\Omega + \int_{\Omega} \underbrace{\|\nabla \times U\|_2^2}_{curl} d\Omega \quad (6.3)$$

3. Curvature regularizer, penalizes the curvature of the displacement field:

$$R[U] = \int_{\Omega} \|\Delta U\|_2^2 d\Omega \quad (6.4)$$

### 6.2.2.1 Diffusion Regularizer

The key here is to apply the diffusion regularizer which has already been employed in the area of optical flow [77] and image registration [78, 187] into our registration formulation (Equation (6.1)). The resulting scheme is called diffusion registration. To make Equation (6.1) more general and to permit its formulation as a EL equation we use an index function  $\delta_q$ , with  $\delta_q : \Omega \rightarrow \{0, 1\}$ ,  $\delta_q(X) = 1$  if  $X \in q$  and 0 otherwise. We rewrite the cost functional of Equation (6.1) as:

$$E[U] = \int_{\Omega} \left( \lambda \sum_{j=1}^N \delta_q(X) (q_j + U(X) - p_j)^2 + (1 - \lambda) \|\nabla U(X)\|_2^2 \right) dX \quad (6.5)$$

where  $\nabla$  is the gradient operator. In order to minimize Equation (6.5) we apply EL. Let's assume the energy functional in integral form to be:

$$E[U] = \int_{\Omega} L(X, U(X), U^{(1)}(X)) dX \quad (6.6)$$

where  $U^{(1)}(X) = \frac{\partial U}{\partial X}$ . The EL equation is:

$$\frac{\partial L}{\partial U}(X, U(X), U^{(1)}(X)) - \frac{d}{dX} \frac{\partial L}{\partial U^{(1)}}(X, U(X), U^{(1)}(X)) = 0 \quad (6.7)$$

Therefore, choosing the first-order derivative of the displacement field  $U = [u_1, u_2]$  as a regularizer leads to an EL system of two second order nonlinear elliptic PDEs:

$$\mu \sum_{j=1}^N \delta_q(X) (q_j + U(X) - p_j) - \left( \frac{\partial^2 U}{\partial x^2} + \frac{\partial^2 U}{\partial y^2} \right) = \begin{pmatrix} 0 \\ 0 \end{pmatrix} \quad (6.8)$$

where  $\mu = \frac{\lambda}{1-\lambda}$ . To solve the PDEs in Equation (6.8) numerically, a simple finite difference method is employed with the homogenous Neumann boundary condition. Discretization of Equation (6.8) with finite differences leads to a sparse linear system that can be solved by the Successive Over-Relaxation (SOR) method. SOR requires an initial estimate  $U = U^0$ , and follows the iteration:

$$u_{h,w,\ell}^{t+1} = \beta u_{h,w,\ell}^t - \frac{\omega}{(4+\mu\delta_q(X))} \left[ \mu \left( \sum_{j=1}^N \delta_q(X) (q_{j,\ell} - p_{j,\ell}) \right) - (u_{h,w-1,\ell}^{t-1} + u_{h+1,w,\ell}^{t-1}) - (u_{h,w+1,\ell}^t + u_{h-1,w,\ell}^t) \right] \quad (6.9)$$

where  $t \in \mathbb{N}$  is the iteration number,  $\beta = 1 - \omega$ ,  $\ell = \{1, 2\}$ ,  $h = 1, \dots, H$ ,  $w = 1, \dots, W$ ,  $H$  and  $W$  are the height and width of the moving image, respectively and  $\omega$  is the relaxation factor. Note that, iterations typically stop when some measure of the distance between  $u^{t+1}$  and  $u^t$  falls below a predefined tolerance. After computation of the new iteration variable  $u^{t+1}$ , we are able to obtain a new image  $M(x + u_1, y + u_2)$  via interpolation. Note that, one of the most interesting features of the diffusion registration method is its speed. This makes this scheme very useful for high resolution applications. Figure 6-3 shows the registration results for diffusion registration. The value of  $\lambda$  is 0.5. Figure 6-3 (d) depicts that the diffusion regularizer

cannot find the exact deformation between two images. This is due to the fact that, the diffusion method penalizes flow variations too much. Therefore, it is necessary to provide solution for Equation (6.1) with different types of regularizer.

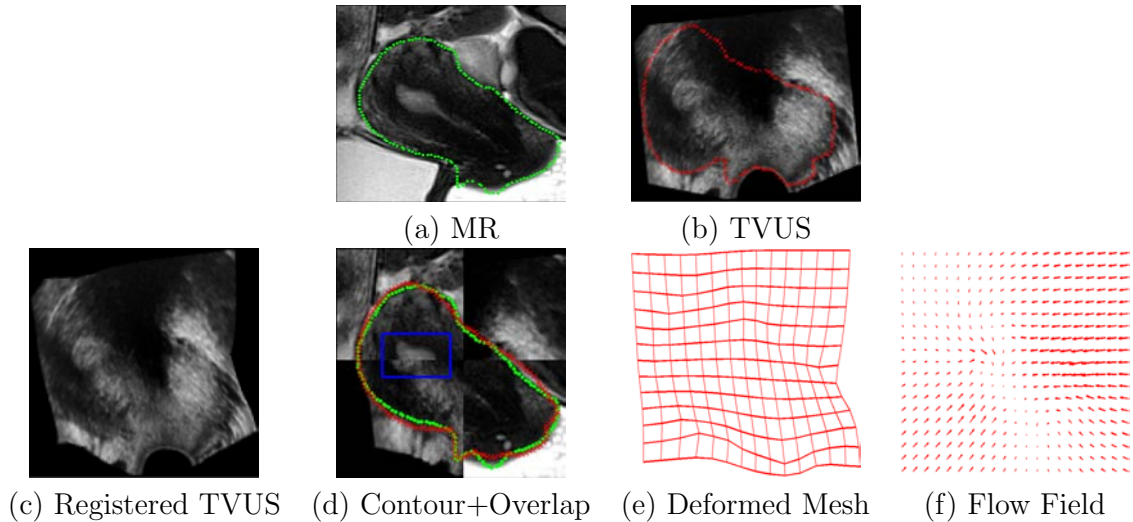


Figure 6-3: Registration results for diffusion regularizer. (a) and (b) depicts the MR and the TVUS image, respectively. (d) shows the overlap images where the top right and the bottom left belong to the deformed TVUS and also the top left and the bottom right belong to the MR data. (c), (e), and (f) illustrate the resulting deformation.

### 6.2.2.2 Divergence and Curl Regularizer

As described in chapter 3, there are various transformation models that can be used to disregard the irregularities resulting from the misalignment of the similarity metric during optimization procedure. Generally, these transformations play an important role in removing or compensating undesired irregularities in the deformation field to make it smooth. Another transformation model that is defined in this section is divergence and curl regularizer. To date, this regularizer has just been used in intensity-based image registration [188–190]. In this section, we show an application of this regularizer to feature-based TVUS-MR image registration.

This regularizer is based on Helmholtz’s decomposition theorem [189, 190]. The theorem states that a vector field with a suitable boundary condition is completely estimated if both its curl and divergence are defined everywhere. Note that in a

bounded region, boundary conditions must be used to uniquely estimate the smooth vector field. On the other hand, in an unbounded region, both the curl and divergence of the vector field are assumed to be vanished at infinity [190]. In other words, any smooth vector field  $U$  that vanishes at infinity can be decomposed into an irrotational (curl-free) and a solenoidal (divergence-free) vector,

$$U = U_{div} + U_{curl} \quad (6.10)$$

By taking the curl  $U_{curl}$  and divergence  $U_{div}$  of Equation (6.10), respectively, we obtain:

$$\begin{cases} \nabla \cdot U = \nabla \cdot U_{div} \\ \nabla \times U = \nabla \times U_{curl} \end{cases} \quad (6.11)$$

Equation (6.11) indicates that the solenoidal component is related to the curl of the function and the irrotational component is related to the divergence of the function. The curl (vorticity) accounts for the presence of a rotating motion, while the divergence is related to the presence of sinks or sources in the deformation field. Therefore, once both the curl and divergence of a vector are specified, the function fully determined [191].

Now, we apply the divergence and curl regularizer into our registration formulation (Equation (6.1)). The resulting scheme is known as div-curl registration. As mentioned previously, to make Equation (6.1) more general and to allow its formulation as a EL equation we use an index function  $\delta_q$ , with  $\delta_q : \Omega \rightarrow \{0, 1\}$ ,  $\delta_q(X) = 1$  if  $X \in q$  and 0 otherwise. We rewrite the cost functional of Equation (6.1) as:

$$E[U] = \int_{\Omega} \left( \lambda \sum_{j=1}^N \delta_q(X) (q_j + U(X) - p_j)^2 + (1 - \lambda) [\varsigma \|\nabla \cdot U(X)\|_2^2 + (1 - \varsigma) \|\nabla \times U(X)\|_2^2] \right) dX \quad (6.12)$$

where  $\lambda$  is a positive scalar and balances the amount of smoothing and  $\varsigma$  is a trade-off between the vortex particles (curl) and source and sink particles (divergence). Therefore, choosing divergence and curl of the displacement field  $U = [u_1, u_2]$  as a

regularizer leads to the EL system of two second order nonlinear elliptic PDEs:

$$\begin{aligned} \mu \sum_{j=1}^N \delta_q(X) (q_{j,1} + u_1(X) - p_{j,1}) - \left( \varsigma \frac{\partial^2 u_1}{\partial x^2} + (1 - \varsigma) \frac{\partial^2 u_1}{\partial y^2} + (2\varsigma - 1) \frac{\partial^2 u_2}{\partial x \partial y} \right) &= 0 \\ \mu \sum_{j=1}^N \delta_q(X) (q_{j,2} + u_2(X) - p_{j,2}) - \left( \varsigma \frac{\partial^2 u_2}{\partial y^2} + (1 - \varsigma) \frac{\partial^2 u_2}{\partial x^2} + (2\varsigma - 1) \frac{\partial^2 u_1}{\partial x \partial y} \right) &= 0 \end{aligned} \quad (6.13)$$

where  $\mu = \frac{\lambda}{1-\lambda}$ . It is clear from Equation (6.13) that when  $\varsigma$  is 0.5 the div-curl registration behaves exactly similar to the diffusion registration. To solve the PDE in Equation (6.13) numerically, a simple finite difference method is employed with the homogenous Neumann boundary condition. Discretization of Equation (6.13) with finite differences leads to a sparse linear system that can be solved by the SOR method with an initial estimate  $U = U^0$ .

$$\begin{aligned} u_{h,w,1}^{t+1} &= \beta u_{h,w,1}^t - \frac{\omega}{(2 + \mu \delta_q(X))} \left[ \mu \left( \sum_{j=1}^N \delta_q(X) (q_{j,1} - p_{j,1}) \right) - (1 - \varsigma) (u_{h+1,w+1,2}^t \right. \\ &\quad - u_{h,w+1,2}^t - u_{h+1,w,2}^t + 2u_{h,w,2}^t - u_{h,w-1,2}^t - u_{h-1,w,2}^t + u_{h-1,w-1,2}^t) \\ &\quad \left. - (\varsigma u_{h,w-1,1}^{t-1} + (1 - \varsigma) u_{h+1,w,1}^{t-1}) - (\varsigma u_{h,w+1,1}^t + (1 - \varsigma) u_{h-1,w,1}^t) \right] \\ \\ u_{h,w,2}^{t+1} &= \beta u_{h,w,2}^t - \frac{\omega}{(2 + \mu \delta_q(X))} \left[ \mu \left( \sum_{j=1}^N \delta_q(X) (q_{j,2} - p_{j,2}) \right) - (1 - \varsigma) (u_{h+1,w+1,1}^t \right. \\ &\quad - u_{h,w+1,1}^t - u_{h+1,w,1}^t + 2u_{h,w,1}^t - u_{h,w-1,1}^t - u_{h-1,w,1}^t + u_{h-1,w-1,1}^t) \\ &\quad \left. - (\varsigma u_{h,w-1,2}^{t-1} + (1 - \varsigma) u_{h+1,w,2}^{t-1}) - (\varsigma u_{h,w+1,2}^t + (1 - \varsigma) u_{h-1,w,2}^t) \right] \end{aligned} \quad (6.14)$$

where  $t \in \mathbb{N}$  is the iteration number,  $\beta = 1 - \omega$ ,  $h = 1, \dots, H$ ,  $w = 1, \dots, W$ ,  $H$  and  $W$  are the height and width of the moving image, respectively and  $\omega$  is the relaxation factor. Note that, iterations typically stop when some measure of the distance between  $u^{t+1}$  and  $u^t$  falls below a predefined tolerance. Figure 6-4 shows the registration results for div-curl registration with different  $\varsigma$ , i.e., in the second row  $\varsigma$  is set to 0.5, in the third row  $\varsigma$  is set to 0.3, and in the fourth row  $\varsigma$  is set

to 0.7. The value of  $\lambda$  is 0.5. In the second row the div-curl registration behaves similar to the diffusion registration. Comparing the third and fourth rows show that when the deformation field is estimated by assigning more weight to the divergence operator, the registration has more accurate local registration accuracy. The blue rectangles in Figure 6-4 (d) show how the structure is deformed with different  $\varsigma$ . The disadvantage of this method is that the mesh folding or irregularities in the estimated deformation field is not guaranteed and the implementation of 3D/2D registration using this method is not trivial at all.

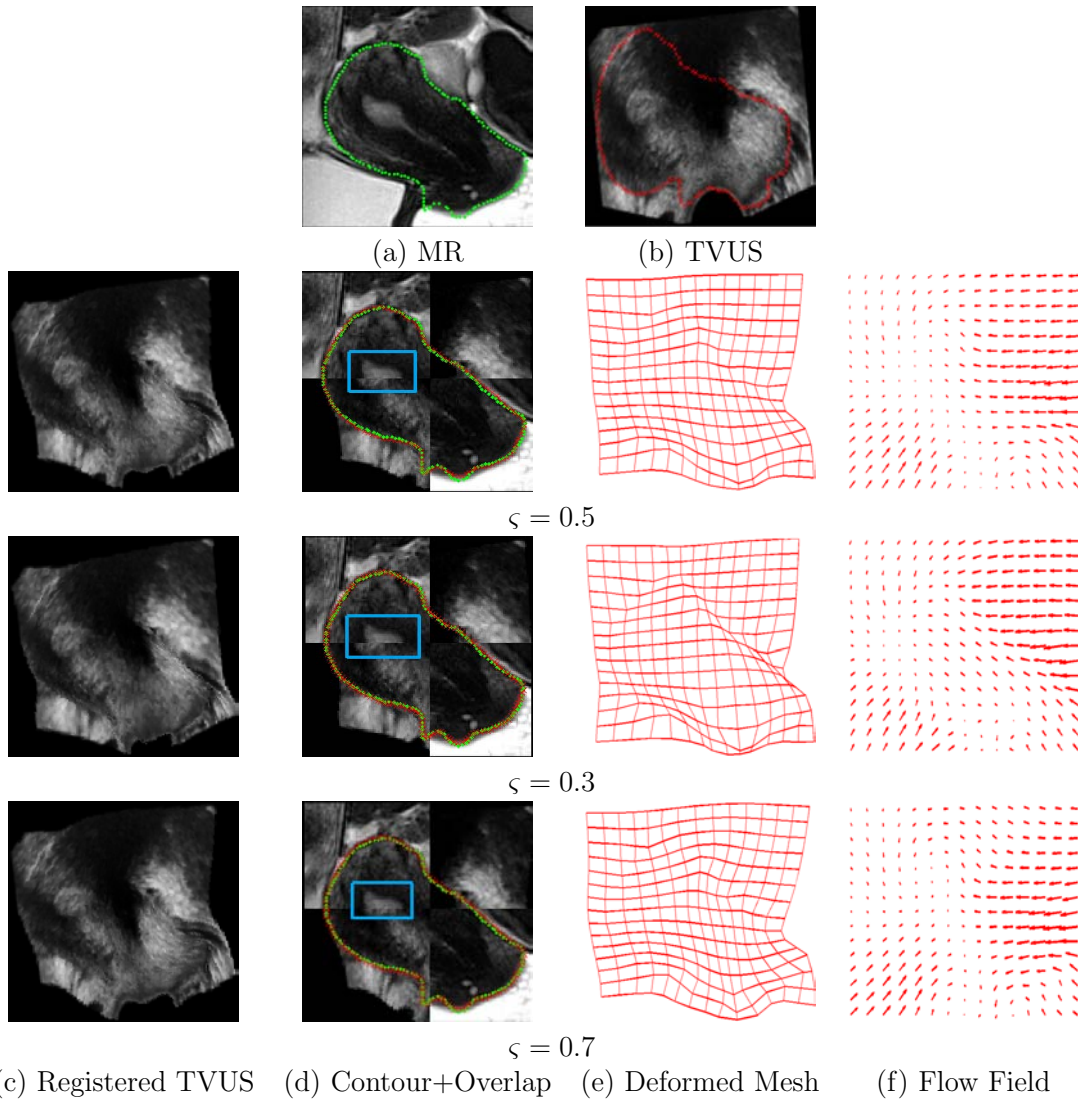


Figure 6-4: Registration results for div-curl registration with different  $\zeta$ . (a) and (b) depicts the MR and the TVUS image, respectively. (d) shows the overlap images where the top right and the bottom left belong to the deformed TVUS and also the top left and the bottom right belong to the MR data. (c), (e), and (f) illustrate the resulting deformation. When  $\zeta = 0.5$  the registration behaves similar to the diffusion registration. When  $\zeta = 0.3$  the divergence operator has less influence on the estimating deformation field than curl operator. When  $\zeta = 0.7$  the curl operator has less influence on the estimating deformation field than divergence operator.

### 6.2.2.3 Curvature Regularizer

One of the main problems with the div-curl and diffusion registration is that they are sensitive to initial positioning of the images to be aligned, since the deformation field is always estimated iteratively. To estimate a good initial position, generally a rigid or a linear affine preregistration step must be performed. If the initial rigid registration is not near the solution, the deformable registration procedure may converge poorly. To solve this issue, Fischer and Modersitzki [78, 79, 192, 193] propose a non-parametric fully intensity-based registration technique which relies on a curvature-based penalizing term. They prove that this approach not only estimate smooth deformation fields but also permits for an automatic rigid registration. Thus, in contrast to the diffusion and div-curl registration techniques, the pre-registration step becomes redundant.

Now, let's apply the curvature regularizer (Equation (6.4)) into our registration formulation (Equation (6.1)). The resulting scheme is known as curvature registration. Similar to our two previous methods, to make Equation (6.1) more general and to permit its formulation as a EL equation we use an index function  $\delta_q$ , with  $\delta_q : \Omega \rightarrow \{0, 1\}$ ,  $\delta_q(X) = 1$  if  $X \in q$  and 0 otherwise. We rewrite the cost functional of Equation (6.1) as:

$$E[U] = \int_{\Omega} \left( \lambda \sum_{j=1}^N \delta_q(X) (q_j + U(X) - p_j)^2 + (1 - \lambda) \|\Delta U(X)\|_2^2 \right) dX \quad (6.15)$$

where  $\Delta$  is the Laplacian operator. Choosing second order derivative of the displacement field as a regularizer leads to the EL system of two fourth order nonlinear elliptic PDEs:

$$\mu \sum_{j=1}^N \delta_q(X) (q_j + U(X) - p_j) + \left( \frac{\partial^4 U}{\partial x^4} + \frac{\partial^4 U}{\partial y^4} \right) = \begin{pmatrix} 0 \\ 0 \end{pmatrix} \quad (6.16)$$

To solve the PDEs a finite difference scheme was used while the free boundary conditions ( $\Delta U = 0$ ) are considered. Discretization of Equation (6.16) with finite differences leads to a sparse linear system that can be solved by the SOR method. SOR

requires an initial estimate  $U = U^0$ , and follows the iteration:

$$\begin{aligned}
u_{h,w,\ell}^{t+1} = & \beta u_{h,w,\ell}^t - \frac{\omega}{\left(12 + \mu \sum_{j=1}^N \delta_q(X)\right)} \left[ \mu \left( \sum_{j=1}^N \delta_q(X) (q_{j,\ell} - p_{j,\ell}) \right) \right. \\
& + \left( u_{h,w-2,\ell}^{t-1} - 4u_{h,w-1,\ell}^{t-1} - 4u_{h+1,w,\ell}^{t-1} + u_{h+2,w,\ell}^{t-1} \right) \\
& \left. + \left( u_{h,w+2,\ell}^t - 4u_{h,w+1,\ell}^t - 4u_{h-1,w,\ell}^t + u_{h-2,w,\ell}^t \right) \right]
\end{aligned} \tag{6.17}$$

where  $t \in \mathbb{N}$  is the iteration number,  $\ell = \{1, 2\}$ ,  $\beta = 1 - \omega$ ,  $h = 1, \dots, H$ ,  $w = 1, \dots, W$ ,  $H$  and  $W$  are height and width of moving image, respectively and  $\omega$  is relaxation factor. Figure 6-5 shows that the overall accuracies of the registration along the boundary of organs are good and also the method provides smooth deformation. However, the curvature regularization provides smoother and more precise results than the diffusion and div-curl registration schemes.

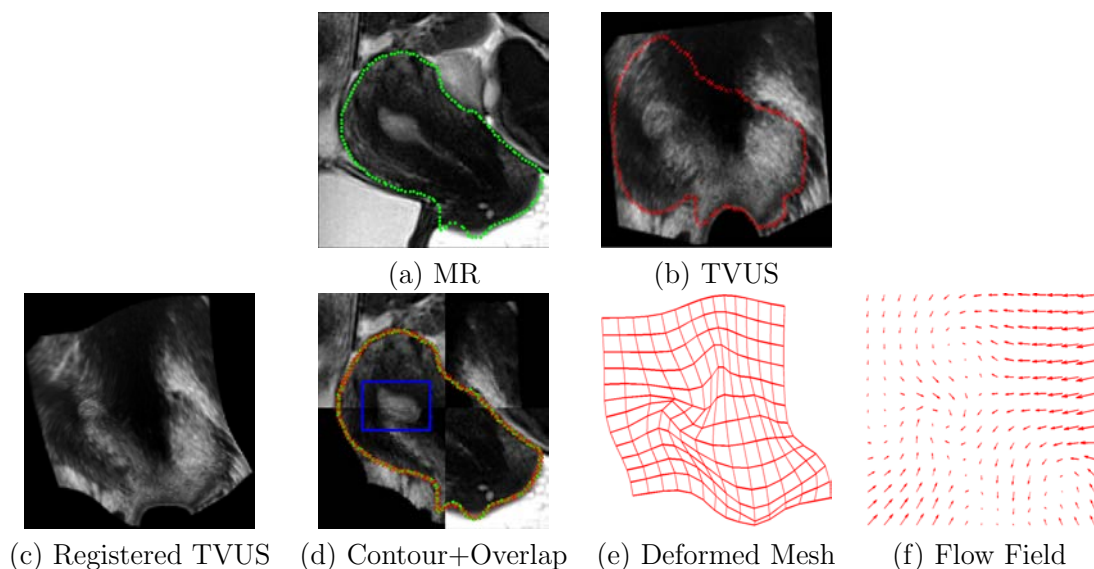


Figure 6-5: Registration results for curvature regularizer. (a) and (b) depicts the MR and the TVUS image, respectively. (d) shows the overlap images where the top right and the bottom left belong to the deformed TVUS and also the top left and the bottom right belong to the MR data. (c), (e), and (f) illustrate the resulting deformation.

## 6.3 Experimental Results

### 6.3.1 Material

The experiments are conducted on ten patients who have small endometrial implants in the pelvic area. For each patient, TVUS and MR imaging are used to examine their pelvic organs. Images used for the experiments have an average image size of  $300 \times 300$ . The reference MR slice from MR volume that corresponds to the moving TVUS image is manually chosen by an expert. Therefore, we assume that the TVUS slice is parallel to the corresponding MR slice. The soft tissue organs such as bladder, uterus, ovary, and rectum in both TVUS and MR slices are manually segmented by an expert and then manually selects 5 to 10 points at each pair of curves. Finally, arc-length parametrization has been used between each adjacent points to establish dense correspondences. We compare the diffusion, div-curl, and curvature registration schemes with TPS which has been proposed by Mitra et al. [186].

### 6.3.2 Results and Discussion

In this section, the proposed methods are discussed and compared with a method from state-of-the-art. For all the experiments, we assumed that the reference MR slice from MR volume that corresponds to the moving TVUS image is manually chosen by an expert and they are rigidly pre-registered for diffusion and div-curl registration schemes. Curvature and TPS registration schemes do not necessarily require an additional rigid pre-registration step as they are invariant to such a transformation. Note that  $\mu$  and  $\omega$  are 0.5 and 1.9, respectively for all the experiments. In the div-curl registration,  $\varsigma$  is 0.7 which means that the divergence operator has more influence on estimating deformation field. The aim of these experiments is to provide a comparison of the four different registration techniques such as diffusion, div-curl, curvature, and TPS [186] and discover which regularizer and registration technique work best in our problem.

We illustrate the registration results on various real-world data. Registration accuracy is evaluated in terms of Dice Similarity Coefficient (DSC), Hausdorff Distance

(HD), Target Registration Error (TRE), and Correlation Coefficient (CC). Meanwhile, two experts (a pelvic radiologist and a gynecologic surgeon) evaluated the quality of the results. In this manner, we setup a registration quality score called 1-to-5 rating scale where 5 is excellent, 4 is good, 3 is fair, 2 is poor, and 1 is bad.

**Reminder.** The DSC assesses the global overlap of the segmented organs. A high DSC value indicates a good overlap between the tissue regions after registration. However, a high DSC does not always mean a good contour overlap. Therefore, HD is used to evaluate the contour accuracy. A low HD value shows good contour overlap. TRE is described as the mean square distance between corresponding points not used in estimating the deformation. A low TRE value shows good local registration accuracy. In our experiments, we select anatomical landmarks in the patient’s body such as boundary of organs and their internal anatomical structures as target points to estimate the local registration accuracy to validate our result. The target points are 10 points which are not used for registration. A CC shows how precise the relationship is between two segmented regions. The value of a CC also ranges from 0, indicating no correlation between two overlap segmented regions, to 1, indicating very highly correlation.

Our method is compared with the method proposed by Mitra et al. [186]. The registration accuracy that measures contour overlap are given in Table 6.2. It is clear that the curvature registration method outperforms the other methods in terms of contour overlap accuracy (DSC and HD). TRE and CC are given in Table 6.3. The TRE values in Table 6.3 indicates that the curvature registration method provides high local registration accuracy. In this table, the CC values shows that the relationship between two segmented regions normally is too low. However, the curvature registration method provides the highest CC value. This is due to the fact that in the curvature registration method, the boundary of segmented region which has dark intensities in both TVUS and MR images is aligned more precisely than other compared methods which leads to the higher CC value. Experts’ evaluation are given in Table 6.4. In all the experiments, the highest value of the DSC, HD, TRE, CC, and

experts' evaluation is for the curvature registration method.

	DSC				HD			
Patient	TPS	Curvature	Div-Curl	Diffusion	TPS	Curvature	Div-Curl	Diffusion
1	0.9955	<b>0.9960</b>	0.9801	0.9743	1.1214	<b>0.6712</b>	3.5942	4.3481
2	0.9708	<b>0.9803</b>	0.9466	0.9276	1.9568	<b>1.1499</b>	2.0544	2.9765
3	0.9904	<b>0.9941</b>	0.9797	0.9422	1.1402	<b>0.7853</b>	1.7014	2.6230
4	0.9781	<b>0.9883</b>	0.9854	0.9597	1.7532	<b>1.0931</b>	5.0176	7.3328
5	0.9925	<b>0.9927</b>	0.9602	0.9548	1.3466	<b>0.8287</b>	2.0016	5.1084
6	0.9902	<b>0.9952</b>	0.9876	0.9882	1.2291	<b>0.3013</b>	1.6174	1.5720
7	0.9889	<b>0.9891</b>	0.9373	0.9301	1.4953	<b>1.1806</b>	8.8649	9.7328
8	0.9948	<b>0.9973</b>	0.9922	0.9915	0.4344	<b>0.0463</b>	0.6659	0.5814
9	0.9916	<b>0.9917</b>	0.9888	0.9831	0.9976	<b>0.5457</b>	1.5029	1.9066
10	0.9910	<b>0.9964</b>	0.9733	0.9718	1.3507	<b>0.1069</b>	2.6997	2.1305
mean	0.9884	<b>0.9921</b>	0.9731	0.9623	1.2825	<b>0.6709</b>	2.9720	3.8312
std. dev.	0.0078	<b>0.0051</b>	0.0189	0.0233	0.4190	<b>0.4171</b>	2.4056	2.8566

Table 6.2: Comparison between TPS [186], curvature, div-curl, and diffusion registration methods. A high DSC value means a good contour region overlap, while a low HD value signifies a good boundary overlap. Bold values indicate the best results.

	TRE				CC			
Patient	TPS	Curvature	Div-Curl	Diffusion	TPS	Curvature	Div-Curl	Diffusion
1	0.6513	<b>0.2849</b>	1.1989	2.7626	0.7473	<b>0.7526</b>	0.7285	0.7184
2	0.5592	<b>0.4486</b>	0.8826	1.3070	0.5564	<b>0.6263</b>	0.5039	0.5426
3	0.3763	<b>0.2478</b>	0.5140	1.4427	0.7843	<b>0.7947</b>	0.7659	0.7323
4	0.5084	<b>0.4356</b>	2.0522	4.3997	0.8563	<b>0.8842</b>	0.8812	0.8708
5	0.5521	<b>0.3315</b>	0.8517	3.1672	0.5741	<b>0.6024</b>	0.4834	0.5312
6	0.4671	<b>0.1265</b>	0.8087	0.8288	0.3395	<b>0.3881</b>	0.3807	0.3067
7	0.6280	<b>0.4545</b>	3.5034	4.9861	0.8080	<b>0.8105</b>	0.7955	0.8027
8	0.2042	<b>0.0913</b>	0.4998	0.6423	0.5112	<b>0.5570</b>	0.4903	0.4891
9	0.4988	<b>0.2238</b>	1.2034	1.2983	0.6969	<b>0.7349</b>	0.6515	0.6738
10	0.7429	<b>0.0866</b>	1.0259	1.1952	0.4096	<b>0.4831</b>	0.4195	0.3862
mean	0.5188	<b>0.2731</b>	1.1541	2.2030	0.6284	<b>0.6634</b>	0.6100	0.6054
std. dev.	0.1509	<b>0.1438</b>	0.9649	1.5403	0.1766	<b>0.1583</b>	0.1759	0.1835

Table 6.3: Comparison between TPS [186], curvature, div-curl, and diffusion registration methods. A low TRE value means good local registration accuracies around target landmarks while a high CC value means a good correlation inside segmented regions after registration. Bold values indicate the best results.

Figures 6-6 and 6-7 depict the registration results for patients 1 and 2. The registration results for the TPS registration method [186], curvature, div-curl, and diffusion registration schemes are illustrated in rows. In both figures, the first row illustrates the reference image (MR) and moving image (TVUS). As shown, endometrial implants are seen in TVUS images and there is no evidence of their existence

	Radiologist				Surgeon			
Patient	TPS	Curvature	Div-Curl	Diffusion	TPS	Curvature	Div-Curl	Diffusion
1	3	<b>5</b>	3	3	4	<b>5</b>	3	3
2	<b>4</b>	<b>4</b>	<b>4</b>	3	<b>4</b>	<b>4</b>	3	3
3	4	<b>5</b>	2	3	3	<b>5</b>	2	2
4	2	<b>5</b>	4	4	<b>5</b>	<b>5</b>	4	2
5	4	<b>5</b>	2	3	3	<b>5</b>	3	2
6	3	<b>4</b>	3	3	4	<b>5</b>	4	3
7	<b>5</b>	<b>5</b>	4	4	<b>5</b>	<b>5</b>	3	3
8	<b>4</b>	<b>4</b>	2	3	3	<b>4</b>	3	2
9	3	<b>4</b>	3	3	3	<b>4</b>	3	3
10	4	<b>5</b>	3	2	<b>5</b>	<b>5</b>	4	2
mean	3.6	<b>4.6</b>	3	3.1	3.9	<b>4.7</b>	3.2	2.5
std. dev.	0.84	<b>0.52</b>	0.82	0.57	0.87	<b>0.48</b>	0.63	0.53

Table 6.4: Experts’ evaluation of the TPS [186], curvature, div-curl, and diffusion registration methods.

in MR images. In Figure 6-6 the endometrial implant is located above the uterus, so that, we chose point correspondences around the uterus to align 2D TVUS image with the MR image. For localizing the endometriosis we applied the displacement field to the yellow curve in the TVUS image and we find the location of endometriosis in MR frame. In Figure 6-7 the endometrial implant is located above the bladder and it is very close to the ovary, so that, we chose point correspondences around both the bladder and ovary to align 2D TVUS image with the MR image. Based on these results, we can conclude that the diffusion and div-curl registration methods do not provide an accurate and smooth displacement field to localize the endometriosis. In addition, these figures show that the diffusion and div-curl registration methods cannot precisely find the deformation between images. The TPS and curvature registration methods can find more precise displacement fields. However, the displacement field for the TPS is not as accurate as the curvature method. For instance, as illustrated in Figure 6-6 (f), we can see that the localization based on the TPS [186] has problem at the top of the boundary. The DSC, HD, TRE, CC, and experts’ evaluation results in Tables 6.2, 6.3, and 6.4 and the experimental results in Figure 6-6 and 6-7 show that the curvature registration method provides more accurate displacement field and more precisely preserve information inside the registered images.

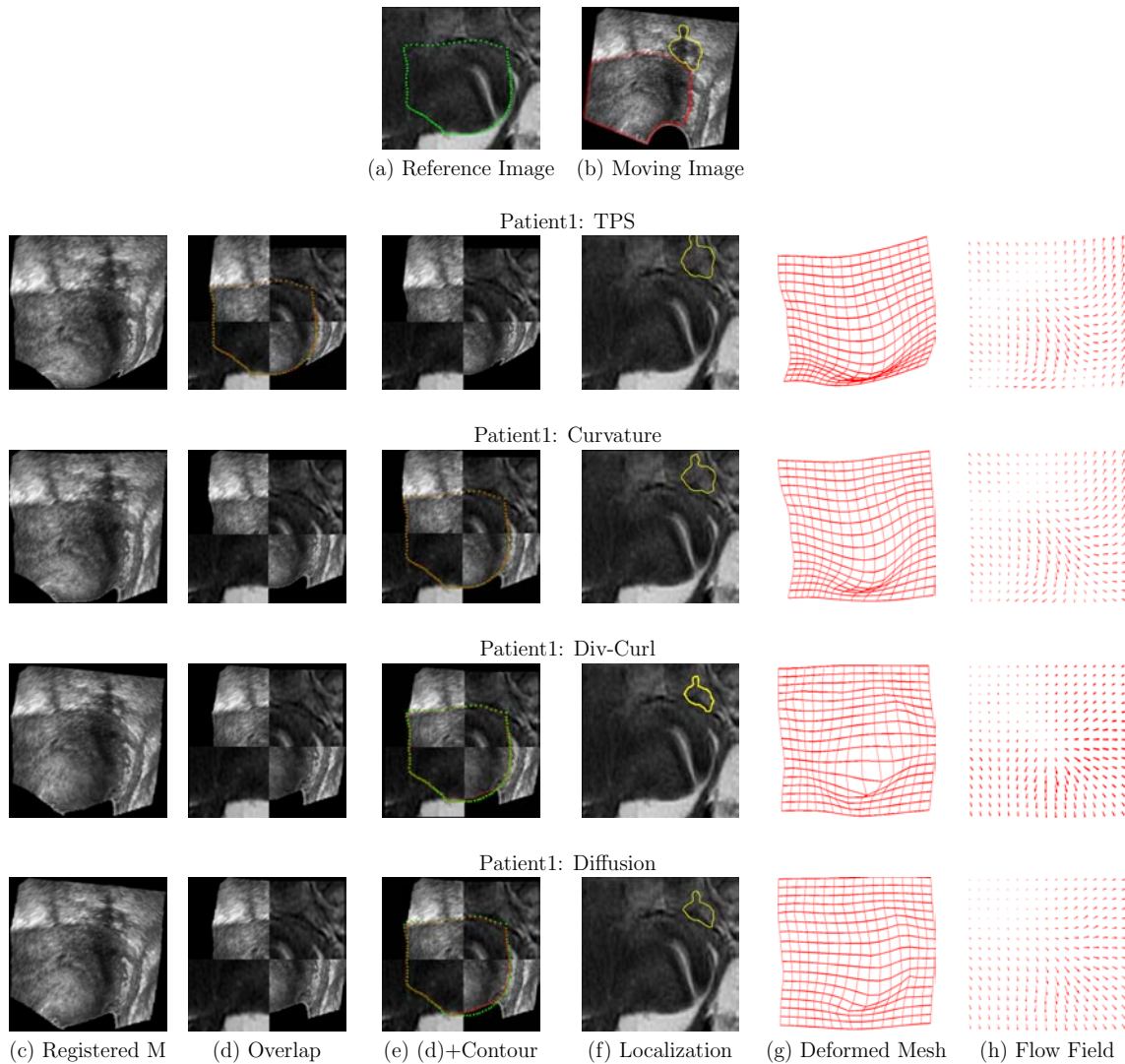


Figure 6-6: Registration results for TPS [186], curvature, div-curl, and diffusion methods in rows. (a) and (b) show MR and TVUS image. Small endometrial implant which is just visible in TVUS image is depicted by yellow curve. (c) shows warped TVUS image. (d) and (e) demonstrate overlay images where the top right and the bottom left belong to the MR data and also the top left and the bottom right belong to the deformed TVUS data. (f) shows the location of the endometrial implant in the MR frame. (g) and (h) depict the deformed mesh and displacement field, respectively.

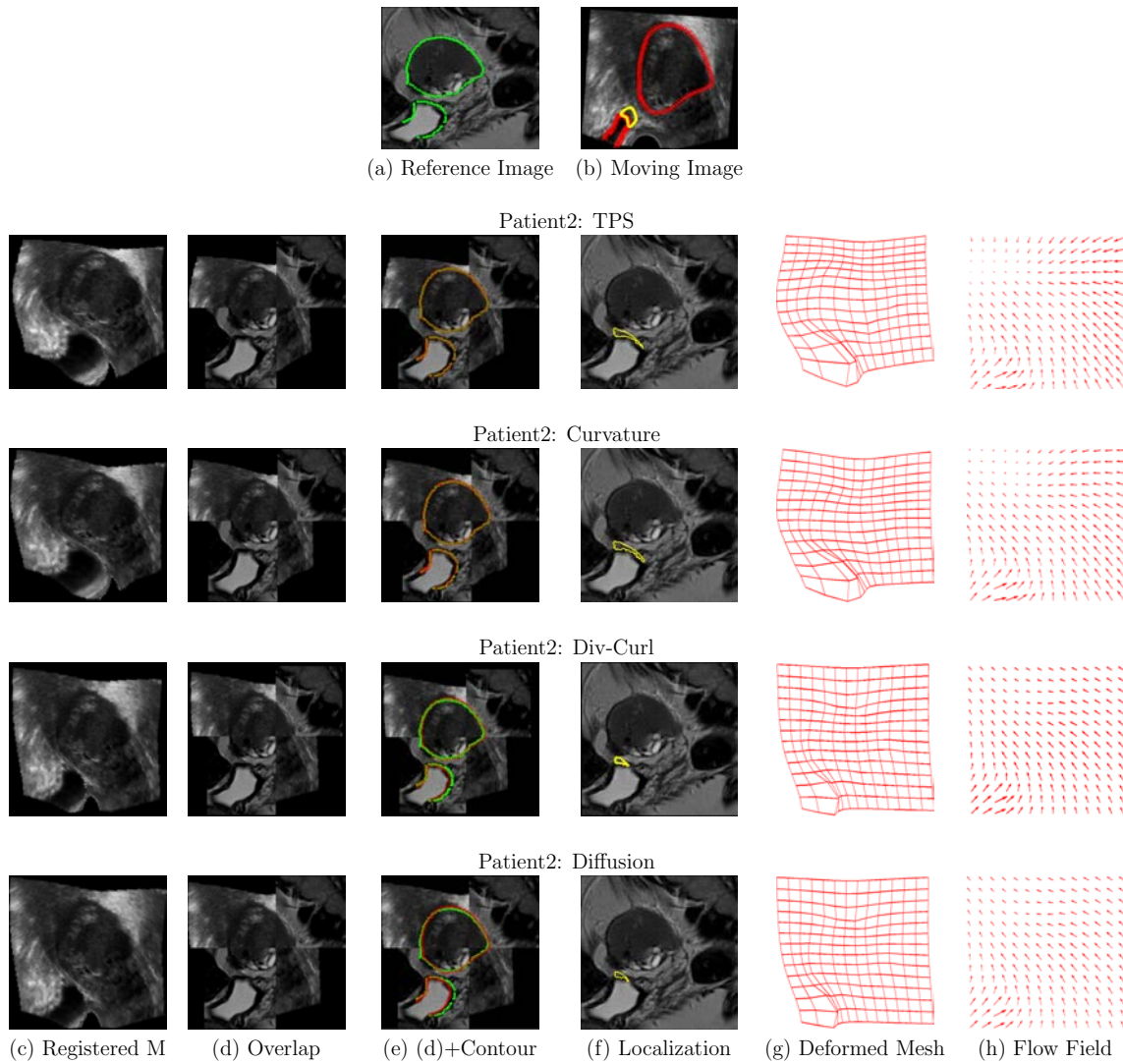


Figure 6-7: Registration results for TPS [186], curvature, div-curl, and diffusion methods in rows. (a) and (b) show MR and TVUS image. Small endometrial implant which is just visible in TVUS image is depicted by yellow curve. (c) shows warped TVUS image. (d) and (e) demonstrate overlay images where the top right and the bottom left belong to the MR data and also the top left and the bottom right belong to the deformed TVUS data. (f) shows the location of the endometrial implant in the MR frame. (g) and (h) depict the deformed mesh and displacement field, respectively.

## 6.4 Conclusion

In this chapter, we have combined bisection arc-length parametrization with variational point-based registration to semi-automatically register and fuse MR with TVUS images to localise endometrial implants. The main purposes of this chapter are to provide a comparison between the variational registration approaches and spline-based registration as well as to investigate which regularizer and registration technique work best in TVUS-MR registration. This is a very important task as there is currently no system available to register TVUS to MR images.

The advantages of using our variational formulation are twofold. First, it allows us to employ different types of regularizer (a differential operator) such as diffusion, div-curl, curvature, or even higher order derivatives of the displacement field. Last but not least, this formulation assumes that the deformation model belongs to some infinite dimension space of functions and this space is motivated by regularizer properties. In other words, our variational formulation does not require us to specify a parametric form as in the spline-based registration method and thus has more flexibility.

The main goal of using variational approach is to model deformation using internal forces. We use three various transformation models such as diffusion, div-curl, and curvature to find out which of these would be the best to remove or compensate undesire irregularities in deformation field to make it smooth while providing precise registration accuracy. The diffusion regularizer is the sum of the norm of the gradients of the deformation field in each dimension. The main advantage of the diffusion registration method is that it is swift. This makes this method applicable for high resolution applications. The major disadvantage of diffusion regularizer is that it penalizes flow variations too much, so that to alleviate this limitation we use another regularizer. Another transformation model that has been used is divergence and curl operator. The curl operator is responsible for the vorticity of the deformation field while the divergence operator is responsible for compressibility of the deformation field. The main advantages of using this regularizer are that a deformation field with

a suitable boundary condition is completely estimated and it is as fast as diffusion method. However, selecting  $\varsigma$  (the trade-off between the curl and divergence) is not an easy task, so that, it can easily lead to the mesh folding or irregularities in the estimating deformation field. In addition, implementing of 3D/2D registration using this scheme is very complex. Since the diffusion and div-curl registration methods are sensitive to global affine transformation, another regularization term that penalizes the curvature of the displacement field has been also proposed. In contrast with diffusion and div-curl registration methods, the pre-registration step becomes redundant.

Based on the advantages and drawbacks of variational and spline-based registration approaches and our experimental results, we find that the curvature registration method is an appropriate choice as it can provide high registration accuracy. In the next chapter, an automatic feature-based registration method will be proposed to even much more decrease user interaction by establishing point correspondences automatically while still relying on the user to segment corresponding organs in both TVUS and MR images.

# Chapter 7

## One-Step ICP-Based 2D/2D Registration

### Contents

---

<b>7.1</b>	<b>Introduction</b>	<b>110</b>
<b>7.2</b>	<b>2D Euclidean Distance Transform</b>	<b>112</b>
<b>7.3</b>	<b>Iterative Closest Point Algorithms (ICP)</b>	<b>115</b>
7.3.1	Variational Two-Step ICP	116
7.3.2	Variational One-Step ICP	118
<b>7.4</b>	<b>Experimental Results</b>	<b>122</b>
7.4.1	Material	122
7.4.2	Results and Discussion	122
<b>7.5</b>	<b>Conclusion</b>	<b>131</b>

---

### 7.1 Introduction

We have seen already that it is important to establish appropriate dense correspondences between the TVUS and MR images in order to register them to localise endometrial implants and provide information about depth of infiltration. Without loss of generality, an intuitive definition of appropriate correspondences is that corresponding points must be in physical vicinity when the curves are manually warped [194]. In this context, previously we had discussed three semi-automatic variational point-based registration methods. In the previous chapter on building correspondences, it was assumed that an expert segmented the organs in both the TVUS and MR images and selected a few corresponding points. More point correspondences were then created using arc-length parametrization between each adjacent points. However, the

main disadvantage of this method lies in manual point correspondence selection. It is often very hard to select points exactly and is a time consuming process. Thus, to reduce the potential expert error and interaction time, we develop in this chapter an automatic 2D/2D deformable registration method to establish point correspondences and estimate deformation between curve correspondences.

Contour-based registration (also known as shape registration) is the basis for many computer vision techniques [195] and medical image analysis [196]. Therefore, many methods regarding contour-based registration can be found in the literature, e.g., [140, 195, 197–201]; see [202] for a general survey. Most of these methods are based on explicit contour representations given by point sets which can be connected by lines or a higher order curve (i.e. spline curves) to form a shape. One of the most used registration algorithms is the ICP algorithm [135], at which we will take a closer look in Section 7.3.1. As the name suggests, it is an iterative procedure that assigns an initial correspondence between the point sets, refines the alignment by means of minimising the distance between pairs of points, then recomputes the correspondences and repeats the alignment step until convergence. In other words, classical ICP has two main steps that are iterated until convergence: (1) closest point computation and (2) transformation estimation. The advantages of ICP algorithms are obvious: they provide good results, if the sought transformation is not too large and are easy to implement. In order to improve the robustness and the computational efficiency of classical two-step ICP, a distance transform was introduced by Fitzgibbon et al. [138]. It is a slightly different distance-based correspondence approach, since it uses a distance map as a basis for establishing correspondences. Without loss of generality, let us briefly discuss about generating a distance transform. Consider the contour and the space in which the contour lies. For each point in space, we can assign a number, which is just the distance to the nearest point on the contour. This then defines a scalar field over the space, which is the distance map. If we regularly sample this distance map over some region, it reduces to a distance map image which includes the original contour. In Fitzgibbon et al.'s [138] method, the distance transform allows them to merge the two inner steps of classical ICP [135]

into only one. Fitzgibbon et al.’s one-step ICP computes rigid 2D/2D and 3D/3D registration of a single pair of curves and surfaces, respectively. The registration error is minimized using the Levenberg-Marquardt algorithm.

In this chapter, we have extended Fitzgibbon et al.’s one-step rigid ICP by using a variational procedure to obtain nonlinear deformations. Our registration method has two main steps: first, the MR and TVUS data are manually segmented by an expert. Second, our deformable ICP method is used to compute a dense deformation field while establishing point correspondences automatically. In this work, we use a variational framework leading to a well-defined one-step formulation of ICP handling multiple curve correspondences. Experimental results show the potential and efficacy of our method. The proposed method compares favorably with classical two-step ICP and Thin-Plate Spline Robust Point Matching (TPS-RPM) [150] on several data sets. The results obtained from semi-synthetic and real-world data show that the performance of the proposed method is better than the two other methods.

## 7.2 2D Euclidean Distance Transform

The Distance Transform (DT) maps each image pixel into its smallest distance to regions of interest [203]. It is a fundamental geometrical operator with great applicability in computer vision and graphics, shape analysis, pattern recognition, image registration, optical flow, and computational geometry [195, 196, 204, 205]. The idea of a DT is quite simple, but it is nevertheless important to explain some concepts and conventions for a correct understanding of this work, especially Section 7.3.2.

The key problem in DT is to calculate the distance from each point of the domain to the closest point of the source data set. In image processing terminology, this is can be defined in the following manner. Let  $I : \Omega \subset \mathbb{Z}^2 \rightarrow \{0, 1\}$  be a binary image where the domain  $\Omega$  is convex and, in particular,  $\Omega = \{1, \dots, h_{max}\} \times \{1, \dots, w_{max}\}$ , where  $h_{max}$  and  $w_{max}$  are the height and width of the image, respectively. By convention, 1 is white and 0 is black. Hence we have an object  $\mathcal{O}$  demonstrated by all the white pixels:

$$\mathcal{O} = \{p \in \Omega \mid I(p) = 1\} \tag{7.1}$$

0	0	0	0	0
0	0	0	0	0
0	0	1	0	0
0	0	1	0	0
0	0	0	0	0
0	0	0	0	0

(a) Binary Image

2.828	2.236	2	2.236	2.828
2.236	1.414	1	1.414	2.236
2	1	0	1	2
2	1	0	1	2
2.236	1.414	1	1.414	2.236
2.828	2.236	2	2.236	2.828

(b) Euclidian Distance Image

Figure 7-1: Numerical example of distance transform. (a) shows a binary image. (b) shows the Euclidean distance of each black pixel to the nearest white pixel.

The set  $\mathcal{O}$ , which is the white pixel ( $p$ ) in  $\Omega$ , is called object whereas the elements of its complement,  $\mathcal{O}^{-1}$ , which is the set of black pixel ( $p'$ ) in  $\Omega$ , is called background. In fact, mathematically speaking, the DT is the transformation that generates a map  $D$  whose value in each pixel  $p'$  is the smallest distance from this pixel to  $\mathcal{O}$ :

$$D(p') := \min \{d(p', p) \mid p' \in \mathcal{O}^{-1}\} = \min \{d(p', p) \mid I(p') = 0\} \quad (7.2)$$

The image  $D$  is called the distance map of  $\mathcal{O}$ .  $D$  can also be called a distance transform, if there is no ambiguity between the image  $D$  and the transformation (DT) that generated it. Note that,  $\mathcal{O}$  must contain at least one pixel, otherwise the output of the DT is undefined. In addition,  $d(p', p)$  is generally taken as the Euclidean distance, given by:

$$d(p', p) = \|p' - p\|_2 = \sqrt{(p'_x - p_x)^2 + (p'_y - p_y)^2} \quad (7.3)$$

Figure 7-1 depicts a numerical example of Euclidean DT. For each pixel in Figure 7-1 (a), the corresponding pixel in the DT of Figure 7-1 (b) holds the smallest Euclidean distance between the black pixel and the object.

Various metrics, in addition to the Euclidean, one can be used to compute the distance in Equation (7.2). Frequently used examples are the city-block ( $d_1$ ) and

chessboard ( $d_\infty$ ), defined by:

$$d_1(p', p) = \|p' - p\|_1 = |p'_x - p_x| + |p'_y - p_y|$$

$$d_\infty(p', p) = \|p' - p\|_\infty = \max\{|p'_x - p_x|, |p'_y - p_y|\} \quad (7.4)$$

Figure 7-2 shows distance images using different distance functions. Note that in this chapter, we will consider the Euclidean distance function to generate DT images.

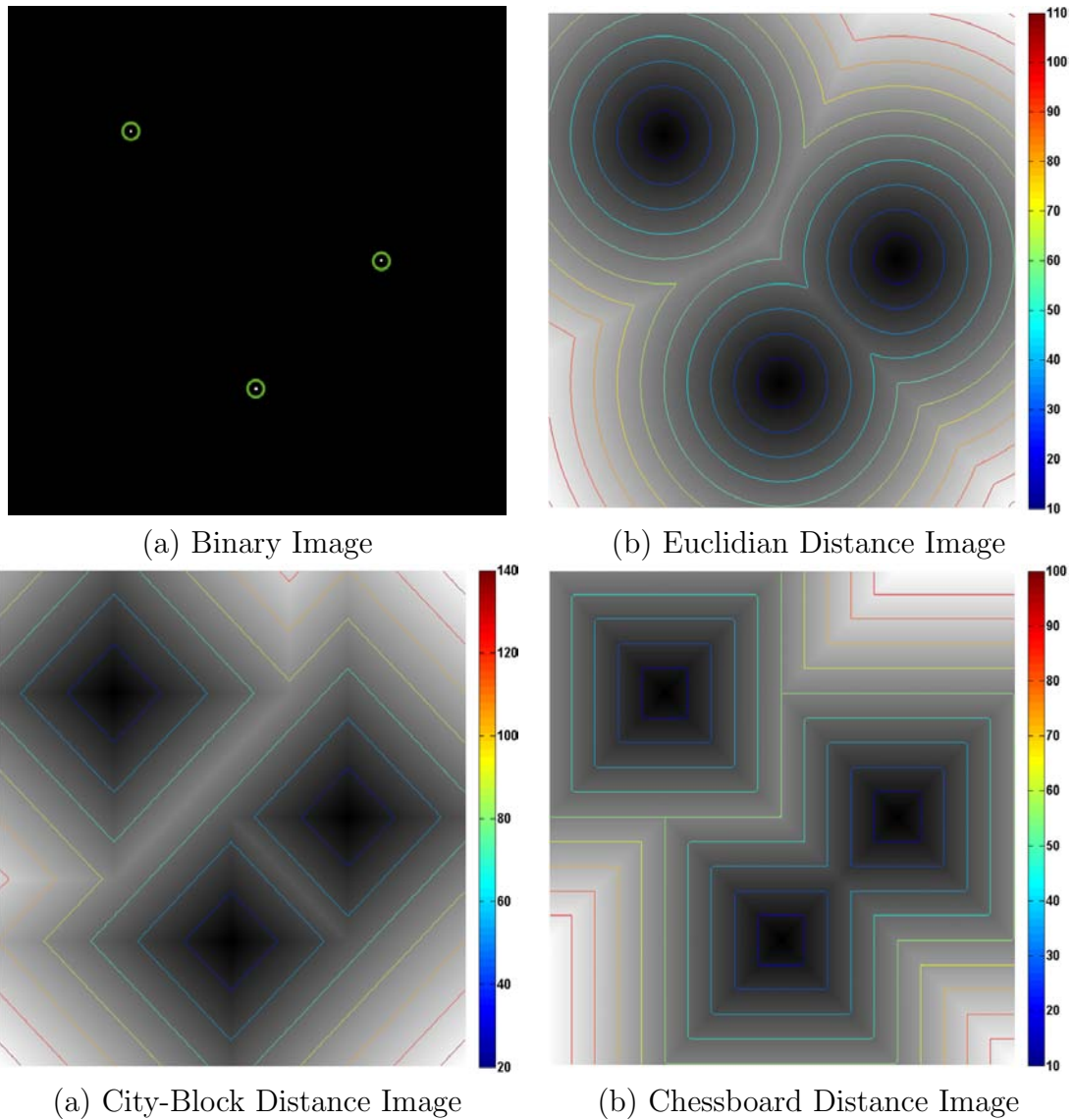


Figure 7-2: An example of generating distance images using (b): Euclidian distance function, (c) city-block distance function, and (d): chessboard distance function. In (a), the dot in centre of each green circle ( $\odot$ ) indicates a white pixel.

## 7.3 Iterative Closest Point Algorithms (ICP)

A general problem in medical image analysis is the registration of point sets [48–51, 53, 54, 138, 186]. Generally, a set of point samples from the organ or tissue is obtained from different images. As mentioned in Chapter 3, the main goal of registration is to bring the data into a common reference frame by estimating the transformations between the data sets. However, this is a difficult task, as correspondences between the point sets are unknown a-priori. A common approach to tackle the problem is the class of algorithms based on the ICP technique introduced by Besl et al. [135]. The classical ICP [135] has two main steps that are iterated until convergence: (1) closest point computation using the nearest neighbour algorithm and (2) global rigid transformation estimation. ICP variant methods can be differentiated by the type of transformation they estimate and by the procedure used to obtain these transformations. As rigid ICP, deformable ICP has two inner steps. Step (2) becomes deformation estimation [134]. This can be done by minimizing an energy including a data term and a smoothing term. The reasons that ICP approach has been driving the attention of researchers over the past decade are due to its simplicity and its performance. Although the initial estimate must be reasonably close to the solution, the process converges relatively fast.

In this section, we remove one of the basic characteristics of ICP; its closed-form inner loop; and employs instead a variational formulation to compute a dense deformation field. While this approach has its roots in Fitzgibbon et al.’s one-step rigid ICP [138], it extends beyond the latter in its emphasis on the estimation of nonlinear deformation most notably with respect to variational formulation. Since our new formulation has one energy functional to simultaneously establish correspondences and estimate deformation field, it improves computational time and reduces the dependence of the classical two-step ICP on the initial estimate.

To employ the ICP approach in order to solve our TVUS-MR registration problem, firstly, the soft tissue organs and nodules in the TVUS moving image  $M$  and in the corresponding 2D MR reference slice  $F$  are manually segmented by an expert.

This step constructs two sets of curves,  $C_M$  and  $C_R$ , representing the boundary of the corresponding organs in both modalities. This is a middle ground choice utilized by many 2D/2D and 3D/3D US-MR registration methods in order to reduce the interaction time and decrease the potential expert error in selecting dense point correspondences. Let  $\Omega$  be a bounded open set of  $\mathbb{R}^2$  representing the TVUS image,  $q$  an arbitrary point in  $C_M \subset \Omega$ , and  $\phi \in W(\Omega, \mathbb{R}^2)$  a dense deformation vector field.  $W$  is a Sobolev space of sufficiently smooth vector fields over  $\Omega$  with appropriate boundary conditions.

### 7.3.1 Variational Two-Step ICP

Contour-based registration is a difficult problem, especially for non-linear deformation. Without prior knowledge the problem is ill-posed. As prior, we use curvature regularization, since in previous chapter, it provides high registration accuracy. To establish point correspondences and estimate deformation between curve correspondences we propose a variational formulation of the two inner steps of ICP with curvature regularization:

step 1: **closest point computation**

$$\zeta(q) = \operatorname{argmin}_{p \in C_R} d^2(p, \phi(q)) \quad (7.5)$$

This defines  $\zeta \in C^1(C_M, C_R)$ , a function that estimates the closest-point  $\zeta(q)$  on  $C_R$ .

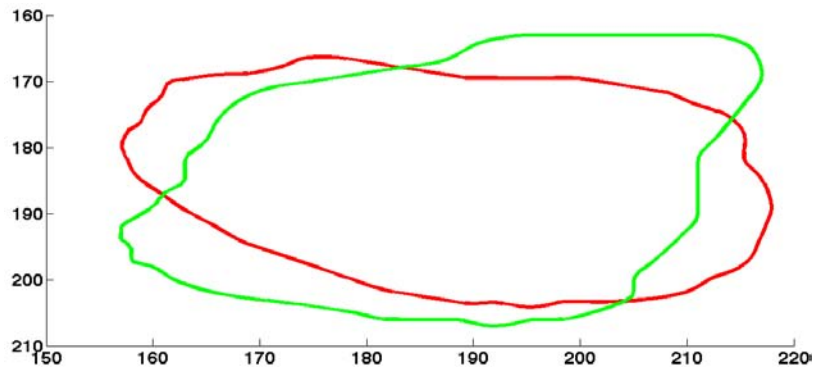
step 2: **deformation estimation**

$$\phi = \operatorname{argmin}_{\phi \in W} \underbrace{\lambda \int_{\gamma} d^2(\phi, \zeta(q)) dq}_{\text{data term}} + (1 - \lambda) \underbrace{\int_{\Omega} \|\Delta\phi\|_2^2 dX}_{\text{regularization term}} \quad (7.6)$$

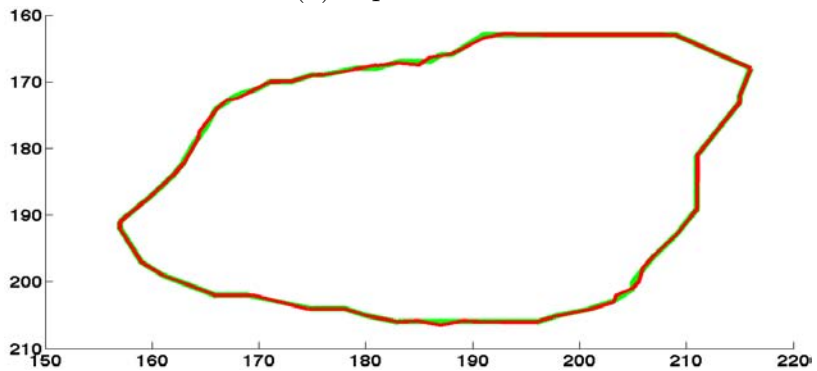
where  $\Delta$  is the Laplacian operator and  $\lambda \in [0, 1]$  is a smoothing parameter.

Both steps in ICP must minimize the error, and thus, ICP is guaranteed to converge to a local minimum [138, 150]. Two-step ICP mainly depends on the nearest-neighbour heuristic used in step 1 which establishes binary point correspondences. It is easy to see that the procedure of establishing correspondences in two-step ICP

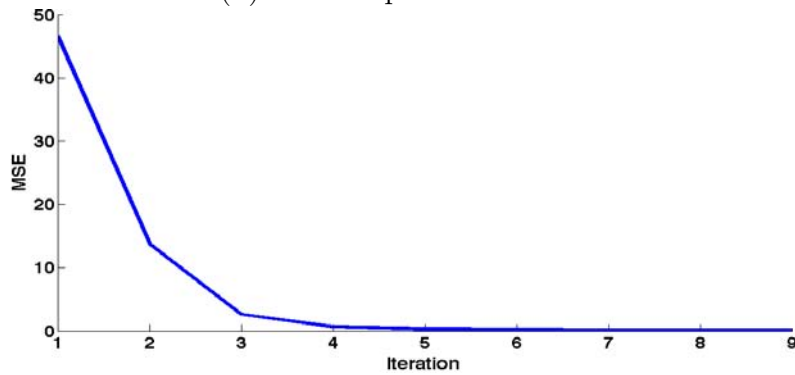
makes it more vulnerable to local minima [150]. The question that may immediately arise is how the two steps can be merged into a single step. Indeed merging two steps into one would result in a single minimization that would improve the convergence rate [138]. To achieve this, as suggested by Fitzgibbon et al. [138], we can use the Euclidean DT. Figure 7-3 shows an example of two-step deformable ICP.



(a) Input Curves



(b) Two-Step ICP Results



(c) Convergence Curve

Figure 7-3: An example of two-step ICP. (a) shows initial moving (red) and reference (green) curves. (b) depicts two-step ICP results. (c) shows the MSE at each iteration.

### 7.3.2 Variational One-Step ICP

We now present our formulation of the registration problem by combining the two steps of the classical formulation in a single step. Substituting Equation (7.5) in (7.6) yields:

$$\phi = \operatorname{argmin}_{\phi \in W} \lambda \int_{C_M} d^2 \left( \phi, \operatorname{argmin}_{p \in C_R} d^2(p, \phi) \right) dq + (1 - \lambda) \int_{\Omega} \|\Delta\phi\|_2^2 dX \quad (7.7)$$

It is clear that  $d^2 \left( \phi, \operatorname{argmin}_{p \in C_R} d^2(p, \phi) \right) = \min_{p \in C_R} d^2(p, \phi)$ . This can be interpreted as the fact that the cost depends on the distance to the closest point but not on the closest point itself. This allows us to rewrite Equation (7.7) as:

$$\phi = \operatorname{argmin}_{\phi \in W} \lambda \int_{C_M} \min_{p \in C_R} d^2(p, \phi) dq + (1 - \lambda) \int_{\Omega} \|\Delta\phi\|_2^2 dX \quad (7.8)$$

We observe that the data term now involves a Euclidean DT ( $D$ ), since  $D \circ \phi = \min_{p \in C_R} d^2(p, \phi)$  by definition. We can now combine  $D$  with Equation (7.8), leading to:

$$\phi = \operatorname{argmin}_{\phi \in W} \underbrace{\lambda \int_{C_M} (D \circ \phi)^2 dq + (1 - \lambda) \int_{\Omega} \|\Delta\phi\|_2^2 dX}_{E[\phi]} \quad (7.9)$$

Equation (7.9) represents a variational problem with  $E$  as cost functional. The next step is to compute the functional form of  $\phi$  using calculus of variation.

#### 7.3.2.1 Euler-Lagrange Equation

A function  $\phi$  that minimizes  $E$  must fulfill the EL differential equation. Several numerical optimization algorithms [104, 105] may then be applied to solve the resulting nonlinear equation. In Equation (7.9), the data term places constraints on the deformation field  $\phi$  at the curve location. To make it more general and to permit its formulation as an EL equation we use an index function  $\delta_{C_M}$ , with  $\delta_{C_M} : \Omega \rightarrow \{0, 1\}$ ,  $\delta_{C_M}(X) = 1$  if  $X \in C_M$  and 0 otherwise. We rewrite the cost functional of Equa-

tion (7.9) as:

$$E[\phi] = \int_{\Omega} (\lambda \delta_{C_M} (D \circ \phi)^2 + (1 - \lambda) \|\Delta \phi\|_2^2) dX \quad (7.10)$$

Let  $\phi^0$  be an initial estimate that can be found by rigid registration. We follow the iteration:

$$\phi^{k+1} = \phi^k + U \quad (7.11)$$

where  $U \in W$  is a dense displacement vector field. We restate our problem as:

$$\min_U E[\phi^k + U] \quad (7.12)$$

By substituting Equation (7.11) into (7.10), we obtain:

$$E[\phi^k + U] = \int_{\Omega} \left( \lambda \delta_{C_M} (D \circ (\phi^k + U))^2 + (1 - \lambda) (\|\Delta U\|_2^2 + \|\Delta \phi^k\|_2^2) \right) dX \quad (7.13)$$

The distance transform  $D$  is nonlinear and can be approximated by its first order Taylor expansion around  $\phi^k$ :

$$E[\phi^k + U] = \int_{\Omega} \left( \lambda \delta_{C_M} (D \circ \phi^k + (\nabla D \circ \phi^k) U)^2 + (1 - \lambda) (\|\Delta U\|_2^2 + \|\Delta \phi^k\|_2^2) \right) dX \quad (7.14)$$

where  $\nabla = [\frac{\partial}{\partial x}, \frac{\partial}{\partial y}]$ . A function  $U$  that minimizes Equation (7.12) must fulfill its EL equation. This is written as a system of two fourth order elliptic PDEs represented by a  $2 \times 2$  symmetric matrix equation:

$$\mu \int_{C_M} (D \circ \phi^k + (\nabla D \circ \phi^k) U) (\nabla D \circ \phi^k) dq + \left( \frac{\partial^4 U}{\partial X^4} \right) = 0 \quad (7.15)$$

where  $\mu = \frac{\lambda}{1-\lambda}$ .

### 7.3.2.2 Numerical Approximation

To solve Equation (7.15) numerically, we discretize the curve  $C_M$  in  $N$  points  $q_1, \dots, q_N$  and  $\Omega$  on the rectangular pixel grid. Note that  $\delta_q(X) = 1$  if  $\exists j \in 1, \dots, N$  such that  $X = q_j$  and 0 otherwise. We consider the unknown function  $U = [u_1, u_2]^T$  on a rectangular pixel grid. Therefore, the discretization of Equation (7.15) leads to a system

---

**Algorithm 7.1** Proposed Algorithm Pseudo-Code.

---

**Input:** A set of points from MR ( $p$ ) & a set of points from TVUS ( $q$ )  
**Result:** Warped surface ( $\phi$ ) % Grid of points  $h_{max} \times w_{max}$  to represent  $\phi$   
**Initialization:**  
 $k \leftarrow 0$  % Iteration counter  
 $q^k \leftarrow q + \phi^0$  % The 2D points  $q$  rigidly register;  $\phi^0$  is an initialization of  $\phi$   
Compute  $D$  and  $\nabla D$  from  $p$  %  $D$  and  $\nabla D$  are used in equation (7.17)  
**while**  $\|\nabla\phi\| > \varepsilon$  **do**  
    Compute  $U$  by iterating equation (7.17)  
     $q^{k+1} \leftarrow q^k + \delta_{q^k} U$  % Update the TVUS curve  
     $\phi^{k+1} \leftarrow \phi^k + U$  % Update the TVUS image  
     $k \leftarrow k + 1$   
**end while**

---

of two PDEs:

$$\begin{aligned} & \mu\delta_q(X) \left( (D(\phi^k(X)) + D_x(\phi^k(X))u_1(X) + D_y(\phi^k(X))u_2(X)) D_\ell(\phi^k(X)) \right) \\ & + \left( \frac{\partial^4 U}{\partial x^4} + \frac{\partial^4 U}{\partial y^4} \right) = 0 \quad \text{for } \ell \in \{x, y\} \end{aligned} \tag{7.16}$$

where  $D_\ell$  is the derivative of  $D$  with respect to  $\ell \in \{x, y\}$ . To solve the PDEs, we use a finite difference scheme with boundary condition  $\Delta U = 0$ . This leads to a sparse linear system that can be solved by SOR:

$$\begin{aligned} u_{1,h,w}^{t+1} &= \beta u_{1,h,w}^t - A \left[ \mu\delta_q(X) \left( D(\phi^k(X)) \frac{\partial D}{\partial x}(\phi^k(X)) \right) + C u_{2,h,w}^t \right. \\ & \quad \left. + (u_{1,h,w-2}^{t+1} - 4u_{1,h,w-1}^{t+1} - 4u_{1,h+1,w}^{t+1} + u_{1,h+2,w}^{t+1}) \right. \\ & \quad \left. + (u_{1,h,w+2}^t - 4u_{1,h,w+1}^t - 4u_{1,h-1,w}^t + u_{1,h-2,w}^t) \right] \\ u_{2,h,w}^{t+1} &= \beta u_{2,h,w}^t - B \left[ \mu\delta_q(X) \left( D(\phi^k(X)) \frac{\partial D}{\partial y}(\phi^k(X)) \right) + C u_{1,h,w}^t \right. \\ & \quad \left. + (u_{2,h,w-2}^{t+1} - 4u_{2,h,w-1}^{t+1} - 4u_{2,h+1,w}^{t+1} + u_{2,h+2,w}^{t+1}) \right. \\ & \quad \left. + (u_{2,h,w+2}^t - 4u_{2,h,w+1}^t - 4u_{2,h-1,w}^t + u_{2,h-2,w}^t) \right] \end{aligned} \tag{7.17}$$

where  $A = \frac{\alpha}{12 + \mu\delta_q(X) \left( \frac{\partial D}{\partial x}(\phi^k(X)) \right)^2}$ ,  $B = \frac{\alpha}{12 + \mu\delta_q(X) \left( \frac{\partial D}{\partial y}(\phi^k(X)) \right)^2}$ ,  $t \in \mathbb{N}$  is the SOR iteration number,  $C = \mu\delta_q(X) \left( \frac{\partial D}{\partial y}(\phi^k(X)) \frac{\partial D}{\partial x}(\phi^k(X)) \right)$ ,  $\beta = 1 - \alpha$ ,  $h = 1, \dots, h_{max}$ ,  $w =$

$1, \dots, w_{max}$ ,  $h_{max}$  and  $w_{max}$  are height and width of  $M$  respectively, and  $\alpha$  is the relaxation factor. The pseudo code of our method is given in Algorithm 7.1. In Algorithm 7.1,  $\varepsilon$  is prespecified threshold and set to be  $10^{-5}$ . Figure 7-4 shows an example of one-step deformable ICP. From Figure 7-4 and 7-3, we can see that one-step ICP provides more accurate results and converges to the global minimum faster.

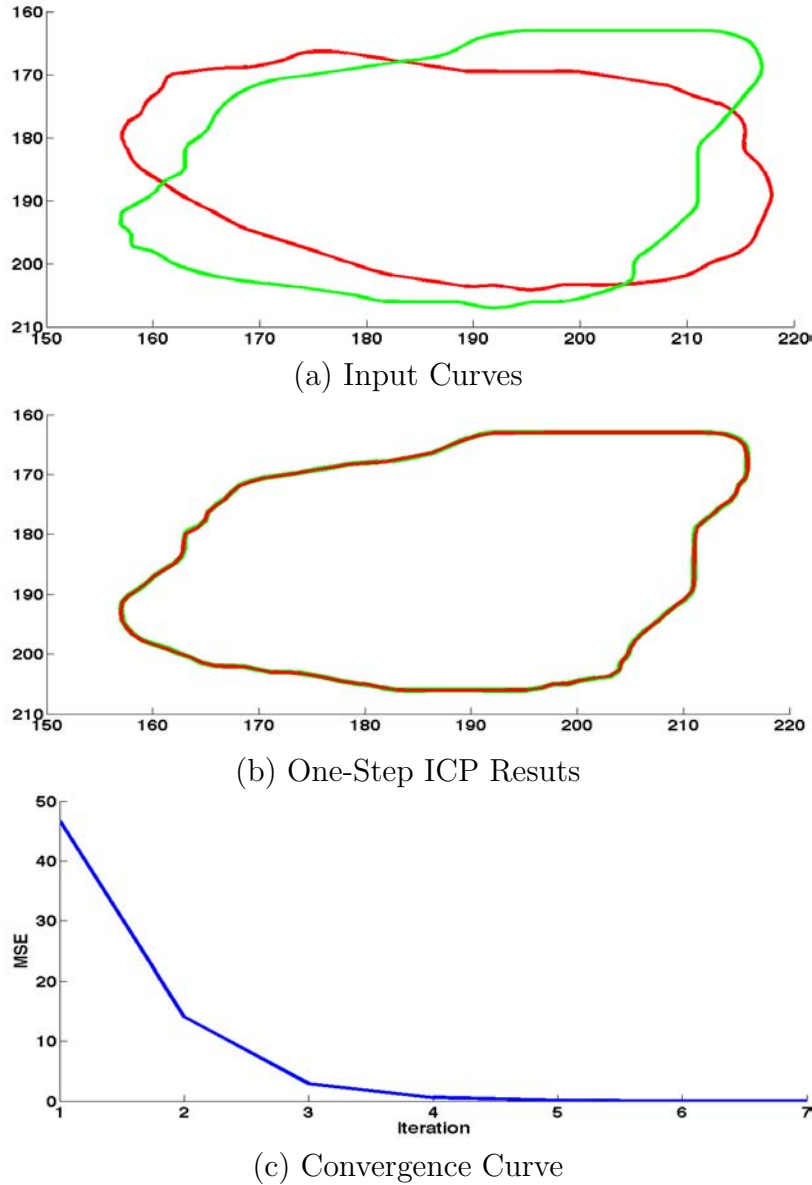


Figure 7-4: An example of one-step ICP. (a) shows initial moving (red) and reference (green) curves. (b) depicts one-step ICP results. (c) shows the MSE at each iteration.

## 7.4 Experimental Results

### 7.4.1 Material

The experiments are conducted on ten patients who have small endometrial implants in the pelvic area. For each patient, TVUS and MR imaging are used to examine their pelvic organs. TVUS and MR Images used for the experiments have an average image size of  $300 \times 300$ . The reference MR slice from MR volume that corresponds to the moving TVUS image is manually chosen by an expert. Therefore, we assume that the TVUS slice is parallel to the corresponding MR slice. The soft tissue organs such as bladder, uterus, ovary, and rectum in both TVUS and MR slices are manually segmented by an expert. We compare our one-step ICP registration scheme with TPS-RPM which has been proposed by Chui et al. [150] and two-step ICP. In addition, we use a point-based registration method [206] as a baseline to evaluate our results.

### 7.4.2 Results and Discussion

We evaluate the proposed method’s performance in comparison with variational two-step deformable ICP, TPS-RPM [150] which is one of the best non-rigid point-set registration methods, and a point-based registration method [206]. We demonstrate the accuracy of the proposed method by quantitative and qualitative tests on semi-synthetic and real world data sets. The true point correspondences are established by an expert in order to be able to use a baseline method to evaluate our results. We also assess the results with quantitative and qualitative evaluations on semi-synthetic data sets, generated to faithfully reproduce patient data features. We conduct a hundred experiments using semi-synthetic data with artificial deformations to test various aspects of the methods. The results are very informative. To demonstrate the applicability in real applications, we also conduct ten tests on patient data. Registration accuracy is evaluated in terms of DSC, HD, TRE, and MSE. In our experiments to estimate TRE, we select anatomical landmarks in the patient’s body such as boundary of organs and their internal anatomical structures. The target points are 10 points which are not used for registration.

#### 7.4.2.1 Tests on Semi-Synthetic Data

Numerous experiments on semi-synthetic data with various degrees of deformation are performed to evaluate one-step ICP's performance. We evaluate the proposed method against two-step ICP and TPS-RPM. In order to generate our semi-synthetic data, the boundary of soft tissue organs such as the bladder, uterus, ovary, and rectum are manually segmented from different MR slices. Then, randomly generated deformations are applied to each curve, and different algorithms are used to recover those deformations. Note that the contours are deformed through increasingly larger degrees of deformation by using advection [207] (see Figure 7-5, first row). The rate of deformation varies between 15% and 75%.

The qualitative results are shown in Figure 7-5. In this figure, we use a single uterus contour with 15%, 30%, 45%, 60%, and 75% average deformation, respectively. Here, we use two contours, one is the deformed version (red curves in the first row of Figure 7-5) of the other (green curves in the first row of Figure 7-5). Note that in this figure, the green curves are the ground truth solutions. We then use one-step ICP, TPS-RPM [150], and two-step ICP to find the best transformation to align the template set onto the ground truth set. The registration results for each compared method are depicted in rows of Figure 7-5. At first and second deformation level (15% and 30%), we can visually observe that all the methods provide good results. This is visually demonstrated by Figure 7-5 (a)-(b). In Figure 7-5 (c)-(d) we make the registration problem more challenging. We deform the uterus contour with 45%, 60%, and 75% average deformation, respectively. We can see that two-step ICP has much poorer performance as compared to the proposed one-step ICP and TPS-RPM [150]. In this figure, we can also see that our method and TPS-RPM provide good results. However, ours establish more accurate correspondences.

In order to assess the behaviour of the methods in a quantitative way, we use all the semi-synthetic data sets and measure MSE to estimate the error between corresponding points. The results of MSE for 20 2D contours with 5 degrees of deformation are shown in Figure 7-6 (a) and (b), respectively. Figure 7-6 demonstrates one-step

ICP, TPS-RPM, and two-step ICP performances for each average deformation. Both one-step ICP and TPS-RPM provide accurate results. Two-step ICP gets trapped in a local minimum. Based on these experiments, we conclude that our method has high registration accuracy and outperforms TPS-RPM.

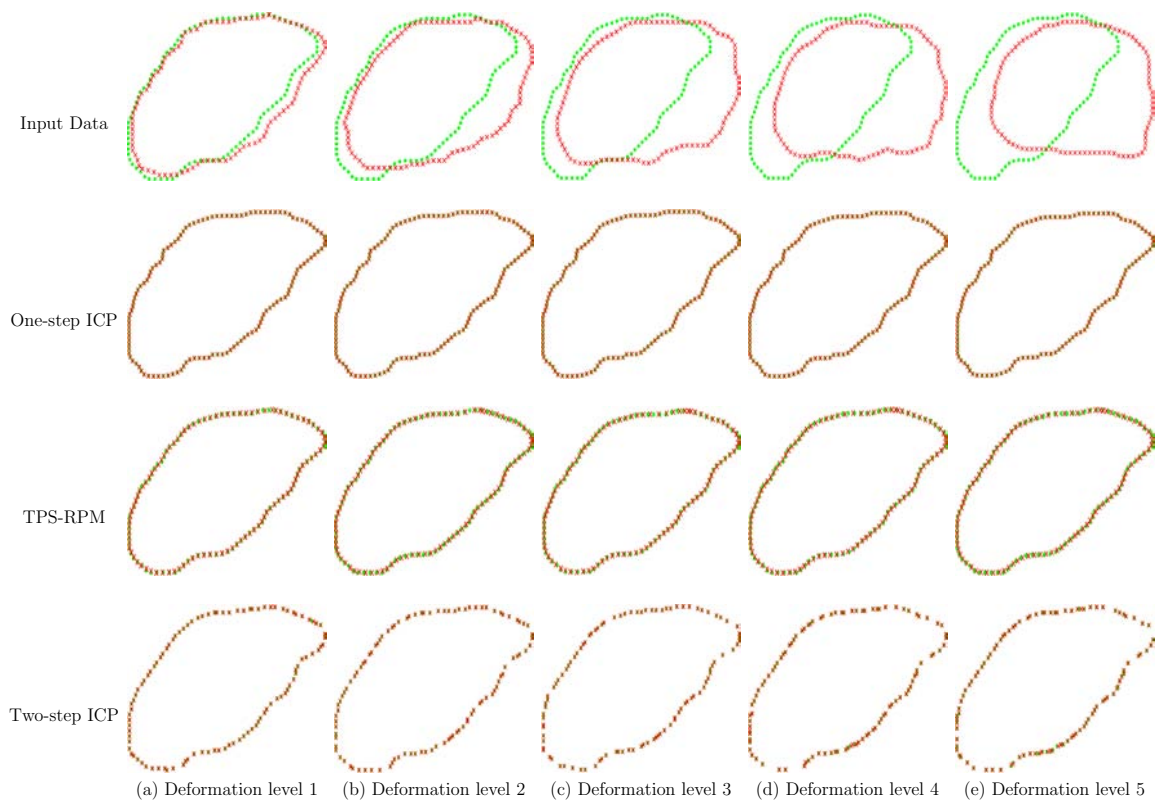
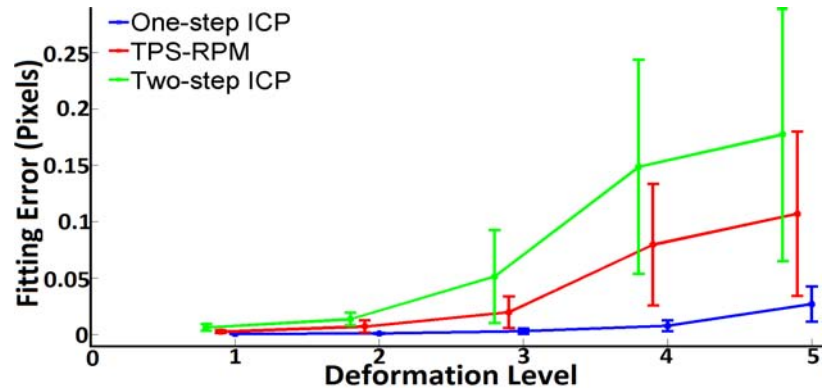
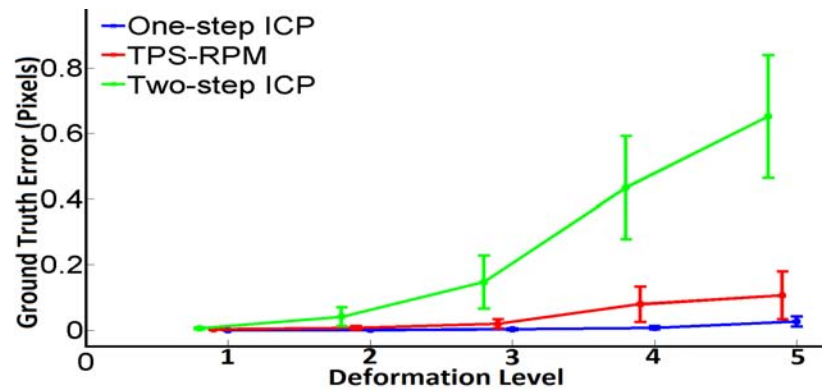


Figure 7-5: Registration results for semi-synthetic contours. A single uterus contour is used with 15%, 30%, 45%, 60%, and 75% average deformation, respectively. The first row shows the reference ( $\bullet$ ) and moving ( $\times$ ) point sets. The reference point set is the ground truth solution. The proposed method (second row) is compared with TPS-RPM (third row) and two-step ICP (fourth row).



(a) MSE between the closest point pairs



(b) MSE between the true correspondences

Figure 7-6: Comparison of one-step ICP with different methods on the semi-synthetic data with respect to deformation level. Our method achieves high registration accuracy compared to the two other methods.

### 7.4.2.2 Tests on Real Patient Data

For real-world data, we use a point-based registration method [206] as a baseline to evaluate our results. In this manner, an expert manually selects control points at each pair of curves. The reasons that we chose [206] is a comparison with the well-known method of the state-of-the-art are given therein. The registration accuracy that measures overlap are tabulated in Table 7.1. It shows that our method outperforms the other methods in terms of contour overlap accuracy. TRE and computational time are tabulated in Table 7.2. It is indicated that the proposed method provides high local registration accuracy and is fast. Tables 7.1 and 7.2 indicate that the proposed method provides promising results as the difference with the baseline method is the smallest one compared to other methods. Moreover, two experts compared our method with the baseline method. In this manner, we setup a registration quality score called 1-to-5 rating scale where 5 is excellent and 1 is bad. The experts' evaluation are given in Table 7.3.

Patient	DSC				HD			
	Point-based	Proposed	TPS-RPM	2-step ICP	Point-based	Proposed	TPS-RPM	2-step ICP
1	0.9943	<b>0.9939</b>	0.9934	0.9842	0.0799	<b>1.2632</b>	1.5661	4.1604
2	0.9897	<b>0.9893</b>	0.9867	0.9816	0.2873	<b>1.2605</b>	1.5345	1.9078
3	0.9946	<b>0.9800</b>	0.9771	0.9427	0.8088	<b>1.6623</b>	1.8384	3.6525
4	0.9819	<b>0.9626</b>	0.9147	0.8195	0.7231	<b>1.7258</b>	2.4013	10.8844
5	0.9960	<b>0.9948</b>	0.9910	0.9874	0.7546	<b>1.7821</b>	2.0539	2.6033
6	0.9898	<b>0.9871</b>	0.9839	0.9803	0.4017	<b>1.5577</b>	2.0539	2.0012
7	0.9954	<b>0.9947</b>	0.9940	0.9918	0.1365	<b>1.0390</b>	1.6994	4.1646
8	0.9833	<b>0.9784</b>	0.9755	0.8916	1.0182	<b>1.6569</b>	2.7194	7.7645
9	0.9960	<b>0.9948</b>	0.9910	0.9874	0.7546	<b>1.7821</b>	2.0539	2.6033
10	0.9947	<b>0.9943</b>	0.9935	0.9936	0.0961	<b>1.0586</b>	1.8003	3.6069
average	0.9916	<b>0.9870</b>	0.9801	0.9560	0.5061	<b>1.4788</b>	1.9721	4.3349
std. dev.	0.0053	<b>0.0106</b>	0.0239	0.0574	0.3447	<b>0.2945</b>	0.3713	2.8489

Table 7.1: Comparison between point-based registration, proposed method, TPS-RPM and two-step ICP. A high DSC value means a good contour region overlap, while a low HD value signifies a good contour overlap. **Bold** values indicate the best results.

Figures 7-7 and 7-8 show the registration results for two different patients. The registration results for the point-based registration method [206], Proposed method, TPS-RPM, and two-step ICP are illustrated in rows. The first row illustrates the reference and moving images. In Figure 7-7, the endometrial implant is infiltrated into the uterus and rectum, so that, the expert manually segments the boundary of

Patient	TRE				Time(sec)			
	Point-based	Proposed	TPS-RPM	2-step ICP	Point-based	Proposed	TPS-RPM	2-step ICP
1	0.1700	<b>0.7880</b>	1.8895	2.2052	7.52	<b>12.79</b>	77.53	14.13
2	0.2630	<b>0.5061</b>	1.4825	1.7540	16.12	<b>18.37</b>	90.64	24.34
3	1.1153	<b>2.2757</b>	4.2002	6.6531	9.59	<b>22.68</b>	83.03	27.96
4	0.1929	<b>1.2486</b>	3.1181	8.1541	7.13	<b>14.78</b>	94.82	15.69
5	0.6510	<b>0.7289</b>	0.9000	1.581	11.03	<b>13.07</b>	96.92	15.31
6	0.3254	<b>0.5056</b>	0.8739	1.2263	8.57	<b>15.92</b>	81.41	23.28
7	0.5062	<b>0.8619</b>	1.2014	4.5932	7.08	<b>12.13</b>	104.06	19.92
8	0.9165	<b>1.8361</b>	4.6130	7.5951	10.02	<b>18.34</b>	99.81	32.44
9	0.2324	<b>0.3914</b>	0.7528	2.2097	9.0830	<b>13.59</b>	92.6530	15.21
10	0.1891	<b>0.9893</b>	2.0904	4.5538	2.8818	<b>13.05</b>	97.95	19.94
average	0.4562	<b>1.0132</b>	1.8404	4.0526	10.2780	<b>15.4720</b>	88.5880	20.8220
std. dev.	0.3356	<b>0.6131</b>	1.2042	2.6430	3.6292	<b>3.3797</b>	9.0889	6.1367

Table 7.2: Comparison between point-based registration method (baseline), proposed method, TPS-RPM and two-step ICP. A low TRE value means good local registration accuracies around target landmarks. **Bold** values indicate the best results.

Patient	Radiologist		Surgeon	
	Point-based	Proposed	Point-based	Proposed
1	4	4	4	5
2	3	4	4	4
3	2	3	3	3
4	5	5	4	5
5	4	3	4	4
6	4	4	3	3
7	5	4	4	3
8	4	4	4	4
9	5	5	5	4
10	5	4	4	2
average	4.1	4.0	3.9	3.7
std. dev.	0.66	0.67	0.56	0.94

Table 7.3: Experts' evaluation of the point-based registration and proposed method.

uterus and rectum in both TVUS and MR images. Note that the depth of infiltration is not clear in the MR image. Therefore, it is necessary to register TVUS with MR image to provide more precise information about depth of infiltration. For localizing the implant, we apply the displacement field to the yellow curve in the TVUS image and we find the new location of endometriosis in the MR image. In Figure 7-8, endometrial implant is located at the top of uterus and can be seen in the TVUS image while there is no evidence of their presence in the MR image. In this example, the expert manually segments uterus in both modalities. Therefore, we use uterus curve correspondences to register TVUS with MR image which leads to localization of endometriosis in the MR frame. From Figures 7-7 and 7-8 we can conclude that the proposed registration method provides an accurate and smooth displacement field to localize the implants.

Finally, the evaluations and the experimental results show that the proposed method gives accurate and smooth displacement fields. Moreover, they demonstrate that the combination of complimentary information from TVUS and MR images is more informative than any of the input modalities. Indeed, the registration provides more precision about implant location and depth of infiltration which consequently simplifies and improves diagnosis.

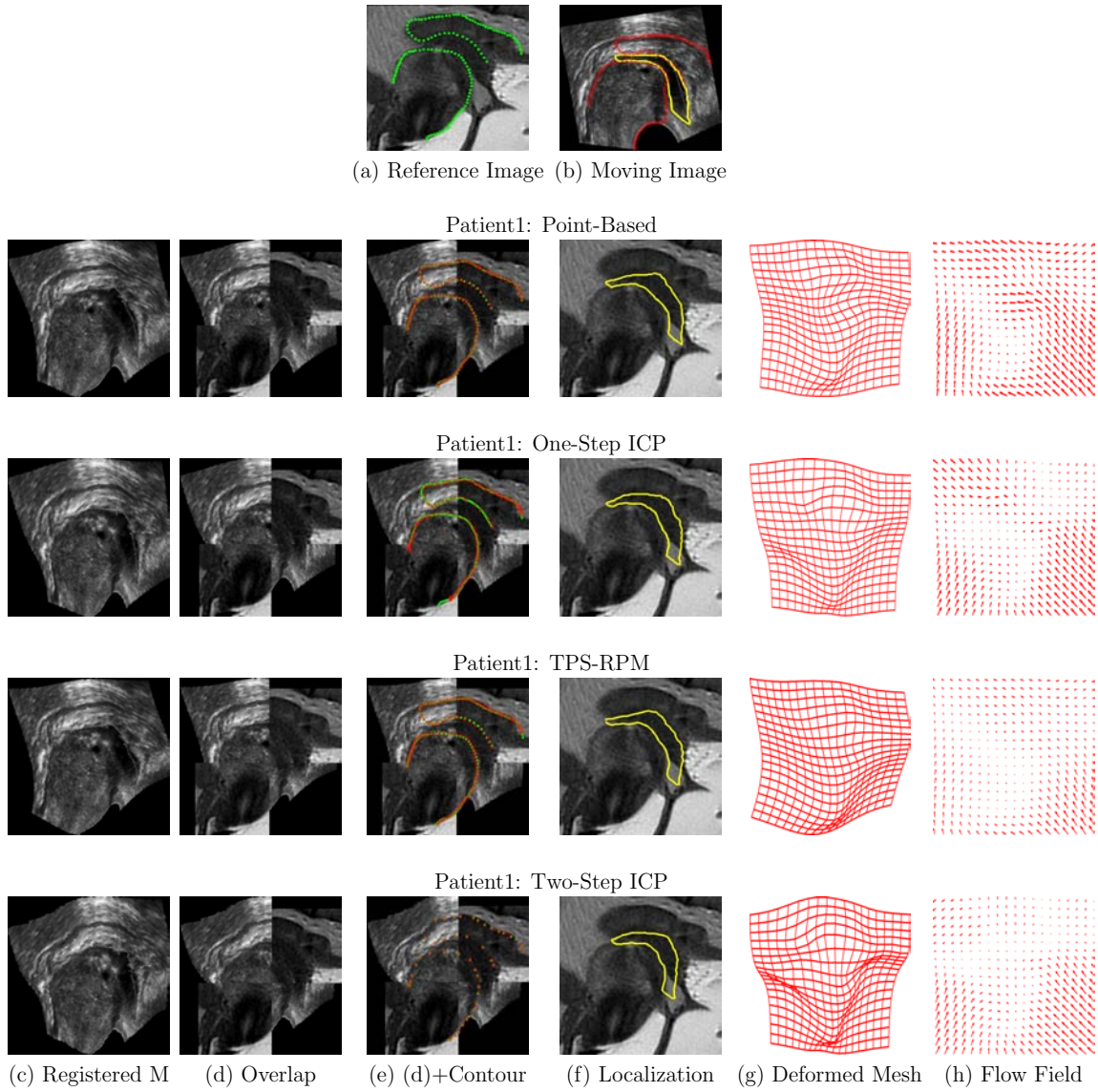


Figure 7-7: Registration results for base-line, one-step ICP, TPS-RPM, and two-step ICP methods in rows. (a) and (b) show MR and TVUS image. Small endometrial implant which is just visible in TVUS image is depicted by yellow curve. (c) shows warped TVUS image. (d) and (e) demonstrate overlap images where the top right and the bottom left belong to the MR image and the top left and the bottom right belong to the deformed TVUS image. (f) shows the location of the endometrial implant in the MR frame. (g) and (h) depict the deformed mesh and displacement field, respectively.

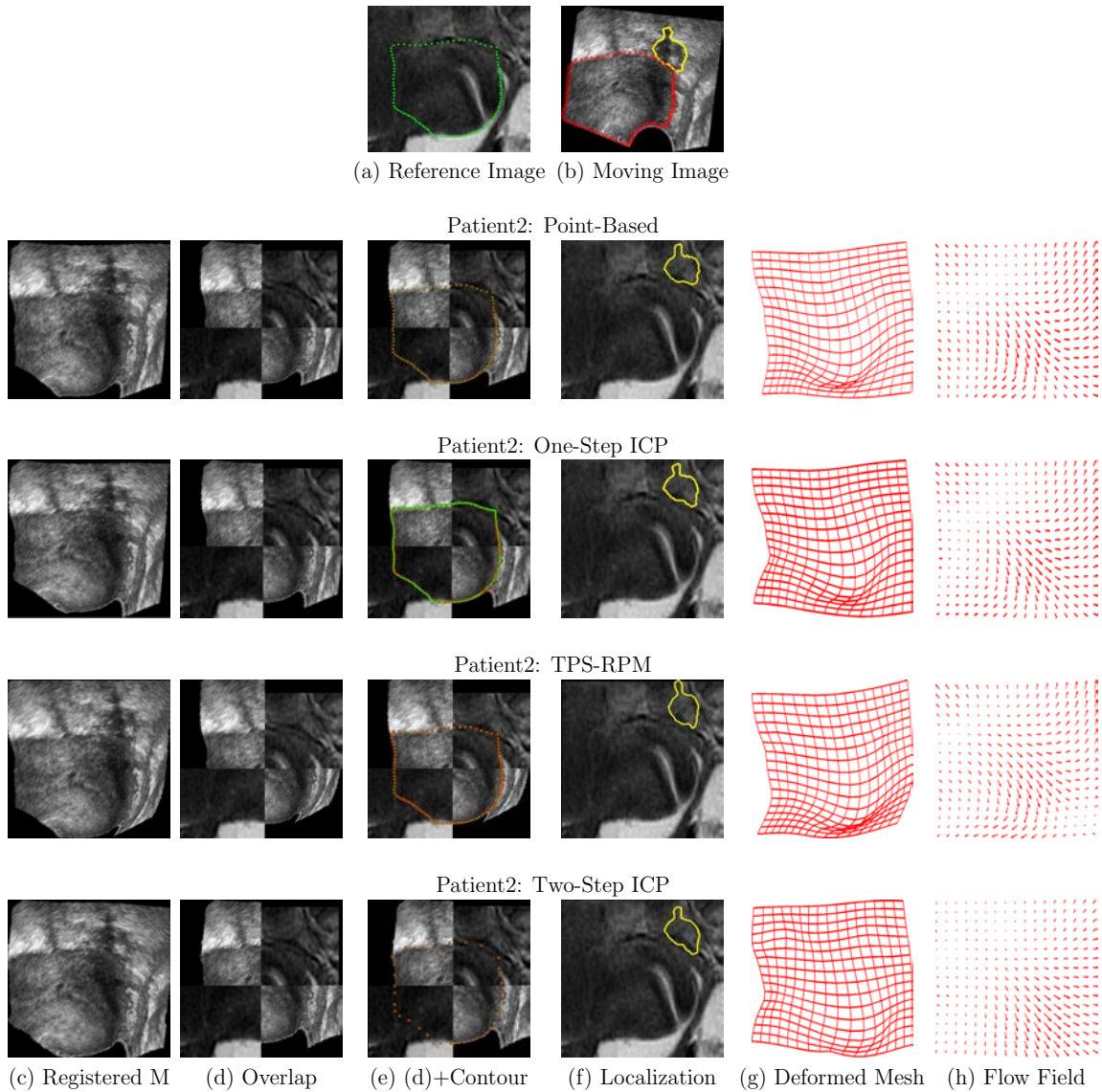


Figure 7-8: Registration results for base-line, one-step ICP, TPS-RPM, and two-step ICP methods in rows. (a) and (b) show MR and TVUS image. Small endometrial implant which is just visible in TVUS image is depicted by yellow curve. (c) shows warped TVUS image. (d) and (e) demonstrate overlap images where the top right and the bottom left belong to the MR image and the top left and the bottom right belong to the deformed TVUS image. (f) shows the location of the endometrial implant in the MR frame. (g) and (h) depict the deformed mesh and displacement field, respectively.

## 7.5 Conclusion

In this chapter, a new framework for 2D/2D TVUS-MR registration is proposed to localize and characterize endometrial tissues. The method uses contour correspondences through a novel variational one-step ICP. In order to obtain point correspondences and local nonlinear deformations, the method uses Euclidean distance maps resulting from MR contours. The performance of the proposed method is evaluated against variational two-step deformable ICP and TPS-RPM. The results obtained from semi-synthetic and real-world data conclude that the performance of the proposed method is better than TPS-RPM and two-step ICP other methods.

The main advantages of one-step ICP over traditional deformable two-step ICP are that it improves computational time and reduces the dependence of the classical two-step ICP on the initial estimate. We also find that two-step ICP is guaranteed to converge to a local minimum, since both steps in ICP must minimize the error (one for establishing correspondences and one for estimating deformation). To improve the convergence rate, we remove closed-form inner loop of two-step ICP by using the Euclidean DT which leads to one energy functional to simultaneously establish correspondences and estimate deformation field.

Up to now, we proposed methods require the selection of a 2D MR slice and use 2D/2D deformable image registration. This is a limitation since the standard TVUS and MR imaging techniques used for diagnosing endometriosis are 2D and 3D, respectively. In next Chapter, we introduce a novel deformable slice-to-volume registration process to overcome this limitation. To this end, we register a 2D TVUS image to a 3D MR data in order to transform the TVUS planar image to a curved 2D surface in MR volume.

# Chapter 8

## One-Step ICP-Based 2D/3D Registration

### Contents

---

<b>8.1</b>	<b>Introduction</b>	<b>132</b>
<b>8.2</b>	<b>Registration Procedure</b>	<b>136</b>
8.2.1	A Variational Formulation for Two-Step ICP	137
8.2.2	A Variational Formulation in One-Step Using Distance Transform	138
<b>8.3</b>	<b>Experimental Results</b>	<b>144</b>
8.3.1	Material and Clinical Motivations	144
8.3.2	Results and Discussion	145
<b>8.4</b>	<b>Conclusion</b>	<b>161</b>

---

### 8.1 Introduction

Up to now, we have proposed various feature-based registration methods to align a 2D TVUS image with a 2D MR image to localise a small endometrial implant and provide information about depth of infiltration. In all previous methods that we have discussed in Chapters 5-7, the reference 2D MR slice from the MR volume that corresponds to the moving 2D TVUS image was manually chosen by an expert. Thus, we have assumed that the TVUS slice is parallel to the corresponding MR slice. Moreover, after analysing the US-MR registration literature (Chapter 4), we realize that even in order to register US to MR images, methods in the state of the art carry out the registration process with the same strategy. This is a limitation since the standard TVUS and MR imaging techniques used for diagnosing endometriosis

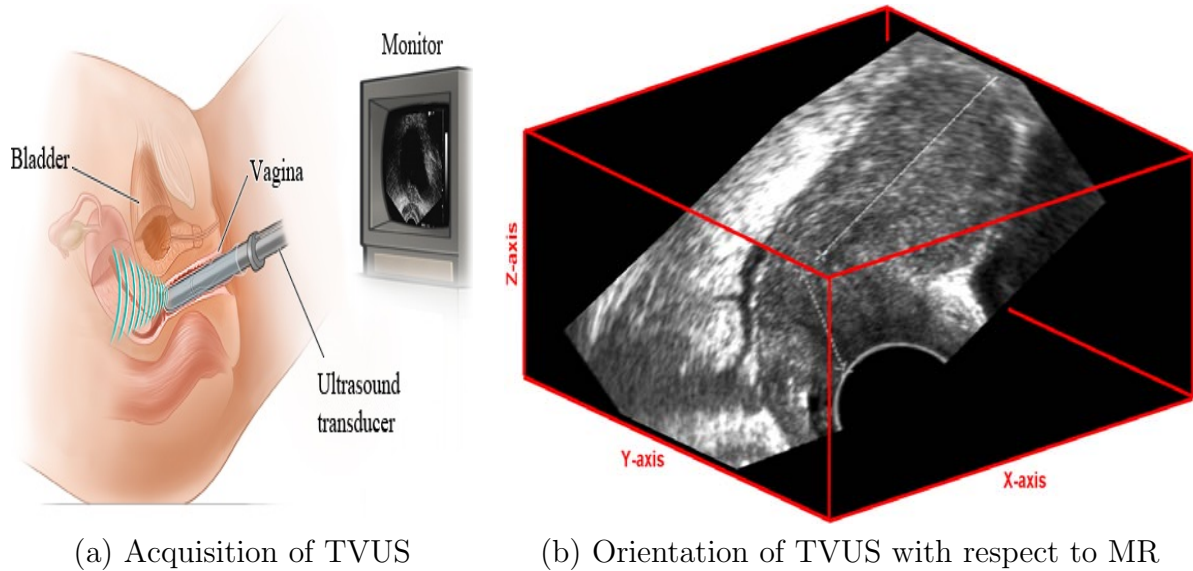


Figure 8-1: An example of showing it is highly impossible to generate a TVUS image to be exactly parallel to one of the MR direction. This example is created to show the concept behind it and indeed in our registration process we do not have any information regarding the exact orientation of TVUS image. (a) is taken from Healthwise<sup>®</sup> Incorporated, [www.healthwise.org](http://www.healthwise.org).

are 2D and 3D, respectively. In other words, a US image generally matches with multiple MR slices so that it is not parallel to any of the MR directions. Hence, this registration problem is intentionally a slice-to-volume registration. To make this statement clear we provide a visual example. In Figure 8-1, it is clear that the TVUS probe can move freely in any direction, thus it is highly impossible to generate a TVUS image to be exactly parallel to one of the MR direction (see Figure 8-1 (b)). Note that in our registration process we do not have the exact orientation of TVUS image because in our setting the probe angle is unknown.

Let us point out again that slice-to-volume registration seeks to find correspondences between a 2D image and a cross-section of volume by a plane or warped surface. This can be considered as an extreme case of 3D/3D registration where one of the images reduces to one slice. As mentioned in Chapter 4, this registration is fundamentally different in comparison to projective registration, since in the later one, one-to-one correspondence between the 2D and 3D data does not exist. Analysing Chapter 4 shows that slice-to-volume registration has not been used to register a 2D

US slice to a 3D MR volume because of yet unsolved technical hurdles. Most methods in the literature rely on an intensity-based similarity measure. However, US-MR registration with an intensity similarity measure usually fails. This is mainly due to the fact that this approach assumes that the images sufficiently correlated which is not the case in our problem (see Chapter 5). Thus, to tackle this registration problem we have chosen to pursue and develop a method based on corresponding geometric features between two images. Dalvi et al. [171] propose a feature-based slice-to-volume approach to rigidly register 2D MR images to 3D MR volumes of the human brain. Their algorithm extracts phase congruency image features that are then matched using classical ICP [135]. However, in order to estimate the deformation between two modalities, establishing point correspondences just at each MR slice are not sufficient due to the large MR inter-slice spacing. To solve this problem, the boundary of organs in each MR slice can be segmented and then a 3D surface may be reconstructed. This fills the MR inter-slice spacing by geometric information. Therefore, we chose to use contour to surface correspondences. We propose a novel variational one-step deformable ICP method that directly registers a set of 2D curves (from TVUS) to a set of corresponding 3D surfaces (from MR). Our method computes a dense deformation field embedding the TVUS domain in the MR coordinate frame while establishing point correspondences automatically. From this registration, any information marked in the TVUS frame such as the boundary of soft tissue organs and endometrial implants may be embedded in the MR frame. This includes the TVUS image itself, and we can thus directly visualize in the MR the deformation induced by the probe at the time TVUS was acquired. Figure 8-2 shows a general framework of our deformable slice-to-volume registration. In this figure, the warped TVUS surface and the location of the endometrial implant are shown in the MR frame. Our contribution in this work are twofold. First, we bring a methodological contribution via the idea of combining TVUS and MR images to both characterize endometrial implants and localize them accurately with respect to one patient’s anatomy. This may improve diagnosis and surgery planning [31]. Second, we bring a technical contribution as a novel one-step ICP derived in a variational framework, and handling multiple curves

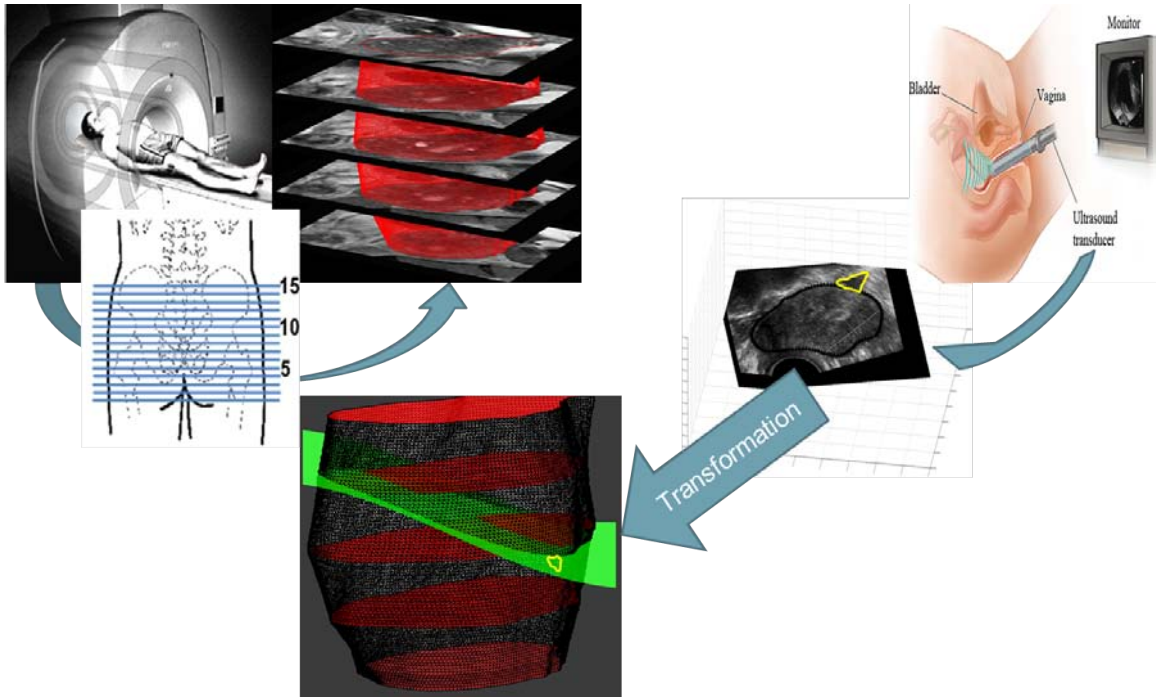


Figure 8-2: The general framework of our deformable slice-to-volume registration method. MR and TVUS imaging techniques are the most common diagnostic tool in the assessment of endometriosis. The MR volumetric data exhibits the patient’s pelvic anatomy, whereas the 2D TVUS image shows the small endometrial implants and its host tissues along with depth of infiltration. After obtaining the images, we must provide the required data to our algorithm which are: 1) segmented endometrial implant and its neighboring organs in 2D TVUS data and 2) 3D models of the corresponding patient’s pelvic organs which are constructed from a set of parallel 2D MR segmented organs. Our method computes a non-linear transformation embedding the 2D TVUS image in the MR coordinate frame while establishing point correspondences automatically.

to surface correspondences, while estimating a deformable transformation. Moreover, one of the main novelties with respect to our previous work is thus the handling of 2D/3D registration. This markedly extends the current literature on ICP. Lastly, an important advantage of our method over point-based methods is that it is extremely mild in terms of operator time.

## 8.2 Registration Procedure

One of the main challenges in TVUS-MR image registration is to correlate TVUS images to MR images. TVUS has relatively poor spatial and tissue contrast resolution compared with MR. Its images have low resolution. It has a small field of view and has a short range of penetration due to the use of a high-frequency transducer. These artifacts as well as multi-modality, multi-dimensionality and soft tissue deformations make TVUS-MR registration challenging, especially in the design of a robust intensity similarity measure. Our solution to this problem uses features. However, the main limitation of this approach is that establishing point correspondences between these two modalities is not possible due to MR inter-slice spaces. Therefore we use the boundary of organs segmented by the radiologist whilst they inspect the images. This is a middle ground choice employed by many 2D/2D and 3D/3D US-MR registration methods to decrease the potential expert error in selecting dense point correspondences and to reduce the interaction time.

We choose TVUS to be our moving image ( $M$ ) and MR to be our reference image ( $F$ ). The soft tissue organs and implants in the TVUS and in the 3D MR reference volume are segmented by an expert. An example is shown in Figure 8-3. Segmentation results in a set of curves  $\gamma$  and a set of surfaces  $S$ , representing the boundary of corresponding organs in both modalities. Let  $\Omega$  be a bounded open set of  $\mathbb{R}^2$  representing the TVUS plane,  $q$  an arbitrary point in  $\gamma \subset \Omega$ , and  $\phi \in W(\Omega, \mathbb{R}^3)$  a 3D dense deformation vector field representing the slice-to-volume registration by embedding the TVUS plane in 3D while deforming it.  $W$  is a Sobolev space of sufficiently smooth vector fields over  $\Omega$  with appropriate boundary conditions. For ease of understanding and simplicity of derivation, we first assume that  $\gamma$  includes only one curve and  $S$  contains only one surface as in the example of Figure 8-3.

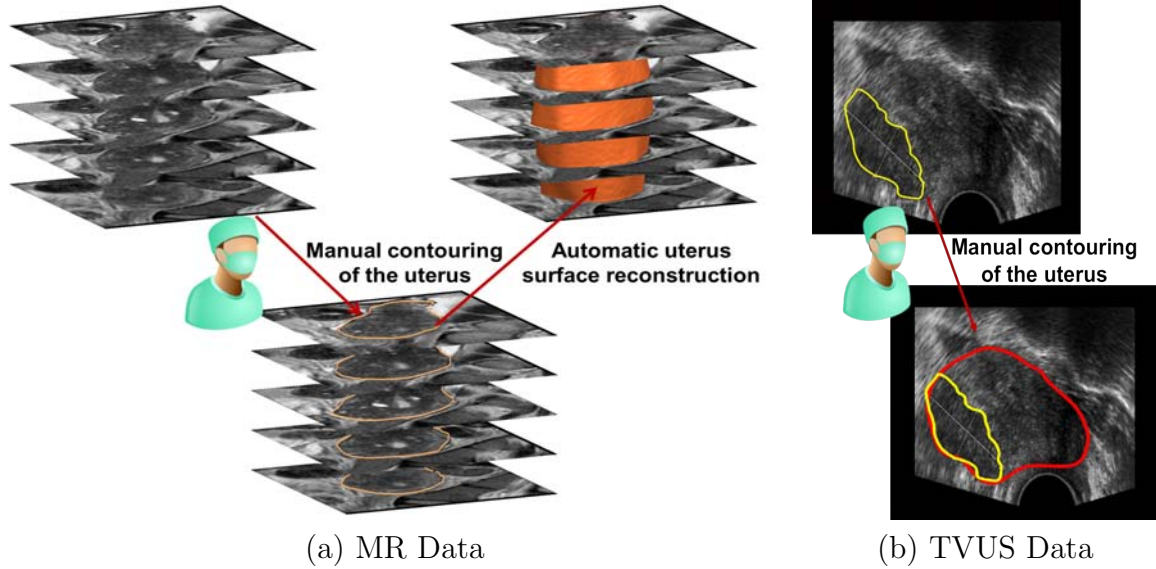


Figure 8-3: An example of generating input data for our registration process. (a) shows the MR volume and uterus surface reconstructed from 5 parallel 2D MR curves. (b) is the TVUS image with segmented uterus (red curve) and endometrial implant (yellow curve).

### 8.2.1 A Variational Formulation for Two-Step ICP

Feature-based slice-to-volume registration is a difficult problem, especially for non-linear deformation. It is well-known that without prior knowledge the problem is ill-posed. As prior, we use local mean curvature regularizer. By doing so, the resulting displacement vector field does not diverge from our expectations. In other words, we impose a bounded Laplacian vector field to insure that the registration outside  $\gamma$  would be estimated by interpolation in a way that the overall transformation smoothly maps the moving image into reference image. Therefore, here, the goal is to find a smooth deformation  $\phi$  that maps points, in any small neighbouring, uniformly.

To establish point correspondences and estimate deformation between a curve and a surface, we employ a variational formulation of the two inner steps of ICP with mean curvature regularization:

step 1: **closest point computation**

$$\zeta(q) = \operatorname{argmin}_{Q \in S} d^2(Q, \phi(q)) \quad (8.1)$$

This implicitly defines  $\zeta \in C^1(\gamma, S)$ , a function that computes the closest-point  $\zeta(q)$  on  $S$ .

step 2: **deformation estimation**

$$\phi = \operatorname{argmin}_{\phi \in W} \underbrace{\lambda \int_{\gamma} d^2(\phi, \zeta(q)) dq}_{\text{data term}} + (1 - \lambda) \underbrace{\int_{\Omega} \|\Delta\phi\|_2^2 dX}_{\text{regularization term}} \quad (8.2)$$

where  $\Delta$  is the Laplacian operator and  $\lambda \in [0, 1]$  is a smoothing parameter.

As discussed in previous chapter, since both steps in ICP must minimize the error, it is guaranteed to stuck in a local minimum [138, 150, 208]. Generally in step 1, ICP tries to establish binary point correspondences using the nearest-neighbour heuristic. However, using this method for establishing correspondences makes it more vulnerable to local minima [150]. In order to improve the convergence rate, we propose to merge the two steps into a single step. Note that merging two steps into one would result in a single minimization that would improve the convergence rate [208]. To achieve this, we employ a Euclidian DT.

## 8.2.2 A Variational Formulation in One-Step Using Distance Transform

We now present our formulation of the registration problem by combining the two steps of the classical formulation in a single step. Combining Equation (8.1) with (8.2) yields to:

$$\phi = \operatorname{argmin}_{\phi \in W} \lambda \int_{\gamma} d^2 \left( \phi, \operatorname{argmin}_{Q \in S} d^2(Q, \phi) \right) dq + (1 - \lambda) \int_{\Omega} \|\Delta\phi\|_2^2 dX \quad (8.3)$$

we know that  $d^2 \left( \phi, \operatorname{argmin}_{Q \in S} d^2(Q, \phi) \right) = \min_{Q \in S} d^2(Q, \phi)$ . This means that the cost function depends on the distance to the closest point but not on the closest point itself. This permits us to reformulate Equation (8.3) as:

$$\phi = \operatorname{argmin}_{\phi \in W} \lambda \int_{\gamma} \min_{Q \in S} d^2(Q, \phi) dq + (1 - \lambda) \int_{\Omega} \|\Delta\phi\|_2^2 dX \quad (8.4)$$

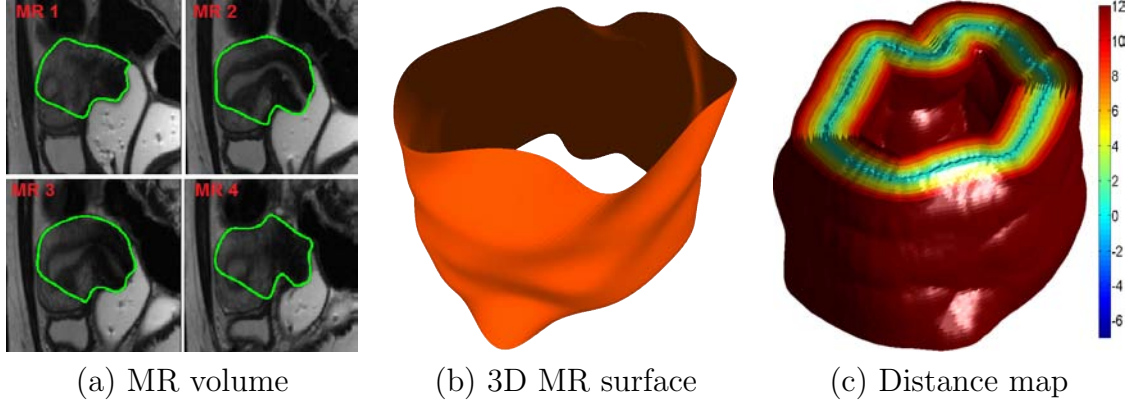


Figure 8-4: An example of generating a distance map. (a) is the MR volume with segmented uterus (green curve). (b) is the 3D uterus surface reconstructed from 4 parallel 2D MR curves. (c) is the distance map which is generated from the 3D MR surface. We use the distance map to solve ICP efficiently.

We see that the data term now includes a DT ( $D$ ), as  $D \circ \phi = \min_{Q \in S} d^2(Q, \phi)$  by definition. The distance map algorithms essentially assign to every voxel (grid point) the distance to the nearest point. This is extremely efficient, fast and simple. Figure 8-4 is an example of the distance map which is generated from a 3D MR surface. We can now substitute  $D$  in Equation (8.4).

$$\phi = \operatorname{argmin}_{\phi \in W} \underbrace{\lambda \int_{\gamma} (D \circ \phi)^2 dq + (1 - \lambda) \int_{\Omega} \|\Delta \phi\|_2^2 dX}_{E[\phi]} \quad (8.5)$$

Equation (8.5) shows a variational problem with  $E$  as cost functional. The next fundamental task is to estimate the functional form of  $\phi$  using calculus of variation.

### 8.2.2.1 Euler-Lagrange Equation and Numerical Approximation

A function  $\phi$  that minimizes  $E$  must fulfill the EL differential equation. Many different numerical optimization algorithms [104, 105] may then be applied to estimate solution for the resulting nonlinear equation. In Equation (8.5), the data term places constraints on the deformation field  $\phi$  at the curve location. To make it more general and to permit its formulation as an EL equation we use an index function  $\delta_{\gamma}$ , with  $\delta_{\gamma} : \Omega \rightarrow \{0, 1\}$ ,  $\delta_{\gamma}(X) = 1$  if  $X \in \gamma$  and 0 otherwise. We rewrite the energy

functional of Equation (8.5) as:

$$E[\phi] = \int_{\Omega} (\lambda \delta_{\gamma} (D \circ \phi)^2 + (1 - \lambda) \|\Delta \phi\|_2^2) dX \quad (8.6)$$

Let  $\phi^0$  be an initial estimate. We define an additive update rule:

$$\phi^{k+1} = \phi^k + U \quad (8.7)$$

where  $U \in W$  is a 3D dense displacement vector field. We restate our problem as:

$$\min_U E[\phi^k + U] \quad (8.8)$$

By substituting Equation (8.6) into Equation (8.8), we obtain:

$$E[\phi^k + U] = \int_{\Omega} \left( \lambda \delta_{\gamma} (D \circ (\phi^k + U))^2 + (1 - \lambda) \left( \|\Delta U\|_2^2 + \|\Delta \phi^k\|_2^2 \right) \right) dX \quad (8.9)$$

The distance transform  $D$  is nonlinear and can be approximated by its first order Taylor expansion around  $\phi^k$ :

$$E[\phi^k + U] = \int_{\Omega} \left( \lambda \delta_{\gamma} (D \circ \phi^k + (\nabla D \circ \phi^k) U)^2 + (1 - \lambda) \left( \|\Delta U\|_2^2 + \|\Delta \phi^k\|_2^2 \right) \right) dX \quad (8.10)$$

where  $\nabla = [\frac{\partial}{\partial x}, \frac{\partial}{\partial y}, \frac{\partial}{\partial z}]$ . A function  $U$  that minimizes Equation (8.8) must fulfill its EL equation. This is written as a system of three fourth order elliptic PDEs represented by a  $2 \times 2$  symmetric matrix equation:

$$\mu \int_{\gamma} (D \circ \phi^k + (\nabla D \circ \phi^k) U) (\nabla D \circ \phi^k) dq + \left( \frac{\partial^4 U}{\partial X^4} \right) = 0 \quad (8.11)$$

where  $\mu = \frac{\lambda}{1-\lambda}$ . To solve the Equation (8.11) numerically, we discretize the curve  $\gamma$  in  $N$  points  $q_1, \dots, q_N$  and  $\Omega$  on the rectangular pixel grid. Note that  $\delta_q(X) = 1$  if  $\exists j \in 1, \dots, N$  such that  $X = q_j$  and 0 otherwise. We consider the unknown function  $U = [u_1, u_2, u_3]^{\top}$  on a rectangular pixel grid. Therefore, the discretization of

Equation (8.11) leads to a system of three PDEs:

$$\begin{aligned} & \mu\delta_q(X) \left( \left( D(\phi^k(X)) + D_x(\phi^k(X))u_1(X) + D_y(\phi^k(X))u_2(X) \right. \right. \\ & \left. \left. + D_z(\phi^k(X))u_3(X) \right) D_\ell(\phi^k(X)) \right) + \left( \frac{\partial^4 U}{\partial x^4} + \frac{\partial^4 U}{\partial y^4} \right) = 0 \quad \text{for } \ell \in \{x, y, z\} \end{aligned} \quad (8.12)$$

where  $D_\ell$  is the derivative of  $D$  with respect to  $\ell \in \{x, y, z\}$ . To solve the PDEs, we use a finite difference scheme with second-order boundary condition ( $\Delta U = 0$ ). This leads to a large but sparse linear system that can be solved by Successive Over-Relaxation (SOR) [89]. The advantages of the iterative solvers like the SOR method are twofold. First, iterative solvers generally perform very well in discarding the higher frequency parts of the error within the first iterations. This behaviour is reflected in a good initial convergence rate [209]. Second, they are suitable for solving large linear equations [210]. The discretization of Equation (8.12) leads to:

$$\begin{aligned} u_{1,h,w}^{t+1} &= \beta u_{1,h,w}^t - A_1 \left[ \mu\delta_q(X) \left( D(\phi^k(X)) \frac{\partial D}{\partial x}(\phi^k(X)) \right) + C_1 u_{2,h,w}^t + C_2 u_{3,h,w}^t \right. \\ & \quad + (u_{1,h,w-2}^{t+1} - 4u_{1,h,w-1}^{t+1} - 4u_{1,h+1,w}^{t+1} + u_{1,h+2,w}^{t+1}) \\ & \quad \left. + (u_{1,h,w+2}^t - 4u_{1,h,w+1}^t - 4u_{1,h-1,w}^t + u_{1,h-2,w}^t) \right] \\ u_{2,h,w}^{t+1} &= \beta u_{2,h,w}^t - A_2 \left[ \mu\delta_q(X) \left( D(\phi^k(X)) \frac{\partial D}{\partial y}(\phi^k(X)) \right) + C_1 u_{1,h,w}^t + C_3 u_{3,h,w}^t \right. \\ & \quad + (u_{2,h,w-2}^{t+1} - 4u_{2,h,w-1}^{t+1} - 4u_{2,h+1,w}^{t+1} + u_{2,h+2,w}^{t+1}) \\ & \quad \left. + (u_{2,h,w+2}^t - 4u_{2,h,w+1}^t - 4u_{2,h-1,w}^t + u_{2,h-2,w}^t) \right] \\ u_{3,h,w}^{t+1} &= \beta u_{3,h,w}^t - A_3 \left[ \mu\delta_q(X) \left( D(\phi^k(X)) \frac{\partial D}{\partial z}(\phi^k(X)) \right) + C_2 u_{1,h,w}^t + C_3 u_{2,h,w}^t \right. \\ & \quad + (u_{3,h,w-2}^{t+1} - 4u_{3,h,w-1}^{t+1} - 4u_{3,h+1,w}^{t+1} + u_{3,h+2,w}^{t+1}) \\ & \quad \left. + (u_{3,h,w+2}^t - 4u_{3,h,w+1}^t - 4u_{3,h-1,w}^t + u_{3,h-2,w}^t) \right] \end{aligned} \quad (8.13)$$

---

**Algorithm 8.1** Proposed Algorithm Pseudo-Code
 

---

```

1: Input: A point cloud from MR ( $Q$ ) & a set of 2D points from TVUS ( $q$ )
2: Result: Warped surface ( $\phi$ ) % Grid of points  $h_{max} \times w_{max}$  to represent  $\phi$ 
3: Initialization:
4:  $k \leftarrow 0$  % Iteration counter
5:  $\iota \leftarrow 10$  % Number of planarity constrained iterations
6:  $q^k \leftarrow q + \phi^0$  %  $q$  embedded in the 3D space;  $\phi^0$  is an initialization of  $\phi$ 
7: Compute  $D$  and  $\nabla D$  from  $Q$  %  $D$  and  $\nabla D$  are used in Equation (8.13)
8: while  $\|\nabla\phi\| > \varepsilon$  do
9:   Compute  $U$  by iterating Equation (8.13)
10:   $q^{k+1} \leftarrow q^k + \delta_{q^k} U$  % Update the TVUS space curve
11:   $\phi^{k+1} \leftarrow \phi^k + U$  % Update the TVUS surface
12:  while  $k < \iota$  do
13:     $\Pi \leftarrow$  least-squares plane projection from  $q^{k+1}$ 
14:     $q^{k+1} \leftarrow \Pi(q^{k+1})$  % Flatten the TVUS space curve
15:     $\phi^{k+1} \leftarrow \Pi(\phi^{k+1})$  % Flatten the TVUS surface
16:  end while
17:   $k \leftarrow k + 1$ 
18: end while

```

---

where  $A_1 = \frac{\alpha}{12 + \mu\delta_q(X)\left(\frac{\partial D}{\partial x}(\phi^k(X))\right)^2}$ ,  $A_2 = \frac{\alpha}{12 + \mu\delta_q(X)\left(\frac{\partial D}{\partial y}(\phi^k(X))\right)^2}$ ,  $A_3 = \frac{\alpha}{12 + \mu\delta_q(X)\left(\frac{\partial D}{\partial z}(\phi^k(X))\right)^2}$ ,  $C_1 = \mu\delta_q(X)\left(\frac{\partial D}{\partial y}(\phi^k(X))\frac{\partial D}{\partial x}(\phi^k(X))\right)$ ,  $C_2 = \mu\delta_q(X)\left(\frac{\partial D}{\partial z}(\phi^k(X))\frac{\partial D}{\partial x}(\phi^k(X))\right)$ ,  $C_3 = \mu\delta_q(X)\left(\frac{\partial D}{\partial y}(\phi^k(X))\frac{\partial D}{\partial z}(\phi^k(X))\right)$ ,  $t \in \mathbb{N}$  is the SOR iteration number,  $h = 1, \dots, h_{max}$ ,  $w = 1, \dots, w_{max}$ ,  $h_{max}$  and  $w_{max}$  are the height and width of  $M$  respectively,  $\beta = 1 - \alpha$  and  $\alpha$  is the relaxation factor. The displacement vector field obtained from Equation (8.13) is used to find the intersection of the MR volume by a warped TVUS surface and to localize an endometrial implant. Note that to make our algorithm more stable, we use an a priori constraint. This is to avoid convergence to a spiky surface which would harm registration. In order to solve this problem, we automatically extract a plane from the TVUS point sets for the first few iterations. To achieve this, we find the closest plane to the TVUS point set in the least squares sense [211]. This choice puts constraints on the warped surface by flattening the TVUS free-form surface. Applying this strong constraint on the original TVUS surface improves the convergence rate of our algorithm. Note that after a few iterations, we relax this constraint. This is due to the fact that after a few iterations we approach the global solution, so the surface has only low frequency features and no longer interferes with

convergence to the correct solution. The pseudo code of our method is given in Algorithm 8.1. In Algorithm 8.1,  $\varepsilon$  is prespecified threshold and set to be  $10^{-5}$ .

### 8.2.2.2 Handling Multiple Surfaces

We now extend our framework to handle multiple pairs of curves and surfaces. In this case, we have  $m$  curves  $\gamma_1, \dots, \gamma_m$  and a set of  $m$  corresponding 3D surfaces  $S_1, \dots, S_m$ . We use each surface  $S_i$  to compute a Euclidean distance transform  $D^i$ . By summing over all curve/surface pairs, Equation (8.6) becomes:

$$E[\phi] = \sum_{i=1}^m \int_{\Omega} \left( \lambda \delta_{\gamma_i} (D^i \circ \phi)^2 + (1 - \lambda) \|\Delta \phi\|_2^2 \right) dX \quad (8.14)$$

where  $\delta_{\gamma_i}(X) = 1$  if  $X \in \gamma_i$  and 0 otherwise. Using EL we obtain a system of three fourth order elliptic PDEs:

$$\mu \sum_{i=1}^m \int_{\gamma_i} (D^i \circ \phi^k + (\nabla D^i \circ \phi^k) U) (\nabla D^i \circ \phi^k) dq + \left( \frac{\partial^4 U}{\partial X^4} \right) = 0 \quad (8.15)$$

Equation (7.15) is discretized by means of a finite difference scheme and leads to a sparse linear system that is solved using SOR, and eventually leading to a very similar pattern as Algorithm 8.1.

## 8.3 Experimental Results

### 8.3.1 Material and Clinical Motivations

The study is carried out on ten patients who have small endometrial implants in the pelvic area. For each patient, TVUS and MR imaging are used to examine their pelvic organs. In our experiments, small implants are detectable with TVUS but difficult to identify with MR. The procedure of collecting data is as follows: first, a TVUS image which includes both endometrial implant and its neighbouring organs is selected for each patient by an expert. Then, 4-5 2D MR slices from the MR volume that closely correspond to the moving 2D TVUS image are chosen by an expert. MR images used for the experiments have an average size of  $400 \times 400 \times 5$  with a voxel resolution of  $0.5 \times 0.5 \times 5 \text{ mm}^3$ . In our experiments, we assume that the TVUS image resembles the middle MR slice of the MR volume. It is, therefore, reasonable to assume that the TVUS slice is parallel to the corresponding MR slice in the first iteration of our algorithm. The soft tissue organs (i.e. bladder, uterus, ovary, rectum) and the implant in the TVUS slice and in the MR slices are segmented by an expert. Then, we use the method proposed by Kels et al. [212] to reconstruct a 3D surface from a set of 2D MR contours. An example of the reconstruction process is shown in Figure 8-5.

In order to be clear why we chose just 4-5 MR slices and not more images, we do indeed need a detailed explanation of the procedure for the diagnosis and treatment of Endometriosis. To evaluate women suspected of having endometriosis, first, ultrasonographic examination is performed. Then, MR imaging is performed in order to provide superior anatomic detail and better defines abnormalities found using ultrasonography. After preoperative imaging examination, a pelvic radiologist must interpret the images and write a report for the gynecologic surgeon. This report must indicate the size, shape, and location of the endometriosis implant and it must highlight the nearby organ(s). Note that the information about the location of endometriosis is not very accurate as ultrasound images do not provide anatomic detail. Therefore, for this purpose, the pelvic radiologist must visually correlate TVUS with each MR images which is not an easy task and more precisely not an accurate way to

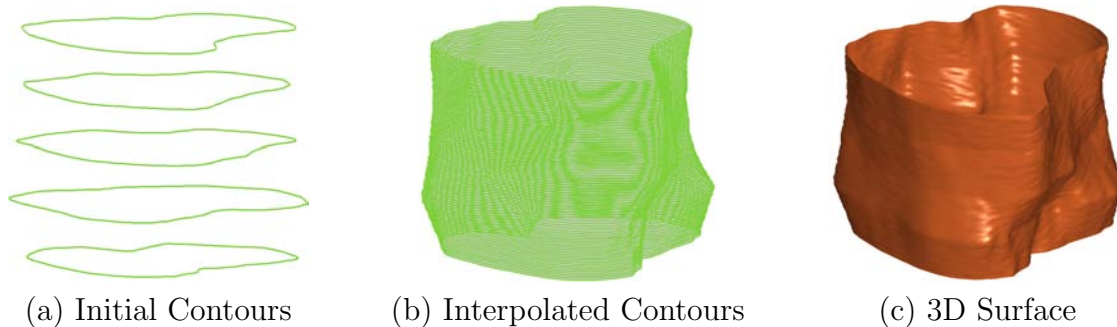


Figure 8-5: Reconstruction of the uterus from parallel 2D MR contours.

align them. In addition to this report, a TVUS image in which the implant is marked as well as 4 to 5 MR slices which clearly show implant’s neighbouring organ(s) must be given to the surgeon. Note that, the reason that just one TVUS is provided to the surgeon is that at the time ultrasonographic examination is performed there is no clues about the location of endometriosis and the radiologist move the probe in any direction in order to find it. This factor along with small field of view of the ultrasound scanners become the main reason that most of the patients’ TVUS images do not include both the implant and its neighbouring organs. Commonly, just one image has this property. Then appropriate pre-surgical planning in accordance with provided data must be made by the surgeon. However, interpreting the preoperative medical images is not an easy task for many surgeons. The results of this difficulty may cause of wrong pre-surgical planning which leads to recurrence or starting the surgery far from the place that the implant is located. Therefore, to ease and improve the pre-surgical planning, we propose to register the available data.

### 8.3.2 Results and Discussion

We evaluate the proposed method’s performance in comparison with two-step deformable ICP. We demonstrate the accuracy of the proposed method by quantitative and qualitative tests on semi-synthetic and real world data sets. The true point correspondences are not available for real patient data sets. However, we assess the results with quantitative and qualitative evaluations on semi-synthetic data sets, generated to faithfully reproduce patient data features. We conduct more than a thousand exper-

iments using semi-synthetic data with artificial deformations to test various aspects of the methods. The results are very informative. The experiments on semi-synthetic data emulate realistic acquisition situations and reveal the expected registration error. We calculate three different quantitative error measures to validate the results. To demonstrate the applicability in real applications, we also conduct ten tests on patient data. To show the generality of our method, we apply it to four different soft tissue organs including the bladder, uterus, rectum, and ovary.

### 8.3.2.1 Tests on Semi-Synthetic Data

**Quantitative error measures.** The first measure is mean square distance between the  $N$  transformed moving points and the corresponding ground truth points. This measure is called the MSE. Since the MSE does not evaluate the shape of the 2D curves embedded in the 3D space, we used another error measure which does not take the position into account, but only assesses the organ’s shape. Being able to compare the curve after registration with the corresponding ground truth curve is essential to verify registration accuracy. To compare curves, we must first find an appropriate representation. To achieve this, the 2D space curves are simply parameterized by their arc-length and 15 points are sampled uniformly. Then, in order to evaluate the similarity between curve pairs, we compare the angle formed by adjacent points. This measure is known as the Shape Error (SE). A low value of SE means that the curve shapes after registration are very similar even if misplaced. Finally, to quantify the local registration error, we use the TRE. The target points used in our experiments are centroids and 10 boundary points which are not used to estimate deformation. A low TRE value shows good local registration accuracy.

**Generate semi-synthetic data.** We create a test collection of 11 different 3D surfaces with 10 degrees of deformation and 11 different intersection curves containing approximately 1200 data in total. To generate semi-synthetic data, the boundary of soft tissue organs such as the bladder, uterus, ovary, and rectum are segmented from five MR slices. Then, we use Kels et al. [212] to reconstruct 3D surfaces from the 2D segmented contours. The reconstructed 3D surfaces are deformed using advec-

tion [207]. In this method, every single point on the surface has a certain value of potential vorticity. The points are transported by their local displacement field on the surface. As a consequence, the surface can be deformed in complicated manners. The advection method is based on Lagrangian calculation. The advection equation is a hyperbolic PDE that governs the motion of the 3D surface ( $S$ ) as it is transported by a known displacement vector field  $U$ :

$$\frac{\partial S}{\partial t} + U \cdot (\nabla S) = 0 \quad (8.16)$$

where  $\frac{\partial}{\partial t}$  is derivative with respect to time. In our experiments,  $U$  is randomly generated. The surface is deformed through increasingly larger degrees of deformation. The rate of deformation varies between 4% and 40%. Moreover, since the TVUS probe can move freely in any direction, it is also important to cut different views of the deformed surface. Therefore, various intersection curves are obtained at eleven different cutting angles in the range between  $0^\circ$  and  $20^\circ$ . An intersection curve is here defined as the intersection of a plane with a 3D surface. The plan's angle is known as the cutting angle. We generate a wide range of curves by tilting the plane. These comprehensive simulations are used to validate our method and test its robustness to organ deformation and probe orientation.

**Results and discussion.** We evaluate the proposed method against deformable two-step ICP. In two-step ICP, the point correspondence problem is solved by the nearest neighbour heuristic which results in significantly poorer performance than the proposed method. To demonstrate the idea, we test both two-step ICP and our method on the same examples. Since we map the warped free-form surface to the planar domain in one-step ICP for 10 iterations, we use the same constraint for two-step ICP.

The qualitative results are shown in Figure 8-6, 8-7, and 8-8. In these three figures, we use a single 3D uterus surface with 4%, 20%, and 40% average deformation, respectively. We use two surfaces, one is the deformed version (Figure 8-6, 8-7, and 8-8 (b)) of the other (Figure 8-6, 8-7, and 8-8 (a)). We also generate three different curves by tilting the cutting plane at each deformation level. The cutting angles are

0° (first row of Figure 8-6, 8-7, and 8-8 (b)), 10° (second row of Figure 8-6, 8-7, and 8-8 (b)), and 20° (third row of Figure 8-6, 8-7, and 8-8 (b)). Then, we assume that these intersection curves are parallel to the middle intersection curve of the original 3D surface (see the red curves in Figure 8-6, 8-7, and 8-8 (a)). This assumption is made to keep the system similar to real world data. In these figures, the green curves are the ground truth solutions.

In order to assess the behaviour of the methods in a quantitative way, we use all the semi-synthetic data sets and measure various distances. The results of MSE, SE, and TRE are depicted in Figure 8-9 and 8-10 (a), (b), and (c), respectively. Figure 8-9 demonstrates one- and two-step ICP performances for 4% (first row of Figure 8-9), 20% (second row of Figure 8-9), and 40% (third row of Figure 8-9) average deformation. In this figure, the slant level varies from 0° to 20° by step of 2°. Figure 8-10 shows one- and two-step ICP registration accuracy for 0° (first row of Figure 8-10), 10° (second row of Figure 8-10), and 20° (third row of Figure 8-10) cutting angle. In this figure, the rate of deformation varies from 0% to 40% by steps of 4%. In Figure 8-9 and 8-10, average error and standard deviations are shown.

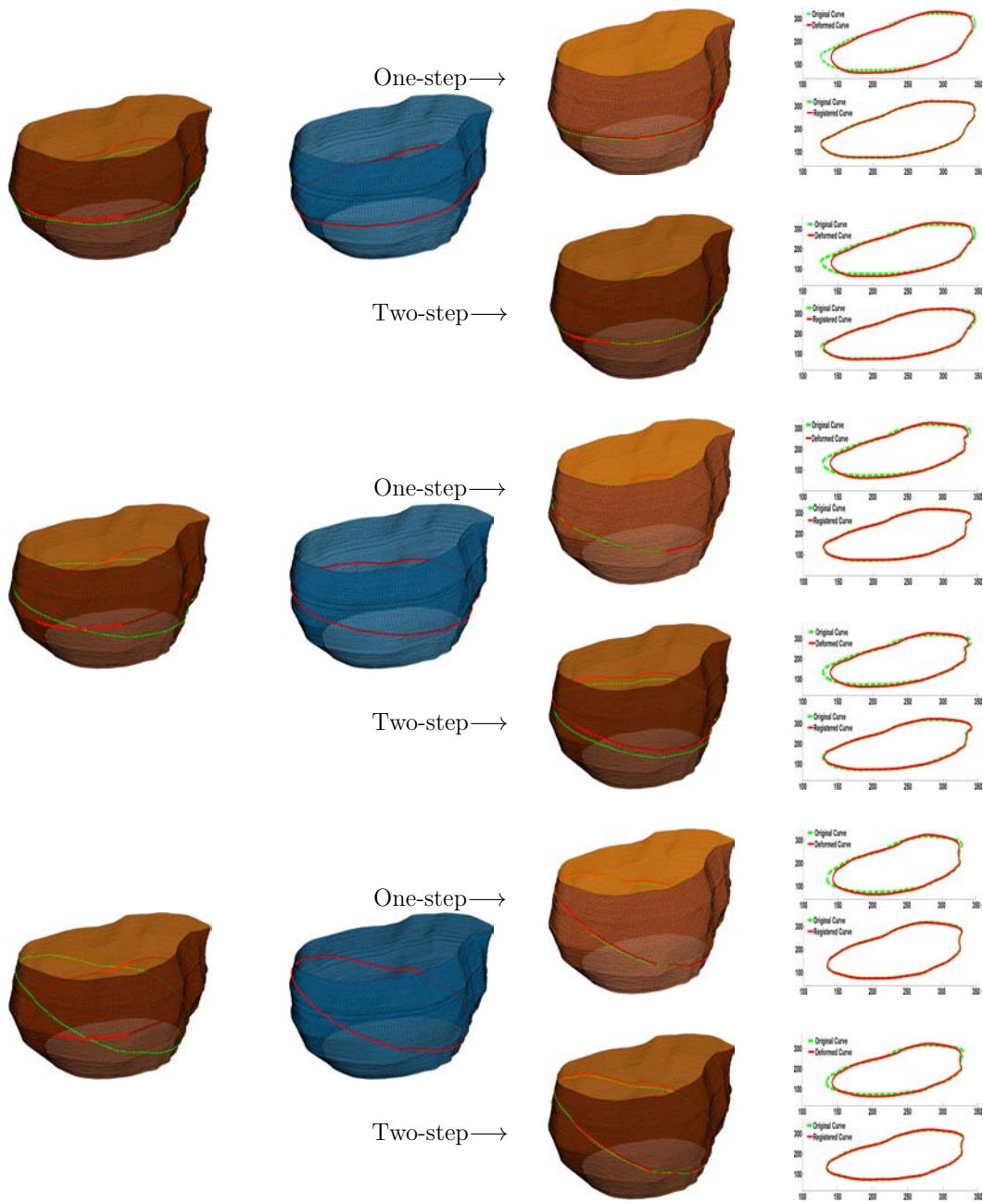
In Figure 8-6, we deform a 3D uterus surface with 4% degree of deformation. Figure 8-6 (b) shows the deformed 3D surface with 3 different intersection curves whose each row belongs to each intersection curve. We then use both one-step and two-step ICP to find the best transformation to align the template set onto the ground truth set. The registration results are depicted in Figure 8-6 (c). In Figure 8-6 (a) and (c), the green curves are ground truth. At this deformation level, we can visually observe that both one-step and two-step ICP provide good results. This is visually demonstrated by Figure 8-6 (d) in which we show a 2D view (X-Y view) of the curves before and after registration. Moreover, to assess the behaviour of the method in a quantitative way, we use all the semi-synthetic data sets with 4% average deformation and calculate errors. The results are shown in the first row of Figure 8-9. The MSE, SE, and TRE show that our method converges to a better solution at a low level of deformation. The MSE and TRE indicated that the two-step ICP gets trapped in a local minimum which leads to a low registration accuracy. The two step ICP becomes

less accurate as the initial solution is further from the ground truth. However, by comparing the SE, it is easy to see that both methods have very similar shapes to their corresponding ground truth. Consequently, from these figures we can conclude that both methods provide good results at this deformation level.

In Figure 8-7 we make the registration problem more challenging. We deform a 3D uterus surface with 20% average deformation. The two-step ICP shows poorer performance and is stuck in a local minimum. In this figure, we can see that our method also gets affected by high cutting angles. The MSE, SE, and TRE in the second row of the Figure 8-9 show that our method converges to a better solution at 20% average deformation. The MSE and TRE indicate that the two-step ICP finds wrong correspondences which result in a poorer registration accuracy. This problem gets much more serious as the initial solution is further from the ground truth. By comparing the SE, it is easy to see that the curves after registration by two-step ICP do not have similar shapes to their corresponding ground truth. Consequently, from these figures we can conclude that two-step ICP has much poorer performance as compared to the proposed one-step ICP.

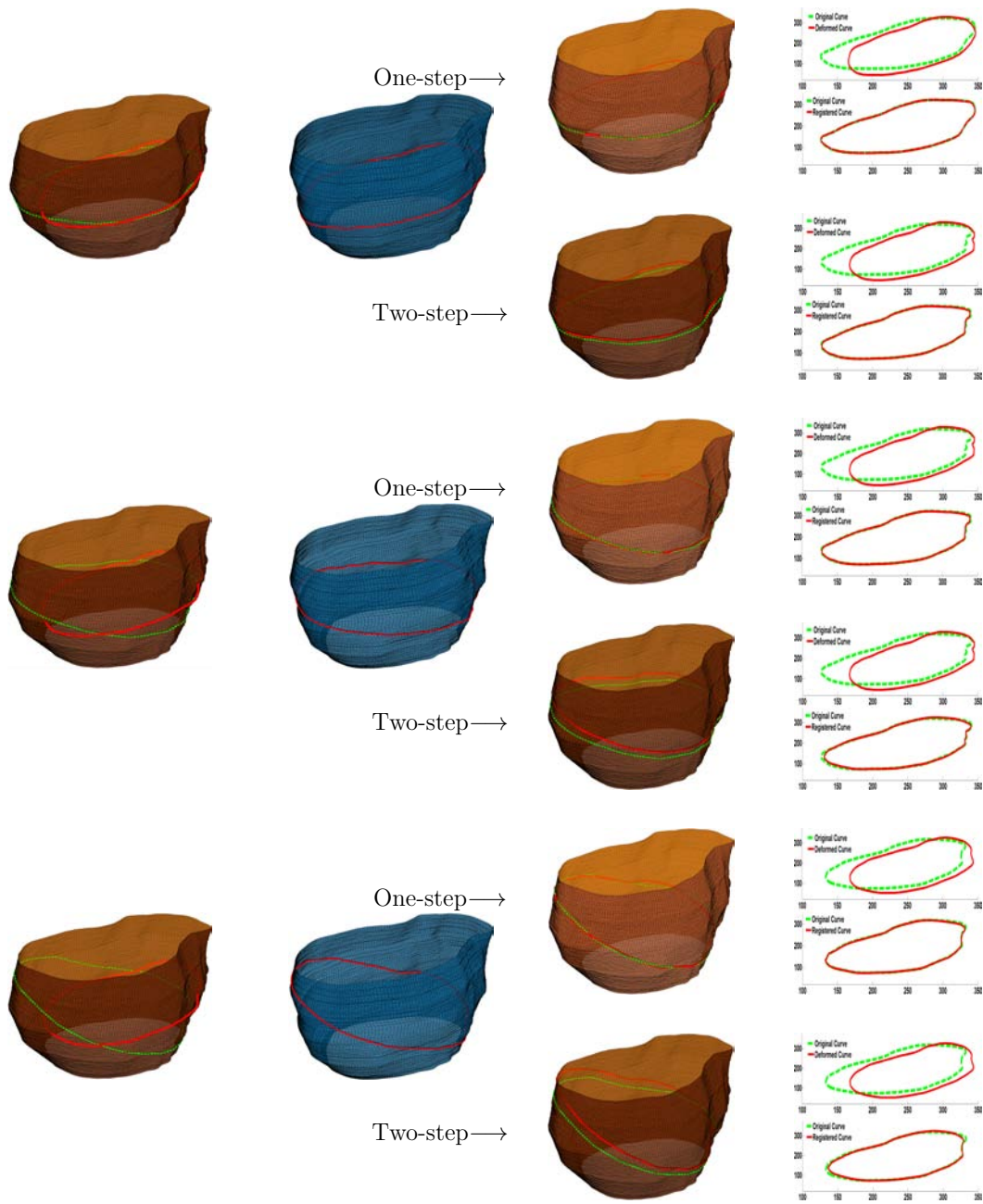
To make the problem much more challenging, we use a 3D uterus surface with 40% rate of deformation. The results are depicted in Figure 8-8. The two-step ICP shows very poor performance. The third row of the Figure 8-9 shows that our method still converges to a acceptable solution at 40% average deformation. The MSE, SE, and TRE indicate that the two-step ICP fails at this level of deformation. Consequently, from these figures we can conclude that two-step ICP fails whereas the proposed method still provides acceptable registration accuracy.

In many cases, we observe that the warped intersection curves in one-step ICP are very close to the ground truth and that the method quickly converges to the optimum. In comparison, the warped intersection curves in two-step ICP gets trapped in local minima and mainly fail. The main reason of failure in this method is because of large initial errors. In addition, failure may happen after the planar constraint is relaxed. Therefore, the warped contour may contain high frequency bumps which results in misplacing correspondences, and the registration process fails. Figure 8-8 shows an



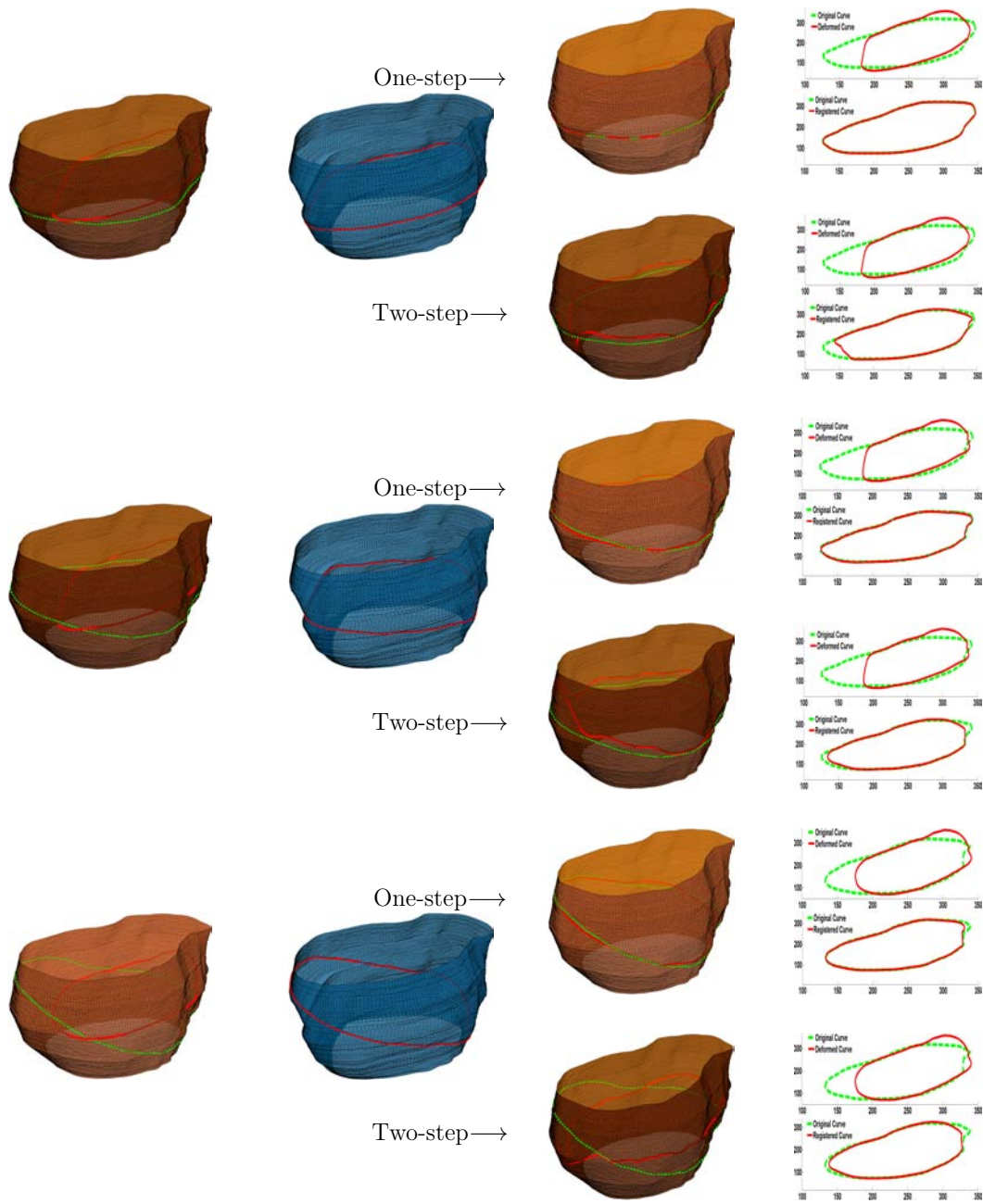
(a) Original 3D Surface (b) Deformed 3D Surface (c) Result (d) X-Y View of Curves

Figure 8-6: Registration results for the proposed method and two-step ICP. The average deformation is 4%. (a): shows the reference 3D uterus surface with the ground truth (green curves) and initial moving (red curves) curves. (b): shows deformed 3D surface with 3 different intersection curves which are obtained at  $0^\circ$ ,  $10^\circ$  and  $20^\circ$  cutting angles (red curves). (c): shows registration results. (d): shows the 2D view of the curves before and after registration.



(a) Original 3D Surface (b) Deformed 3D Surface (c) Result (d) X-Y View of Curves

Figure 8-7: Registration results for the proposed method and two-step ICP. The average deformation is 20%. (a): shows the reference 3D uterus surface with the ground truth (green curves) and initial moving (red curves) curves. (b): shows deformed 3D surface with 3 different intersection curves which are obtained at  $0^\circ$ ,  $10^\circ$  and  $20^\circ$  cutting angles (red curves). (c): shows registration results. (d): shows the 2D view of the curves before and after registration.



(a) Original 3D Surface (b) Deformed 3D Surface (c) Result (d) X-Y View of Curves

Figure 8-8: Registration results for the proposed method and two-step ICP. The average deformation is 40%. (a): shows the reference 3D uterus surface with the ground truth (green curves) and initial moving (red curves) curves. (b): shows deformed 3D surface with 3 different intersection curves which are obtained at  $0^\circ$ ,  $10^\circ$  and  $20^\circ$  cutting angles (red curves). (c): shows registration results. (d): shows the 2D view of the curves before and after registration.

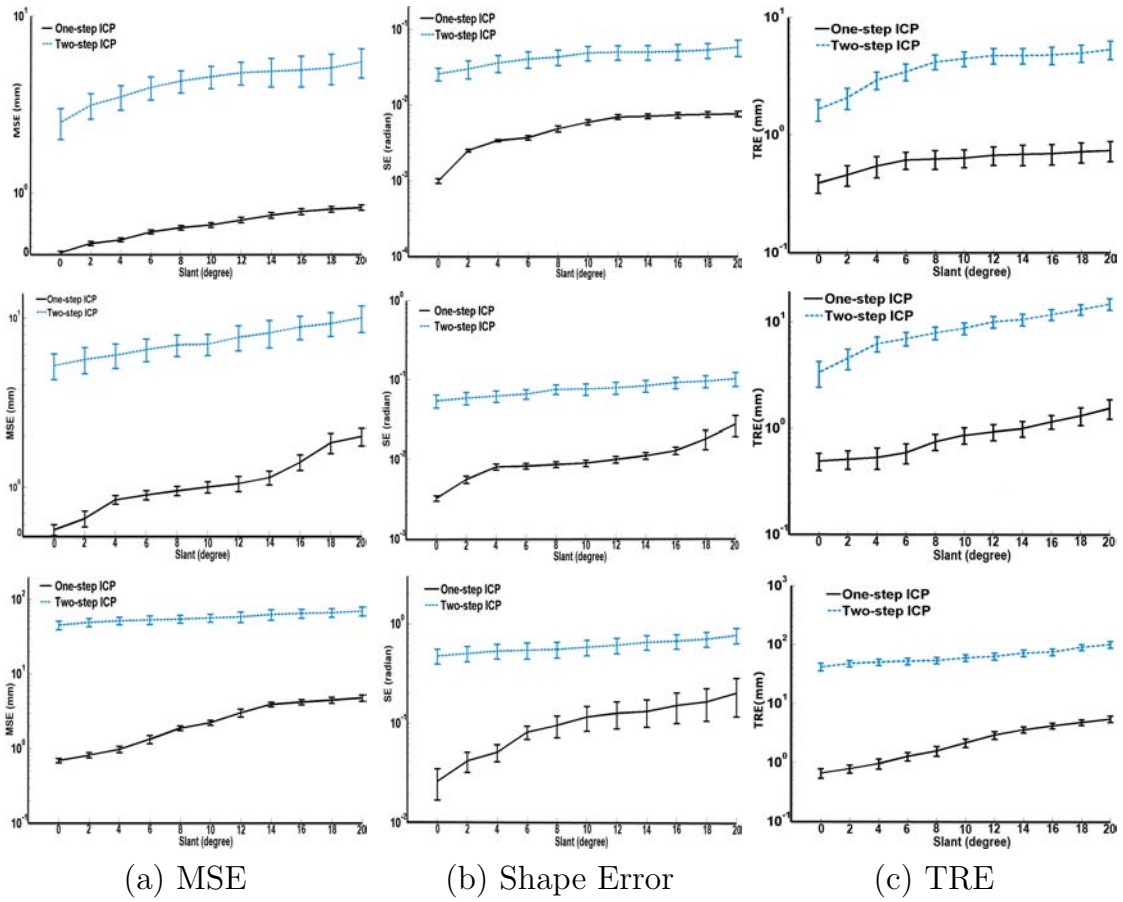


Figure 8-9: Comparison of the proposed method with two-step ICP on semi-synthetic data sets with respect to cutting angle (slant). The results for 4%, 20%, and 40% deformations are shown at each row.

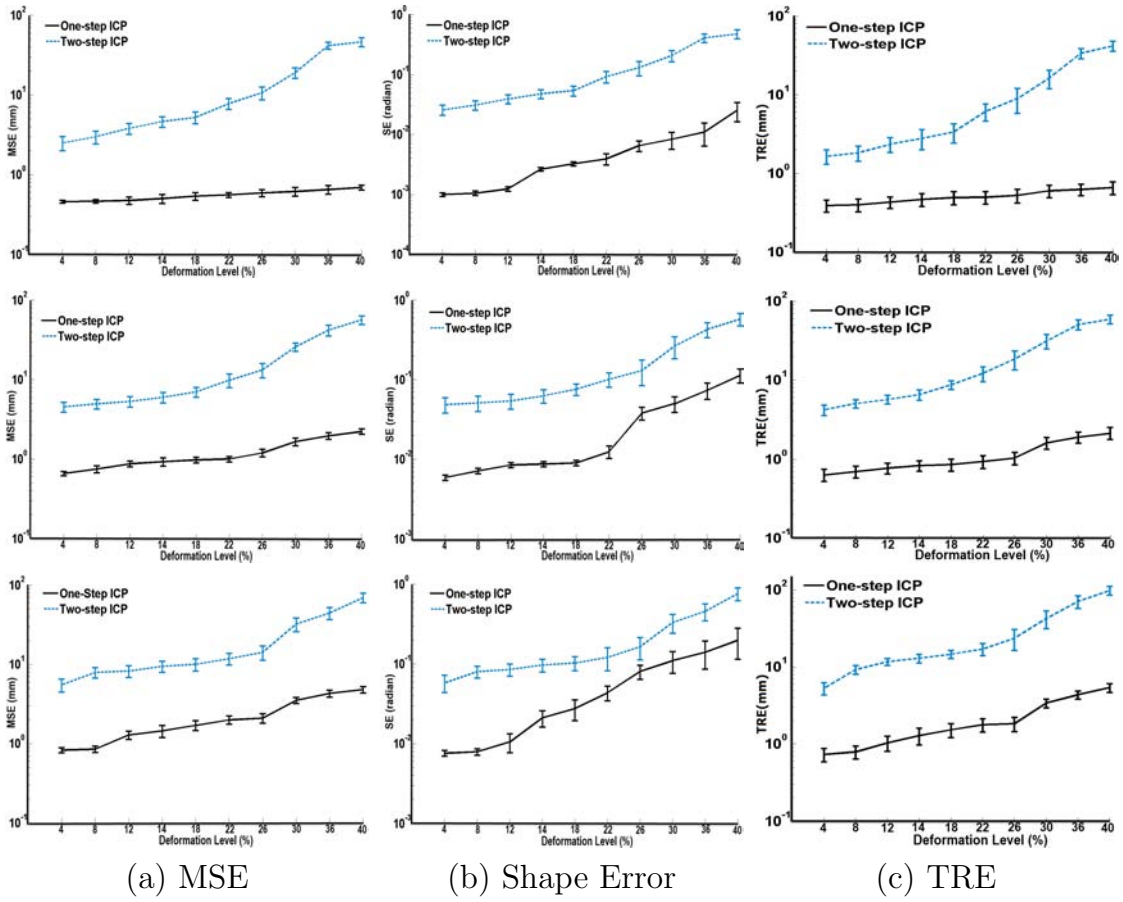


Figure 8-10: Comparison of the proposed method with two-step ICP on semi-synthetic data sets with respect to deformation. The results of 3 different intersection curves which are obtained at  $0^\circ$ ,  $10^\circ$  and  $20^\circ$  cutting angles are depicted at each row.

extreme example of such cases. Two-step ICP finds wrong correspondences and fails to retrieve the correct solution. We observe that the high frequency bumps have a strong influence on the matching process, causing the solution to get trapped in a local minimum. From Figure 8-9 and 8-10, we can deduce that one-step ICP is stable and less sensitive to the initial solution. Moreover, one-step ICP error gracefully degrades as the level of deformation and the cutting angle increase.

### 8.3.2.2 Tests on Real Patient Data

Data from real patients with small implants are used to validate methodology of combining TVUS with MR and to compare our method against two-step ICP. In our experiments, small implants are seen in TVUS but, hard to identify with MR data. Therefore, 2D TVUS images are used to detect small endometrial implants and to segment the visible soft tissue organs whereas MR volumes are used to create a 3D geometric model of the corresponding organs. A TVUS image is manually selected for each patient by a clinician and corresponds to the middle MR slice. This assumption considers as an initial solution for both algorithms. The soft tissue organs such as bladder, uterus, ovary, and rectum as well as the implant in the TVUS slice and in the MR slices are segmented by an expert. We then reconstruct a 3D surface from these parallel 2D MR contours. To show how our method improves diagnosis, we use 10 different patients to localize small implants. The registration results for 2 patient data are shown in Figure 8-11 and 8-12. We use one surface in Figure 8-11 and two surfaces in Figure 8-12. The registration results for the proposed method and two-step ICP are illustrated in columns. Note that endometrial tissues (yellow curves in Figure 8-11 and 8-12 (a)) are seen in the TVUS images and there is no evidence of their presence in the MR data.

Figure 8-11 shows registration results for a single surface. Figure 8-11 (a) shows the 2D TVUS slice. In this figure, the uterus and endometrial tissue can be distinguished by red and yellow, respectively. Figure 8-11 (b) shows MR slices with slice thickness of 5 mm. In this figure, the boundary of the uterus is segmented from five MR slices. Then, we reconstruct the 3D surfaces from the 2D segmented contours.

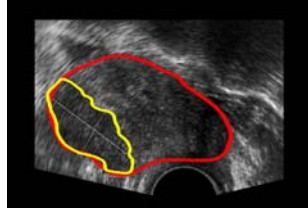
The reconstructed 3D uterus surface is shown in Figure 8-11 (b). We then use both one-step and two-step ICP to map the 2D TVUS slice onto the 3D uterus surface. The registration results for the proposed method and two-step ICP are depicted in Figure 8-11 (c) and (d), respectively. Figure 8-11 (e) illustrates the overlap images where the top belongs to the rendered MR image and the bottom belongs to the TVUS image. To generate render MR image, first for each pixel in the TVUS image, the corresponding voxel in the MR volume is found by using the estimated displacement fields. This allows us to fill each pixel in the TVUS image with the intensity of the corresponding MR voxel. Note that, the intensity of a floating voxel is obtained via bi-cubic interpolation of its integer neighbours. The resulting displacement field (Figure 8-11 (g) and (h)) is used to map implant shape onto the MR surface, see Figure 8-11 (i) and (j). Furthermore, this figure show how the implants are infiltrating into the uterus. Since the ground truth is not available for patient data sets, we cannot assess the method with with quantitative evaluations. However, the quantitative evaluations on the semi-synthetic data sets may help us to assess the results. Since we do not have high level of deformation between two modalities, we expect high registration accuracy for both methods. Note that the two-step ICP normally has less registration accuracy as compared with the proposed method.

Figure 8-12 shows registration results for a multiple surface. Figure 8-12 (a) shows the 2D TVUS slice. In this figure, the ovary, bladder, and endometrial tissue are segmented using expert knowledge. The soft tissue organs (ovary and bladder) and endometrial tissue can be identified by red and yellow, respectively. Figure 8-12 (b) shows MR slices with slice thickness of 5 mm. In this figure, the boundaries of the ovary and bladder are segmented from four MR slices. Then, we reconstruct the 3D surfaces from the 2D segmented contours. The reconstructed 3D ovary and bladder surfaces are shown in Figure 8-12 (b). We then use both one-step and two-step ICP to find the best transformation to align the 2D TVUS slice onto the 3D MR surface. The registration results for the proposed method and two-step ICP are depicted in Fig. ??fig10 (c) and (d), respectively. Figure 8-12 (e) illustrates the overlap images where the middle belongs to the rendered MR image and the top and bottom belong

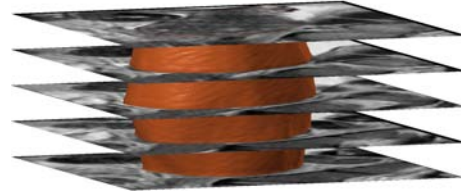
to the TVUS image. The resulting displacement field (Figure 8-12 (g) and (h)) is used to map endometrial tissue shape onto the MR surface, see Figure 8-12 (i) and (j). Based on our quantitative evaluations on the semi-synthetic data sets, we expect high registration accuracy for both methods. This is due to that the bladder and ovary do not have complex deformations.

Our registration accuracy has also been evaluated by an expert, namely a pelvic radiologist. A precise registration algorithm must accurately align all corresponding organs and pelvic anatomical structures across modalities. The expert uses these features to visually assess our registration method. We provide the following data to the expert: MR slices, 3D patient-specific organ model(s), TVUS planar image, embedded TVUS surface, rendered MR image, and embedded TVUS surface with 3D MR surface. Examples of these are shown in Figure 8-11 and 8-12. We setup a registration quality score called 1-to-5 rating scale where 5 is excellent and 1 is bad. The expert evaluation is given in Figure 8-13 (a). Note that the dash line means that the expert could not evaluate the results. It shows that our method mainly provides high registration accuracy, except for patient 9. From the expert's point of view, the registration results for patient 9 could not be evaluated since all organs (bladder and uterus) and pelvic anatomical structures (cervix, endometrium, and vaginal wall) in the TVUS surface were to be compared with 4 different MR slices (see Figure 8-11 (b)).

Finally, the evaluations and the experimental results show that the proposed method gives accurate and smooth displacement fields. They demonstrate that the combination of complimentary information from TVUS and MR images is more informative than any of the input modalities. Indeed, the registration provides more precision about implant location and depth of infiltration which consequently improves accuracy of diagnosis and preoperative surgery planing. This is due to the fact that the reconstructed MR surface may help the surgeons to avoid the MR images itself, as they are interested to the shape of the pelvic organs which leads to a better understanding of the MR images. Moreover, our registration provides more precise information about depth of infiltration and location of the implant on the MR frame

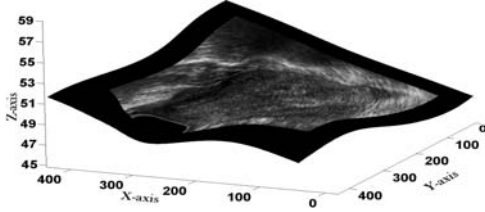


(a) TVUS



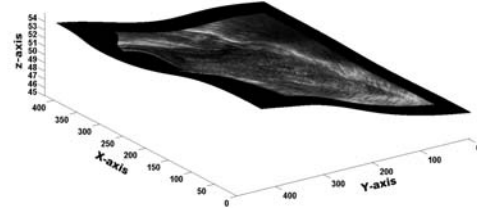
(b) MR Surface

One-Step ICP

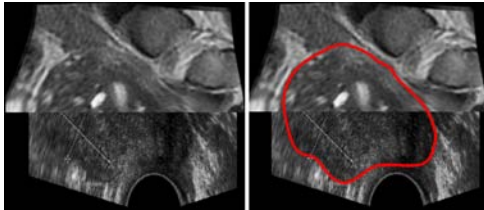


(c) Registered TVUS

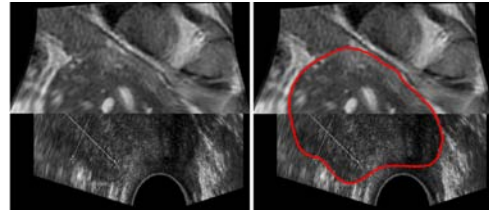
Two-step ICP



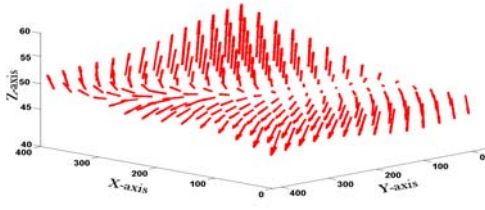
(d) Registered TVUS



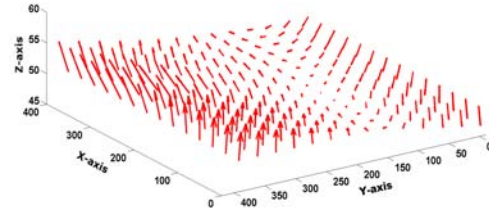
(e) Overlap W/O and W/ Curve



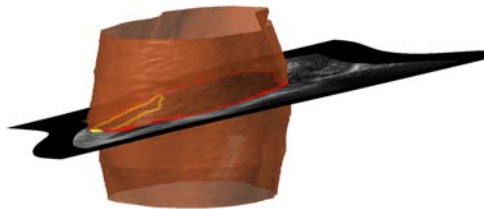
(f) Overlap W/O and W/ Curve



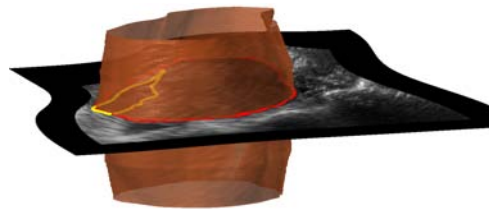
(g) Flow Field



(h) Flow Field



(i) Localization



(j) Localization

Figure 8-11: Example for a single surface. The registration results for the proposed method and two-step ICP are demonstrated in columns. (a): shows a TVUS slice in which the uterus and implant are depicted in red and yellow, respectively. (b): 3D uterus surface. (c) and (d): show warped free-form surfaces. (e) and (f): show the overlap images where the top belongs to the rendered MR image and the bottom belongs to the TVUS image. (i) and (j): depict endometrial implant after registration on the MR surface.

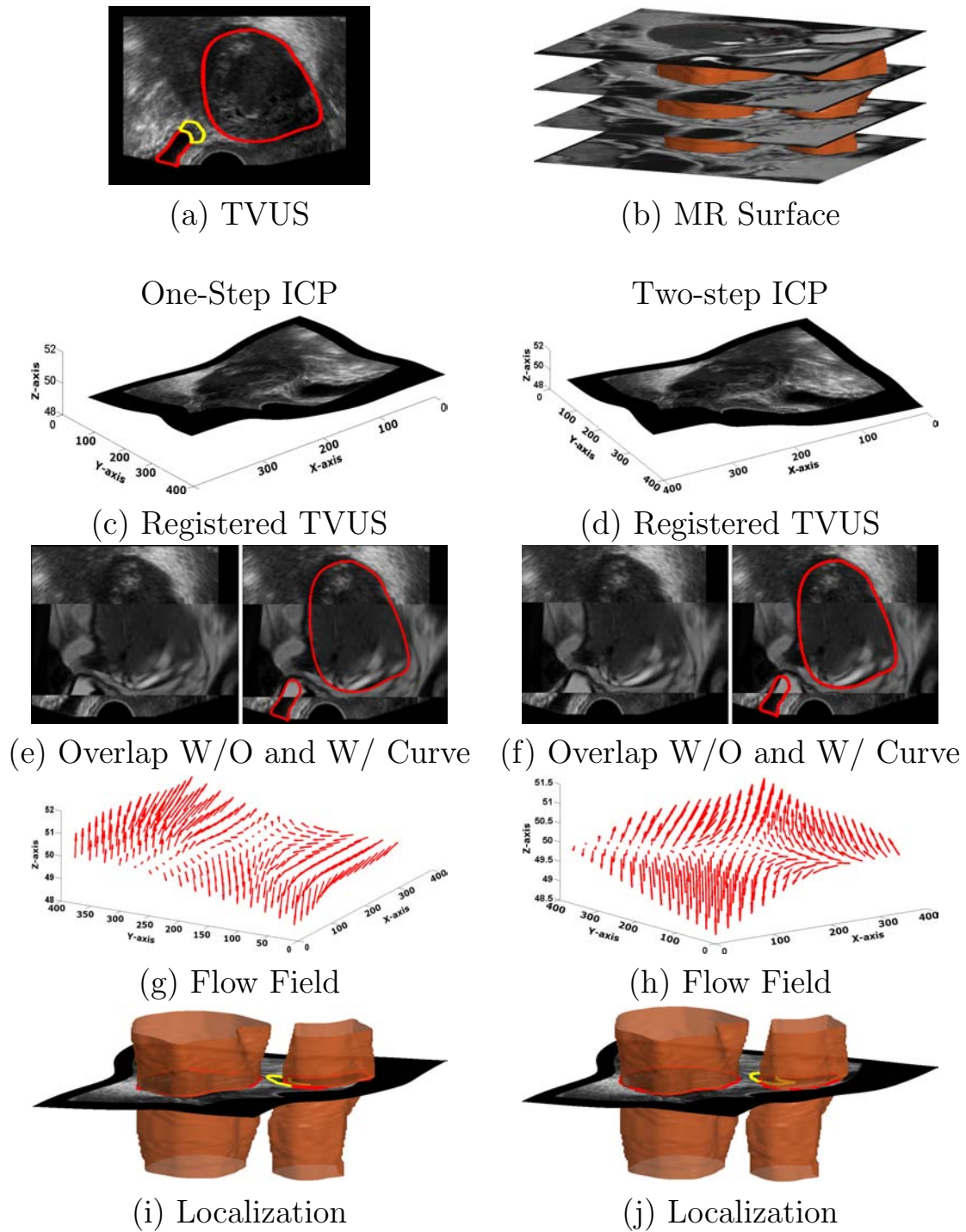
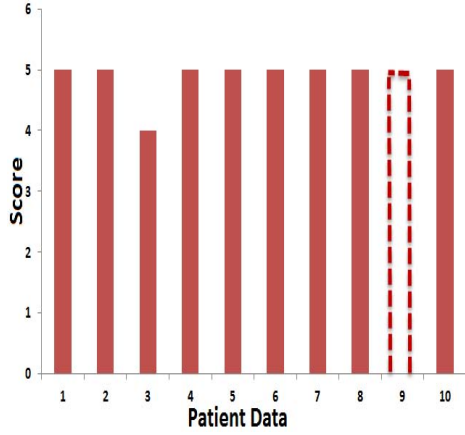
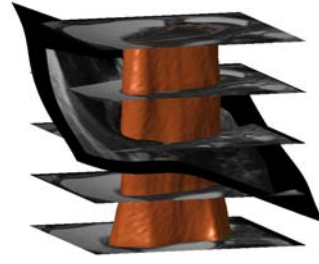


Figure 8-12: Example for two surfaces. The registration results for the proposed method and two-step ICP are demonstrated in columns. (a): shows a TVUS slice in which the bladder, ovary, and implant boundaries are depicted in red and yellow, respectively. (b): 3D ovary and bladder surfaces. (c) and (d): show warped free-form surfaces. (e) and (f) show the overlap images where the middle belongs to the rendered MR image and the top and bottom belong to the TVUS image. (i) and (j) depict endometrial implant after registration on the MR surface.



(a) Evaluations



(b) TVUS Surface on MR frame (patient 9)

Figure 8-13: Expert’s evaluation of the proposed method. We setup a registration quality score where 5 is excellent, 4 is good, 3 is fair, 2 is poor, 1 is bad, and dash line means not rateable. (a) shows expert’s evaluation result. (b) shows the TVUS surface embedded on the MR frame for patient data 9. Patient 9 can not be evaluated because the embedded 2D TVUS surface must be compared with 4 different MR slices.

which can improve the diagnosis and treatment of the endometriosis.

## 8.4 Conclusion

We have proposed a new framework for deformable slice-to-volume registration to localize and characterize endometrial tissues. Our method uses a variational one-step deformable ICP method that registers a set of 2D contours to a set of corresponding 3D surfaces. Our method computes a dense deformation field embedding the TVUS domain in the MR coordinate frame while establishing point correspondences automatically. In order to obtain point correspondences and nonlinear deformations, the method uses Euclidean distance maps resulting from MR surfaces. Our method handles multiple pairs of curves and surfaces. To make our algorithm more stable, we use a least squares planar constraint on the warped surface. Applying this strong constraint on the original TVUS surface improves convergence rate. We relax the constraint after a few iterations. This is due to the fact that after a few iterations we approach the global solution, so that the surface has only low frequency features and no longer interferes with convergence to the correct solution.

We evaluate the proposed method’s performance in comparison with two-step deformable ICP. We show the accuracy of the proposed method by quantitative and qualitative tests on semi-synthetic and real world data sets. Since the ground truth is not available for patient data sets, we assess the results with quantitative and qualitative evaluations on semi-synthetic data sets, generated to reproduce real patient data features. We conduct more than one thousand two hundreds experiments using semi-synthetic data with artificial deformations to test various aspects of the methods. The quantitative error measurements on semi-synthetic data sets provide a crude assessment of our algorithm in a clinical context. To demonstrate the applicability in real applications, we also conduct ten tests on patient data.

Qualitative and quantitative tests on semi-synthetic data and clinical data sets clearly depict the accuracy of our method. Experimental error analysis show that our method remarkably reduce the error compare to two-step ICP. Experimentally we see that even with high deformation and slant (40% and 20°, respectively), our alignment approach has less than 10 mm mean square error between true point correspondences

and still works very well. In contrast, two-step ICP has more than 100 mm mean square error for the same deformation and slant, from which we can conclude that our procedure is much less sensitive to increment of deformation and slant and can provide reliable results. The average execution time of the process is  $153.82 \pm 11.74$  s with MATLAB code.

# Chapter 9

## Conclusion and Future Work

### 9.1 Conclusion

In this manuscript, for the first time, we have investigated algorithms to spatially align preoperative TVUS and MR female pelvic organs to localise endometrial implants and exhibit depth of infiltration on the pelvic anatomy. This registration is a significantly difficult task, since two different imaging modalities are involved and non-linear geometric transformations are required to cope with the soft-tissue deformations. Another difficulty lies in the limitations of the medical imaging techniques. For instance, MR reveals the complex pelvic anatomy in high resolution images, whereas TVUS image depicts small endometrial implants and their depth of infiltration on the host tissue in low resolution images. Therefore, the key advantage of TVUS-MR registration is that mapping endometrial implants from the TVUS images into the MR images can ease the task of gynecologic surgeons in interpreting preoperative data, because TVUS-MR fusion may prevent them to investigate each image individually. This may help them to make a better preoperative surgical planning as the size, shape, location, depth of infiltration, and resection lines are clearly exhibited on the global pelvic anatomy, not just on the host tissue. Consequently, this simply leads to more precise treatment of endometriosis without harming the healthy tissue around it. Based on these advantages, we proposed various TVUS-MR image registration algorithms for different setting i.e. 2D/2D and 2D/3D.

Chapter 4 provides an extensive review on the existing methods related to US-

MR image registration, ICP-based algorithms and 2D/3D medical image registration methods. There is currently no system to register TVUS images with MR images of the female pelvis. The analysis of the US-MR image registration literature led to the consensus that all these methods try to either register a pair of 2D images or a pair of 3D volumetric data. The methods have been classified into three different categories such as intensity-based, feature-based, and hybrid methods. We see that there are very few works related to US-MR intensity-based registration, since the methods based of intensity usually fail due to the large intensity variations. On the other hand, feature-based registration is mainly used to register US with MR images, since it can be applied to any image. To improve the convergence rate and accuracy of intensity- and feature-based methods, some researchers combined both approaches. It is also observed that spline-based deformable models have been mainly used as a transformation model. We have also discussed the state-of-the-art of the ICP algorithms. ICP algorithms establish a set of correspondences by searching for closest point to moving data on the reference data, and estimate a transformation which maps the moving data to reference data via established correspondences. There is a large number of ICP algorithms trying to improve the computational time or robustness. In order to improve both the robustness and the computational efficiency of classical two-step rigid ICP, a distance transform is introduced. Moreover, the analysis of the 2D/3D medical image registration literature led to the consensus that slice-to-volume registration received less attention than projective registration. Most methods in the slice-to-volume literature rely on an intensity-based similarity measure. However, US-MR registration with an intensity similarity measure is not probably the proper approach.

Chapter 5 provides a comparison of the two different registration approaches including an intensity-based method and a feature-based method. Since there is currently no system available to register TVUS to MR images, we investigate the applicability of these methods in TVUS-MR registration problem. Therefore we choose a feature-based registration using TPS deformations with manual point selection and an intensity-based registration using NMI and B-splines deformations to register and

fuse pre-operative TVUS into MR images. The NMI approach makes direct use of the original image data and the other is based on matching discrete geometric feature points. We observed that feature-based registration approach is an appropriate choice as it applies to any image and provides high registration accuracy. However, it is highly a user-dependent method. On the other hand, the intensity-based approach is a limited method, because the probabilistic relationship between TVUS and MR images does not mainly exist. Therefore, all the methods which have been proposed in this thesis are based on a set of geometric features of common objects.

Chapter 6 presents a variational semi-automatic feature-based deformable image registration and fusion between pre-operative MR and TVUS images. Since, the endometrial implants can be seen in the TVUS images, there is no corresponding points at implants. Thus, we must use the implant's neighbouring organs to find the deformation between TVUS and MR images. To achieve this, we propose a point-based registration method to obtain a high accuracy solution of PDEs. Notably the solution of the PDEs is the displacement vector field. For localizing the implant we apply the displacement field to the implant in the TVUS image and we find the location of endometriosis in MR frame. Note that the main limitation of the point-based approach lies on the establishing dense point correspondences which is often a challenging and time-consuming process. To decrease the effect of this limitation, we use a parametrization-based approach between shape contours to define dense correspondences. In this way, the expert first segments the organs and selects a few point correspondences. Then, more point correspondences are then established using parametrization between each adjacent points. After establishing point correspondences, we model the deformable image registration as a deformation process of certain material driven by internal forces. We use three different types of regularizer including diffusion, divergence and curl, and curvature. Furthermore, our model is not dened on the basis of a finite set of parameters and it is more suited in the case of no prior knowledge. Therefore, it has greater flexibility than spline-based methods such as TPS and B-splines. We compare our method with the TPS registration method. Experimental results illustrate that diffusion-based registration cannot pro-

vide precise deformation field. We also discover that in div-curl registration method, finding the trade-off between the curl and divergence is not an easy task, so that, it can easily lead to the mesh folding. In addition, implementing of 3D/2D registration using this scheme is very complex. A common disadvantage of the diffusion and div-curl registration methods is that both are sensitive to global affine transformation, so that a pre-registration step is an necessary task. To skip the pre-registration step, we propose to use curvature regularizer. Based on the advantages and drawbacks of each method and our experimental results, we observe that the curvature registration method is an appropriate choice as it can provide high registration accuracy. Meanwhile, the reason that the curvature registration can provide better accuracy than TPS registration is because the curvature registration only assumes that the deformation model belongs to some infinite dimension space of functions and this space is motivated by regularizer properties. Therefore, the formulation of the problem does not require us to specify a parametric form as in the spline-based registration method and thus has more flexibility.

Chapter 7 presents a registration method that uses contour correspondences through a variational one-step deformable ICP method. Contour-based registration is the basis for many computer vision techniques and medical image analysis. Among all the existing methods, ICP-based algorithms are one of the most used algorithms in this context. In ICP-based algorithms, both point correspondences and transformation parameters can be established and estimated automatically. The major advantage of the contour-based registration methods is that they do not need an expert user establishes point correspondences manually which is a challenging and time-consuming process. In other words, these methods decrease user interaction by establishing point correspondences registration steps automatically while may still relying on the user to segment the corresponding contours. Therefore, we take the advantage of contour-based method in TVUS-MR registration problem to decrease the user interaction which moves the algorithm toward clinical application. Our method is based on the ICP used distance transform method. The distance transform merges the two inner steps of classical ICP. However, the existing one-step ICP computes rigid 2D/2D and

3D/3D registration of a single pair of curves and surfaces, respectively. Since, there is a large deformation between soft-tissue organs in TVUS and MR images, we need to extend this method to obtain non-linear geometric transformations. In this purpose, we extend one-step rigid ICP by using a variational procedure to obtain nonlinear deformations. Our registration method has two main steps: first, the MR and TVUS data are manually segmented by an expert. Second, our deformable ICP method is used to compute a dense deformation field while establishing point correspondences automatically. Since, we deal with the variational problem, we must obtain a high accuracy solution for elliptic PDEs. Once again the solution of these PDEs is the displacement vector field which must be applied to the implant in the TVUS image to localise the endometrial implants in MR frame. The novelty of this work is methodological and technical, from respectively the registration based approach to the diagnosis of endometriosis and a variational framework leading to a well-defined one-step formulation of ICP handling multiple curve correspondences. The experimental results on both semi-synthetic and clinical data reveal that the one-step ICP improves computational time and reduces the dependence of the classical two-step ICP on the initial estimate. We also find that two-step ICP is guaranteed to converge to a local minimum, since both steps in ICP must minimize the error. The reason that the one-step ICP decreases the dependency on initial registration solution is that this method removes closed-form inner loop of two-step ICP by using the Euclidean DT which leads to one energy functional to simultaneously establish correspondences and estimate deformation field. The experimental results also show that the proposed method is better than TPS-RPM in terms of both computational time and local registration accuracy.

In Chapters 5 – 7, we have examined various registration methods to find which strategy and technique work best in our problem. In all these methods, the reference 2D MR slice from the MR volume that corresponds to the moving 2D TVUS image was manually chosen by an expert. Therefore, we have assumed that the TVUS slice is parallel to the corresponding MR slice. This is a limitation since the standard TVUS and MR imaging techniques used for diagnosing endometriosis are 2D and

3D, respectively. In other words, a US image generally matches with multiple MR slices so that it is not parallel to any of the MR directions. Hence, this registration problem is deliberately a slice-to-volume registration. Therefore, in Chapter 8, we describe a variational one-step deformable ICP method that directly registers a set of 2D curves in the 2D TVUS image to a set of corresponding 3D surfaces in the 3D MR volume. This method computes a dense deformation field embedding the TVUS domain in the MR coordinate frame while establishing point correspondences automatically. In order to establish point correspondences and obtain non-linear transformation parameters, the method uses Euclidean distance maps resulting from MR surfaces. Our method handles multiple pairs of curves and surfaces. To make our algorithm more stable, we use a least squares planar constraint on the warped surface just for a few iterations. Applying this strong constraint on the original TVUS surface improves convergence rate, since high frequencies on the warped surface can interfere with convergence. The qualitative and quantitative tests on semi-synthetic data and clinical data sets show that our method remarkably reduce the error compare to two-step ICP.

In summary, the main advantages of TVUS-MR slice-to-volume registration approach over 2D/2D image registration are twofold. Firstly, This approach removes the assumption that the TVUS slice is parallel to the corresponding MR slice. This assumption is not perfectly true as a TVUS image generally is not parallel to any of the MR directions. Therefore, this is significantly important to discard this assumption, since the goal of endometriosis treatment is to resect the endometriosis without harming the healthy tissue around it. However, to achieve this, we need very accurate procedures in order to precisely localize endometriosis. By considering this assumption, the accuracy of localization can decrease, so that slice-to-volume registration is needed to enhance preoperative surgical planning. As mentioned before, each MR slice of the MR volume can just depict the location of large tissues, and combination of all these slices can help the surgeons to visually reconstruct 3D structures of the patient's pelvic organs. However, such a reconstruction prone to large error, since the pelvic has complex 3D structures. So a computer-aided recon-

struction system must be used to accurately reconstruct 3D models of the patient's organs. This simply enhances the anatomy of this complex part of the body. Thus, the second advantage of slice-to-volume registration approach is that the surgeons do not need to deeply investigate each imaging modality, since all the necessary information needed to make an accurate preoperative surgical planning are provided as a new volumetric image which removes redundant information. Note that this new image contains the patient-specific organ model from 3D MR volume as well as shape, size, location, depth of infiltration of endometrial implants from 2D TVUS images, and resections lines. This new image eases the task of surgeons to make better decisions to avoid under- or over-cutting during surgery.

## 9.2 Future Work

A main challenge in this manuscript is finding the MR slices corresponding to the TVUS slice without using of the EM tracker or 3D TVUS. Therefore, we need to validate our proposed methods by using an EM tracker. All the methods can be speeded up by C++ coding or GPU programming and thus may be useful for real-time multimodal fusion of female pelvic images.

From a clinician's point of view, two fundamental questions have not been answered. The first one is how much registering a 2D TVUS with a 3D MR can improve the surgery planning. The second one is what the influence is of mapping an endometrial implant into a 3D patient-specific organ model on the surgery. Therefore, we have yet to perform medical examinations to find out answers to these questions. To achieve this, some patients with symptomatic disease who underwent surgery must be selected in the study. Then, we need to ask surgeons to investigate both MR and TVUS data, separately, and then make pre-operative surgical planning, in which the location of implants and resection lines must be clearly defined on the MR images. Then, the classical procedure of making surgical planning and our method must be compared to surgery results. In this manner, we can observe the accuracy of the surgical planning based on the classical procedure and ours.

In order to improve surgical procedures to accurately resect the endometrial im-

plants during laparoscopic surgery, we must enrich the surgeon's video data using Augmented Reality (for more details, see [213–215]). This can be done with overlaying the reconstructed 3D patient-specific organ model included implant's location, depth of infiltration, and resection lines with camera's video frame. This an important task, since the pelvic organs can exhibit strong deformation when manipulated with laparoscopic tools. Therefore, the surgeons can easily harm the healthy tissue around the implant or they can under-cut it. The latter one, cause the pain returns and the patient needs recurrence in the short term.

# Appendix A

## Image Resolution Enhancement

### Contents

---

<b>A.1 Introduction</b>	<b>171</b>
<b>A.2 Image resolution enhancement</b>	<b>172</b>
<b>A.3 Proposed algorithm for 3D images</b>	<b>173</b>
<b>A.4 Experimental result</b>	<b>175</b>

---

### A.1 Introduction

In recent years, the demand for resolution enhancement of pictorial data in medical images has been increased in order to assist clinicians to make accurate diagnosis. The tasks of resolution enhancement in medical images is generally to enlarge a region of interest. However, the main issue of concern is preserving more details in the enlarged image. In general, interpolated images have some problems such as losing the contrast and blurring the details. Thus, a robust medical image resolution enhancement technique must be able to cope with these two issues.

Nearest neighbor, bilinear and bicubic are the most well known interpolation techniques. However, the wavelet transform is playing a significant role in image resolution enhancement and many algorithms have been using it recently. Among other works, Chang et al. [216] and Carey et al. [217] have attempted to estimate the significant coefficients by examining the evolution of a wavelet transform's extrema among the same type of sub-band. The significant coefficients were used to improve the sharpness of the enhanced resolution image and edge detection algorithm were used to create

a model for detecting edges in higher frequency sub-bands. Only coefficients with significant magnitudes were estimated as the evaluation of the wavelet coefficients. Temizel et al. [218] applied wavelet domain zero padding in order to generate an initial high resolution approximation. Such approximation usually involves smoothing and ringing that could be resolved by applying a cycle spinning methodology.

Our aim in this paper is to propose a method for 3D image resolution enhancement based on discrete stationary wavelet transforms to generate sharp high resolution images. More specifically, we first increase the quality of edges using a shape function [219] and then use both the discrete and the stationary wavelet transforms to decompose the resulting image into low and high frequency sub-bands. The proposed method shows that the results obtained in [220], in the 2D case, could be further improved by considering the mean of the high frequency sub-band coefficients. To assess the efficiency of our method, we have considered comparisons with some conventional and state-of-art image resolution techniques such as bi-linear, bicubic, Wavelet Zero Padding (WZP), Discrete Wavelet Transform-Based Image Resolution Enhancement [221], and Image Enhancement by using Discrete and Stationary Wavelet Decomposition [220]. Note that the 2D version of the proposed method outperforms the state of the art and its extension to 3D enhancement based on wavelet transforms is completely new to the best of our knowledge.

The rest of the paper is organized as follows. Section 2 is a brief review of previous image enhancement work. Section 3 presents the proposed method to enhance image resolution. Results and discussions are provided in section 4 and the paper is concluded in section 5.

## **A.2 Image resolution enhancement**

There are various wavelet based methods which have been used for medical image resolution enhancement. However, just two state-of-art techniques have been implemented for comparison purposes. The first technique is DWT-based resolution technique [221], and the second one is image resolution enhancement by using DWT and Stationary Wavelet Transform (SWT) [220].

**DWT-based image resolution enhancement** The method consists of combining high frequency sub-bands using DWT and the input low resolution image to achieve a sharper result. The method can be summarized as follows:

- *use DWT to decompose the input image into sub-band images*
- *apply bicubic interpolation to sub-band images*
- *subtract the low frequency sub-band image from input low resolution image*
- *add the difference image to high frequency sub-bands*
- *apply bicubic interpolation to above estimated detail coefficients and low resolution input image to reach the required size for inverse DWT.*

**Image resolution enhancement by using DWT and SWT** In this method one level DWT is employed to decompose the input image into four different sub-band images. The three high frequency sub-bands images which contain the high frequency components of the input image are interpolated by bicubic interpolation. Furthermore, SWT has been employed to minimize information loss due to the downsampling in DWT. This is followed by combining all the high frequency sub-band images to generate new corrected high frequency sub-band images. Note that, the input image and the new corrected high frequency sub-band images can be interpolated for higher enlargement. Finally, inverse DWT is applied to create the high resolution image.

### **A.3 Proposed algorithm for 3D images**

As already stated, smoothing caused by interpolation techniques create a serious problem on edges. Hence, preserving edges must result in better output images. The complete block diagram of the 2D proposed algorithm is illustrated in Figure 1. In order to apply the proposed algorithm to 3D images, the 3D DWT has been chosen to preserve the edges. In the proposed algorithm, one level DWT is applied to decompose a 3D low resolution image into eight different sub-band images. The high frequency sub-bands such as HHH, HHL, HLH, LHH, LHL, LLH, and HLL (where H

and L are High and Low coefficients) contain the edges of the low resolution image. Furthermore, the size of high frequency components of DWT is increased by 3D bicubic interpolation with factor 2. Note that downsampling of sub-band images in DWT cause the information loss in the sub-bands. Thus, 3D SWT is employed to reduce this information loss. While the high frequency sub-bands in both DWT and SWT have the same size their mean must be computed to correct all the high frequency sub-band coefficients. For higher enlargement, the bicubic interpolation

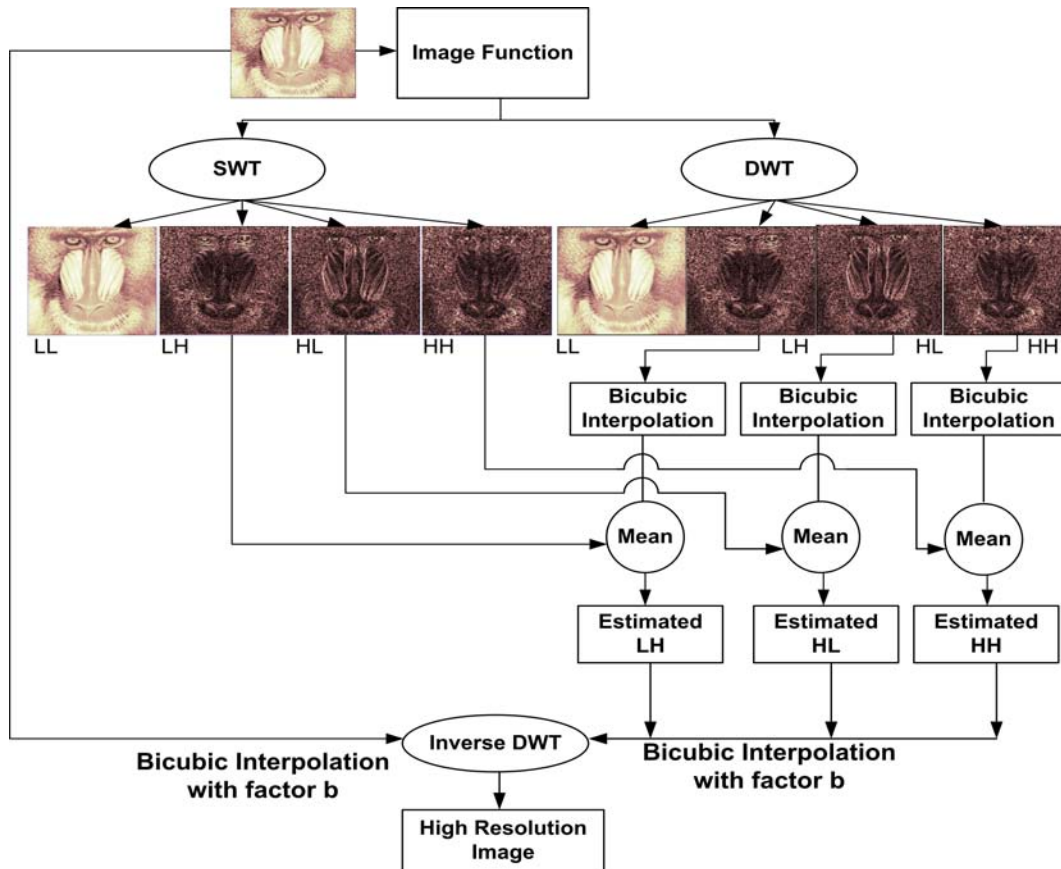


Figure A-1: The Block Diagram of the 2D Proposed Algorithm. Taken from [220] and modified.

technique can be applied to the new corrected high frequency sub-bands. It is worth to note that the low resolution image is created by low-pass filtering of the high resolution image [222]. As mentioned before, the shape function which has been explained by Tai et al. [219] applied to the input low resolution image to enhance the edge intensities. Thus, it results in preserving more edge information while the

proposed method estimates the coefficients. Accordingly, in order to increase the quality of the enhanced image, the improved input image is used instead of using the low frequency sub-band which contains less information than the original high resolution image. Also by interpolating the input image and the estimated high frequency components with factor  $(\frac{b}{2})$ , the 3D inverse DWT produces a sharper high resolution image than the interpolated image obtained by interpolation of the input image directly. This is due to the fact that the proposed method preserves more high frequency components after the corrections obtained by computing the mean of high frequency sub-bands than interpolating the input image directly.

## A.4 Experimental result

In this section, the proposed method is discussed and compared with other resolution enhancement techniques. We will use 2D natural images, 2D slices of 3D volumetric MRI images, and 3D MRI images (S01, S02, S03), as shown in Table 2 and Figure 3. As a ground truth for accuracy evaluation purposes we consider a high resolution version of these gray level images with a size of  $512 \times 512$  for 2D images and  $512 \times 512 \times 24$  for 3D images. The high resolution images were downsampled by a factor of 4 to create low resolution images.

The error between ground truth and reconstructed images is expressed in terms of the peak signal-to-noise ratio (PSNR) values. PSNR, which has been generally applied for quality measurement in the field of image processing, can be defined by the following expression:

$$PSNR = 10 \log_{10} \frac{255 \times 255}{\frac{1}{HW} (\sum_{i=1}^H \sum_{j=1}^W (I_1(i, j) - I_2(i, j))^2)} \quad (\text{A.1})$$

where  $H$  and  $W$  are respectively the height and the width of the original high resolution image  $I_1$  and enhanced image  $I_2$ .

The PSNR values for 2D images are given in Table 1 for four times enlargement. This table evaluates the accuracy of the proposed method with conventional and state-of-art resolution enhancement techniques. It is clear from Table 1 that the proposed

method outperforms the other methods. Figures 2 confirms that the reconstructed images using the proposed technique in (d), comparing to the other methods in (b) and (c), improved the portrayal of salient image feature such as edges and contours.

Table 2 (Left) is a comparison between the 2D version of our method and the state of the art, both applied on a set of 2D MRI slices. The values in each row are obtained as a mean over the PSNR value on each slice. In order to have a comparison with the 3D version of our method, Table 2 (Right) shows the mean PSNR values computed over the 24 slices for each 3D image.

For display purposes, the proposed algorithm was applied to the full 3D MRI image volume (S01) shown in Figure 3 (a) to illustrate the original low resolution image with a size of  $128 \times 128 \times 6$ . Low resolution Slices are shown in Figure 3 (b). In Figure 3 (c) the proposed algorithm was applied to the 3D low resolution image in order to enhance the resolution to a full isotropic  $512 \times 512 \times 24$  image; the resulting 2D slices are shown in Figure 3 (d). The PSNR results in Table 1 and 2 and the simulation results in Figures 2 and 3 show that the proposed method has sharper edge features, more details, and visually it is closer to the original image compared to the conventional and state-of-art image resolution enhancement results.

Method	Lena	Baboon	Head	Brain
Bi-linear	22.27	20.09	25.93	23.64
Bicubic	24.03	21.63	27.09	24.96
WZP (Db. 9/7)	25.76	21.99	29.81	26.07
discrete and stationary wavelet decomposition [220]	26.94	22.61	30.12	28.02
DWT based image resolution enhancement [221]	29.09	22.84	31.31	28.86
Proposed method	30.81	25.16	32.26	30.33

Table A.1: PSNR (dB) Results for  $4\times$  Resolution Enhancement (from  $128 \times 128$  to  $512 \times 512$ ).

Method	S01	S02	S03	Method	S01	S02	S03
Bi-linear	20.31	19.01	20.65	Bi-linear	26.82	25.45	27.12
Bicubic	20.36	19.06	20.74	Bicubic	26.89	25.55	27.24
DSWD [220]	22.81	21.08	23.28	DSWD [220]	28.20	27.38	29.07
DWT [221]	26.83	25.25	27.23	DWT [221]	33.49	32.13	34.72
Our method	27.46	26.51	28.60	Our method	34.57	33.40	35.71

Table A.2: Average PSNR (dB) for Left: 2D Slices; Right: Overall Slices of 3D Images.

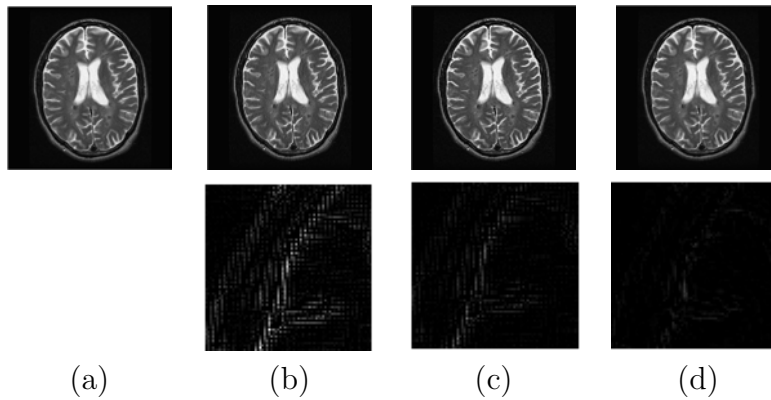


Figure A-2: (a) Original Low Resolution Image, (b) Discrete and Stationary Wavelet Decomposition; (c) Discrete Wavelet Transform-Based Image Resolution Enhancement; (d) Proposed Technique and the Residual Images of the Close-up Scene for Specific Block Size in the Second Row.

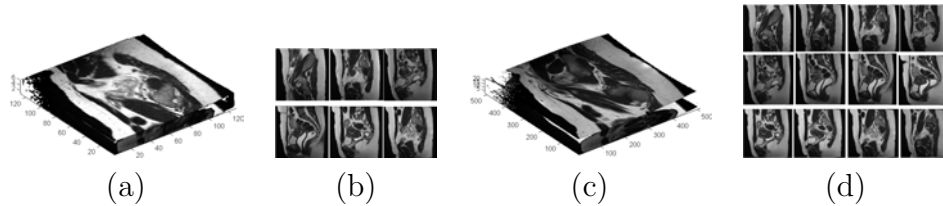


Figure A-3: (a) 3D Original Low Resolution Image (S01), (b) 2D Slices of 3D Low Resolution Image, (c) 3D Enhanced Resolution Image, (d) Odd 2D Slices of 3D Enhanced Resolution Image.

# Bibliography

- [1] P. K. Doi, “Computer-aided diagnosis in medical imaging: Historical review, current status and future potential,” *Computerized Medical Imaging and Graphics*, vol. 31, pp. 198–211, 2007.
- [2] H. Fujita, Y. Uchiyama, T. Nakagawa, D. Fukuoka, Y. Hatanaka, T. Hara, G. N. Lee, Y. Hayashi, Y. Ikedo, X. Gao, and X. Zhou, “Computer-aided diagnosis: The emerging of three cad systems induced by japanese health care needs,” *Computer Methods and Programs in Biomedicine*, vol. 92, pp. 238–248, 2008.
- [3] T. W. Way, *Computer-aided Diagnosis of Pulmonary Nodules in Thoracic Computed Tomography*. PhD thesis, University of Michigan, 2008.
- [4] G. S. Lodwick, C. L. Haun, E. Smith, R. F. Keller, and E. D. Robertson, “Diagnosis of primary bone tumor,” *Radiology*, vol. 80, p. 273275, 1963.
- [5] P. H. Meyers, C. M. Nice, H. C. Becker, W. J. Nettleton, J. W. Sweeney, and G. R. Meckstroth, “Automated computer analysis of radiographic images,” *Radiology*, vol. 83, p. 10291033, 1964.
- [6] F. Winsberg, M. Elkin, J. Macy, V. Bordaz, and W. Weymouth, “Detection of radiographic abnormalities in mammograms by means of optical scanning and computer analysis,” *Radiology*, vol. 89, p. 211215, 1967.
- [7] M. L. Giger and K. Suzuki, *Computer-Aided Diagnosis*. Elsevier, 2008.
- [8] J. M. Sanches, J. C. Nascimento, and J. S. Marques, “Medical image noise reduction using the sylvesterlyapunov equation,” *IEEE Transactions on Image Processing*, vol. 17, p. 15221539, 2008.
- [9] Y. Diez, A. Oliver, X. Llado, and R. Marti, “Comparison of registration methods using mamographic images,” in *International Conference on Image Processing*, 2010.
- [10] N. Shareef, D. L. Wang, and R. Yagel, “Segmentation of medical images using legion,” *IEEE Transactions on Medical Imaging*, vol. 18, p. 7491, 1999.
- [11] J. Ulen, P. Strandmark, and F. Kahl, “An efficient optimization framework for multi-region segmentation based on lagrangian duality,” *IEEE Transactions on Medical Imaging*, vol. 32, pp. 178–18, 2013.

- [12] A. Osareh and B. Shadgar, "A computer aided diagnosis system for breast cancer," *International Journal of Computer Science*, vol. 8, pp. 223–240, 2011.
- [13] L. Chamie, R. Blasbalg, R. Pereira, G. Warmbrand, and P. Serafini, "Findings of pelvic endometriosis at transvaginal us, mr imaging, and laproscopy," *RadioGraphics*, vol. 31, pp. 71–100, 2011.
- [14] P. A. Rogers, T. M. D’Hooghe, A. Fazleabas, C. E. Gargett, L. C. Giudice, G. W. Montgomery, L. Rombauts, L. A. Salamonsen, and K. T. Zondervan, "Priorities for endometriosis research: Recommendations from an international consensus workshop," *Reproductive Sciences*, vol. 16, pp. 335–346, 2009.
- [15] G. D. Adamson, S. Kennedy, and L. Hummelshoj, "Creating solutions in endometriosis: Global collaboration through the world endometriosis research foundation," *Journal of Endometriosis*, vol. 2, pp. 3–6, 2010.
- [16] R. F. Grasso, R. D. Vescovo, R. L. Cazzato, and B. B. Zobel, "Pelvic endometriosis: A mr pictorial review," *Obstetrics and Gynecology: Endometriosis-Basic Concepts and Current Research Trends*, vol. 53, pp. 389–394, 2013.
- [17] M. Mangler, N. Medrano, J. Bartley, S. Mechsner, D. Speiser, A. Schneider, and C. Kohler, "Value of diagnostic procedures in rectovaginal endometriosis," *Australian and New Zealand Journal of Obstetrics and Gynaecology*, vol. 53, pp. 389–394, 2013.
- [18] D. W. Cramer and S. A. Missmer, "The epidemiology of endometriosis," *Annals of the New York Academy of Sciences*, vol. 955, pp. 11–22, 2002.
- [19] L. A. Moser, "The case of endometriosis, an adlerian perspective," Master’s thesis, Adler Graduate School, September 2007.
- [20] J. A. Sampson, "Metastatic or embolic endometriosis, due to the menstrual dissemination of endometrial tissue into the venous circulation," *The American Journal of Pathology*, vol. 3, pp. 93–110, 1927.
- [21] A. Bokor, *Semi-invasive Diagnosis of Endometriosis*. PhD thesis, Semmelweis University, 2010.
- [22] J. L. Simpson, S. E. abd L. R. Malinak, and V. J. Buttram, "Heritable aspects of endometriosis. i. genetic studies," *American Journal of Obstetrics and Gynecology*, vol. 137, pp. 327–331, 1980.
- [23] J. L. Simpson, S. E. abd L. R. Malinak, and V. J. Buttram, "Endometriosis," *The New England Journal of Medicine*, vol. 360, pp. 268–279, 2009.
- [24] K. Ballard, K. Lowton, and J. Wright, "What the delay? a qualitative study of women’s experience of reaching a diagnosis of endometriosis," *Journal of Fertility and Sterility*, vol. 86, pp. 1296–1301, 2006.

- [25] L. Manganaro, V. Vinci, S. Bernardo, P. Storelli, E. Fuggetta, P. Sollazzo, A. Ticino, M. E. Sergi, R. Brunelli, P. B. Panici, and M. G. Porpora, “The role of 3.0t mri in the assessment of deep endometriosis located on the uterosacral ligaments,” *Journal of Endometriosis and Pelvic Pain Disorders*, vol. 5, pp. 10–16, 2013.
- [26] I. Brosens, P. Puttemans, R. Campo, S. Gordts, and K. Kinkel, “Diagnosis of endometriosis: Pelvic endoscopy and imaging techniques,” *Best Practice and Research Clinical Obstetrics and Gynaecology*, vol. 18, pp. 285–303, 2004.
- [27] R. J. Bast, T. Klug, E. S. John, E. Jenison, J. Niloff, H. Lazarus, R. B. RS, T. Leavitt, C. Griffiths, L. Parker, V. jr. Zurawski Vand, and R. Knapp, “A radioimmunoassay using a monoclonal antibody to monitor the course of epithelial ovarian cancer,” *The New England Journal of Medicine*, vol. 309, pp. 883–887, 1983.
- [28] E. Berkes, A. Bokor, and J. Rigo, “Current treatment of endometriosis with laparoscopic surgery,” *Journal of Orvosi Hetilap*, vol. 151, pp. 1137–1144, 2010.
- [29] A. Kennedy and C. M. Peterson, “Transvaginal sonography in reproductive endocrinology and infertility,” *Reproductive Endocrinology and Infertility*, 2010.
- [30] S. L. Antonsen, *The Value of PET/CT, MRI, Ultrasonography and Biochemical Analyses for Preoperative Staging of Endometrial Cancer Patients*. PhD thesis, University of Copenhagen, 2012.
- [31] S. Giusti, F. Forasassi, L. Bastiani, V. Cela, N. Pluchino, V. Ferrari, E. Fruzzetti, D. Caramella, and C. Bartolozzi, “Anatomical localization of deep infiltrating endometriosis: 3d mri reconstructions,” *Abdominal Imaging*, vol. 37, 2012.
- [32] E. Kreyszing, “On the calculus of variations and its major influence on the mathematics of the first half of our century,” *Journal of The American Mathematical Monthly*, vol. 101, p. 902908, 1994.
- [33] J. Ferguson, “A brief survey of the history of the calculus of variations and its applications,” tech. rep., Cornell University, 2004.
- [34] A. Cherkaev and E. Cherkaev, “Calculus of variations and applications,” tech. rep., The University of Utah, Department of Mathematics, 2003.
- [35] G. Allasia, R. Cavoretto, and A. D. Rossi, “Lobachevsky spline functions and interpolation to scattered data,” *Computational and Applied Mathematics*, vol. 32, pp. 71–87, 2013.
- [36] I. J. Schoenberg, *Mathematical time exposures*. Mathematical Association of America, 1982.

- [37] W. J. Gordon and R. F. Reisenfeld, *B-spline Curves and Surfaces*. Computer Aided Geometric Design, 1974.
- [38] C. de Boor, *A Practical Guide to Splines*. Springer-Verlag, 1978.
- [39] F. BRUNET, *Contributions to Parametric Image Registration and 3D Surface Reconstruction*. PhD thesis, Université d’Auvergne, November 2010.
- [40] R. L. Hardy, “Multiquadric equations of topography and other irregular surfaces,” *Journal of Geophysical Research*, vol. 76, pp. 1905–1915, 1971.
- [41] M. J. D. Powell, “The theory of radial basis function approximation,” *Journal of Advances in Numerical Analysis*, vol. 2, pp. 105–210, 1990.
- [42] E. Kansa, “Multiquadrics —a scattered data approximation scheme with applications to computational fluid-dynamics —ii solutions to parabolic, hyperbolic and elliptic partial differential equations,” *Journal of Computers and Mathematics with Applications*, vol. 19, pp. 147–161, 1990.
- [43] R. Schaback, “Multivariate interpolation by polynomials and radial basis functions,” *Journal of Constructive Approximation*, pp. 293–317, 2005.
- [44] B. Fornberg, “On a fourier method for the integration of hyperbolic equations,” *Journal of Numerical Analysis*, vol. 4, pp. 509–528, 1975.
- [45] W. Madych and S. Nelson, “Bounds on multivariate polynomials and exponential error estimates for multiquadric interpolation,” *Journal of Approximation Theory*, vol. 70, pp. 94–114, 1992.
- [46] J. Duchon, “Interpolation des fonctions de deux variables suivant le principe de la flexion des plaques minces,” *Journal of Analyse Numeriques*, vol. 10, pp. 5–12, 1976.
- [47] F. Bookstein, “Principal warps: Thin-plate splines and the decomposition of deformations,” *IEEE Transactions on Pattern Analysis and Machine Intelligence*, vol. 11, no. 6, pp. 567–589, 1989.
- [48] J. Mitra, A. Oliver, R. Marti, X. Llado, and J. C. Vilanova, “Multimodal prostate registration using thin-plate splines from automatic correspondences,”
- [49] J. Mitra, Z. Kato, R. Marti, A. Oliver, , X. Llado, , D. Sidibe, S. Ghose, J. C. Vilanova, J. Comet, and F. Meriaudeau, “A spline-based non-linear diffeomorphism for multimodal prostate registration,” *Medical Image Analysis*, vol. 16, pp. 1259–1279, 2012.
- [50] J. Mitra, Z. K. S. Ghose, D. Sidibe, R. Marti, X. Llado, A. Oliver, J. C. Vilanova, and F. Meriaudeau, “Spectral clustering to model deformations for fast multimodal prostate registration,” in *International Conference on Pattern Recognition*, 2012.

- [51] J. Mitra, R. Marti, A. Oliver, X. Llado, J. C. Vilanova, and F. Meriaudeau, “A comparison of thin-plate splines with automatic correspondences and B-splines with uniform grids for multimodal prostate registration,” in *SPIE Medical Imaging*, vol. 7964, 2011.
- [52] M. Cui, P. Wonka, A. Razdan, and J. Hu, “A new image registration scheme based on curvature scale space curve matching,” *The Visual Computer*, pp. 607–618, 2007.
- [53] J. B. A. Maintz and M. A. Viergever, “A survey of medical image registration,” *Medical Image Analysis*, vol. 2, no. 1, pp. 1–36, 1998.
- [54] A. Sotiras, C. Davatzikos, and N. Paragios, “Deformable medical image registration: a survey,” *IEEE Transaction on Medical Imaging*, vol. 32, pp. 1153–1190, 2013.
- [55] J. Fitzpatrick, D. Hill, Y. Shyr, J. West, C. Studholme, and C. Maurer, “Visual assessment of the accuracy of retrospective registration of mr and ct images of the brain,” *IEEE Transactions on Medical Imaging*, vol. 17, pp. 571–585, 1998.
- [56] J. Maintz, P. van den Elsen, and M. Viergever, “Evaluation of ridge seeking operators for multimodality medical image matching,” *IEEE Transactions on Pattern Analysis and Machine Intelligence*, vol. 18, pp. 353–365, 1996.
- [57] G. Subsol, J. Thirion, and N. Ayache, “A scheme for automatically building three-dimensional morphometric anatomical atlases: Application to a skull atlas,” *Journal of Medical Image Analysis*, vol. 2, pp. 37–60, 1998.
- [58] G. Borgefors, “Hierarchical chamfer matching: A parametric edge matching algorithm,” *IEEE Transactions on Pattern Analysis and Machine Intelligence*, vol. 16, pp. 447–461, 1988.
- [59] X. Wang, S. Elberl, M. Fulham, S. Som, and D. Feng, *Data Registration and Fusion*. Elsevier, 2007.
- [60] C. Maurer, J. Fitzpatrick, M. Wang, R. Galloway, R. Maciunas, and G. Allen, “Registration of head volume images using implantable fiducial markers,” *IEEE Transactions on Medical Imaging*, vol. 16, pp. 447–462, 1997.
- [61] T. Peters, B. Davey, P. Munger, and R. Comeau, “Three-dimensional multimodal image-guidance for neurosurgery,” *IEEE Transactions on Medical Imaging*, vol. 15, pp. 121–128, 1996.
- [62] J. Thirion, “New feature points based on geometric invariants for 3d image registration,” *International Journal of Computer Vision*, vol. 18, pp. 121–137, 1996.

- [63] L. G. Brown, "A survey of image registration techniques," *Journal of the Association for Computing Machinery (ACM) Computing Surveys*, vol. 24, pp. 325–376, 1992.
- [64] P. A. V. de Elsen, J. B. A. Maintz, E. J. D. Pol, and M. A. Viergever, "Automatic registration of ct and mr brain images using correlation of geometric features," *IEEE Transaction on Medical Imaging*, vol. 14, pp. 384–396, 1995.
- [65] N. Samavati, *Deformable Multi-Modality Image Registration Based on Finite Element Modeling and Moving Least Squares*. PhD thesis, McMaster University, 2009.
- [66] J. Weese, P. Rche, T. Netsch, T. Blaffert, and M. Quist, "Gray-value based registration of ct and mr images by maximization of local correlation," pp. 656–663, Proc. of Medical Image Computing and Computer Assisted Intervention, 1999.
- [67] B. Zitová and J. Flusser, "Image registration methods: A survey," *Image and Vision Computing*, vol. 21, pp. 977–1000, 2003.
- [68] P. Viola and W. M. Wells, "Alignment measurement by maximizing of mutual information," pp. 16–23, Internation Conference of Computer Vision, 1995.
- [69] A. Collignon, F. Macs, D. Delacre, D. Vandermeulen, P. Suetens, and G. Marchal, "Automated multimodality image registration based on information theory," pp. 263–274, Internation Conference of Information Processing in Medical Imaging, 1995.
- [70] J. P. W. Pluim, J. B. A. Maintz, and M. A. Viergever, "Mutual information based registration of medical images: A survey," *IEEE Transactions on Medical Imaging*, vol. 22, pp. 986–1004, 2003.
- [71] C. E. Shannon, "A mathematical theory of communication," *The Bell System Technical Journal*, vol. 27, pp. 379–423, 1948.
- [72] C. Studholme, D. Hill, and D. Hawkes, "An overlap invariant entropy measure of 3d medical image alignment," *Pattern Recognition*, vol. 32, p. 7186, 1998.
- [73] W. H. Press, S. A. Teukolsky, W. T. Vetterling, and B. P. Flannery, *Numerical Recipes: The Art of Scientific Computing*. Cambridge University Press, 2007.
- [74] J. Rexilius, "Physics-based nonrigid registration for medical image analysis," Master's thesis, Medical University of Luebeck, September 2011.
- [75] C. Broit, *Optimal Registration of Deformable Images*. PhD thesis, University of Pennsylvania, 1981.
- [76] G. Christensen, *Deformable Shape Models for Anatomy*. PhD thesis, Washington University, 1994.

- [77] B. K. P. Horn and B. G. Schunck, “Determining optical flow,” *Artificial Intelligence*, vol. 17, pp. 185–204, 1981.
- [78] B. Fischer and J. Modersitzki, “Fast diffusion registration,” *AMS Contemporary Mathematics, Inverse Problem, Image Analysis, and Medical Imaging*, vol. 313, pp. 117–129, 2002.
- [79] B. Fischer and J. Modersitzki, “A unified approach to fast image registration and a new curvature based registration technique,” *Linear Algebra and its Applications*, vol. 380, pp. 107–124, 2004.
- [80] S. Klein, M. Staring, and J. P. W. Pluim, “Evaluation of optimization methods for nonrigid medical image registration using mutual information and b-splines,” *IEEE Transactions on Image Processing*, vol. 16, pp. 2879–2890, 2007.
- [81] A. Cauchy, “méthod générale pour la résolution de systèmes d’équations simultanées,” *Comptes Rendus de Académie des Sciences*, vol. 25, p. 536538, 1847.
- [82] J. C. Culioli, “Introduction l’optimisation,” *Ellipses Marketing*, 1994.
- [83] M. J. D. Powell, “An iterative method for finding stationary values of a function of several variables,” *The Computer Journal*, vol. 5, p. 147151, 1962.
- [84] J. Nelder and R. A. Mead, “A simplex method for function minimization,” *The Computer Journal*, vol. 7, p. 308313, 1965.
- [85] J. E. Dennis, Jr., and J. J. Moré, “Quasi-newton methods, motivation and theory,” *Society for Industrial and Applied Mathematics*, vol. 19, p. 4689, 1977.
- [86] W. C. Davidon, “Variable metric method for minimization,” *SIAM Journal on Optimization*, vol. 1, p. 117, 1991.
- [87] R. Fletcher, *Practical Methods of Optimization*. John Wiley and Sons, 1987.
- [88] D. W. Marquardt, “An algorithm for least-squares estimation of nonlinear parameters,” *SIAM Journal on Applied Mathematics*, vol. 11, p. 434441, 1963.
- [89] Y. Saad, *Iterative Methods for Sparse Linear Systems: Second Edition*. Society for Industrial and Applied Mathematics, 2003.
- [90] F. Maes, D. Vandermeulen, and P. Suetens, “Comparative evaluation of multi-resolution optimization strategies for multimodality image registration by maximization of mutual information,” *Medical Image Analysis*, vol. 3, p. 373386, 1999.
- [91] D. M. Greig, B. T. Porteous, and A. H. Seheult, “Exact maximum a posteriori estimation for binary images,” *Journal of the Royal Statistical Society*, vol. 51, pp. 271–279, 1989.

- [92] Y. Boykov, O. Veksler, and R. Zabih, “Fast approximate energy minimization via graph cuts,” *IEEE Transaction on Pattern Analysis and Machine Learning*, vol. 23, pp. 1222–1239, 2001.
- [93] J. Pearl, *Probabilistic Reasoning in Intelligent Systems: Networks of Plausible Inference*. Morgan Kaufmann, 1988.
- [94] Q. Yang, L. Wang, and N. Ahuja, “A constant-space belief propagation algorithm for stereo matching,” pp. 1458–1465, International Conference on Computer Vision and Pattern Recognition, 2010.
- [95] N. Komodakis and G. Tziritas, “Approximate labeling via graph cuts based on linear programming,” *IEEE Transaction on Pattern Analysis and Machine Learning*, vol. 29, pp. 1436–1453, 2007.
- [96] B. Glocker, N. Komodakis, G. Tziritas, N. Navab, and N. Paragios, “Dense image registration through mrfs and efficient linear programming,” *Medical Image Analysis*, vol. 12, p. 731741, 2008.
- [97] R. Keys, “Cubic convolution interpolation for digital image processing,” *IEEE Transactions on Signal Processing, Acoustics, Speech, and Signal Processing*, vol. 29, p. 11531160, 1981.
- [98] A. K. Singh, J. Kruecker, S. XU, N. Glossop, P. Guion, K. Ullman, P. L. Choyke, and B. J. Wood, “Initial clinical experience with real-time transrectal ultrasoundography-magnetic resonance imaging fusion-guided prostate biopsy,” *British Journal of Urology International*, pp. 841–854, 2008.
- [99] L. R. Dice, “Measures of the amount of ecologic association between species,” *Ecology*, vol. 26, p. 297302, 1945.
- [100] D. P. Huttenlocher, G. A. Klanderman, and W. J. Rucklidge, “Comparing images using the hausdorff distance,” *IEEE Transaction in Pattern Analysis and Machine Intelligence*, vol. 15, p. 850863, 1993.
- [101] M. Groher, D. Zikic, and N. Navab, “Deformable 2d-3d registration of vascular structures in a one view scenario,” *IEEE Transaction on Medical Imaging*, vol. 28, pp. 847–860, 2009.
- [102] K. Rohr, “Elastic registration of multimodal medical images: A survey,” *KI-Künstliche Intelligenz*, vol. 3, pp. 11–17, 2000.
- [103] L. Chmielewski and D. Kozinska, “Image registration,”
- [104] J. Modersitzki, *Numerical Methods for Image Registration*. Oxford University Press, 2004.
- [105] J. Modersitzki, *Flexible Algorithms for Image Registration*. SIAM, 2009.

- [106] A. A. Goshtasby, *Image Registration Principles, Tools and Methods*. Springer, 2012.
- [107] M. Deshmukh and U. Bhosle, “A survey of image registration,” *International Journal of Image Processing*, vol. 5, pp. 245–269, 2011.
- [108] A. Roche, X. Pennec, G. Malandain, and N. Ayache, “Rigid registration of 3d ultrasound with mr images: a new approach combining intensity and gradient information,” *IEEE Transactions on Medical Imaging*, vol. 20, pp. 1038–1049, 2001.
- [109] A. Roche, G. Malandain, X. Pennec, and N. Ayache, “The correlation ratio as a new similarity measure for multimodal image registration,” in *Proc. of Medical Image Computing and Computer-Assisted Intervention*, pp. 1115–1124, 1998.
- [110] M. D. Craene, A. du Bois d’Aische, and B. Macq, “Multi-modal non-rigid registration using a stochastic gradient approximation,” in *International Symposium Biomedical Imaging*, 2004.
- [111] J. Mitra, Z. Kato, R. Marti, A. Oliver, , X. Llado, , D. Sidibe, S. Ghose, J. C. Vilanova, and F. Meriaudeau, “Prostate multimodality image registration based on b-splines and quadrature local energy,” *International Journal for Computer Assisted Radiology and Surgery*, vol. 7, pp. 445–454, 2012.
- [112] D. C. Liu and J. Nocedal, “On the limited memory method for large scale optimization,” *Mathematical Programming*, vol. 45, p. 503528, 1989.
- [113] C. Reynier, J. Troccaz, P. Fournieret, A. Dusserre, C. Gayjeune, J. Descotes, M. Bolla, and J. Giraud, “Mri/trus data fusion for prostate brachytherapy. preliminary results,” *Medical Physics*, vol. 31, pp. 1568–1575, 2004.
- [114] R. Szeliski and S. Lavallee, “Matching 3-d anatomical surfaces with non-rigid deformations using octree-splines,” *International Journal of Computer Vision*, vol. 18, pp. 171–196, 1996.
- [115] V. Daanen, J. Gastaldo, J. Y. Giraud, P. Fournieret, J. L. Descotes, M. Bolla, D. Collomb, and J. Troccaz, “Mri/trus data fusion for brachytherapy,” *International Journal of Medical Robotics*, vol. 2, p. 256261, 2006.
- [116] R. Narayanan, J. Kurhanewicz, K. Shinohara, D. E. Crawford, A. Simoneau, and J. S. Suri, “Mri-ultrasound registration for targeted prostate biopsy,” in *Proc. IEEE International Symposium on Biomedical Imaging*, 2009.
- [117] H. M. Ladak, F. Mao, Y. Wang, D. B. Downey, D. A. Steinman, and A. Fenster, “Prostate boundary segmentation from 2d ultrasound images,” in *Proc. IEEE Computer Methods and Programs in Biomedicine*, 2000.
- [118] C. Goodall, “Procrustes methods in the statistical analysis of shape,” *Royal Statistical Society*, vol. 53, pp. 285–339, 1991.

- [119] D. Shen, E. Herskovits, and C. Davatzikos, “An adaptive-focus statistical shape model for segmentation and shape modeling of 3d brain structures,”
- [120] H. M. Ladak, F. Mao, Y. Wang, D. B. Downey, D. A. Steinman, and A. Fenster, “Clinical application of a 3d ultrasound-guided prostate biopsy system,” *Urologic Oncology*, vol. 29, pp. 334–342, 2011.
- [121] V. Karnik, A. Fenster, and J. Bax, “Assesment of image registration accuracy in 3-dimentional transrectal ultrasound guided prostate biopsy,” *Medical Physics*, vol. 37, 2010.
- [122] Lange, Eulenstein, Hnerbein, and Schlag, “Vessel-based non-rigid registration of mr/ct and 3d ultrasound for navigation in liver surgery,” *Computer Aided Surgery:Journal Of The International Society For Computer Aided Surgery*, no. 5.
- [123] S. Ghose, A. Oliver, R. Mari, X. Llado, J. Freixenet, J. C. Vilanova, and F. Meriaudeau, “Texture guided active appearance model propagation for prostate segmentation,” *Prostate Cancer Imaging*, 2010.
- [124] Y. Hu, H. U. Ahmed, C. A. an D. Pendse, M. Sahu, M. Emberton, D. Hawkes, and D. Barratt, “Mr to ultrasound image registration for guiding prostate biopsy and interventions,” in *Proc. of Medical Image Computing and Computer Assisted Intervention*, p. 787794, 2009.
- [125] Y. Hu, H. U. Ahmed, Z. Taylor, C. Allem, M. Emberton, D. Hawkes, and D. Barratt, “Mr to ultrasound registration for image-guided prostate interventions,” *Medical Image Analysis*, year = 2012, volume = 16, pages = 687703,.
- [126] A. Cosse, “Diffeomorphic surface-based registration for mr-us fusion in prostate brachytherapy,” in *Proc. IEEE Mediterranean Electrotechnical Conference*, pp. 903–907, 2012.
- [127] X. Pennec, P. Cachier, and N. Ayache, “Understanding the demons algorithm: 3d non-rigid registration by gradient descent,” p. 597605, *Proc. of Medical Image Computing and Computer Assisted Intervention*, 1999.
- [128] X. Lu, S. Zhang, Y. Zha, and Y. Chen, “Three-dimentional nonrigid registration and fusion for image-guided surgery navigation system,” *Proc. of Medical Image Computing and Computer Assisted Intervention*, 2010.
- [129] J. T. Nicholas, B. A. Brian, and C. G. Jams, “Directly manipulated free-form deformation image registration,” *IEEE Transaction on Image Processing*, vol. 18, pp. 624–635, 2009.
- [130] L. A. Vese and S. J. Osher, “Image denoising and decomposition with total variation minimization and oscillatory functions,” *Journal of Mathematical Imaging and Vision*, vol. 20, pp. 7–18, 2004.

- [131] X. Lu, S. Zhang, H. S., and Y. Chen, “Mutual information-based multimodal image registration using a novel joint histogram estimation,” *Journal of Computerized Medical Imaging and Graphics*, vol. 32, pp. 202–209, 2008.
- [132] T. M. Lehmann, C. Gonner, and K. Spitzer, “Survey: Interpolation methods in medical image processing,” *IEEE Transaction on Medical Imaging*, vol. 18, pp. 1049–1075, 1999.
- [133] T. Lange, N. Papenberg, S. Heldmann, J. Modersitzki, B. Fischer, H. Lamecker, and P. Schlag, “3d ultrasound-ct registration of the liver using combined landmark-intensity information,” *International Journal of Computer Assisted Radiology and Surgery*, vol. 4, no. 1, pp. 79–88, 2009.
- [134] B. Amberg, S. Romdhani, and T. Vetter, “Optimal step nonrigid icp algorithm for surface registration,” in *IEEE Computer Vision and Pattern Recognition*, 2007.
- [135] P. J. Besl and N. D. McKay, “A method for registering of 3-d shapes,” *IEEE Transaction on Pattern Analysis and Machine Intelligence*, vol. 14, pp. 239–256”, 1992.
- [136] Y. Chen and G. Medioni, “Object modeling by registration of multiple range images,” in *International Conference on Robotics and Automation*, vol. 3, pp. 2724–2729, IEEE, 1991.
- [137] S. Rusinkiewicz and M. Levoy, “Efficient variants of the icp algorithm,” *International Conference on 3D Digital Imaging and Modeling*, 2001.
- [138] A. W. Fitzgibbon and M. Levoy, “Robust registration of 2d and 3d point sets,” *Image and Vision Computing*, pp. 1145–1153, 2003.
- [139] A. Myronenko and X. Song, “Point set registration: Coherent point drift,” *IEEE Transaction on Pattern Analysis and Machine Intelligence*, vol. 32, pp. 2262–2275, 2010.
- [140] Z. Zhang, “Iterative points matching for registration of free form curves and surfaces,” *International Journal of Computer Vision*, vol. 13, 1994.
- [141] J. L. Bentley, “Multidimensional binary search trees used for associative searching,” *Communications of the Association for Computing Machinery*, vol. 18, p. 509517, 1975.
- [142] J. H. Friedman, J. L. Bentley, and R. A. Finkel, “An algorithm for finding best matches in logarithmic expected time,” *ACM Transactions on Mathematical Software*, vol. 3, p. 209226, 1977.
- [143] D. A. Simon, *Fast and Accurate Shape-Based Registration*. PhD thesis, Carnegie Mellon University, 1996.

- [144] A. Nuchter, K. Lingemann, and J. Hertzberg, “Cached k-d tree search for icp algorithms,” International Conference on 3-D Digital Imaging and Modeling, 2007.
- [145] K. Pulli, “Multiview registration for large data sets,” International Conference on 3-D Digital Imaging and Modeling, 1999.
- [146] U. Castellani and A. Bartoli, *3D Shape Registration*. 3D Imaging, Analysis, and Applications, 2012.
- [147] F. Hampel, P. Rousseeuw, E. Ronchetti, and W. Stahel, *Robust Statistics: The Approach Based on Influence Functions*. Wiley, 1986.
- [148] U. Castellani, A. Fusiello, and V. Murino, “Registration of multiple acoustic range views for underwater scene reconstruction,” *Computer Vision and Image Understanding*, vol. 87, p. 7889, 2002.
- [149] J. Phillips, R. Liu, and C. Tomasi, “Outlier robust icp for minimizing fractional rmsd,” p. 427434, International Conference on 3-D Digital Imaging and Modeling, 2007.
- [150] H. Chui and A. Rangarajan, “A new point matching algorithm for non-rigid registration,” *Computer Vision and Image Understanding*, vol. 89, pp. 114–141, 2003.
- [151] W. Wells, “Statistical approaches to feature-based object recognition,” *International Journal of Computer Vision*, vol. 21, pp. 63–98, 1997.
- [152] A. D. J. Cross and E. R. Hancock, “Graph matching with a dual-step em algorithm,” *IEEE Transactions on Pattern Analysis and Machine Intelligence*, vol. 20, pp. 1236–1253, 1998.
- [153] G. Hinton, C. Williams, and M. Revow, *Adaptive Elastic Models for Hand-printed Character Recognition*. Advances in Neural Information Processing Systems, 1992.
- [154] S. Gold, A. Rangarajan, C. P. Lu, S. Pappu, and E. Mjolsness, “New algorithms for 2-d and 3-d point matching: Pose estimation and correspondence,” *Pattern Recognition*, vol. 31, pp. 1019–1031, 1998.
- [155] A. Rangarajan, H. Chui, and F. Bookstein, “The softassign procrustes matching algorithm,” *Information Processing in Medical Imaging*, pp. 29–42, 1997.
- [156] H. Chui, J. Rambo, J. Duncan, R. Schultz, and A. Rangarajan, “Registration of cortical anatomical structures via robust 3d point matching,” *Information Processing in Medical Imaging*, 1999.
- [157] H. Livyatan, Z. Yaniv, and L. Joskowicz, “Gradient-based 2d/3d rigid registration of fluoroscopic x-ray to ct,” *IEEE Transaction on Medical Imaging*, vol. 22, pp. 1395–1406, 2003.

- [158] J. Yao and R. Taylor, “Deformable 2d-3d medical image registration using a statistical model: Accuracy factor assessment,” *American Journal of Science and Engineering*, vol. 1, 2012.
- [159] R. S. J. Estépar, C. Westin, and K. G. Vosburgh, “Towards real time 2d to 3d registration for ultrasound-guided endoscopic and laparoscopic procedure,” *International Journal for Computer Assisted Radiology and Surgery*, vol. 4, 2009.
- [160] P. Markelj, D. Tomaževič, B. Likar, and F. Pernuš, “A review of 3d/2d registration methods for image-guided interventions,” *Medical Image Analysis*, pp. 642–661, 2012.
- [161] M. Groher, *2D-3D Registration of Vascular Images Towards 3D-Guided Catheter Interventions*. PhD thesis, Technical University of Munich, 2008.
- [162] C. Barry, C. Allott, N. John, P. Mellor, P. Arundel, D. Thomson, and J. Waterton, “Three-dimensional freehand ultrasound: Image reconstruction and volume analysis,” *Ultrasound in Medicine and Biology*, vol. 23, pp. 1209–1224, 1997.
- [163] P. Coupe, P. H. N. Azzabou, and C. Barillot, “3d freehand ultrasound reconstruction based on probe trajectory,” in *Proc. of Medical Image Computing and Computer-Assisted Intervention*, pp. 597–604, 2005.
- [164] R. Rohling, *3D Freehand Ultrasound: Reconstruction and Spatial Compounding*. PhD thesis, University of Cambridge, 1998.
- [165] S. Heldmann and N. Papenberg, “A variational approach for volume-to-slice registration,” pp. 624–635, *Proc. of Medical Image Computing and Computer Assisted Intervention*, 2009.
- [166] B. Fei, J. L. Durek, D. T. Boll, J. S. Lewin, and D. L. Wilson, “Slice-to-volume registration and its potential application to interventional mri-guided radio-frequency thermal ablation of prostate cancer,” *IEEE Transaction on Medical Imaging*, vol. 22, pp. 515–524, 2003.
- [167] S. Gill, P. Abolmaesumi, S. Vikal, P. Mousavi, and G. Fichtinger, “Intraoperative prostate tracking with slice-to-volume registration in mri,” in *Proceedings of the International Conference of the Society for Medical Innovation and Technology*, pp. 154–158, 2008.
- [168] S. Xu, G. Fichtinger, R. Taylor, and K. Cleary, “3d motion tracking of pulmonary lesions using ct fluoroscopy images for robotically assisted lung biopsy,” in *Medical Imaging 2004: Visualization, Image-Guided Procedures, and Display*, vol. 5367, pp. 394–402, SPIE, 2004.
- [169] E. Ferrante and N. Paragios, “Non-rigid 2d-3d medical image registration using markov random fields,” pp. 163–170, *Proc. of Medical Image Computing and Computer Assisted Intervention*, 2013.

- [170] S. Osechinskiy and F. Kruggel, "Slice-to-volume nonrigid registration of histological sections to mr images of the human brain," *Journal of Anatomy Research International*, 2010.
- [171] R. Dalvi and R. Abugharibeh, "Fast feature based multi slice to volume registration using phase congruency," pp. 5390–5393, Proc. IEEE Engineering in Medicine and Biology Society, 2008.
- [172] D. Mattes, D. R. Haynor, H. Vesselle, T. K. Lewellen, and W. Eubank, "Pet-ct image registration in the chest using free-form deformations," *IEEE Transactions on Medical Imaging*, vol. 22, no. 1, pp. 120–128, 2003.
- [173] D. Rueckert, L. I. Sonoda, C. Hayes, D. L. G. Hill, M. O. Leach, and D. J. Hawkes, "Nonrigid registration using free-form deformations: Application to breast MR images," *IEEE Transactions on Medical Imaging*, vol. 18, pp. 712–721, 1999.
- [174] F. Bookstein, "The measurement of biological shape and shape change," *Lecture Notes in Biomathematics*, vol. 24, 1978.
- [175] F. Bookstein, "Linear methods for nonlinear maps: Procrustes fits, thin-plate splines, and the biometric analysis of shape variability," *Brain Warping*, pp. 157–181, 1999.
- [176] F. Bookstein, *Morphometric Tools for Landmark Data*. Cambridge University Press, 1991.
- [177] K. Rohr, H. Stiehl, R. Sprengel, T. Buzug, J. Weese, and M. Kuhn, "Landmark-based elastic registration using approximating thin-plate splines," *IEEE Transactions on Pattern Analysis and Machine Intelligence*, vol. 20, pp. 526–534, 2001.
- [178] S. Lee, G. Wolberg, K. Chwa, and S. Shin, "Image metamorphosis with vscattered feature constraints," *IEEE Transactions on Visualization and Computer Graphics*, vol. 2, pp. 337–354, 1996.
- [179] S. Lee, G. Wolberg, and S. Shin, "Scattered data interpolation with multilevel b-splines," *IEEE Transactions on Visualization and Computer Graphics*, vol. 3, pp. 228–244, 1997.
- [180] E. Bardinet, L. Cohen, and N. Ayache, "Tracking and motion analysis of the left ventricle with deformable superquadrics," *Medical Image Analysis*, vol. 1, pp. 129–149, 1996.
- [181] H. Prautzsch, W. Boehm, and M. Paluszny, *Bézier and B-Spline Techniques*. Springer-Verlag, 2002.
- [182] D. Forsey and R. H. Barrells, "Hierarchical b-spline refinement," *Computer Graphics*, vol. 22, pp. 205–212, 1988.

- [183] G. Wahba, *Spline Models for Observational Data*. Society for Industrial and Applied Mathematics, 1990.
- [184] F. Maes, A. Collignon, D. Vandermeulen, G. Marchal, and P. Suetens, “Multimodality image registration by maximization of mutual information,” *IEEE Transactions on Medical Imaging*, vol. 16, pp. 187–198, 1997.
- [185] C. Studholme, D. Hill, and D. Hawkes, “Automated 3d registration of mr and pet brain images by multi-resolution optimization of voxel similarity measures,” *Medical Physics*, vol. 24, pp. 25–35, 1997.
- [186] J. Mitra, R. Marti, A. Oliver, X. Llado, S. Ghose, and Z. Kato, “A non-linear diffeomorphic framework for prostate multimodal registration,” in *Digital Image Computing: Techniques and Applications*, pp. 31–36, IEEE, 2011.
- [187] J. P. Thirion, “Image matching as a diffusion process: An analogy with maxwell’s demons,” *Medical Image Analysis*, vol. 2, pp. 243–260, 1998.
- [188] M. Y. Chu, H. M. Chen, C. Y. Hsieh, T. H. Lin, H. Y. Hsiao, G. Liao, and Q. Peng, “Adaptive grid generation based non-rigid image registration using mutual information for breast mri,” *Journal of Signal Processing System*, vol. 54, pp. 54–63, 2009.
- [189] H. Y. S. Hsiao, *Helmholtz’s Theorem Based Parametric Non-Rigid Image Registration*. PhD thesis, University of Texas, December 2009.
- [190] M. S. R. Alam, “Implementation of divergence and curl operators embedded cost function in deformable image registration for adaptive radiotherapy,” Master’s thesis, Politecnico Di Milano, December 2011.
- [191] J. M. Jin, *Theory and Computation of Electromagnetic Fields*. Wiley.
- [192] B. Fischer and J. Modersitzki, “Ill-posed medicine - an introduction to image registration,” *Inverse Problems*, vol. 24, pp. 117–129, 2008.
- [193] B. Fischer and J. Modersitzki, “Curvature based image registration,” *Journal of Mathematical Imaging and Vision*, vol. 18, pp. 81–85, 2003.
- [194] R. Davies, C. Twining, and C. Taylor, *Statistical Models of Shape Optimization and Evaluation*. Springer, 2008.
- [195] B. Rosenhahn, T. Brox, D. Cremers, and H.-P. Seidel, “A comparison of shape matching methods for contour based pose estimation,” in *International Workshop on Combinatorial Image Analysis*, vol. 4040 of *Lecture Notes in Computer Science*, pp. 263–276, Springer, 2006.
- [196] N. Paragios, M. Rousson, and V. Ramesh, “Non-rigid registration using distance functions,” *Computer Vision and Image Understanding*, vol. 89, pp. 142–165, 2003.

- [197] R. W. Brockett and P. Maragos, “Evolution equations for continuous-scale morphology,” in *IEEE International Conference on Acoustics, Speech and Signal Processing*, vol. 3 of *Lecture Notes in Computer Science*, p. 125128, 1992.
- [198] J. Feldmar and N. Ayache, “Rigid, affine and locally affine registration of free-form surfaces,” *International Journal of Computer Vision*, vol. 18, 1996.
- [199] L. J. Latecki and R. Lakämper, “Shape similarity measure based on correspondence of visual parts,” *IEEE Transactions on Pattern Analysis and Machine Intelligence*, vol. 22, 2000.
- [200] N. Paragios, M. Rousson, and V. Ramesh, “Distance transforms for non-rigid registration,” *Computer Vision and Image Understanding*, vol. 23, 2003.
- [201] K. Siddiqi, A. Shokoufandeh, S. Dickinson, and S. Zucker, “Shock graphs and shape matching,” *International Journal of Computer Vision*, vol. 35, 1999.
- [202] R. Veltkamp and M. Hagedoorn, “State-of-the-art in shape matching,” tech. rep., Utrecht University, 1999.
- [203] A. Rosenfeld and J. Pfaltz, “Sequential operations in digital picture processing,” *Journal of the Association for Computing Machinery*, vol. 13, pp. 471–494, 1966.
- [204] R. Fabbri, L. D. F. Costa, J. C. Torelli, and O. M. Bruno, “2d euclidean distance transform algorithms: A comparative survey,” *Journal of the Association for Computing Machinery Computing Surveys*, vol. 40, 2008.
- [205] C.-S. Chiang, *The Euclidean Distance Transform*. PhD thesis, Purdue University, August 1992.
- [206] A. Yavariabdi, C. Samir, A. Bartoli, D. D. Ines, and N. Bourdel, “Mapping endometrial implants by 2d/2d registration of tvus to mr images from point correspondences,” in *International Symposium Biomedical Imaging*, IEEE, 2013.
- [207] T. Bennett, *Transport by Advection and Diffusion*. Wiley, 2012.
- [208] A. Yavariabdi, C. Samir, A. Bartoli, D. D. Ines, and N. Bourdel, “Contour-based tvus-mr image registration for mapping small endometrial implants,” in *Proc. of the Fifth on Computational and Clinical Applications in Abdominal Imaging at MICCAI*, 2013.
- [209] A. Bruhn, J. Weickert, C. Feddern, T. Kohlberger, and C. Schnorr, “Real-time optic flow computation with variational methods,” pp. 222–229, *Proc. of Computer Analysis of Images and Patterns*, 2003.
- [210] N. Jamil, “A comparison of direct and indirect solvers for linear systems of equations,” *International Journal of Emerging Sciences*, vol. 2, pp. 310–321, 2012.

- [211] S. J. Ahn, *Least Squares Orthogonal Distance Fitting of Curves and Surfaces in Space*. Springer, 2004.
- [212] S. Kels and N. Dyn, “Reconstruction of 3d objects from 2d cross-sections with the 4-point subdivision scheme adapted to sets,” *Computers & Graphics*, vol. 35, no. 3, pp. 741–746, 2011.
- [213] M. Feuerstein, *Augmented Reality in Laparoscopic Surgery New Concepts for Intraoperative Multimodal Imaging*. PhD thesis, Technischen Universität München, 2007.
- [214] H. Fuchs, M. A. Livingston, R. Raskar, A. State, J. R. Crawford, P. Rademacher, S. H. Drake, and A. A. Meyer, “Augmented reality visualization for laparoscopic surgery,” in *In Proceedings of the First International Conference on Medical Image Computing and Computer-Assisted Intervention*, pp. 934–943, 1998.
- [215] T. Collins, D. Pizarro, A. Bartoli, M. Canis, and N. Bourdel, “Realtime wide-baseline registration of the uterus in laparoscopic videos using multiple texture maps,” in *In Proceedings of the Augmented Reality Environments for Medical Imaging and Computer-Assisted Interventions*, pp. 162–171, 2013.
- [216] G. Chang and M. Vetterli, “Resolution enhancement of images using wavelet transform extrema extrapolation,” in *Proc. Int. Conf. Acoustics, Speech, Sig. Process*, 1995.
- [217] W. K. Carey, D. B. Chuang, and S. S. Hemami, “Regularity-preserving image interpolation,” *IEEE Trans. on Image Proc.*, vol. 8, pp. 1293–1297, 1997.
- [218] A. Temizel and T. Vlachos, “Wavelet domain image resolution enhancement using cycle spinning and edge modelling,” in *Proc. EUSIPCO*, 2005.
- [219] W. C. Yen, Y. Y. Chen, and Y. W. Chang, “An enlargement method using undecimated wavelet transform and shape function,” in *International Conference on Intelligent Information Hiding and Multimedia Signal Processing*, 2009.
- [220] H. Demirel and G. Anbarjafari, “Image resolution enhancement by using discrete and stationary wavelet decomposition,” *IEEE Trans. Image Proc.*, vol. 99, 2010.
- [221] H. Demirel and G. Anbarjafari, “Discrete wavelet transform-based satellite image resolution enhancement,” *IEEE TGRS*, 2011.
- [222] A. Temizel, “Image resolution enhancement using wavelet domain hidden markov tree and coefficient sign estimation,” *IEEE ICIP*, pp. 381–384, 2007.